Bridging the capability gap in environmental gamma-ray spectroscopy

Adam Varley

2015

Submitted to Biological and Environmental Sciences

School of Natural Sciences

University of Stirling

Scotland

For the degree of Doctor of Philosophy

Supervisor:

Prof. Andrew Tyler

UNIVERSITY OF
STIRLING

Statement of originality

I hereby confirm that this PhD thesis is an original piece of work conducted independently by the undersigned and all work contained herein has not be submitted for any other degree.

All research has been duly acknowledged and cited:

Signature of Candidate:

Adam Varley

Date

General abstract

Environmental gamma-ray spectroscopy provides a powerful tool that can be used in environmental monitoring given that it offers a compromise between measurement time and accuracy allowing for large areas to be surveyed quickly and relatively inexpensively. Depending on monitoring objectives, spectral information can then be analysed in real-time or post survey to characterise contamination and identify potential anomalies.

Smaller volume detectors are of particular worth to environmental surveys as they can be operated in the most demanding environments. However, difficulties are encountered in the selection of an appropriate detector that is robust enough for environmental surveying yet still provides a high quality signal. Furthermore, shortcomings remain with methods employed for robust spectral processing since a number of complexities need to be overcome including: the non-linearity in detector response with source burial depth, large counting uncertainties, accounting for the heterogeneity in the natural background and unreliable methods for detector calibration.

This thesis aimed to investigate the application of machine learning algorithms to environmental gamma-ray spectroscopy data to identify changes in spectral shape within large Monte Carlo calibration libraries to estimate source characteristics for unseen field results. Additionally, a 71 × 71 mm lanthanum bromide detector was tested alongside a conventional 71 × 71 mm sodium iodide to assess whether its higher energy efficiency and resolution could make it more reliable in handheld surveys.

The research presented in this thesis demonstrates that machine learning algorithms could be successfully applied to noisy spectra to produce valuable source estimates. Of note, were the novel characterisation estimates made on borehole and handheld detector measurements taken from land historically contaminated with ^{226}Ra. Through a novel combination of noise suppression and neural networks the burial depth, activity and source extent of contamination was estimated and mapped. Furthermore, it was demonstrated that Machine Learning techniques could be operated in real-time to identify hazardous ^{226}Ra containing *hot particles* with much greater confidence than current deterministic approaches such as the gross counting algorithm. It was concluded that remediation of ^{226}Ra contaminated legacy sites could be greatly improved using the methods described in this thesis.

Finally, Neural Networks were also applied to estimate the activity distribution of ^{137}Cs, derived from the nuclear industry, in an estuarine environment. Findings demonstrated the method to be theoretically sound, but practically inconclusive, given that much of the contamination at the site was buried beyond the detection limits of the method.

It was generally concluded that the noise posed by intrinsic counts in the 71 × 71 mm lanthanum bromide was too substantial to make any significant improvements over a comparable sodium iodide in contamination characterisation using 1 second counts.

Acknowledgements

During the course of my PhD I have received support from a number of people. First of all, this collection of work would never have been possible if it were not for the encouragement, expertise and overall enthusiasm of my supervisor Professor Andrew Tyler. His willingness to listen, provide prompt feedback and end every conversation with an effervescent laugh made him a real pleasure to work with and I look forward to continue such adventures.

Special thanks must also be given to Professor Leslie Smith for all things data-driven, Mike Davies for his guidance in Monte Carlo modelling, Pete Burgess for a truly commercial perspective on this topic and Dr. Paul Dale, not just for his fondness of critique (especially of me), but also his willingness to allow me to accompany SEPA onto the majority of sites involved in this thesis. To those who helped me with fieldwork, totably during testing times that always managed to leave me with a smile on my face: Stuart Bradley, Christopher Sneddon, Corynne Mcquire and Mark Toner.

Personal friends who were never that far away from a barstool on Friday night, most notably Alan Law, Romauld Rouger, Rebecca Barclay, Charles Perfect, Thomas Parker, Lucy Kirkpatrick, Izzy Jones, Renee Hermans, Zara Pattinson, Emma, Caroline, Rachel and Keith, Jens, Cerian, Amani, Junyao, Pierre… thankfully the list goes on.

A massive thank you must go to my Father, Richard Varley, for all his kind proof reading and his loving nature in general. Also, my sister, Laura, for all the long distance phone calls to keep me on track. Derrick and Diane for your loving support

and good taste in whisky and wines, respectively. My brother for your curious nature. And too my many other family members to mention…

For looking after me and constantly being my emotional pillar, my dearest Rebecca. I hope you continue to be as supportive and loving wherever life takes us and no matter how testing I become.

Finally, to my wonderful late mother, Gill Varley, and late grandmother “Nain”. It has been under your constant love, support and guidance that have got me to where I am today. So, I dedicate this to you: the Matriarchs.

Contents

5 Remediating radium contaminated legacy sites: advances made through Machine Learning in routine monitoring of "hot" particles. 119

1 Introduction

1.1 Radioactivity in the environment

Radioactivity is an integral part of the environment, from the bombardment of cosmic rays from space and subsequent excitation products to primordial radioisotopes and their respective decay chains that can be linked back to the formation of the universe itself (Dauer, 2002). Humans have evolved around natural sources of radiation and as a result have built up, to a certain extent, a biological resistance to its ionising effects. Nonetheless, significant implications on human health were only formally recognised with exposure to anthropogenic-derived radionuclides (Stannard & Baalman Jr, 1988).

The first well documented example of human exposure to radioactivity is that of ^{226}Ra, a naturally occurring radioactive material (NORM) first isolated from pitchblende by Marie and Pierre Curie (Gillmore et al., 2012). ^{226}Ra was used in a wide range of military, confectionary and pharmaceutical products (Tyler et al., 2013). Perhaps the most beneficial application of ^{226}Ra was when it was mixed with ZnS to produce a seemingly unbroken light source, otherwise known as “Undark” (Stebbings, 2001). This composite famously led to high morbidity and mortality rates among the New Jersey radium workers of the mid 1920s, bringing about what would form the foundation of contemporary radiological protection countermeasures (Stannard & Baalman Jr, 1988).

Although the worldwide production of ^{226}Ra decreased considerably after World War II, vast inventories of waste has given rise to a large number of localised contaminated sites across the world that still pose a significant health risk today, for example Olen in Belgium and the Denver radium site in the the United States (Adams, 1993, Landa, 1993, Adsley et al., 2004). In the UK, it is thought that many radium contaminated legacy sites either lay undiscovered or remain overlooked. What is more, when considering ^{226}Ra has a half-life of 1600 years, these sites represent a serious issue for future generations and not just our own (DECC, 2012).

The bombings of Hiroshima and Nagasaki in 1945 abruptly brought us into the modern nuclear age. Since then, a wide diversity of fission and activation products have consistently been introduced into the environment from further nuclear weapons detonations and accidental and authorised releases from nuclear facilities (Maučec et al., 2004). Perhaps the most important long-term contributor to the environmental radiation dose is ^{137}Cs (Miller, 2007). Its radiological prominence is partly due to its chemical properties and its relatively long half-life of 32 years which has allowed it to readily disperse over the globe presenting a complex spatial and temporal distribution (Povinec et al., 2003). In certain regions, particularly close to a major source of ^{137}Cs, highly contaminated areas can be encountered.

In the UK, the Sellafield nuclear reprocessing plant on the west coast of Cumbria provides a textbook example. It has legitimately released ^{137}Cs into the Irish Sea since the early 1950s. An unexpected outcome of these releases is that a significant proportion of the total inventory has been remobilised from the Irish Sea leading to accumulation in coastal sediments presenting a potential exposure pathway for the general population (Cook et al., 1997).

Taken on a worldwide scale, average human exposure to natural radiation still dwarfs that of anthropogenic radiation by an order of magnitude (Dauer, 2002). However, sites that are highly contaminated with ^{226}Ra or ^{137}Cs have the potential to cause significant radiological harm to sections of the general public. What is more, public perception studies reveal that the radioactive waste associated with these types of site is still considered as high risk by society (Slovak, 2012).

Radioactively contaminated land is particularly hazardous when *hot particles* are encountered (Dale et al., 2008). *Hot particles* are by definition small highly radioactive heterogeneous fragments of contamination that could be handled or ingested by a member of the public (Tyler et al., 2013). However, significant difficulties are encountered when trying resolve *hot particles* from less hazardous homogeneous contamination using conventional detection approaches (Dale et al., 2013). This scenario presents a significant challenge to overcome to provide public safety and reassurance (ICRU, 2006).

1.2 Environmental monitoring

There are a number of sampling procedures that can make up an environmental radioactivity monitoring approach. The implementation of these methods is very much dependent on the monitoring objectives, which are designed to assess potential exposure pathways. Sampling methods can range from human habits surveys to water and food sampling. Activity of contamination contained in the soil potentially presents a number of exposure pathways (ICRU, 2006). As a result, source characteristics must be accurately estimated for a contaminated soil, for example information regarding the radio-contaminant's activity and depth and whether it is likely to be heterogonous or homogeneous in form.

This task can be achieved using soil sampling, which can provide a suite of information describing different types of radionuclides and respective activities. Nonetheless, it is labour intensive, very expensive, and subsequently, can result in poor spatial representation due to a lack of sample points (Tyler, 2008). Conversely, air kerma measurements will acquire an instant dose rate, thereby allowing large areas to be rapidly mapped with a high spatial density. However, this method offers no distinction between radionuclides, making the important step of soil activity estimation almost impossible.

It has become evident that neither of these sampling methods can practically characterise changes in depth and activity that occur on a local scale: a capability that is of particular importance when searching for *hot particles* or highly active localised homogeneous contamination (Tyler et al., 2010).

1.3 Environmental gamma-ray spectroscopy

Environmental gamma-ray spectroscopy is a powerful monitoring tool, which utilises the penetrative qualities of gamma radiation to detect, and crucially differentiate the energy of photons, that exit the soil and interact with the detector. The resulting pulse height spectrum can then be unfolded using features such as full energy peaks, to isolate different radionuclides, and regions that accumulate scattered photons, to infer the amount of shielding (depth) between a source and the detector.

Traditionally, a large number of short measurements are taken during an environmental gamma-ray spectroscopy survey in order to maximise the spatial density of sampling points and thus allow for the coverage of large areas. Ultimately, reliable interrogation of spectral data can provide a means of characterising extensive areas of contamination. Due to this capability, gamma-ray spectroscopy has become the mainstay of large-scale radio-contaminant mapping (Hovgaard, 1997, Aage et al., 1999, IAEA, 1998, Allyson & Sanderson, 2001, Dickson, 2004) and has been instrumental in *hot particle* detection (Davies et al., 2007, Long & Martin, 2007, Kock et al., 2010). As a result, it has been expanded onto numerous platforms, such as handheld (Plamboeck et al., 2006), carborne (Dowdall et al., 2012), aerial (Aage et al., 1999), unmanned aerial vehicles (Martin et al., 2015), borehole (Bugai et al., 2005) and sub-aqua (Dennis et al., 2007).

1.4 Challenges facing environmental gamma-ray spectroscopy

Despite gamma-ray spectroscopy being a powerful environmental monitoring tool, there still remain a number of challenges associated with the characterisation of radioactive contaminated land. This is especially the case when using practical smaller volume detectors that can be routinely deployed.

The first issue encountered is that no single detector can fulfil all of the specifications needed for the practical demands of routine deployment. For instance, High Purity Germanium (HPGe), although it provides the highest energy resolution accessible, its practical application in rugged terrain is limited due to its need to be constantly cooled making detection units heavy and immobile (Davies et al., 2007). A more robust alternative is sodium iodide (NaI:Tl) (Adsley et al., 2004). Nonetheless, it lacks the required energy resolution to confidently separate common environmental radionuclides (Tyler, 1999).

The second issue is how to reliably process the spectral output of a detector to obtain the most representative characterisation information: solving this problem is however innately difficult as a number of confounding factors must be addressed.

Firstly, the signal received by any detector will contain pronounced contributions from background sources, primarily the natural radioelements ^{40}K and the ^{238}U and ^{232}Th series (Kluson, 2001). Furthermore, this signal will not remain constant as changes in geology, density, moisture content, chemical composition and atmospheric pressure can bring about considerable changes in differential photon flux (Dickson, 2004). Accounting for these benign systematic changes presents a significant challenge. A further problem is confronted with the burial of a source. Not only will its total flux diminish according to the inverse square law, but also the overall shape of the spectrum will change non-linearly with increasing amounts of soil overburden (Wei et al., 2010). This introduces a complex multivariate problem, and at the same time, represents a significant calibration challenge, which can be difficult to account for using conventional analytical calibration methods (Maučec et al., 2009). A final issue, that affects smaller volume detectors in particular, is that large counting uncertainties can introduce a significant noise component within an environmental gamma-ray spectrum owing to the short count times used (Du et al., 2010).

As a consequence of these complications, straightforward spectral processing algorithms are regularly adopted in the field, most of which are based on rigid assumptions about the source distribution, which may quickly become invalid as the detector moves away from any calibration area. Here, we explore whether the additional information that can be recovered from spectra, acquired in real time or near real-time, can be used to improve our understanding of source distribution.

Through this, the problems that have hindered traditional rigid approaches could be overcome and an overall improvement to calibration accuracy for mobile gamma spectrometry surveys could be realised.

1.5 Thesis aims and objectives

The general aim of this work was to develop a multidisciplinary approach to improve the measurement accuracy of source estimates made on spectra, obtained using small volume detectors, over short count times. The proposed method could then be operated alongside or instead of traditional long count time or large volume measurements, ultimately allowing for large areas to be surveyed and the maximisation of radio-contaminant information.

The approach will be demonstrated on land impacted by historical ^{226}Ra contamination and estuarine environments contaminated with ^{137}Cs derived from the nuclear industry. The general aim will be achieved through the following objectives:

- Identify a potential alternative detector to sodium iodide with intention of comparing detectors directly at contaminated sites.
- Develop Monte Carlo calibration spectra for individual detectors to relevant sources and geometries.
- Investigate and implement Machine Learning algorithms trained with Monte Carlo calibration spectra to unfold field data obtained at contaminated sites.

1.6 Thesis structure

This thesis is divided into 9 chapters, 4 of which are published or in the process of being published. The author had the lead in their production. Prior to these four research manuscripts, chapter 2 provides an appreciation of the fundamentals of environmental gamma-ray spectroscopy, the detectors employed and the current spectral processing methods used to interpret spectral output. Chapter 3 goes on to outline in detail the generic methods used in the development of the science presented in the research manuscripts.

The four original research manuscripts can be found in chapters 4-7. The details of the environmental monitoring challenges being addressed along with the details of the contamination being monitored are also presented in each of these four papers.

Chapter 4 investigates the application of Neural Networks to characterise deep ^{226}Ra contamination using borehole measurements taken with a 51 x 51 mm NaI:Tl.

I. Varley A., Tyler A., Smith L. and Dale P. (2015) Development of a neural network approach to characterise ^{226}Ra contamination at legacy sites using gamma-ray spectra taken from boreholes, *Journal of Environmental Radioactivity*, **140**, 130-140

Chapter 5 also focuses on ^{226}Ra contamination, but with respect to detecting near surface dwelling *hot particles*. This paper compares two Machine Learning algorithms and two 71 x 71 mm handheld detectors (NaI:Tl and LaBr:Ce).

II. Varley A., Tyler A., Smith L., Dale P. and Davies M. (2015) Remediating radium contaminated legacy sites: Advances made through machine learning in routine monitoring of “hot” particles, *Science of the Total Environment*, **521–522**, 270–279

Chapter 6 uses a similar setup to chapter 5, but emphasis turns towards characterising the depth and activity of homogeneous ^{226}Ra.

III. Varley A., Tyler A., Smith L., Dale P. and Davies M. Mapping the spatial distribution and activity of ^{226}Ra at legacy sites through Machine Learning interrogation of gamma-ray spectroscopy data, *Science of the Total Environment,* **545-546**, 654-661

Chapter 7 applies a similar approach to characterise layered homogeneous ^{137}Cs deposits.

IV. Varley A., Tyler A., Smith L. and Davies M. Rapid high resolution mapping of activity and burial depth of ^{137}Cs deposits using Machine Learning to unfold gamma-ray spectra, *unpublished manuscript*

Chapter 8 goes on to discuss the implications of the research as a whole and makes suggestions for future work and prospects for environmental gamma-ray spectroscopy and chapter 9 presents the key conclusions arising from the research.

2 Principles of environmental gamma-ray spectroscopy

2.1 Outline

The intention of this chapter is describe the fundamental principles underlying environmental gamma-ray spectroscopy, the detectors applied and the current spectral processing methods used to interpret a detector's spectral output. These descriptions encompasses brief descriptions of how radioactivity is formed, what are the principal types of radiation that can be encountered in the environment and what are main sources of the most common radioelements that contribute environmental radioactivity.

A large section of this chapter is then dedicated to explaining the processes that lead to effective detection and the different types of detectors and their individual properties. Following this, a systematic review of the latest detection technology is embarked on, with a summary and justifications of why a particular detector was purchased for this project.

The final part of this chapter concentrates on the development of photon transport equations and the most common spectral analysis methods used in environmental gamma-ray spectroscopy.

2.2 The occurrence of radiation

If an element's nucleus is unstable, after a certain amount of time depending on the isotope, it will decay by releasing matter or electromagnetic radiation, otherwise known as radiation (Figure 2-1A). The once excited parent nucleus is then either left as a stable daughter element or as an unstable nucleus, but at a lower energy level as a result of the initial loss of energy (radiation emission), ultimately leading to further decay and the formation of decay chains (Figure 2-1B). A unit of radioactivity, the Becquerel, is named after its discoverer Henry Becquerel and quantifies the number of disintegrations per second (Ford, 2004).

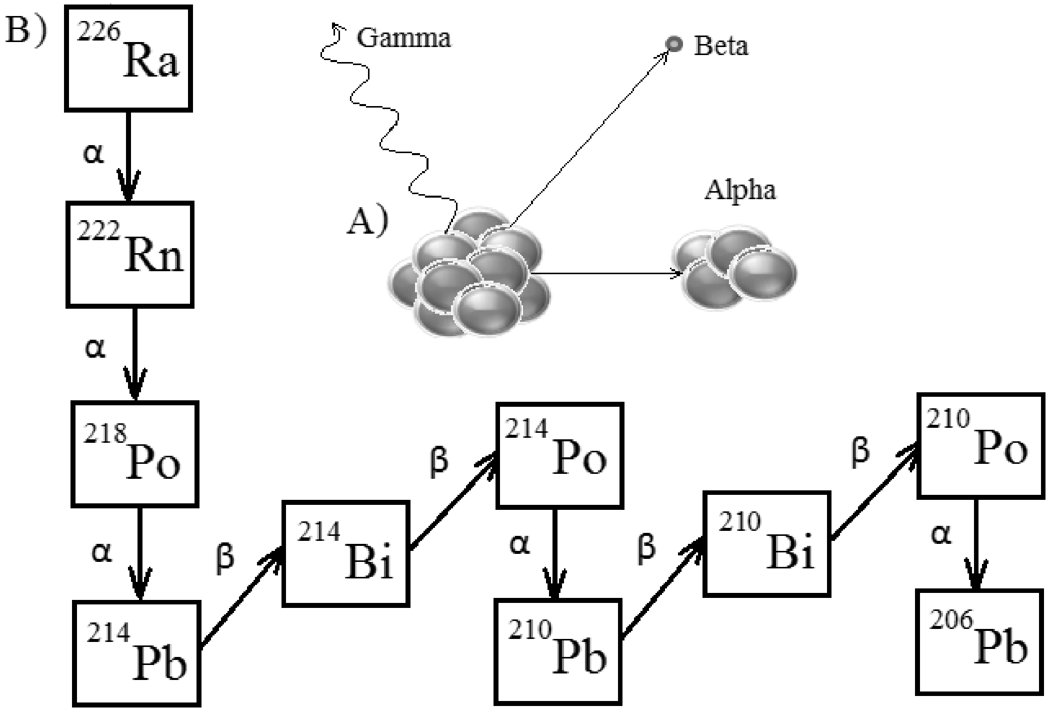

Figure 2-1. A) Decay processes B) Decay chain starting with ^{226}Ra and ending with stable ^{206}Pb

The radiations of primary concern from a radiological protection prospective released during this process are alpha and beta particles and gamma rays (L'Annunziata, 2012). Neutrons are also a noteworthy particle, although they are significantly less commonly within the environment in comparison to the abovementioned particles, therefore attributing considerably less dose.

Alpha and beta particles have the greatest linear energy transfer as they are continuously affected by charge-related coulombic interactions with the matter they are travelling through. Consequently they are attenuated relatively efficiently.

Gamma rays, on the other hand, do not possess electrostatic charge hence they are not affected by coulombic interactions (Evans & Noyau, 1955). Instead, gamma rays require a direct interaction with either the nucleus or the electron clouds surrounding the nucleus. As a result, a materials ability to attenuate gamma-rays is considerably less compared to charged particles, such as alpha and beta particles. Subsequently, gamma-rays can travel significant distances through matter. This phenomena means, depending of course on the initial energy of the gamma ray, that gamma rays are fundamental in the detection of a source at relatively large distances and behind large amounts of shielding (Beck et al., 1972).

The manifestation of a gamma ray is associated with the de-excitation of the nucleus to a lower energy level emitting any excess energy from the nucleus, post alpha or beta decay. This outcome means gamma radiation can be used as a proxy to detect more hazardous emissions. A further importance of gamma radiation is that it can be found in the majority of naturally occurring and anthropogenic decay chains found within the environment. Additionally, each de-excitation is monoenergetic, which indicates that it releases a quantum of energy each time it decays acting as fingerprint for the individual radionuclide emitting it. From an environmental detection standpoint, gamma rays will often be utilised as the first line approach in the detection of a natural source or a radio-contaminant.

2.3 Sources of gamma radiation in the environment

2.3.1 Primordial radionuclides

There are about 340 naturally occurring radionuclides that are present in measurable quantities contained within the Earth’s crust, water bodies and atmosphere (Eisenbud

& Gesell, 1997). Within the Earth's crust, the most notable primordial radionuclides are ^{40}K and the three decay series: Uranium, Actinium and Thorium whose parents or starting members are ^{238}U, ^{235}U and ^{232}Th respectively. All of these natural radionuclides emit detectable gamma radiation at some stage in their decay chain. It must be noted that contributions from the Actinium series are small, compared to those of ^{40}K and the Uranium and Thorium series, owing to the very small quantities found within the environment (Ball et al., 1991).

The presence of these primordial radionuclides can be attributed to the parent having a half-life close to or longer than the age of the Earth (4.7×10^9 years). It is thought that heavier elements were once in existence, for example ^{236}U and ^{240}Pu, but they have since decayed leaving their daughters, which presently make the current decay series.

Other radionuclides can also be found in very small quantities at isolated sites. ^{239}Pu and ^{239}Np can be formed within natural fission reactor sites, such as Oklo in Gabon, due to neutron bombardment of ^{238}U (Eisenbud & Gesell, 1997).

2.3.2 Cosmic radiation

Radiation originating from outer space, known as cosmic radiation, can be measured Earth's surface . This radiation consists primarily of protons, neutrons and alpha particles. Cosmic radiation is thought to be the product of supernovae, of which the vast majority of particles are prevented from reaching the Earth's surface by interactions taking place with atoms contained within the atmosphere (Ackermann et al., 2013). A direct consequence of atmospheric shielding can be realised when considering that 80% of cosmic radiation at sea level is contributed by muons (Eisenbud & Gesell, 1997).

2.3.3 Anthropogenic radionuclides

There have been vast quantities of anthropogenic-derived radionuclides that have been released into the environment over the course of the 20th and 21st century (Stannard & Baalman Jr, 1988, Boubaker Askri et al., 2008). There have been substantial contributions in the form of chemically concentrated Naturally Occurring Radioactive Materials (NORM) from industrial processes such mineral and petroleum processing and historic activities such as the radium industry (Read et al., 2013). Examples of NORM include: ^{226}Ra, ^{224}Ra, ^{232}Th, ^{238}U and ^{235}U. Although on a lesser scale, there have been further contributions to the environment in the form of fission (^{137}Cs, ^{134}Cs, ^{131}I, ^{90}Sr) and activation (^{60}Co, ^{14}C and ^{99}Tc) products from the nuclear industry, weapons testing and hospital discharges to name a few sources (Dauer, 2002).

Eisenbud and Gesell (1997) provide a detailed account of the various anthropogenic radionuclides, and the pathways they have taken to get into the environment.

2.4 Physical interactions of gamma radiation with matter

To gain an appreciation into environmental gamma-ray spectroscopy an understanding of the physical interactions of gamma-rays must first be acknowledged. There are a number of different ways gamma radiation can interact with matter, and the photoelectric cross-section, or more precisely, the probability of collision between it and the material it is passing through, is very important. However, at the relatively low energy range (<5 MeV) relevant to environmental radiation detection, three interactions are of relevance: photoelectric absorption, Compton scattering and pair production. In addition to these inelastic processes, elastic processes principally coherent scattering, also take place. For a complete description refer to Evans and Noyau (1955).

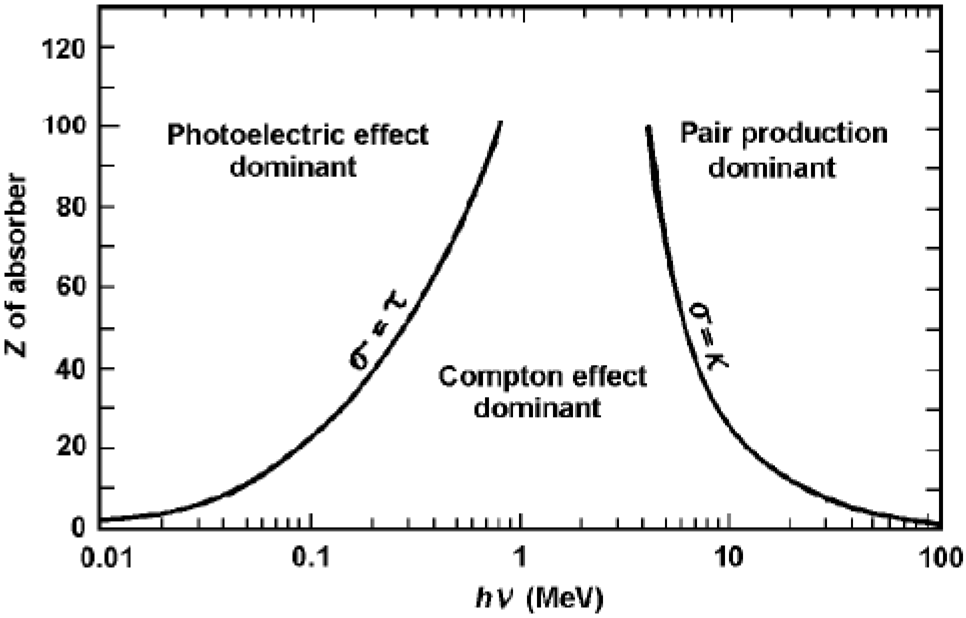

Figure 2-2. Z value plotted against photon energy (hv), displaying the likelihood of the three interaction processes (Evans & Noyau, 1955).

2.4.1 Photoelectric absorption

Out of the three interactions, photoelectric absorption is the desired energy deposition process in a detector as the incoming photon deposits all of its energy in a single event. For a gamma photon with sufficient energy, this normally occurs with one of the K orbital electrons given that they are the mostly tightly bound. A desired characteristic of any gamma detector is to have as larger photoelectron cross-section as possible; this is why materials with higher Z number are preferred (Figure 2-2). During the process of photoelectric absorption, an orbital electron that is ejected out of its orbit then becomes a photoelectron, whose remaining kinetic energy reflects the orbital binding energy subtracted from the original energy of the incoming photon (Figure 2-3B). An electron in an outer shell or a free electron promptly fills the vacancy made by the photoelectron; this results in the emission of an X-ray which tends to be absorbed close to the site of emission (Allyson, 1994).

2.4.2 Compton scattering

Much like photoelectric absorption, Compton scattering involves one of the orbital electrons, preferentially one of the higher energy orbitals K, L or M. This process becomes dominant for the energies emitted by most common gamma sources as electron orbital binding energies are exceeded (Figure 2-3). The incoming photon transfers a portion of its energy to an orbital electron, such that the electron is ejected from the atom as a recoil electron. As a result of the collision with considerations of energy and momentum being conserved, both the electron and the gamma photon, which has lost energy, are scattered in different directions (Figure 2-3C). The angle of scatter of the incidence photon can be predicted by the Klein-Nishina formula (Knoll, 2010). Noteworthy, the probability of forward scattering becomes significantly greater with increasing energy above 100 keV (Onsager, 1938).

It must be appreciated that a number of these events can occur for a single incident gamma ray, so its path can vary substantially when travelling through a thick material. A large proportion of Compton interactions eventually lose enough energy that they result in photoelectric absorption.

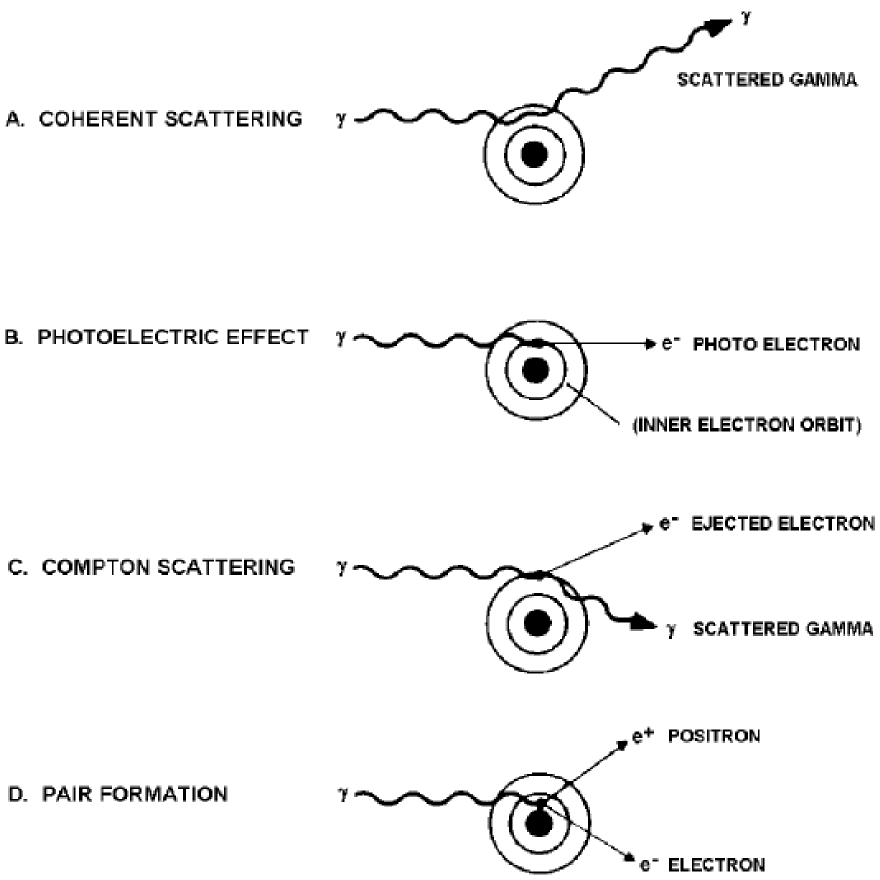

Figure 2-3. Schematic drawing of gamma ray interactions (Evans & Noyau, 1955).

2.4.3 Pair production

In the event a gamma photon exceeds twice the rest mass energy of an electron (1.02 MeV), pair production becomes energetically possible. However, the probability of this process is significantly improved with increasing photon energy above the 1.02 MeV threshold (Figure 2-2). The interaction must take place within the coulomb field of the nucleus, therefore a gamma ray of sufficient energy enters the nucleus and its energy is transferred to a positron-electron pair and any excess energy is transferred as kinetic energy shared by the charged particles (Figure 2-3D) (Evans & Noyau, 1955). Within any gamma-ray spectrum exists two ever present features, the single and double escape peaks, which are brought about by the pair production process (Wainio & Knoll, 1966).

2.4.4 Coherent (elastic) scattering

Coherent scattering occurs as a result of an incident photon colliding with the orbital electrons, but unlike inelastic scattering events, virtually no energy deposition occurs although its direction is altered (Figure 2-3A). Consequently, when taking a modelling approach these events must be accounted for. The probability of a coherent elastic scattering event taking place with the nucleus is about 0.1% of that of inelastic interactions (Knoll, 2010).

2.5 Principals of gamma-ray spectroscopy

The primary aim of gamma-ray spectroscopy is to convert as much of the incident gamma photon in as short a time as possible into electric charge; so individual events can be efficiently processed by the electronics of the detector (Figure 2-4). At the present time, a differential pulse height spectrum can be built up from this electronic signal, which is directly proportional to the energy deposited by a gamma ray in a detector, and easily analysed using standard software on a laptop or tablet. There are number of different types of detectors that are commercially available, most of which serve distinct purposes, for example the use of ion chambers to estimate dose (Knoll, 2010). However, for the purpose of identification of specific radionuclides using discrete gamma emissions, it has been inorganic scintillation detectors and solid-state semiconducting diodes that have met both commercial and research requirements. It must be noted that large organic plastic scintillators, for example polyvinyl toluene often used in homeland security, were ruled out early in this study due to their poor resolution and unmanageable size needed to gain sufficient energy efficiencies (Ely et al., 2006). This section will briefly cover the properties of a detector that lead to effective detection. Following this, a systematic review of semiconducting diodes, conventional inorganic scintillators and the promising cerium activation halides will be presented.

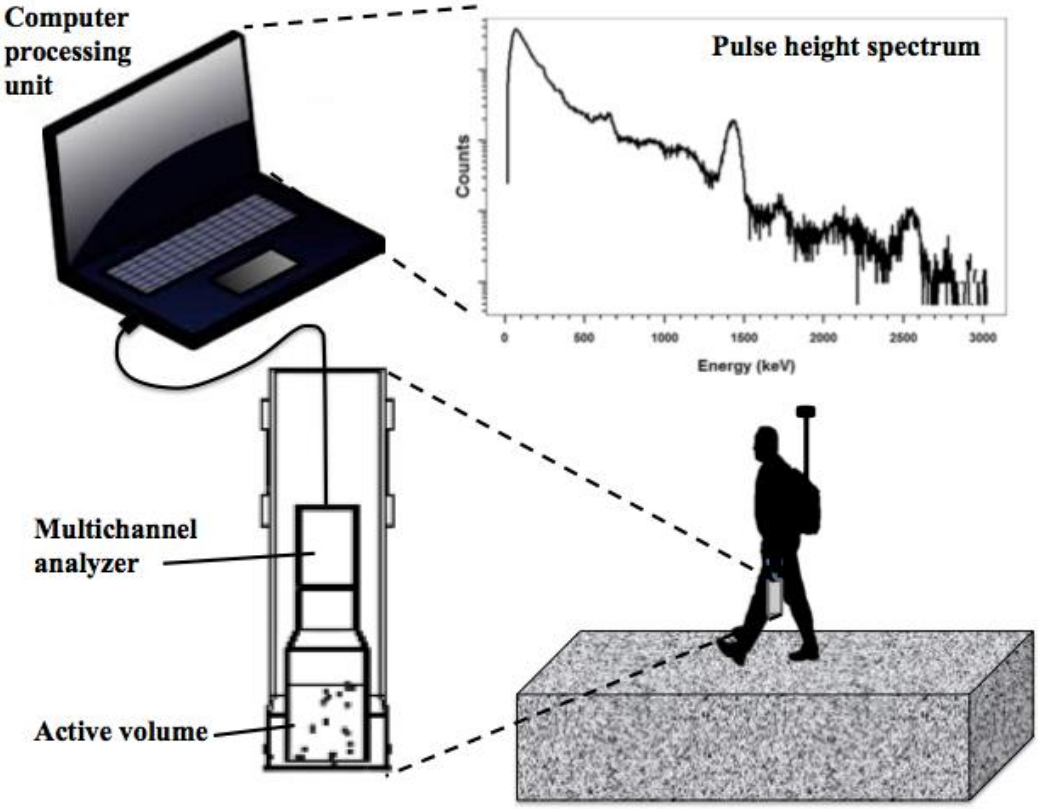

Figure 2-4. Typical field setup for a detector

2.5.1 The process of detection

The initial stage of nuclear detection involves a physical interaction between the detector and the particle of interest. In gamma-ray spectroscopy, this starts with an interaction, as described in section 2.4, between an incident photon and the active volume of a detector. This essentially incurs a loss of energy, through the production of high-energy electrons creating vacancies within inner orbital shells of the detection material. Subsequently, high energy electrons and internal formation of auger electrons, X-rays, positrons, bremsstrahlung and subsequent gamma rays corresponding to positron annihilation, will go on to further ionise other parts of the detector (Narayan et al., 2012). Essentially as energy is lost, more secondary electrons are formed through ionisation, unless energy exits the detectors active volume where it will be effectively lost and not detected.

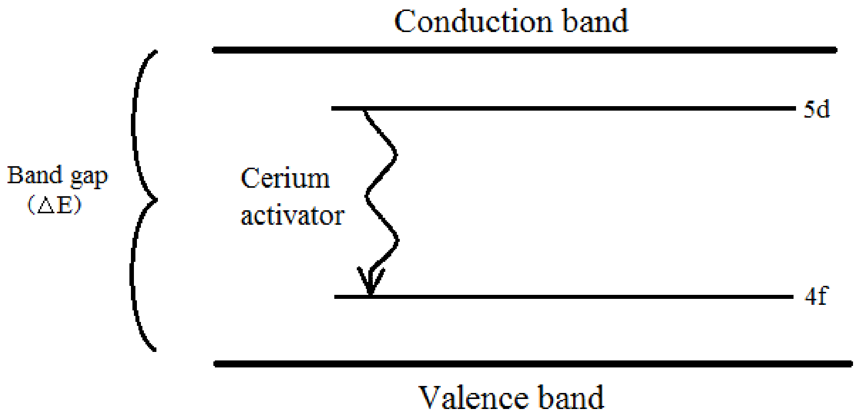

Figure 2-5. Schematic diagram demonstrating band theory of a cerium doped scintillator.

The main difference between scintillators and semiconducting diodes is the amount of energy required to elevate an electron into an excited state. This can best be explained using band theory (Wallace, 1947). An electron is elevated from a ground state (valence band) to an excited state (conduction band), depositing a specific amount of energy from the incident photon; creating an electron-hole pair (Figure 2-5). Throughout the path of the gamma ray a number of electron-hole pairs will be formed. The electron-hole pair will then migrate through the crystal lattice until the de-excitation process takes place, when the energy of the electron-hole pair is returned to ground state, resulting in the emission of energy. In scintillators this manifests as light and in semiconducting diodes it forms an electric charge.

2.5.1.1 *Scintillators*

For a scintillator, if a pure ionic lattice was used, for example pure sodium iodide, wavelengths emitted are too short to be efficiently converted to photoelectrons by the photocathode in the photomultiplier tube. To get around this problem, crystals tend to be doped with an impurity, known as an activator, which modify the band structure of the crystal (Figure 2-5). In the case of sodium iodide this is thallium. The dopant acts as a lumniscence centre for migrating electron-hole pairs to de-excite through, allowing emission of visible wavelengths of light. A second benefit is that, due to the sparsity of the lumniscence centres, self-absorption near to the site of emission is dramatically reduced making the crystal effectively transparent. A photomultiplier tube or photodiode is then used to collect light and amplify the signal.

2.5.1.2 *Semi conducting diodes*

In reality, band theory describes a covalent-bonding orbital electron or free electron being excited and allowed to migrate through the crystal structure and for semiconducting diodes this creates charge that can be interpreted. Interestingly, what sets semiconducting diodes apart from other crystalline structures is that they have a very small band gap of a few electron volts whereas a scintillator has a typical band gap in the order of 100 electron volts. However as the gap is so small in semiconducting diodes, electrons can easily be thermally excited between energy states, to counteract this some semiconducting diodes, such as High Purity Germanium, require the crystal to be sufficiently cooled to liquid nitrogen temperatures (77ºK). An electric field is applied across the crystal with aim of encouraging the flow of electron-hole pairs to an electrode to gain a signal. Subsequently through this method, semi-conducting diodes tend to produce the highest quality signal.

2.5.2 Detector properties

Spectra produced by different detectors exposed to the same source will almost certainly be different owing to variations in composition, detector geometry, outer casing and electronics. The way in which a detector will respond to a source of radiation is known as its response function. There are a number of important properties that can influence a detector's response function, which are described below.

2.5.2.1 *Light output*

When a quantum of radiation enters the active volume of a scintillator, the aim is for all of the energy to be captured and converted into as many information carriers as possible, visible photons in the case of a scintillator, to successfully generate reliable photoelectron statistics. The amount of visible photons emitted is dependent on the crystal field splitting energy, generated by the interaction of the orbital electrons surrounding a non-metal cation and metal anion contained within a crystal (Ballhausen, 1962). A split in energy or degeneracy (ΔE) is formed between the shared orbital electrons enabling excitation from the lower lying energy set to the higher lying energy set (Birowosuto et al., 2006). In principle, small values of ΔE should result in a high light output. Noteworthy, this property does not affect semi-conducting diodes as signal is processed electronic charge.

2.5.2.2 *Energy resolution*

How a detector responds to a monoenergetic source of radiation is known as its resolution. The width of the peaks reflects the amount of statistical fluctuation occurring in information carriers within the detector: essentially the narrower the peak the better resolution. This measurement is standardised by using the Full-Width at Half-Maximum (FWHM). There are a number of reasons for resolution loss even when full energy deposition occurs such as statistical noise, electronic noise and shifts in gain. Primarily, resolution loss occurs in scintillators as a result of statistical broadening or fluctuation in light reaching the photocathode that, in turn, leads to fluctuations in photoelectrons leaving the photocathode. Therefore, high light output and reducing light loss are vital in maintaining good resolution. For the latter argument, efforts should be made during growth processes to ensure uniformity within the crystal’s structure to minimise self-absorption. Additionally, efforts should be made during the assembly of the instrument to maximise reflection of the outer casing to channel low energy light towards the photocathode. Drifts in gain, the assembly of contact points and warming up of the crystal can bring about losses in energy resolution in semiconducting diodes.

2.5.2.3 *Linearity*

The departure from absolute proportionality occurs as the response of the detector varies with changing energy. If statistical broadening was the sole contributor to resolution loss at lower energies then the following equation would apply (20).

$$Resolution = \frac{K}{\sqrt{E}} \quad (1)$$

Where K equals the constant of proportionality and E equals energy. Deviations from the above equation, represent additional inputs of variations, for example self-absorption or damage to the crystal.

2.5.2.4 *Efficiency*

The efficiency of a detector is the ability of its active volume to detect a specific activity of radiation at a particular energy. This involves a photon being attenuated by the material it is travelling through. Hence, it is the density and Z number of elements contained within the crystal, with all the dimensions and geometry of the detector that determine this property. Naturally, as energy of a photon is increased the efficiency of the material to stop that energy will decrease; consequently efficiency is measured as a function of energy. This is dependent on the attenuation of the material making up the active volume of the detector.

$$A = A_0 e^{-\mu x} \quad (2)$$

Where A_0 is the flux of the incident gamma beam and A is the flux after attenuation of the material, x (cm) is the distance through the material and μ (cm^{-1}) is the attenuation coefficient (eq 2).

In order to gain an appreciation of a detector's efficiency, including shielding from the endcap and outer canning, integrated over a 4π geometry, it is best to perform empirical experiments. Assessment of this characteristic can be performed by rotating a point source around the axial plane of the detector and recording the relative intensity of the peak as a function of incident angle (Helfer & Miller, 1988). Once a detector is properly characterised, this provides a framework for interpolation and extrapolation that would otherwise be limited through laboratory experiments alone (Santo et al., 2012).

2.5.2.5 *Decay time*

The time it takes for the formation and migration of an electron into a lumniscence centre is much shorter than the time it takes for the electron to de-excite (decay). The time taken for the energy to be emitted, in a scintillator, as light is heavily dependent on the decay process, which takes the form of an electron cascade (de Haas et al., 2005). Ideally, the fast element of decay is desired, known as fluorescence (Onsager, 1938). However, delayed radiative de-excitation processes known as phosphorescence can cause afterglow, this can, in high count rate situations, cause problems as pulses overlap leading to dead time.

2.5.2.6 *Temperature stability*

The light output of a scintillator can be affected by temperature usually leading to unwanted decreases in light output, this usually happens for the majority of scintillators as temperature is increased, leading to a loss in resolution. However, out in the field it is often not the active volume of the detector that causes loss in resolution, instead the electronics particularly the photomultiplier tube can be a lot more sensitive to temperature change (Moszyński et al., 2006).

Table 2-1. Properties of a number of commercially available detectors.

Property

Detector	Resolution (FWHM (%) at 662 keV)	Density (g cm^{-2})	Decay time (ns)	Light output (photons MeV^{-1})	Intrinsic activity (Bq cc^{-1})
NaI:Tl	~7	3.67	230	38000	~0
LaBr:Ce	~3.5	5.29	28	63000	0.4
LaCl:Ce	~4.6	3.79	26	46000	1.2
CeBr	~4.1	5.1	17	68000	~0
BGO	~10	7.12	300	15000	~0
CsI:Tl	~8	4.51	20	2000	~0
BaF_2	~9.5	4.89	1	14000	~0
PVT	~180	1.3	~2	~10000	~0
HPGe	~0.2	5.32	NA	NA	~0
ZnCdTe	1.75	6	NA	NA	~0

2.5.3 Scintillation detectors

At present, no single scintillation crystal fulfils all detection requirements and as a result most are used for very specific jobs. For instance, BaF_2 has been shown to be the material of choice in high count rate situations as it has an incredibly fast decay component of 1ns (**Table 2-1**). Another example is the application of bismuth germanate (BGO) for high counting efficiency, owed to its remarkably high density (Knoll, 2010).

However, Sodium Iodide (NaI:Tl), which is one of the original crystal structures to be used in gamma-ray spectroscopy, still remains the most popular environmental scintillation detector, because of its robustness and commercial availability. NaI:Tl can be grown relatively inexpensively into large ingots (>16 l), which enables very high efficiencies to be reached despite its comparatively low density (3.67 g cm^{-2}). The material offers an acceptable light output (38000 photons/MeV), a deviation from linearity of ± 0.06 keV^{-1} and as it is a scintillator, its power requirements and weight are relatively low. Its main drawback, however, is its relative low resolution (~7% at 662 keV) (Table 2-1). For the purpose of direct estimation of radionuclide concentration (Bq g^{-1}) and aerial deposition (Bq m^{-2}), from background counts, peaks often require sprectral stripping (Tyler, 1999). Spectral stripping is described in more detail in section 2.6.3.1.

2.5.4 Solid state semiconducting diodes

The primary semiconducting diode used in gamma spectroscopy today, utilises High Purity Germanium (HPGe), because of its high density and its ability to be grown in comparatively large sizes, enabling it to stop highly penetrating gamma radiation. Before techniques were available to make germanium pure enough for gamma spectroscopy germanium lithium (GeLi) semiconducting diodes were used. However, once a GeLi detector had been cooled it could not be warmed up to room temperatures again (Beck et al., 1972). HPGe, first made commercially available in the mid 70’s, is the highest resolution detector available; this can be seen when observing its FWHM of 0.2 % at 662 keV (Table 2-1) (Knoll, 2010).

Unfortunately, there are a few drawbacks to this type of detector. They must be cooled to very low temperatures in order to gain the desired resolution, as the smallest size of band gap must be obtained. This is achieved by either using liquid nitrogen (77ºK) or large electronic cooling devices, making power requirements high and considerably heavier than comparable scintillation detectors. Consequently, they are certainly not as portable as scintillators. Furthermore, HPGe are considerably more expensive, at almost 30 times the cost of NaI:Tl detectors of a comparable size and efficiency; a key variable influencing detector choice, particularly if high efficiency is required (Table 2-1). Yet, in the case of a complex radiation field, consisting of contributions from many radionuclides, the use of HPGe is logical.

ZnCdTe is another semiconductor of interest given that it can be operated at ambient temperatures (Table 2-1). However, very low efficiencies can only be obtained, as crystals can only be grown in relatively small ingots (~2 cm^3) at the present time (Knoll, 2010). Therefore, the environmental application of these detectors is limited, but in high-count rate situations their application becomes more appealing (Martin et al., 2015).

2.5.5 Cerium activated halides

2.5.5.1 *Lanthanum halides*

In 2001, the combined effort of Delft and Bern universities produced some of the first commercially available, cerium-doped, lanthanum halide crystals (Menge et al., 2007). Two of these crystals LaBr:Ce and LaCl:Ce have demonstrated outstanding scintillator characteristics such as, high effective Z and density, very high light yield, emission wavelengths well matched to common photocathodes, fast decay times all of these factors leading to outstanding resolution (~3.5% and ~4.6% respectively (FWHM) at 662 keV) (Knoll, 2010) (Table 2-1). Consequently, they have potential to serve as intermediate resolution detectors between NaI:Tl and relatively bulky solid state detectors (HPGe) (Iltis et al., 2006).

Over the last decade extensive research on both the Lanthanum halide crystals has been undertaken (Milbrath et al., 2007, Menge et al., 2007). The majority of this work concentrates on their ability to outperform traditional crystals used as scintillators such as NaI:Tl, over a wide range of laboratory conditions: temperature, photon intensity and energy range (Menge et al., 2007, Pausch et al., 2007, Sullivan et al., 2008). However, as of yet, a limited amount of research has been performed in the environment using this group of scintillators.

LaBr:Ce has been shown to outperform LaCl:Ce in the majority of cases. Its energy resolution (<3.5%), decay time (26 ns) and light output (63000 photon MeV^{-1}) are superior (Table 2-1). These factors alone would seem to underline it as a more suitable scintillation material to be used in the environment. More crucially, for the low count rate, short count time situations in which this detection material is going to be used in, the level of intrinsic activity contained within LaCl:Ce (1.2 Bq cc^{-1}) is considerably more than LaBr:Ce (0.4 Bq cc^{-1}).

The main drawback of the Lanthanum halides is that they naturally contain 0.089% of ^{138}La which has a half-life of 1.02×10^{11} years (Tsutsumi & Tanimura, 2006). 66.4% of its decay results in electron capture producing an excited state of Ba, which decays causing a gamma ray corresponding to a 1436 keV gamma emission (Figure

2-6). As a result of outer electron reconfigurations, barium also sources x-rays in the 35 keV region (Saint Gobain, 2009) (Figure 2-7).

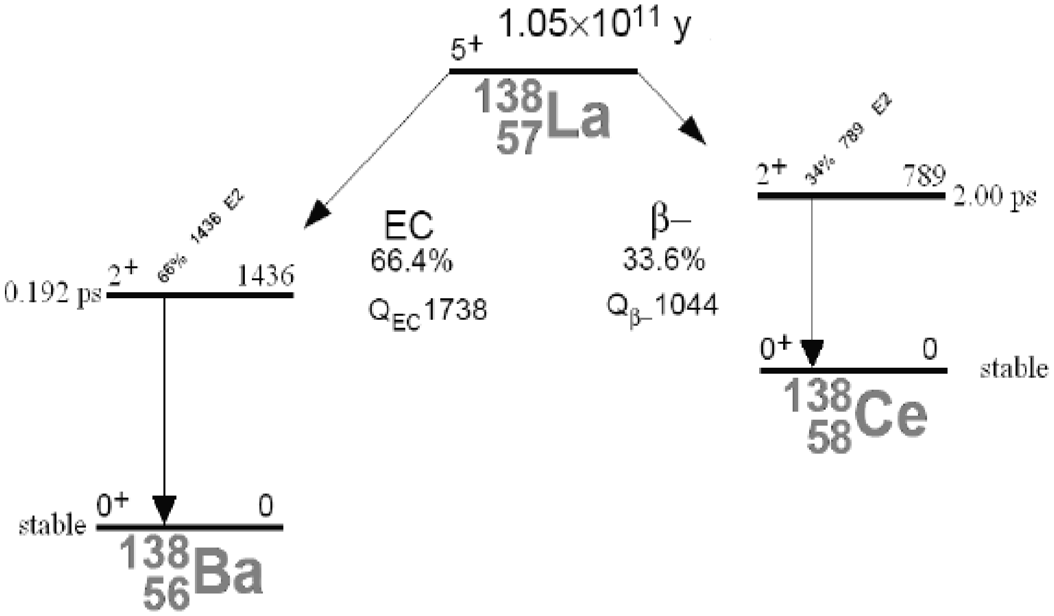

Figure 2-6. Decay of intrinsic lanthanum within the lanthanum halide detectors.

Concurrently, 33.6% beta decays to ^{189}Ce causing a beta continuum (< 255 keV), that then emits a gamma ray of 789 keV in coincidence with the beta continuum, thus producing another continuum at above 789 keV (Figure 2-6). Resultantly, spectral measurements of low intensity, low energy gamma rays (< 100 keV) can be somewhat hindered by the occurrence of high energy x-rays and the beta continuum (Tsutsumi & Tanimura, 2006) (Figure 2-7).

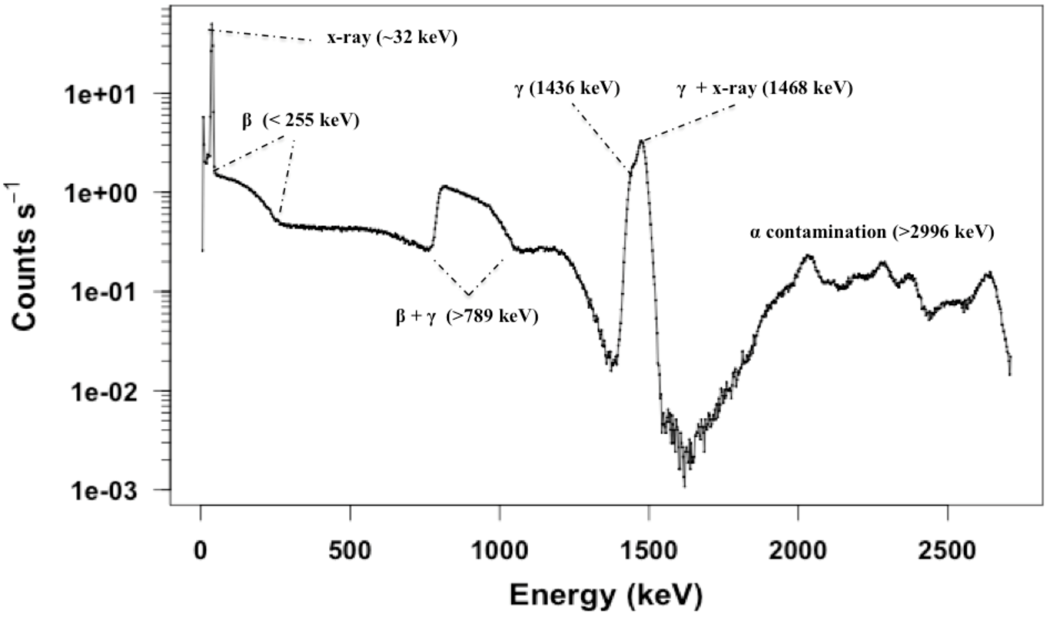

Figure 2-7. Spectrum of intrinsic activity for 71 × 71 mm LaBr:Ce with significant contributions labelled.

Up until recently, ^{227}Ac provided additional background within the Lanthanum halide crystals(Milbrath et al., 2007), but through careful selection and purification of raw materials, α background has now been reduced to 0.02 Bq cc^{-1} (Iltis et al., 2006). Additionally, computational removal of intrinsic counts has been performed with varying degrees of success (Guss et al., 2010).

Clearly LaCl:Ce (£12,000) is cheaper than LaBr:Ce (£20,000) for a 3 × 3 inch detector, but its performance is inferior (Table 2-1). The fact that its intrinsic background activity is about 3 fold greater, in the intermediate energy regions of interest in environmental metrology (10-2700 keV), and its resolution is poorer (4.6 %) makes LaBr:Ce the more suitable choice considering the conditions that it will be used in i.e. the requirement for sensitive low count application in these intermediate energy regions.

2.5.6 Cerium Bromide

Cerium bromide possesses similar scintillation characteristics to that of the lanthanum halides but has the added advantage that it does not possess the same intrinsic activity, with only slight background counts identified, most likely attributed to minor alpha contamination (Guss et al., 2009). It has a very short decay time of 16ns, better than both the lanthanum halides. Its resolution (4.1% FWHM at 662 keV) is similar to that of LaCl:Ce, but there have been mixed reports of its resolution ranging between 3.6-6.8% for varying sizes of detector (Table 2-1) (Guss et al., 2010). The reason for the range of resolution could be initiated by self-absorption processes taking place within the crystal, thus with increasing crystal size resolution will degrade (Drozdowski et al., 2008). This is of real concern, given that relatively large crystals will almost certainly be required in order to obtain enough signal in low count rate situations as encountered within the environment.

At the present time, CeBr crystals are only available in 51 × 51 mm dimensions; regrettably this does not reach desired efficiencies compared to what LaBr:Ce offers. Furthermore, projected prices reveal that a 71 × 71 mm CeBr crystal would cost in the region of £25,000, more than both the lanthanum halides with no real advantage of resolution.

2.5.7 Discussion of detector selection

It becomes clear that no detector clearly stands out from the others as advantages and disadvantages are encountered for all detector types. However, LaBr:Ce would appear to be the most promising at the present time (written July 2012). The reason for this is that it has the highest resolution and can be commercially made in 71 x 71 mm sizes that will supply sufficient signal, owed to its increased energy efficiency, for the short count times required by handheld surveys. Additionally, the radionuclides investigated during this thesis, such as ^{226}Ra and ^{137}Cs, have primary gamma emissions in relatively clean areas of the intrinsic contaminated spectrum (Figure 2-6).

The main reasons against the selection of LaCl:Ce for this application is that the self-activity is too high. Regrettably, the decision against selecting CeBr is primarily based upon its size at this point. That said, with the inevitability of further advances in crystal growth, this detector could be a genuine option for future applications due to superior energy compared to NaI:Tl and considerably less contamination than the lanthanum halides. Initial laboratory testing of the purchased 71 x 71 mm LaBr:Ce detector is presented in Appendix I.

2.6 Current spectral processing methods

Prior to descriptions of spectral processing methods used to derive activity estimations; it seems appropriate to provide an explanation of the driving factors behind spectral response. Interpretation of spectral response is not a straightforward process as numerous environmental factors can influence photon flux before interacting with the detector. Such factors as topography (Laedermann et al., 1998), soil moisture and density (Beck et al., 1972), vegetation cover (Gering et al., 1998) and heterogeneities within the sediment column itself (Korun et al., 1994) can shield primary photons by absorption or scattering processes. It must be noted that interception of radionuclides by vegetation during atmospheric fallout events can also elevate photon fluence rates in the air. Additionally, it was shown by Beck et al. (1972)

that the chemical composition of a soil can cause increases in attenuation, predominantly at low energies (<150 keV). This issue is covered in section 3.3.3 since it has implications for environmental modelling.

The importance of the aforementioned factors, in terms of the relative change they incur on surface fluence rates, may be overshadowed when considering changes in source depth distribution occur within the soil column. This is where this method encounters considerable difficulty when trying to quantify activity distribution (Kastlander & Bargholtz, 2005). Confronting this problem has become the focus of numerous research efforts. In the majority of cases, solutions involve initial assumptions about the activity of specific radionuclide in the air surrounding the detector and principally the distribution of both natural and the radio-contaminant of interest. For the most part, depending on the distance from a respective point or extended source of interest, air activities are considered to be homogeneous (Thummerer & Jacob, 1998). However, soil radionuclide distribution can vary substantially: hence a number of different models have been developed to account for this occurrence.

2.6.1 Estimation of source depth and distribution using photofluence equations

Before describing relevant depth distributions, it is crucial to regard the burial depth of the radionuclide not as its Cartesian coordinate depth with respect to the soil column, air and detector, but rather as its effective depth or mass per unit area (x) (g cm^{-2}) (eq 3). This term takes into account the density (ρ) or photoelectron cross-section of the linear depth (z') of the soil above the source (Tyler et al., 1996a).

$$\int_0^z \rho(z')dz' \tag{3}$$

For more complex source distributions varying depth and in turn density will also affect the activity of that layer as increasing overburden compresses lower layers. As a direct result of changes to activity and photoelectric cross section brought about by varying density, activity should be described as activity per unit area (Bq m^{-2}) at depth x (g cm^{-2}) (Tyler, 2008). However, weights are routinely quoted in legislative text, for example Bq kg^{-1}.

2.6.1.1 *Angular response calibration*

Before any estimations of source distribution can be made from spectra obtained from the environment, a detector's response to a specific energy source, integrated over an infinite half space, must first be predicted. In the majority of work undertaken in the past, the most common way of doing this was deterministically.

Initially, an assumption is made regarding the distribution of an individual radionuclide and then photon fluence equations are solved over the chosen geometry. For instance, if the source is assumed to be uniformly distributed throughout the soil, the fluence rate at the soil surface will not change along the surface plane of the soil, but the distance through soil and air to the detector will as changes in zenith angle ($\pi/2$) occur. Therefore, calculations must take into account changes in photopeak count rate (s^{-1}) brought about by the detectors angular dependence. This geometric relationship between source and detector has been described by a number of studies (Beck et al., 1972, Tyler, 2008) (eq 4).

$$\frac{N}{A} = \frac{N}{N_0} - \frac{N_0}{\psi} - \frac{\psi}{A} \tag{4}$$

The number of counts under a photopeak or the number of photons detected (N) is directly proportional to the activity per units per area (Bq m^{-2}), volume (Bq m^{-3}) or mass (Bq kg^{-1}) (A). This is known as the calibration coefficient at energy E; this relationship is shown in equation (4), where:

-N/N_0 is the angular correction factor for energy E normalised to the detector's face (N_0/ψ). This must be applied to extended sources or in the case of a moving detector in the search for *hot particles.* This feature is dependent on the geometry of the materials and their densities making up the entire detection unit. This parameter can be empirically or computationally established and is heavily influenced by the length to diameter ratio of the active volume (Helfer & Miller, 1988).

-N_0/ψ is measured experimentally using a plain beam of photons at energy E normal to the detector face (N_0). This factor is solely dependent on detector characteristics, namely the efficiency of the detector as described in section 2.5.2.4.

-ψ/A is the ratio of the gamma flux, at energy E, at the surface of the detector, with respect to the activity in the soil column, with contributions integrated over a 2π geometry. This term takes into account the scattering of photons purely by the soil and air between the source and detector. This term is primarily influenced by the energy and distribution of a source, soil and air density and height of detector.

It must be appreciated as a direct effect of the significantly different attenuation coefficients of air and soil, the cross section being analysed, or where the photons are originating from, is relatively shallow in the z direction, but considerably larger in the x and y directions. Comparisons to a dinner plate can be made where decreasing photon energy will cause a relative decrease in depth, but an increase in width.

By combining integration the two functions N/N_0 and ψ/A, what is known as a circle of influence (COI), for Energy E, can be obtained. A COI is simply where 90% of the gamma photons of energy E originate. For example, a photon of 609 keV typically has a COI of 7 m for a detector at 1 m height for uniform depth distribution (Tyler 2007).

2.6.1.2 *Uniform distribution*

Modelling a uniformly distributed source, assumed for most natural occurring radionuclides, was described in the original studies performed by Beck et al. (1972). The following calculation for angular correction factor for a detector at height h (cm) from the ground, at energy E (keV) and integrated over the zenith (θ) and azimuthal angles (φ) is shown below in equation (5).

$$\mathrm{z\varphi} = \int_0^{2\pi} \int_0^{\frac{\pi}{2}} \int_{\frac{h}{cos\theta}}^{\infty} \frac{A\gamma_{100}\sigma_{det,\theta,\varphi}}{4\pi X_{tot}^2}\, X_{tot}^2\, sin\theta\, e^{-\mu_a\rho_a X_a}\, e^{-\mu_s\rho_s X_s}\, dr\, d\theta\, d\varphi \quad (5)$$

The following terms apply for equation 4, 5, 7 and 8.

A = Photon flux at the surface (photon second^{-1} cm^{-2})

γ_{100} = Number of gamma photons emitted per 100 decays

$\sigma_{det,\theta,\varphi}$ = Effective detector cross-section taking into account geometry, density and angular dependence.

X_s= Path length in soil

X_a = Path length in air

X_{tot} = Total path length of gamma an incident gamma photon ($X_s + X_a$) (cm)

μ_a = Mass attenuation coefficient in air (cm^{-1})

μ_s = Mass attenuation coefficient in soil (cm^{-1})

ρ_s = Density of soil ($g\ cm^{-3}$)

ρ_a = Density of air

r = Radius of circular area

Allyson (1994) modified Beck et al. (1972) original equation to obtain the COI where C equals φ(r,θ) and r is the radius of the circle of detection (eq 6).

$$COI_r = \frac{C_r}{C_\infty} \tag{6}$$

2.6.1.3 *Exponential distribution*

An exponential distribution, where the highest activity is found at the surface with activity decreasing in an exponential manner with depth as a result of diffusion coefficients, is a common feature of relatively recent bomb fallout (Beck et al., 1972) (Figure 2-8). By relatively recent, the author means the source in question has had time to penetrate into the soil column, this is in contrast to fresh bomb fallout where the source would be planar along the soil-air interface. In the case of an exponential distribution, when modelling its angular correction factor a new term (eq 7) has to be added to equation 5.

This is because the equation has to factor in the relaxation of activity in the z direction into the angular correction factor (N/N_0) and total fluence rate (ψ/A). This exponential function, isolated in equation 7, includes the term known as the reciprocal of relaxation length α (cm^{-1}). Appreciably, with the source introduced on a planar surface on top of the soil column, diffusion processes take place spreading the source down the soil profile (Tyler et al., 1996b).

$$e^{\left[-\left(\frac{\alpha}{\rho_s}\right)\rho_s z\right]} \qquad (7)$$

Where ρ_S is density of the soil and z (cm) is the linear depth.

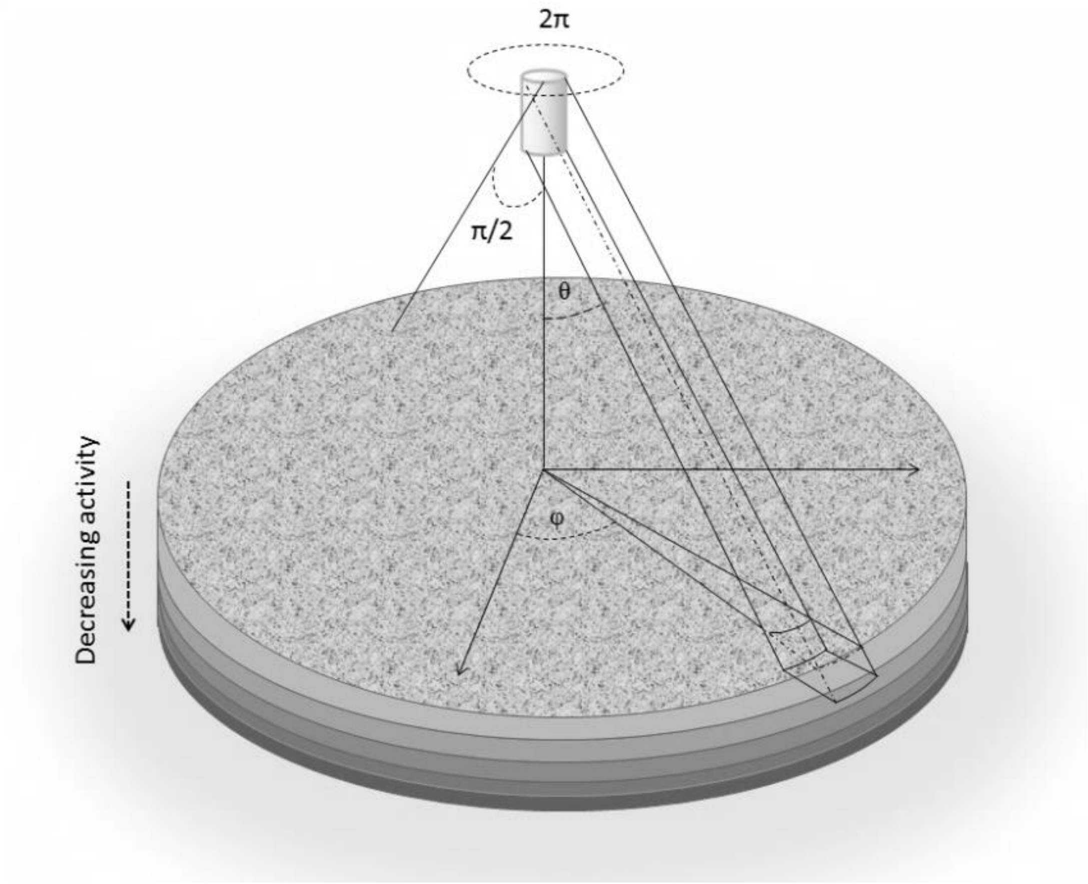

Figure 2-8. Example coordinates of an *in situ* detector setup over an exponentially distributed source.

Naturally, α will vary within the environment on spatial and temporal scales dictated by the chemical and physical behaviour of both soils and individual radionuclides (Tyler, 1994). Observed α values tend to decrease with the age of deposition as the radionuclide penetrates deeper into the soil column (Beck et al., 1972).

$$C = \int_0^{2\pi} \int_0^{\frac{\pi}{2}} \int_{\frac{h}{cos\theta}}^{\infty} \frac{Ae^{\left[-\left(\frac{\alpha}{\rho_s}\right)\rho_s z\right]}\gamma_{100}\sigma_{det,\theta,\varphi}}{4\pi X_{tot}^2} X_{tot}^2 \, sin\theta \, e^{-\mu_a \rho_a X_a} \, e^{-\mu_s \rho_s X_s} \, dr \, d\theta \, d\varphi \qquad (8)$$

2.6.1.4 *Subsurface maximum*

After a period of time, relatively non-radioactive overburden (compared to the original deposited activity) can develop over the top of an exponential distribution creating a subsurface maximum. This can be modelled by a Lorentz function (Hillmann et al., 1996) or by simply fitting a polynomial and integrating with respect to mass (Tyler, 2008). The latter method introduces a term called the mean mass depth β (cm). This can be derived by integrating activity with respect to mass (x) (9).

$$\beta = \frac{\int_0^\infty xA(x)dx}{\int_0^\infty A(x)dx} \tag{9}$$

For practical reasons, β is the section where the highest activity originates from within the soil column, or the peak activity of the distribution. For this reason, instead of integrating, equal mass depth intervals can be used simplifying calculations (Tyler, 1999).

2.6.1.5 *Point source*

A point source geometry, which is often assumed for *hot particles*, can also be derive from photon fluence equations. However, equations are somewhat simplified with integration only taking place, over the angle θ, if movement through the radiation field of a particle is required: effectively modelling a line source.

2.6.1.6 *Limitations of photon fluence equations*

Photon fluence equations are innately deterministic, therefore if the analyst wants to derive full spectral properties, such an approach becomes mathematically unfeasible even for moderately complex geometries. This is brought about by the stochastic nature of radiation transport. Therefore, for full spectral reconstruction the only practical options are *in situ* calibration or Monte Carlo simulations (described in section 3.3)

2.6.1.7 *In situ calibration*

Due to the multifaceted relationship between the response of the detector with source activity and distribution, *in situ* measurements are normally calibrated in the field with soil samples (Tyler, 2008). Tyler et al. (1996b) demonstrated a reliable approach of strategically sampling the area around a detector's field of view (Figure 2-8). A single core is taken directly underneath the detector and 5 hexagonal shells, at 2, 8, 32, 128 and 258 m, are formed by taking 6 cores on the outside of individual shells. The midpoint of individual shells should correspond to the COI (eq 6).

This method takes into account lateral heterogeneity in source distribution and provides the opportunity to investigate variation in soil chemical composition on the lateral plane. Another advantage of this method is that it provides error estimates for individual shells allowing uncertainty to be quantified. Whereas, solving traditional photon fluence equations assumes uniform distribution in the x and y planes and thus no quantification of uncertainty can be made. Its ability to take into account lateral spatial heterogeneity allows for a more representative calibration. Yet, it must be appreciated how time consuming this method can be in comparison to empirical solutions of Monte Carlo simulations

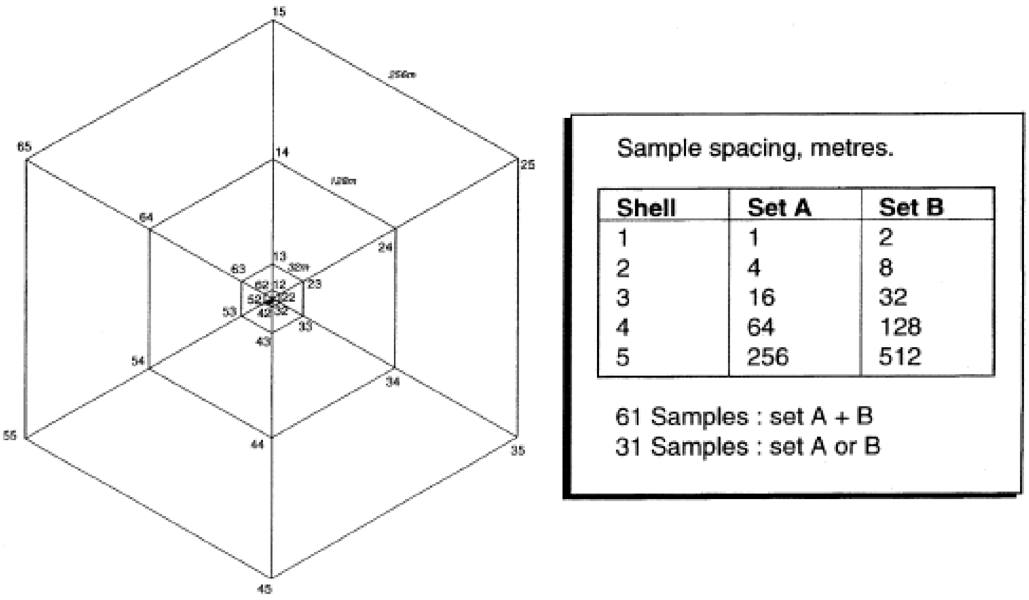

Sample spacing, metres.

Shell	Set A	Set B
1	1	2
2	4	8
3	16	32
4	64	128
5	256	512

61 Samples : set A + B
31 Samples : set A or B

Figure 2-9. Hexagonal strategic sampling plan for the calibration of Airborne Gamma Spectroscopy Reproduced from (Tyler et al., 1996b) with permission from Andrew Tyler.

2.6.2 Spectral interpretation methods used for depth and activity estimation

There are a number of common methods of depth quantification, which have been extensively used for estimating the depth and activity of a point source (Maučec et al., 2004), activity and mean mass depth (β) of a subsurface maximum (Tyler et al., 1996b), surface activity and the reciprocal of relaxation length (α) of exponentially distributed sources (Hillmann et al., 1996) or the depth of a slab source (Thummerer & Jacob, 1998).

2.6.2.1 *The two line method*

The two line method requires a radionuclide, or inference from two separate radionuclides in equilibrium, producing two or more intense gamma energy lines

(Miller et al., 1994). From this, a regression relationship can be estimated, built up from laboratory calibration experiments making use of the greater attenuation of the lower energy line (Figure 2-10). Noteworthy, the larger difference in energy between lines will generate the most reliable estimation. Additionally, caution must be applied when using energy lines below 150 keV as chemical composition of soil can cause varying degrees of attenuation (Feng et al., 2012).

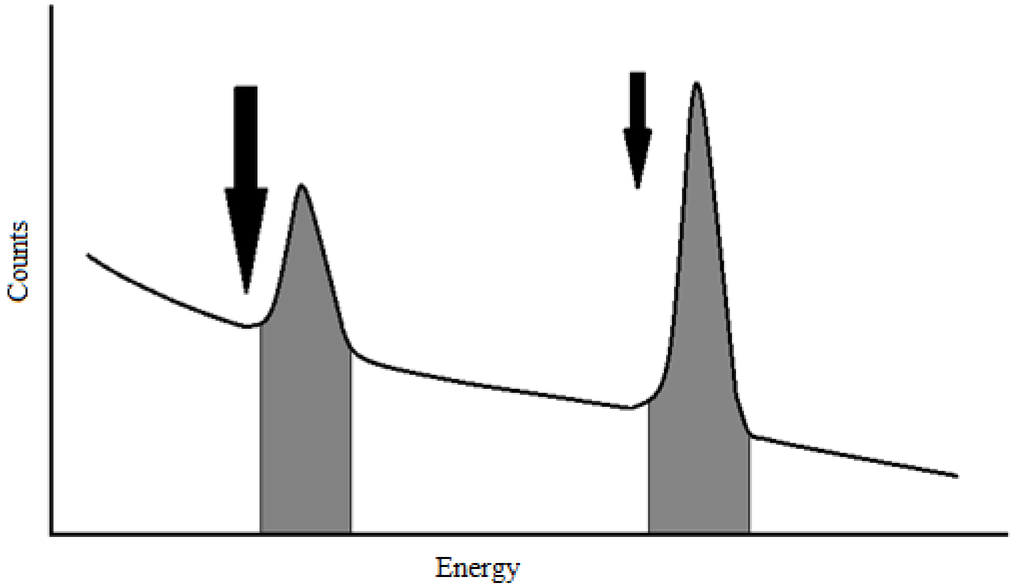

Figure 2-10. Schematic diagram demonstrating the principles behind the two line method.

Importantly, to work out full energy counts for this type of problem net counts (peak) must be separated from gross counts (background continuum). This is typically performed by taking the average of a set number of channels either side of the full energy peak, then averaging these two values and multiplying by the number of channels under the full energy peak. This is known as the “windows method” and by the nature of the calculation, obtaining enough counts within the window to satisfy certain statistical criteria, for example below 5% uncertainty, can take a long time particularly in low net count rate or high background situations.

2.6.2.2 *Peak to Valley method*

The peak to valley or the forward scattering method, unlike the two line method, requires only one intense gamma emission. Instead of relying purely on the attenuation properties of full energy photopeaks, it utilises the forward scattering region between the Compton edge and full energy photopeak. As a particle’s depth is increased, the amount of forward scatter, best described as a grazing angle experienced between a full energy photon and an electron at rest, increases proportionally with the amount of material between source and detector. Therefore as depth is increased, the amount of counts in the forward scattering valley region increases, at the same time as, the full energy photopeak decreases.

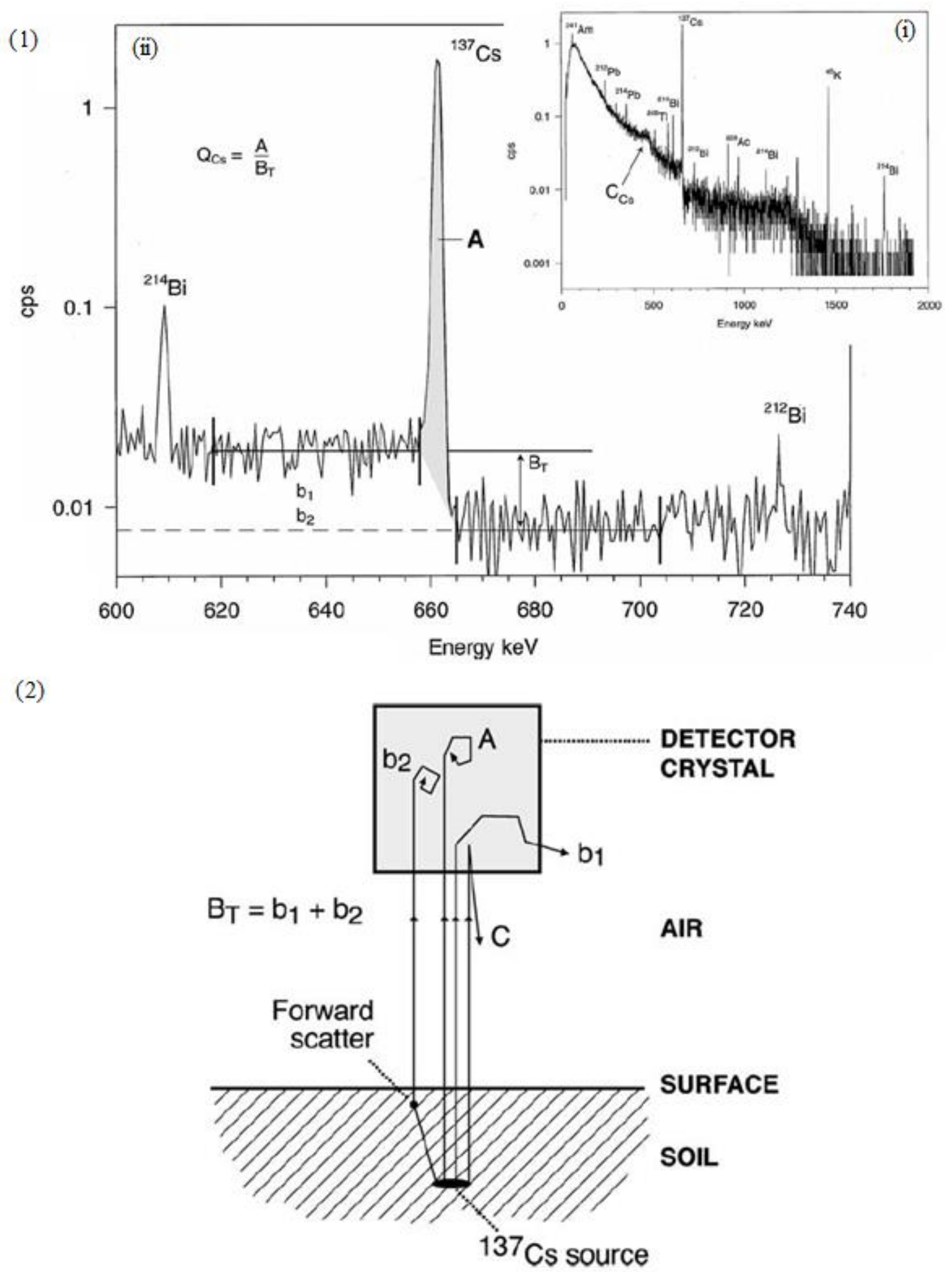

Figure 2-11. Example environmental spectrum taken by a HPGe detector (i) highlighting the ^{137}Cs region of interest at 662 keV, with contributing counts to the peak. (A) and the valley region (B_T) identified (ii). (2) Schematic diagram illustrating the physical interactions contributing to spectral shape. Reproduced from (Tyler, 2008) with permission from Andrew Tyler.

The physical interactions leading to spectral features in a HPGe environmental spectrum are described in Figure 2-11. For a single gamma-emitting source, the region between the full energy peak, where a photon deposits all its energy into the detector (A), and the Compton edge, formed as a result of full energy backscatter with the detector material (C), theoretically there are only two types of interactions contributing counts. The first are escape peaks (b_1), where a photon deposits nearly all of its energy within the detector but escapes out of its active volume near the end of its path. There are a number of factors influencing this occurrence, many of which have been discussed in previous chapters, such as angular dependence and geometry of the detector. This occurrence, however, can be characterised through physical characterisation or Monte Carlo simulations and counts can be subtracted from the valley region (B_T). The remaining contributions to the valley region are from forward scattering events (b_2) taking place with material in between the detector and source. The amount of these events transpiring will be directly proportional to depth. Thus, an empirical approach can be taken (Tyler et al., 1996b).

It must be stated that to attain acceptable uncertainty in individual regions, long count times are requisite and spectral stripping is often required clean out contributions from the natural radioelements in lower energy resolution detectors (Tyler, 2008).

2.6.2.3 *Full spectral analysis*

Sometimes if a detector has been calibrated very carefully to a well-known source geometry, assuming factors such as density and distribution do not change for the *in situ* measurement, then full spectral analysis (FSA) can be performed (Hendriks et al., 2001). The advantage of FSA is that counts from the whole spectrum can be used reaching desired statistical uncertainty faster; particularly utilising robust contemporary algorithms such as non-negative least squares regression (Caciolli et al., 2012). To avoid complications, counts below approximately 250 keV are more often than not excluded to eliminate low energy Compton scatter, backscattering contributions and electronic effects. However, this method relies on a large number of counts spread across the entire spectrum in order to produce a reliable fit: a scenario that is not always obtainable using smaller volume detectors.

2.6.2.4 *Lead collimators*

The use of lead collimators or lead shielding has been used to predict depth distribution (Feng et al., 2008, Feng et al., 2012). The method entails using different geometries of lead collimators in front of the detector to shield incident photons, thus allowing for the estimation of depth directly from angular response and change in field of view (Whetstone et al., 2011).

This method does have the potential to estimate considerably complicated source geometries, but in order for the method to work, numerous measurements must be taken with variation of shielding arrangements making application challenging and often time constraints, involved in surveying, have meant other methods have been preferred.

2.6.3 Background suppression techniques

For a low resolution detection system, such as many scintillators, full energy peaks often overlap and counts from one peak can be impractical to differentiate from the its neighbouring peak as separation can introduce significant amount of uncertainty.

This is of significant importance with regards to the large number of energy peaks accompanying the natural decay series (i.e. Uranium and Thorium), whose contributions tend to make up the majority of the observed “background”. With energy peaks overlapping each other, regions of interests can become increasingly hard to identify leading to poor quantification of individual radionuclide activity.

To combat this problem, low resolution systems often have a background suppression procedure performed on them in order to give a better representation of the source being analysed, especially when it is weak and could become easily concealed by background counts. There are a number of background suppression methods that are common place in the field of gamma spectroscopy, most of which can be performed in real time.

2.6.3.1 *Spectral stripping*

The method of spectral stripping involves the use of concrete calibration pads, which are doped with known activities of ^{40}K and the Uranium and Thorium series (Grasty et al., 1991). By analysing the detectors response, ratios of all of the natural peaks and their scattering routines can be established. Relatively “cleaner” higher energy windows, for example 2016 keV (^{232}Th), 1764 keV (^{238}U) and 1462 keV (^{40}K) can be monitored and used to subtract proportional contributions from lower energy windows. This method can effectively be used on most anthropogenic radionuclides of interest i.e. ^{137}Cs or ^{131}I. Although, for ^{226}Ra this becomes fairly complex given that it appears as part of the ^{238}U series.

It must be noted that the spectral stripping method can lead to over stripping, in some cases where negative counts can be produced within certain low count windows.

Additionally, the mere nature of subtracting counts from the spectrum introduces a large amount of uncertainty, to counteract this longer counting times or larger detection volumes are required. As a general rule, spectral stripping tends to only be implemented on large volume detectors mounted on aircraft or carborne platforms, as uncertainties on smaller detectors can be unworkable.

2.6.3.2 *Noise Adjusted Singular Value Decomposition*

Noise Adjusted Singular Value Decomposition is best used with large data sets. The data are processed by taking the covariance of individual spectral regions and producing a set of uncorrelated eigenvectors, of which the first 8 or so are thought to contain the majority of signal (Hovgaard, 1997). These spectral components are then ordered, in order of magnitude and the least important components producing the smallest values from the mean spectra, which should correspond to statistical noise. A number of these components are then dropped; leaving an essentially statistically stripped data set (Aage et al., 1999). This technique is described in detail in section 3.5.1.3.

2.6.3.3 *Maximum Noise Fraction*

Maximum Noise Fraction adopts a similar approach to Noise Adjusted Singular Value Decomposition, by means of decomposition of the spectral dataset using eigen analysis (Green et al., 1988). However, the methods differ through the way in which they attempt to normalise the dataset. Maximum Noise Fraction, used routinely in hyperspectral and image analysis, normalises the data by the noise estimated from shift differences in the data, instead of normalising by the variance as with Noise Adjusted Singular Value Decomposition (Dickson, 2004). Similar results have been noted for individual the methods, although methods tend to be implemented on large volume detectors mounted on vehicles (Aage & Korsbech, 2003) or aircraft (Hovgaard & Grasty, 1997). Additionally, as the whole dataset is required for spectral processing these techniques are strictly post-processing.

2.6.3.4 *Digital filters*

The use of digital filters utilising algorithms to strip airborne gamma spectra real time has been employed. Although the method shows little improvement over traditional spectral stripping techniques for natural radionuclides, the identification of peaks of low energy emitting radionuclides such as ^{241}Am has shown progression (Guillot, 2001). Numerous filtering methods can also be found through the literature (Gutierrez et al., 2002, Cresswell & Sanderson, 2009). Again, filters can be unreliable when applied to the noise of data from short dwell time, small volume, detectors (Alamaniotis et al., 2013a)

2.7 Summary

The fundamentals of gamma-ray transport in the environment have been described including their origin, the most prolific sources gamma radiation in the environment and their detection using modern techniques

Additionally, a thorough detection review has been performed, the conclusion of which deemed a 71 × 71 mm lanthanum bromide detector to be the most promising for this application at the present time.

Furthermore, a comprehensive development of photon fluence equations for specific geometries was presented, alongside brief accounts of current methods used to:

estimate depth and activity, calibrate instruments and reduce noise within a spectral dataset. From this latter section it becomes clear that conventional spectral processing methods do not provide a suitable means to cope with the noise presented in data obtained using smaller volume detectors over short dwell times as presented in many surveys and in the research manuscripts in this thesis.

3 General Materials and Methods

3.1 Outline

This section outlines the general methods used to support the research manuscripts in this thesis. It first introduces the manner in which data were collected. Following this, an in-depth description of modelling approach used to develop artificial calibration datasets is outlines encompassing Monte Carlo simulations and the process of developing training and cross validation datasets.

Finally, the algorithms implemented in the research chapters and fitting procedures followed are described in full.

3.2 Data collection

All spectral data were collected over the course of this thesis using Ortec's Maestro software (ORTEC, 2005). Spectral data was presented as 1024 channel ASCII files and for chapter 5, 6, 7, in which handheld detectors were used, 1 second counts were obtained using the .JOB file system implemented in Maestro. ASCII files were then read using an in-house piece of software written in JAVA code called Stirling Mobile Gamma Spectroscopy System (SMoGSS). At the same time as reading spectra, GPS coordinates were obtained and matched by SMoGSS to the relevant spectrum using an SSX blue differential GPS device. This device recorded to an accuracy of 0.6 m. SMoGSS also has real-time readout and alarm capabilities. To eliminate bias in the acquisition of randomly sampled spectra alarms were turned off during surveys.

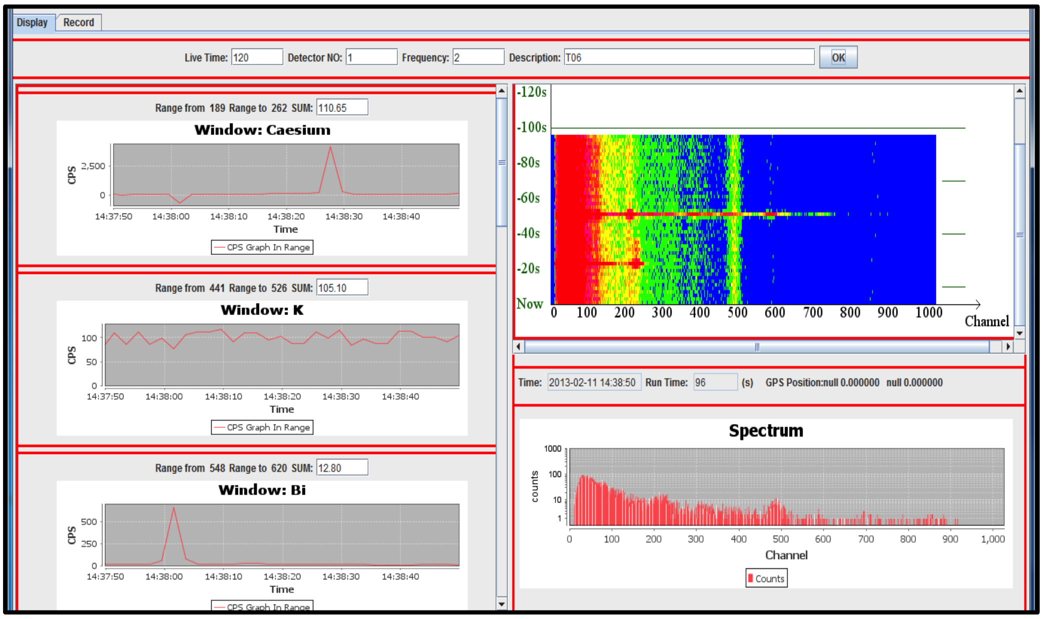

Live Time: 120 Detector NO: 1 Frequency: 2 Description: T06

Range from 189 Range to 262 SUM: 110.65

Range from 441 Range to 526 SUM: 105.10

Range from 548 Range to 620 SUM: 12.80

Time: 2013-02-11 14:38:50 Run Time: 96 (s) GPS Position:null 0.000000 null 0.000000

Figure 3-1. Screen grab taken from operational SMoGSS

3.3 Monte Carlo modelling

Monte Carlo Simulations (MCS) were undertaken to acquire adequate spectral responses to serve as calibration spectra; this approach was taken to replicate field spectra as best as possible, and eventually permit environmental variables to be extrapolated. The software package Monte Carlo N Particle (MCNP) code was used in this thesis, which is distributed by the Radiation Safety Information Computation Centre, Oak Ridge National Laboratories in the United States. The software enables the user access to the vast physical data libraries built up over the course of six decades. The required geometry must be coded in MCNP’s in-house code. The code treats an arbitrary three-dimensional configuration of materials in geometric cells bounded by specified surfaces (Briesmeister, 1993).

For photons, the code accounts for incoherent and coherent scattering, the possibility of fluorescent emission after photoelectric absorption, and absorption in electron-positron pair production (Briesmeister, 1993). Electron and positron transport processes account for angular deflection through multiple Coulomb scattering, collisional energy loss with optional straggling, and the production of secondary particles including K x-rays, knock-on and Auger electrons, bremsstrahlung, and annihilation gamma rays from positron annihilation at rest. The transportation process is generated using random numbers to simulate the path of a photon through system until a point is reached where it has lost all of its energy or exits the region of interest. This procedure is executed in efficient Fortran code.

Tallies are then used to collect useful information about the modelled physical system. In this project, differential energy photon tallies (F8) were applied inside the active volume of the modelled detector (Fehrenbacher et al., 1996). This allowed for full spectral reconstruction whereby results in each individual bin represent the average tally flux per starting particle. Therefore, overall spectral shape and intensity (pulse height distribution) could then be related to the specific activity and source geometry modelled.

Final tally values embody the mean flux of photons and since Monte Carlo is innately a stochastic process, the uncertainty associated with the mean value will be governed by Poisson statistics (Crawley, 2012). Thus, the standard deviation forms the square root of the total count (mean). Essentially, to reduce relative uncertainty associated with each tally, the greater the number of particles is needed at the start of the problem (Likar et al., 2000). This presents a trade-off between the computer time and statistical uncertainty. A variance reduction technique is described and implemented in section 4.4.2.1 to optimise this process. Generally, simulations were divided to run in parallel on a 16 core computer processor.

3.3.1 Benchmark experiments

The first step in obtaining reliable spectral responses involves accurately defining the geometry of the detectors used in this study to ensure that the vast majority of spectral counts match up to that of controlled source geometry. A scenario like this is difficult to perform in the laboratory as the complex geometries posed by the walls and floors introduce large uncertainties. Arguably this could be performed in a lead castle together with a point source, although it is more effective to gauge the angular dependence of the detector to a 2π geometry as found in the environment (Allyson & Sanderson, 2001). Subsequently, flat calibration pads at the British Geological Survey, Keyworth, Nottinghamshire, England were employed as experimental benchmarks (Figure 3-2).

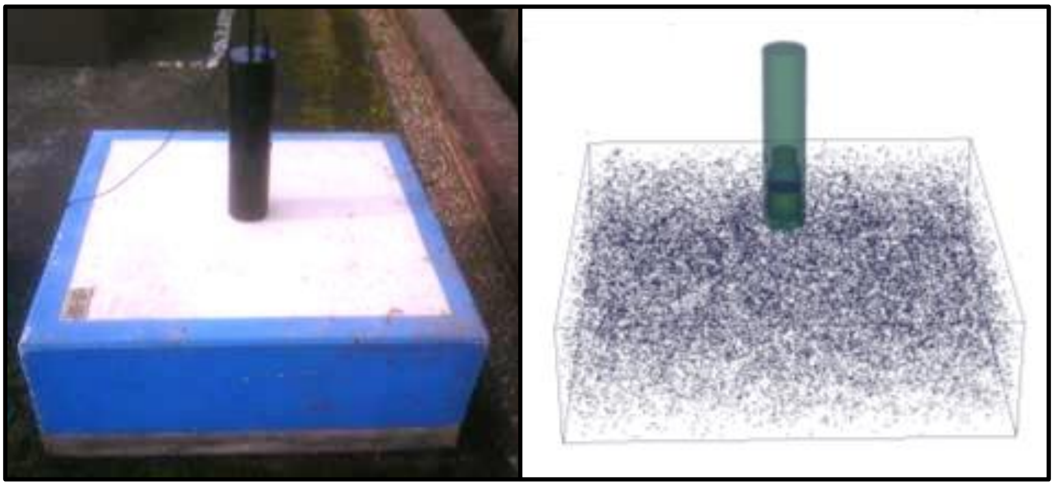

Figure 3-2. Lanthanum bromide detector in its case placed on a ^{232}Th calibration pad alongside an MCNP visualisation.

Three detectors were used in this project: a 51 x 51 mm NaI:Tl employed in chapter 4 and the two 71 x 71 mm (LaBr:Ce and NaI:Tl) handheld detectors featured in chapters 5, 6 and 7. All benchmark spectra are included in Appendix 1

For all detectors a reasonable fit between Monte Carlo and experimental results was found, for instance all chi squared values were highly significant (<0.005). Accurately modelled spectra are observed for the NaI:Tl detectors Appendix II. In contrast, deviations can be visually seen in LaBr:Ce results. There are a number of reasons behind these findings. Firstly, the lower energy resolution possessed by the NaI:Tl detectors permits minor discrepancies between the modelled and experimental to be smoothed over. In the instance of the higher energy resolution LaBr:Ce examples of inconsistencies are more visible, for example in the ^{232}Th pad.

Further inaccuracies are magnified for LaBr:Ce brought about by small amounts of spectral drift between individual pad measurements and the background pad. Owed to its large intrinsic component full spectral stripping led to over stripping in some areas of the spectrum notably in the 1468 keV region. Since NaI:Tl does not have significant intrinsic counts, over stripping was not as noticeable.

Finally, the positions of the pads at the calibration facility brought about additional disparities as there was incomplete removal of background components. This is especially noticeable in spectra taken using the LaBr:Ce detector from the ^{40}K pad where contributions from the ^{238}U series (609 and 1764 keV peaks) are clearly visible Appendix II. This represents a key limitation in the measurement technique used. Placing the pads in identical positions could have negated this effect. Interestingly, this cannot be observed using the NaI:Tl detectors, providing further evidence for the favoured use of LaBr:Ce instead of NaI:Tl due to its higher energy resolution.

3.3.2 Geometric modelling of contamination

The contaminated sites that where the focus of this thesis posed a wide range of contamination geometries. So as to obtain representative spectral responses to all possible source geometries and therefore provide an accurate means to estimate activity, modelling assumptions had to be made. This was especially the case in chapters 4, 5 and 6 whereby ^{226}Ra contamination was known to be highly heterogeneous at those sites. In some areas what could be classified as point source geometries could be positively identified, for example the *in situ* dial and oil gauge (Figure 3-3). However, in other areas no such items could be found instead finely distributed contamination was responsible for the elevated signal (Figure 3-3c). Individual chapters provide details into exact modelling assumptions and fitting routines, therefore brief description is given here for summary.

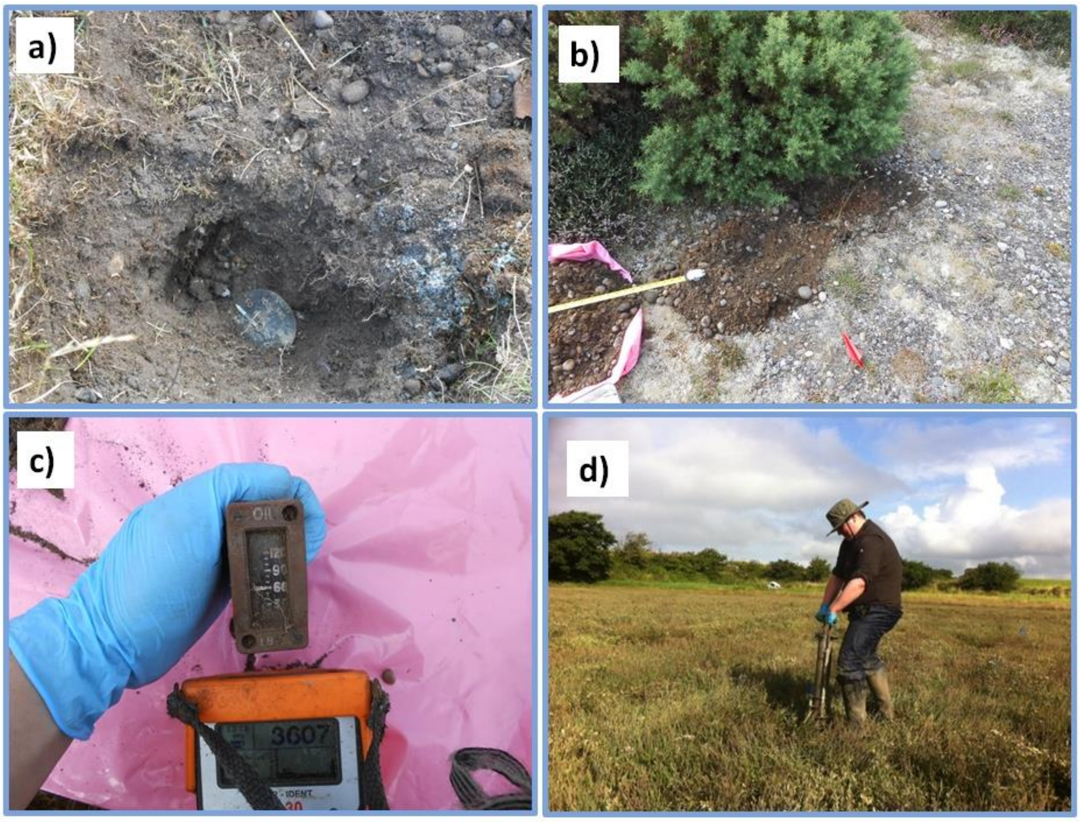

Figure 3-3. a) *In situ* ^{226}Ra dial b) Homogenous ^{226}Ra contamination c) ^{226}Ra containing oil gauge d) Core being extracted ^{137}Cs from homogeneous contaminated site.

Due to the unpredictable nature of contamination at individual sites, model geometries were simplified conditional to the circumstances and objectives of the specific piece of work. For instance, the most challenging piece of work from a modelling point of view was chapter 4, since the detector (51 x 51 mm) had relatively low efficiency and the aim was to separate extended sources from point sources and provide activity and depth estimate. Therefore, in this chapter both extended contamination (with varying extension) and point source were modelled in MCNP (Figure 4-1).

Chapters 5 and 6, similarly involved modelling ^{226}Ra contamination using 71 x71 mm detectors (NaI:Tl and LaBr:Ce) over a short acquisition time (1 second), but the objectives were different. In chapter 5, *hot particle* detection was the objective, resultant in only point sources being modelled. Instead, chapter 6 focussed on characterising large areas of homogenous ^{226}Ra contamination, therefore minor heterogeneities, for example many point sources, are smoothed over under the assumption of a homogenous model. Chapter 7 takes advantage of core profiles to fit a custom ^{137}Cs depth profile model to semi-infinite plane (Figure 3-3d). To recreate a full spectrum the detector's field of view had to be estimated.

3.3.3 Energy considerations

At the vast majority of sites large changes in chemical composition of the geological matrix can take place (Tyler, 2008). A common example is the presence masonry or the exposure of bedrock. This can introduce a large amount of uncertainty with regards to Monte Carlo spectral reconstruction at energies below 150 keV (Figure 3-4). This is due to photoelectric absorption becoming the dominant photon interaction process, which is highly dependent on the Z number of the absorbing material (section 2.4.1). Hence, large changes in chemical composition bring about significant changes in photon flux received by the detector. Therefore, in chapter 5 where *hot particles* were modelled, energies below 150 keV were disregarded from analysis.

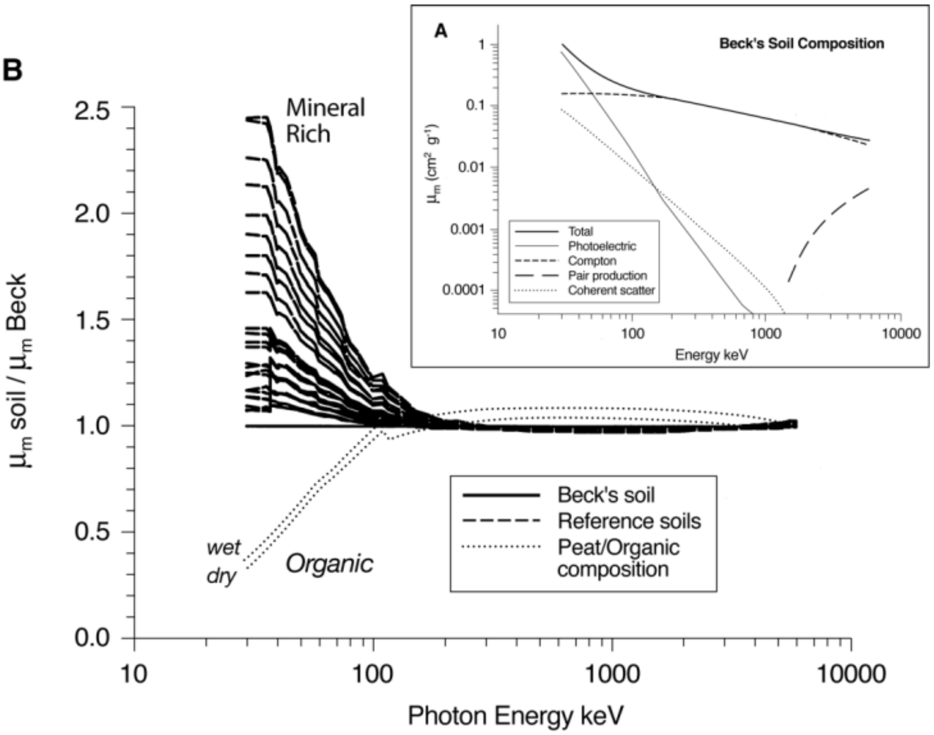

Figure 3-4. (A) Photon cross sections for Beck's soil composition (Beck *et al.*, 1972) from 30 to 6000 keV. (B) Comparison of μ_m for a range of soil compositions relative to Beck's soil composition. After Tyler (1999), Allyson (1994) and Tyler (1994). Taken from Tyler, 2008 with permission from Andrew Tyler.

A further energy consideration was made in chapters 4, 6 and 7, in which contamination was assumed to be homogeneous distributed (for example simulated background) or as an extended contamination source. Through the Monte Carlo simulation of these sources, it was appreciated that backscattering contributions, in the energy region approximately below 300 keV, from photons originated from close to the surface could introduce a large amount of uncertainty (Caciolli et al., 2012). Therefore, for this type of analysis energy below 300 keV was disregarded.

3.4 Dataset construction

For the purposes of training and cross validating different algorithms, which were then used on real data, an approach was developed and employed throughout the data chapters of this thesis. Although, short definitions are provided in individual studies this section provides a more detailed account of the development process. A flow diagram is provided to illustrate the steps (Figure 3-5).

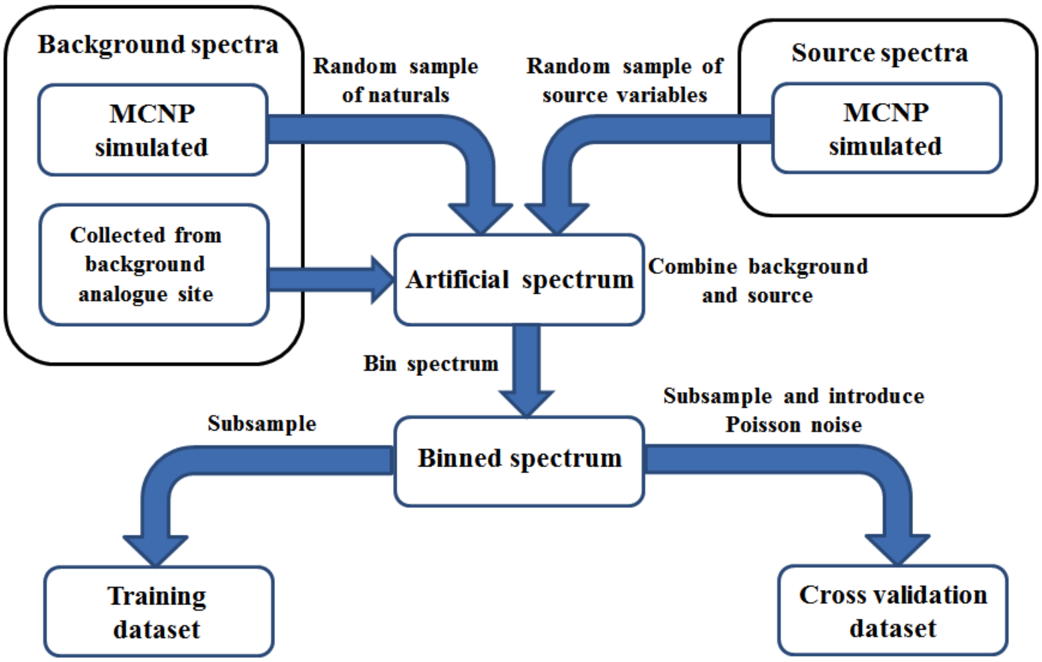

Figure 3-5. Flow diagram illustrating the development method for training and cross validation dataset.

The production of each dataset had one commonality in that source spectral response for a particualar detector, obtained by randomly changing response variables (i.e. depth, activity or distribution), were produced using MCNP (Figure 3-5). Each spectrum was run long enough so as to attain the least amount of uncertainty associated with individual tally bins (Moreira et al., 2010). This typically meant running individual problems for the maximum number of random starting particles in MCNP (2 x 10^9).

Background spectra were obtained in a number of different ways (Figure 3-5). In chapters 4 and 7, no analogue site was available to obtain background spectra. In these cases background spectra were simulated using MCNP, which attempted to encompass real changes in the natural background elements and density. This involved assumptions regarding the concentration of natural radioelements that are detailed in individual chapters.

Where an analogue site could be identified, spectra were collected rather than attempting to simulate background conditions. Spectral dataset were then spiked with simulated source spectra as demonstrated in chapters 5 and 6 (Figure 3-5). Figure 3-6 graphically illustrates the random spiking routine of a background time-series with MCNP source spectra operated in chapter 5.

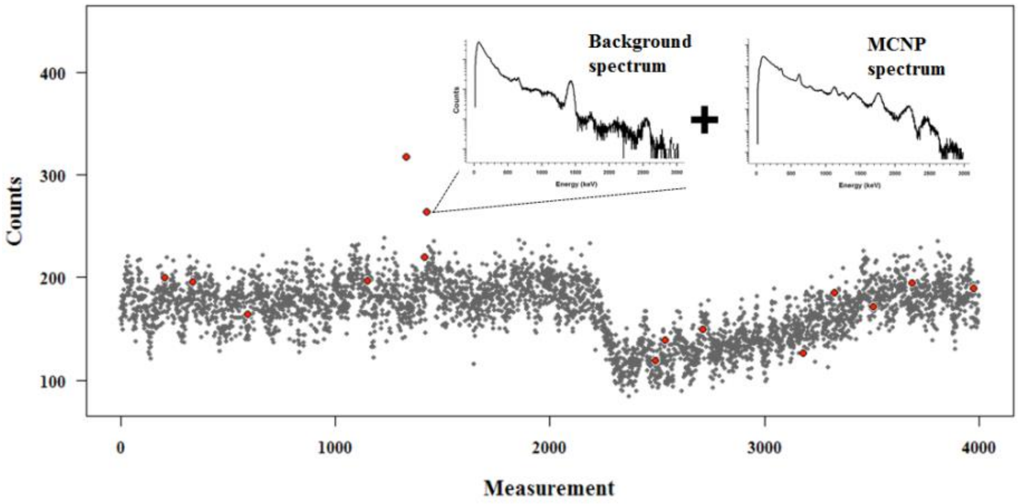

Figure 3-6. Spiking MCNP source spectra into the time series of a background dataset. Y axis indicates gross counts.

Combining background and source spectra produced an artificial spectral dataset containing statistically defined spectra (Figure 3-5). At this point spectra were binned to alleviate some counting noise and to reduce the dimensionality from 1024 channels to approximately 13-30 bins (see chapter methodologies for details). This dataset was then randomly sampled producing two subsamples: training and cross validation datasets. The training dataset remained as it was after binning. Crucially, this was the dataset used to fit deterministic algorithms and train and test Machine Learning algorithms.

In order to generate a dataset that was representative of noisy environmental spectra, that field results could be compared to, a validate dataset was produced. The cross validation dataset was used to assess the performance of different algorithms (see individual chapters for assessment criteria). Final algorithms, which produced the best results on the cross validation dataset, were then used to process field spectra, yielding source characteristic information.

3.5 Algorithms

There are a number of different algorithms used in this study and brief accounts of each can be found in respective chapters. However, in this section detailed descriptions are provided of the methods used. In this work algorithms are separated into two groups: deterministic and Machine Learning algorithms.

3.5.1 Deterministic algorithms

Deterministic algorithms are constructed through equation bases models, and once fitted, will produce the same answer given identical input. This makes the deterministic algorithms, based on conventional statistical assumptions, reasonably straightforward to apply and interpret (Kock et al., 2012). In this thesis three deterministic algorithms are featured.

3.5.1.1 *Gross counting alarm*

Gross counting (GC) algorithms are used extensively in the field of gamma-ray spectroscopy and are featured in chapters 5 and 6 (Ely et al., 2004, Jarman et al., 2008). The technique treats the entire spectrum as a single bin and can be used, in its most basic form, to map extensive areas in an attempt to identify hotspots as demonstrated in Chapter 6 and in other works (Adsley et al., 2004).

In chapter 5 a rolling mean filter of the previous few measurements is employed in order to estimate the background of a site (*N*) (eq 10). The principal aim of this procedure is to capture anomalous changes in signal at a site that could manifest as a result of *hot particles*. There are a number of mathematically derived rolling mean filters that can be used in an attempt to adapt to natural background variation taking place at a site (Shumway & Stoffer, 2013). Such algorithms attempt to model the autocorrelation presented in the gross signal, brought about by changes in the concentration in the natural radioelements and soil density and composition (Kock et al., 2012). A critical threshold (T) can then be established for the purpose of identifying anomalous signal. Alternatives to conventional lag-based algorithms can be employed including the data fusion algorithm the Kalman filter (Jarman et al., 2008).

$$T = N + K\sqrt{N} \tag{10}$$

In chapter 5, equation 3 was used as the deterministic benchmark to compare Machine Learning algorithms to. In this form K (sigma multiplier) defines the number of standard deviations ($\sqrt{N}$) above N the alarm threshold should be set. In theory, if a substantial increase in signal is received, the alarm should sound as T is breached. Section 5.4.1 details the optimisation of the parameters K and the number of lags used on the moving mean.

3.5.1.2 *Spectral comparison ratios*

Spectral comparison ratios were utilised in chapter 5 as a real-time noise reduction step prior to the application of Machine Learning algorithms. This procedure required a spectrum to be divided into non-overlapping energy bins (Du et al., 2010). Detailed descriptions of the binning process can be found in section 5.3.4.2.

$$SCR_i = N_1^c - \frac{N_1^B}{N_i^B} N_i^c \tag{11}$$

Each spectral bin was then transformed into the time series according to equation 11. Where N_i^c is bin *i*, and N_1^c is the first bin, of the current measured spectrum. N_i^B and N_1^B are a respective moving means of bin *i* and the first bin of the previous spectra (Trost & Iwatschenko, 2002). Similar moving mean algorithms, as described in section 3.5.1.1, can be used to characterise the autocorrelation of individual bins (Jarman et al., 2008). This produces a transformed spectrum where the first channel is 0 and all channels contained within a background spectrum should be close to zero as small temporal variations are expected to occur (Du et al., 2010).

3.5.1.3 *Principal Component Analysis*

Principal component analysis (PCA) can be implemented in order to reduce the noise of a dataset. Another useful outcome is that the dimensionality of useful signal can be significantly reduced. Essentially the method transforms raw spectra into orthogonal components (named principal components or PCs), which are ordered in accordance to the overall variance they contribute to the dataset. PCs contributing the largest variance are thus considered to contain "real" signal elements. Higher order PCs are assumed to contain mainly correlated noise (Du et al., 2010). The following description of PCA follows closely that of Mauring and Smethhurst (2005).

The mechanics of PCA and eigen analysis can be found in the literature, of which Hotelling (1933) provides a particularly thorough review. Mathematically, PCA is performed using eigen-decomposition of the covariance matrix A^TA, where A is an input spectral dataset made up of m observations with n energy bins (equation 12).

$$\mathrm{A}^T\mathrm{A} \tag{12}$$

$$A = CS \tag{13}$$

m = number of observations

n = number of energy bins

A = spectral matrix ($m \times n$)

C = loadings ($m \times n$)

S = principal components ($n \times n$)

The input spectrum A_m can then be represented by linear combinations of loadings (C) of PCs (S). The essence of PCA is to describe the dataset through a set of orthogonal latent variables related to the variance. The first variable or PC is fitted to maximise the variance between all of the input channels (Aage et al., 1999). A simpler way of viewing this is that PC 1 will take the form of the mean spectrum of the entire dataset (Figure 3-7). The second PC would be the mean shape of the resulting differences after the PC 1 is subtracted from the dataset (Figure 3-7).

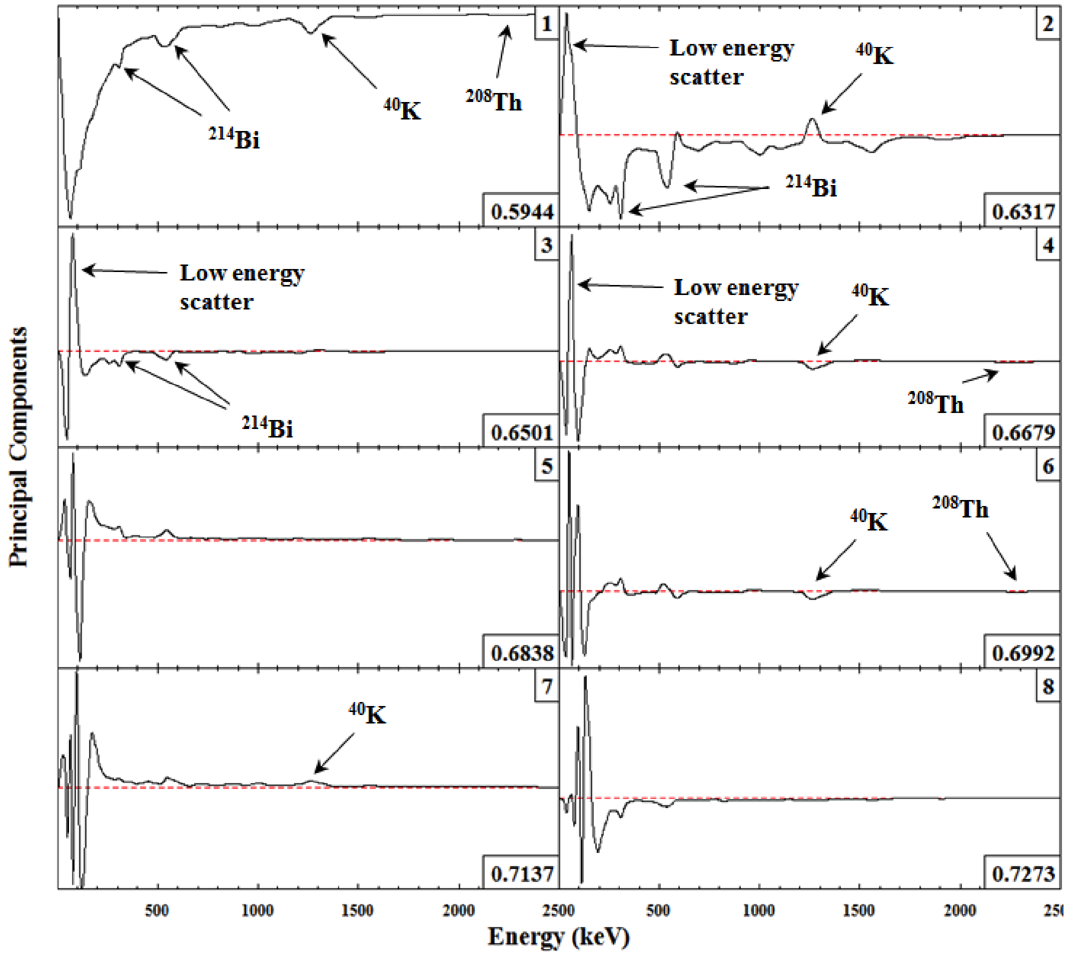

Figure 3-7. Principal Components of a 71 × 71 mm NaI:Tl dataset.

Note prominent peaks have been identified.

Figure 3-7 presents a plot of the first 8 PCs taken from a ^{226}Ra contaminated site acquired using a Na:Tl detector. Immediately structure can be identified within first few PCs. The dominant peaks attributed to ^{214}Bi (daughter of ^{226}Ra) and the natural radioelements ^{40}K and ^{208}Th (daughter of ^{232}Th) can easily be acknowledged. Importantly some peaks occur in antiphase with each other, notably ^{214}Bi and ^{40}K in PC2, indicating greater negative loading values of PC 2 will increase the amount of

^{226}Ra signal present in the spectrum compared to ^{40}K. Such patterns within loadings formed the basis for Machine Learning algorithms to interpret source characteristic from, such as depth and activity. This is the reason PCA was used extensively in chapters 4, 6 and 7. A disadvantage of PCA type analysis is that it cannot be employed in real-time and therefore is strictly a post-processing tool (Cresswell & Sanderson, 2009).

Utilising PCA in spectral analysis however presents two constraints. Firstly, data must be centred on the origin instead of around the sample mean, which conventional PCA adheres to. This can be overcome by using Singular Value Decomposition. A second constraint is that Singular Value Decomposition then requires the variance in individual channels to be the same. Due to the stochastic nature of photon detection, which is collected as counts, it is known that this is not the case since lower count rates, typically at higher energies, will have relatively more uncertainty associated with them (Dickson, 2004). Hovgaard (1997) suggested a simple solution to this problem. The best fit of the mean spectrum to the individual spectrum will provide a good estimate of the mean count rate to the individual spectrum. Therefore, A (eq 6) can be transformed into A_{new} through matrix equations 14-17.

$$Sum(i) = \sum_{j=1}^{m} A(i,j) \tag{14}$$

$$S(j) = \frac{\sum_{k=1}^{m} A(i,k)}{Sum(i)} \tag{15}$$

$$SN(j) = \frac{S(j)}{\sum_{k=1}^{m} S(k)} \tag{16}$$

$$A_{na}(i,j) = \frac{A(i,j)}{\sqrt{SN(j) * Sum(i)}} \tag{17}$$

Where individual channels *s(i)* (eq 15) are divided by the sum of each spectrum *Sum(i)* (eq 14). This process normalises the channel to the sum of the spectrum. After which, all channels are normalised by the sum of the normalised channel producing the weighted matrix *SN(j)* (eq 16). The original spectral matrix *A* is weighted by square root of this weighted matrix *SN(j)* multiplied by the sum of each spectrum *Sum(i)* (eq 17). This produces an equivalent noise-adjusted spectral matrix A_{na}.

At this point, Singular Value Decomposition (eq 18) can be performed on the noise-adjusted spectral matrix A_{na}.

$$A_{na} = UWV^T \tag{18}$$

Where V are the eigenvectors (or PCs) of covariance matrix $A_{na}{}^{T}A_{na}$ and the eigenvalues are the square of the elements W. The PCs are rescaled by the multiplying them by SN(j) (eq 16) and the loadings (C) are rescaled by multiplying them by *Sum(i)* (eq 14).

3.5.1.4 *Mahalanobis distance*

Mahalanobis distance allows for the rescaling of multivariate data by taking into account correlation between input variables (Mahalanobis, 1936). The transformed data can then be considered in Euclidean scales allowing for conventional statistical assumptions (such as Gaussian distributions) to be applied. Chapters 4 and 6 briefly cover Mahalanobis distance where it is employed to separate source signals from benign background signal within PCA transformed data. Here a more comprehensive discussion of Mahalanobis distance is given.

$$MD = \sqrt{(x-\mu)^T . S^{-1} . (x - \mu)} \tag{19}$$

Where (x) is a vector of data with mean (μ), and the covariance matrix between observations is S (eq 19). The Mahalanobis distance is the mean-centred Euclidean distance weighted by the variance of, and the covariance between, each vector element (x_1, x_2, x_3 …). In assuming a parent multivariate Gaussian distribution, Mahalanobis distance can be statistically modelled using the chi-squared distribution (Runkle, 2006). A visual example of Mahalanobis distance is provided in Figure 3-8, seen as a slightly angled ellipse enabling correlations between Principal Components to be taken into account. This example demonstrates deeper particles (red dots) are harder to separate from the background (blue dots) than particles closer to the surface (yellow dots).

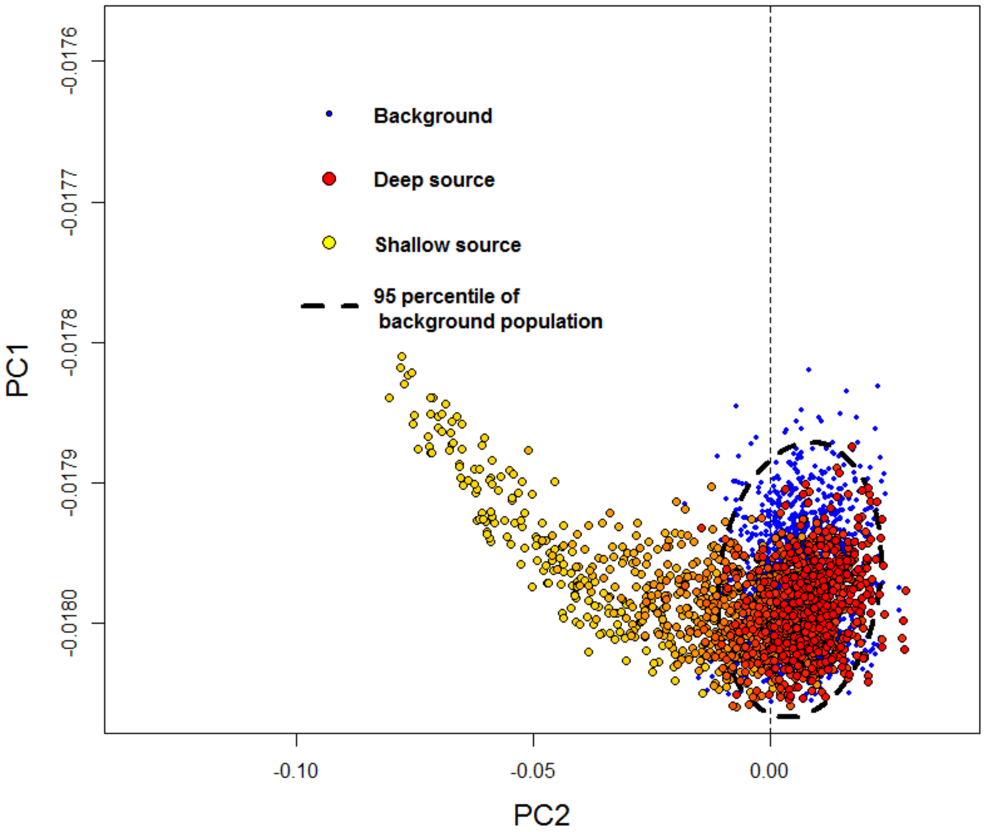

Figure 3-8. Visual example of Mahalanobis distance (95 percentile elliptical ring) for background and a ^{226}Ra source with different burial depths.

3.5.2 Machine Learning algorithms

Machine learning (ML) algorithms are essentially pattern recognition techniques that are driven by a set of training data (Ao et al., 2010). They are particularly useful when input parameters are of high dimensionality and present nonlinearities that are difficult to map to response variables using conventional formulaic means (Fagan et al., 2012). Due to these qualities the use of ML to interpret gamma-ray spectroscopy data is justified owed to the high dimensionality of spectral data, nonlinearities occurring across the spectrum posed by source burial and complex noise distributions (Du et al., 2010). As of yet however, ML has not become commonplace in environmental gammaspectroscopy.

In this study two ML algorithms were implemented: Neural Networks (NN) and Support Vector Machines (SVM).

3.5.2.1 *Neural Networks*

A NN is composed of a number of processing units known as nodes that are separated into three distinct layers: the input, hidden and output (Figure 3-9). The input layer is a collection of the nodes defining the explanatory variables of the problem. The hidden layer can in fact be made up of one or more layers and the output layer, contains the desired response variables. Each hidden neuron contains an activation function, for example hyperbolic tangent or sigmoidal. Critically, it is a combination of multiple nonlinear activation functions possessing different weights that provides NN with the capability to learn complex nonlinear relationships. Interestingly, neural networks without a hidden layer can be directly compared to generalised linear models (Yoshida et al., 2002).

Each node has its own weight set, with the weights defining the strength of the connections between neurons in adjacent layers (Pilato et al., 1999). The weights are varied and optimised during a training phase where the error between predicted outputs and desired output of the specified training set is minimised in an iterative fashion (Medhat, 2012). In this work, this process was achieved by using the resilient backpropogation algorithm (Riedmiller & Braun, 1993). The R package RSNNS was used to construct and train all NNs (Bergmeir & Benítez, 2012a). NNs were adapted to solve both classification and regression problems.

Figure 3-9 provides a visualisation of the architecture one of a NN used to estimate the ^{137}Cs depth distribution in chapter 7. It can be seen that 8 inputs (the first 9 PCs) and 15 hidden neurons could be used to adequately describe the relationship between spectral response (after being transformed into PC space) and source distribution. See chapter 7 for full details.

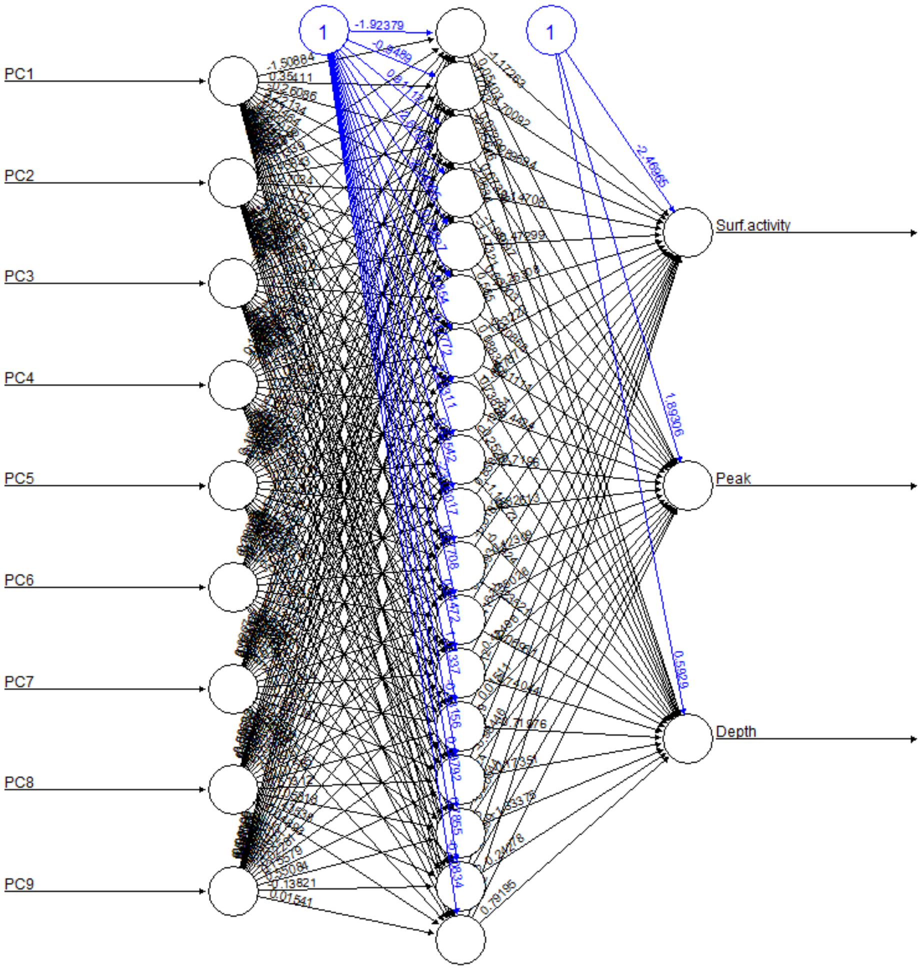

Figure 3-9. Schematic diagram of a neural network showing input, hidden and output layers with weighted connections between neurons and biases on individual neurons.

However, decisions had to be made throughout the research manuscripts of this thesis, regarding the architecture of individual NNs. This included the number of neurons in the hidden layer, the number of inputs (for PCA transformed data) and the number of learning epochs.

All decisions on optimised architectures were made by minimising the root mean square error on the cross-validation dataset, which was considered as close as possible to actual environmental spectra (section 3.4). To optimise this process, an extensive grid search was coded into the software package R. Since there were only two or three parameters that needed to be optimise in individual problems the time spent searching the grid space was achievable (i.e. 24-48 hours). In the event of further parameters, or even to make the process more streamlined, more complex optimisation algorithms could be implemented such as the simplex algorithm (Dragović et al., 2006) or particle swarm optimisation (Wei et al., 2010).

An example of optimising the number of input PCs in the NNs featured in chapter 4 is illustrated (Figure 3-10). Global minima were found by using between 3 and 5 PCs as inputs. Decisively, using larger amounts of PCs did not improve results as the root mean square error increases.

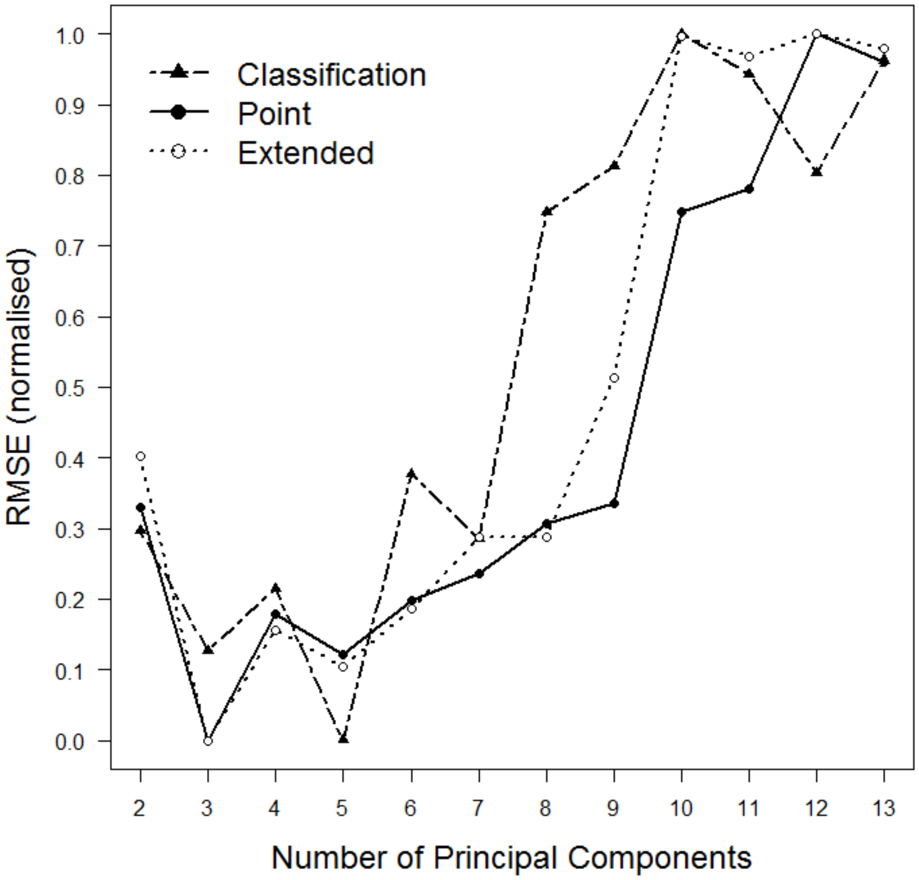

Figure 3-10. The root mean square error (normalised) associated with changing the number of Principal Components as input neurons for the Neural Networks: Classification, Point and Extended. For details see section 4.5.

3.5.2.2 *Support Vector Machines*

Support Vector Machines (SVM) were used in chapters 4 and 5, purely for classification purposes. SVM can be implemented for regression problems, but in this work NN were preferred as multiple response variables could be built into a single model.

SVM approach the solution of a nonlinear classification problem differently to NN. Instead of implementing a complex network of nodes with variable weights and nonlinear activation functions, SVM introduce maximal-separating hyperplanes into the feature space (Cortes & Vapnik, 1995). The procedure of fitting a linear maximal-separating hyperplane mathematically is convoluted; therefore it will not be repeated here. For an extensive description refer to James et al. (2013). However, from a conceptual angle, the description of the processes that lead to accurate class separation is reasonably intuitive.

First consider two populations that do not overlap in space. In this case a geometric hyperplane can be introduced into the feature space, with the aim of maximising the distance between itself and training observations (James et al., 2013). The new margin can now be reliably used to make class predictions on unseen data.

Complications, nonetheless, arise in the event that two populations are overlapping and cannot be separated using a linear hyperplane without including training points in the wrong category (Figure 3-11). In this instance, a so-called *soft margin classifier* is established, which allows some of the training observations to violate the class boundary. The use of correctly structured soft margin can allow for a very accurate optimised surface boundary to be constructed that takes into account noisy classes (Sharma et al., 2012). Importantly, points within the soft margin (dotted lines) are often referred to as support vectors (Figure 3-11). A real strength of *soft margin classifier* is that large weights are put onto these support vectors, so much so, that if these points move slightly so does the geometry of the hyperplane, even with no movement from other points in the training dataset.

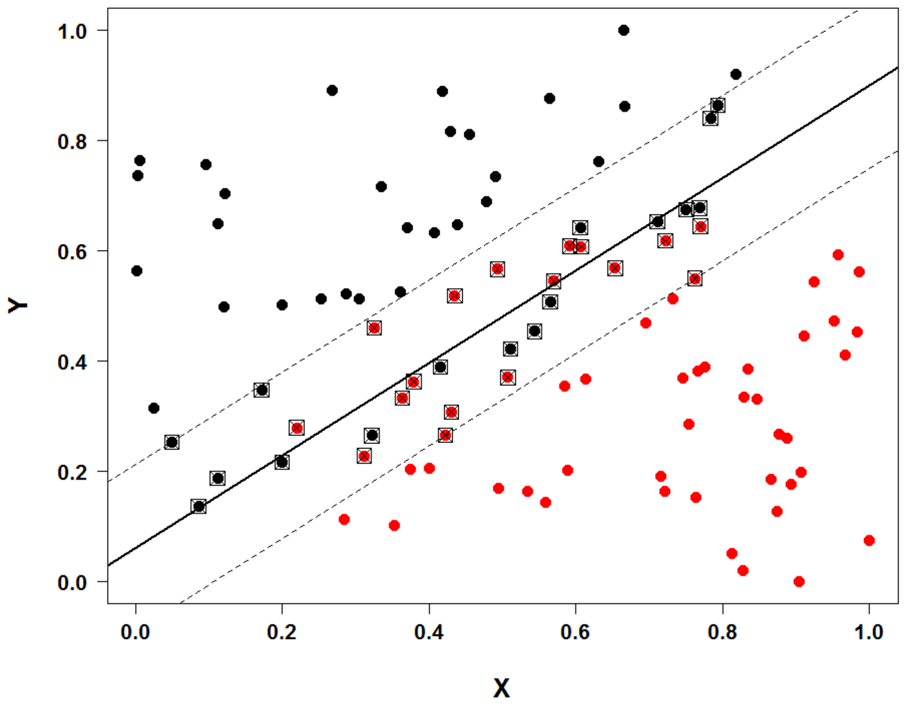

Figure 3-11. The insertion of a maximum-separating hyperplane (full line) into a noisy classification problem through the implementation of a *Soft margin classifier* (dotted lines). Support vectors are identified by squares.

Nonlinear class boundaries pose a new problem. No longer can a straight-line divide the two classes reliably and introduction of nonlinear surfaces becomes incredibly mathematically cumbersome. Boser et al. (1992) introduced an ingenious technique of overcoming this obstacle by introducing kernel functions to enlarge the feature space ensuring dot products of the support vectors could be easily computed. This allowed the introduction of *soft margin classifiers* providing a means of separating complex populations without using vast quantities of computer memory (James et al., 2013). This technique is referred to as the "kernel trick" (Smola et al., 1998). There are a number of commonly applied kernels to perform this task including: polynomial, sigmoid, radial basis function and spline (Sangeetha & Kalpana, 2010). The Radial Basis Function kernel was used throughout this thesis as produced the best classification results. The R package "e1071" was used in chapter 5 and 6 (Dimitriadou et al., 2008).

On a Radial Basis Function kernel there were two parameters that have to be optimised. The first tuning parameter, "C", indicates the bias-variance trade-off or fuzziness of the hyperplane. Generally, greater values of C will enable the fitting algorithm more support vectors to utilise making the *soft margin* wider (Figure 3-11). However, greater values of "C" can cause overgeneralisation.

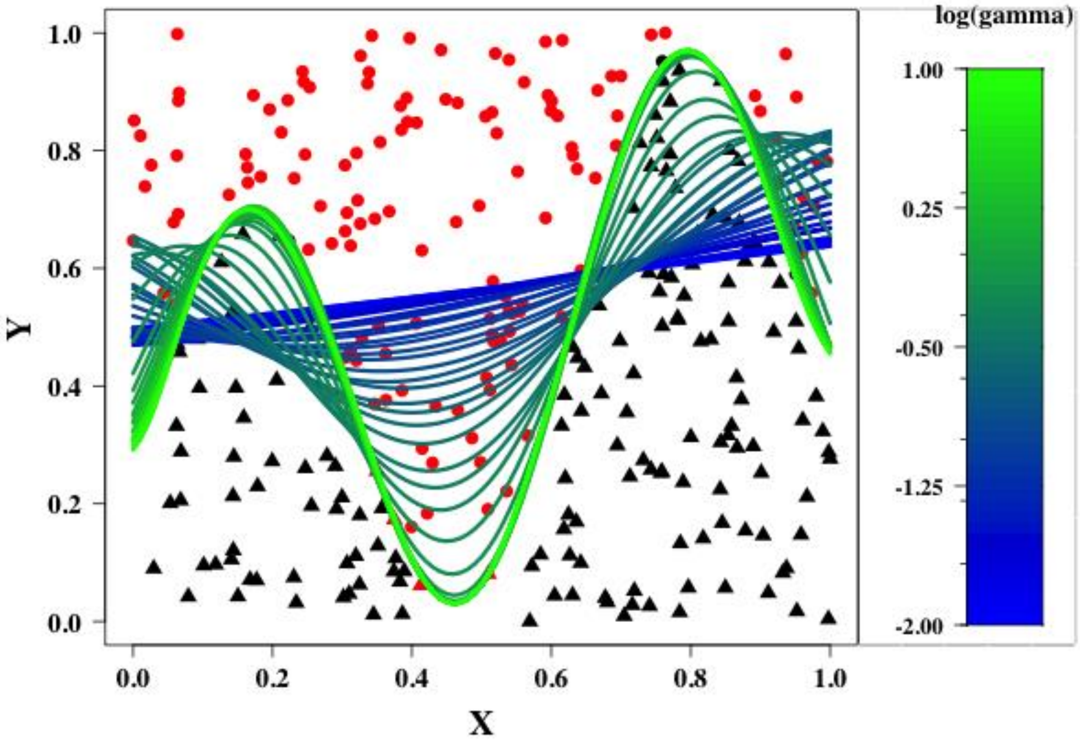

Figure 3-12. Radial basis function kernel applied to nonlinear space. Variation of the gamma parameter on the kernel provides an adaptable fit into the feature space.

The second parameter is gamma, specifying the shaping function used on the Radial Basis Function, which defines the flexibility of boundary separating classes. Figure 3-12 demonstrates the outcome on the separating boundary by varying the gamma parameter for an arbitrary nonlinear problem. For this example, a greater gamma parameter produced a more reliable fit. However, for other problems the greater gamma parameters could cause over-fitting to the training data.

Individual problems, particularly in high dimensions, as found within this thesis, both the parameters “C” and gamma had to be varied with caution to avoid over-fitting. This was performed using a grid search.

3.5.3 Summary

A detailed account of the methods used in this thesis has been described in support of brief accounts provided in individual research manuscripts due to the demands of scientific publishing style. This chapter has included detailed descriptions of the Monte Carlo regimes taken, the procedure used to build training and cross validation datasets and the deterministic and Machine Learning algorithms employed.

4 Development of a Neural Network approach to characterise ^{226}Ra contamination at legacy sites using gamma-ray spectra taken from boreholes

Adam Varley[1], Andrew Tyler[1], Leslie Smith[2], Paul Dale[3]

[1]Department of Biological and Environmental Sciences, University of Stirling, Stirling, FK9 4LA

[2]Department of Computing Science and Mathematics, University of Stirling, Stirling, FK9 4LA

[3] Scottish Environmental Protection Agency, Radioactive Substances, Strathallan House, Castle Business Park, Stirling, FK9 4TZ

Varley A., Tyler A., Smith L. and Dale P. (2015) Development of a neural network approach to characterise ^{226}Ra contamination at legacy sites using gamma-ray spectra taken from boreholes, *Journal of Environmental Radioactivity*, **140**, 130-140

4.1 Abstract

There are a large number of sites across the UK and the rest of the world that are known to be contaminated with ^{226}Ra owing to historical industrial and military activities. At some sites, where there is a realistic risk of contact with the general public there is a demand for proficient risk assessments to be undertaken. One of the governing factors that influence such assessments is the geometric nature of contamination particularly if hazardous high activity point sources are present. Often this type of radioactive particle is encountered at depths beyond the capabilities of surface gamma-ray techniques and so intrusive borehole methods provide a more suitable approach. However, reliable spectral processing methods to investigate the properties of the waste for this type of measurement have yet to be developed since a number of issues must first be confronted including: representative calibration spectra, variations in background activity and counting uncertainty. Here a novel method is proposed to tackle this issue based upon the interrogation of characteristic Monte Carlo calibration spectra using a combination of Principal Component Analysis and Artificial Neural Networks. The technique demonstrated that it could reliably distinguish spectra that contained contributions from point sources from those of background or dissociated contamination (homogenously distributed). The potential of the method was demonstrated by interpretation of borehole spectra collected at the Dalgety Bay headland, Fife, Scotland. Predictions concurred with intrusive surveys despite the realisation of relatively large uncertainties on activity and depth estimates. To reduce this uncertainty, a larger background sample and better spatial coverage of cores were required, alongside a higher volume better resolution detector.

4.2 Introduction

4.2.1 Origin and regulation of radium contaminated land

At the start of 20th century, radium was being used for a multitude of purposes, including medicines, confectionaries and what would prove to its most beneficial use: a seemingly unbroken light source known as “Undark” (Kathren, 1998). Since these early explorations, not only has our understanding improved into the radioactive emissions released by radium and its decay series but also the detrimental mechanisms with which they interact with living tissue (Rundo, 1993, Paschoa, 1998). In the United Kingdom (UK), many redundant radium artefacts are now classified and controlled as low or intermediate level radioactive waste (HMSO, 1996).

Although the majority of radium production ended in the UK by the 1930’s, radium salts were still imported for medical, industrial and military purposes into the 1960’s (Tyler et al., 2013). In the absence of contemporary legislation, considerable quantities of highly radioactive radium waste were discarded by means of burial (Harvie, 1999). Only in 1960 was the use, keeping and disposal of radioactive sources controlled by statute through the Radioactive Substances Act 1960 and later the Radioactive Substances Act 1993 (HMSO, 1996). Examples of these legacy burial sites have also been identified in other parts of Europe and North America (Adams, 1993, Landa, 1993, Adsley et al., 2004).

It has been conservatively estimated that in the UK alone there are between 150 and 250 Radium Contaminated Legacy Sites (RCLS), but the number could be closer to 1000 (DECC, 2012). Considering the possible extent of contamination and the risk to society they pose, legislation has now been passed in UK allowing environmental regulatory agencies to identify, assess and, if needs be, designate radioactively contaminated land (Tyler et al., 2013).

4.2.2 Characterisation of radium contamination

Following the potential identification of any land as being contaminated with radium, the land has to be accurately characterised providing a foundation for subsequent dose calculations and risk assessments. This will determine whether actions are required in terms of remediation. Estimates of the source's activity, burial depth and lateral extent must be provided. Furthermore, knowledge of the localised extent of the source can be instrumental in proposed remediation strategies. Localised extent can be defined by source geometries where the contamination can be considered more of a point source (in extreme cases referred to as a "hot" particle) or dissociated (or more appropriately an extended homogenous source). This will have implications on exposure pathways, transport processes, received dose and ultimately risk. In general, a point source (PS) is considered to be more hazardous, since human contact may result in a much higher dose than extended homogenous source (EHS) of similar activity. In the scenario where the risk a PS poses is considered too high, it should either be removed and disposed of or isolated to prevent human exposure (Dale et al., 2008). However, areas of contamination cannot always be categorised as singular PS or EHS. Often, many PS of similar activity (usually low activity) can be identified, either attributed to a number of small radioactive items or larger items mechanically broken up (Patton et al., 2013). This eventuality can be thought of as a Heterogeneous Source (HS), but separating HS from EHS via non-invasive methods can be very challenging. The aim of this work is to characterise highly radioactive PS.

4.2.3 Detection of radium contamination

For the most part, *in situ*, mobile and airborne gamma-spectrometry are the workhorses for large scale radioactive contamination land characterisation as alternative empirical methods tend to be :expensive and time consuming, and can often be unrepresentative (Aage et al., 1999, IAEA, 2003, Tyler, 2008, Kock et al., 2012). The majority of this research has been focussed on ^{137}Cs detection for extended sources (Boson et al., 2009a, Carrazana González et al., 2012) and “hot” particle detection (Maučec et al., 2004, Davies et al., 2007, Tyler et al., 2010). Up to now, however, very few researchers have focussed their efforts on characterising RCLS (Thummerer & Jacob, 1998, Adsley et al., 2004, Haddad et al., 2014). Yet, with an increasing awareness of the potential number of contaminated sites in existence, it is essential that efficient methods be developed for their rapid and accurate characterisation.

At any RCLS, the principal contaminant tends to be ^{226}Ra and its progeny which is a reflection of the long half-life of ^{226}Ra and its persistence in the environment. Direct gamma-spectrometry of ^{226}Ra in the environment is challenging as it only has one relatively weak low energy gamma ray from which to infer its activity (186 keV). Subsequently its daughter products (^{214}Bi and ^{214}Pb) are conventionally used as a proxy measure. However, this can be inherently problematic as secular equilibrium is not always encountered as a result of ^{222}Rn emanation (Crossley & Reid, 1982, Ball et al., 1991, Dickson, 1995). To address this issue, many studies assume the fulfilment of equilibrium introducing systematic uncertainty to any ^{226}Ra activity estimations (Thummerer & Jacob, 1998, Hendriks et al., 2001). Before reliable approximations of depth, activity and localised distribution of ^{226}Ra can be made, four inherent confounding factors must first be respected:

- If the photon flux at the detector is low, gaining acceptable uncertainty on the measurement can be impractical as Poisson statistics concede the error is the square root of the total count.
- ^{226}Ra and daughter products form part of the ^{238}U decay series that can be observed in varying amounts in any background environmental gamma spectrum where variations can occur over a scale of meters.
- As a source is buried an exponential decrease in unscattered photons is observed with the vast majority of photons that reach the detector being scattered.
- At energies below 150 keV, photons, although numerous, tend to undergo photoelectric absorption making the composition of the geological matrix an important control on photon flux (Tyler, 1999, Tyler, 2008). Backscattered photons (<250 keV) can also be challenging to interpret.

These factors, acting in combination, influence the confidence with which a source in the presence of a typically heterogeneous background radiation field can be resolved. Moreover, once a source has been identified, considerable uncertainties relating to its localised extent and activity can remain. It is for these reasons *in situ* and mobile gamma-spectroscopy of ^{226}Ra PS, below observed activity thresholds (<70 MBq), is considered impractical below depths of about 70 cm. This is because the majority of the source signal, particularly the intense low energy peaks below 609 keV, is enveloped by background noise with increasing source depth. Measurements beyond this depth must therefore be addressed with borehole measurements (Wilson & Conaway, 1991, Meisner et al., 1995, Adsley et al., 2004, Bugai et al., 2005).

4.2.4 The borehole measurement

Borehole measurements are customarily taken as a depth series, when the detector is lowered into the borehole. Ensuing spectra can then provide knowledge into layers of contamination if sufficient spatial coverage is performed to validate extrapolation (Bugai et al., 2005, Adsley et al., 2004). Otherwise, the shape and magnitude of standalone spectra offer insight into localised source arrangements (Giles & Dooley, 1998). Subtle changes occurring within the spectrum's overall shape, suggestive of alterations in source geometry and activity, could potentially correspond to the presence of contamination. Identifying such changes is invaluable in the search for hazardous "hot" particles in close proximity of the borehole (Wilson et al., 1997). For a detailed review of borehole measurements refer to Kobr et al. (2005).

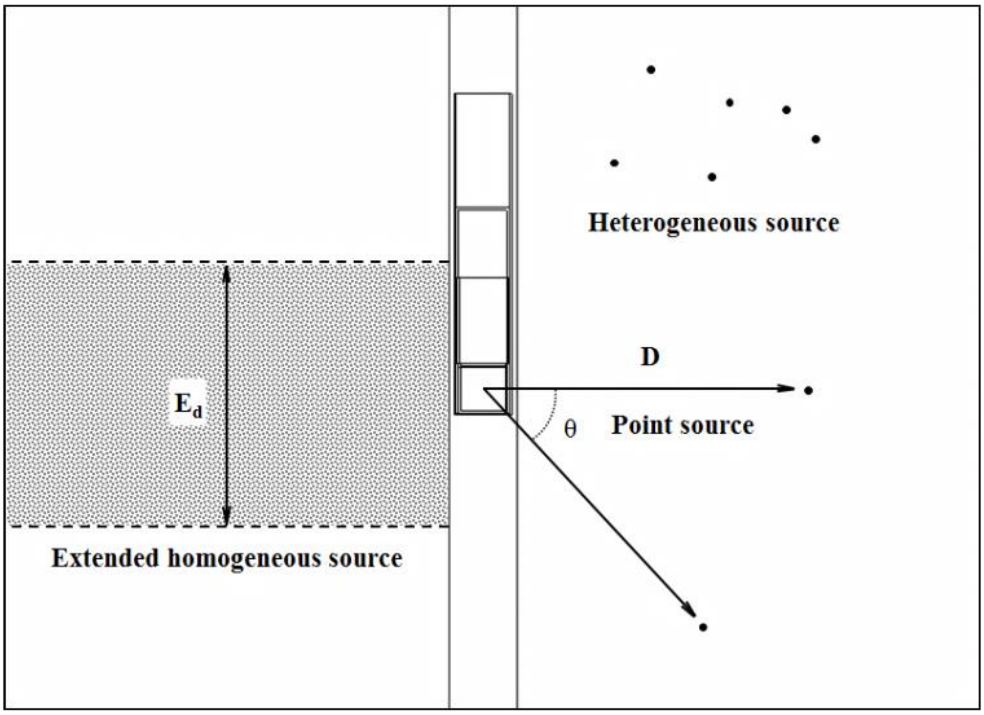

Figure 4-1. Cross-section of the detector in the borehole including the source geometries of interest: extended homogeneous source, point source and heterogeneous source

The source geometries, extended homogeneous source (EHS), point source (PS) and for completeness heterogeneous source (HS) are illustrated alongside the detector in a borehole geometry (Figure 4-1). First consider a PS, where *D* is the mass thickness of shielding (g cm^{-2}) and θ is its angle perpendicular to the axis of detector. The measure mass thickness was preferred over Euclidean distance, since it takes into account the amount of shielding, related to the density of soil, which can significantly vary with depth and lateral position (Tyler, 2008). Secondly, an EHS can be described by E_d indicating its vertical depth with its midpoint at the centre of the detector's active volume. For completeness the final geometry HS, is a differing number of PS at variable *D* from the detector; this eventuality will be considered by this study as EHS.

Exploring the parameters, E_d and D, as spectral shape drivers is the fundamental aim of this study. Nevertheless, other parameters known to influence spectral shape, although not the primary focus in this study, such as soil density and the constituent that make up background must be added by way of assessing the uncertainties that will be introduced to any conclusions of activity and geometry.

4.3 Spectral processing

Without contamination present, changes in the shape and magnitude of borehole spectra will almost exclusively be due to deviations in background activity (^{40}K, ^{238}U series and ^{232}Th series) and shielding influences brought about by changes in soil density and composition. If a site is contaminated, it is the fundamental goal of a surveyor to differentiate between these benign background fluctuations in spectral shape and those initiated by the presence of ^{226}Ra contamination. However, establishing information from spectra that have relatively sparse counts contributed from contamination can be very difficult. Additionally, in most cases there is likely to be a continuum of activities, shielding arrangements and source geometries within contaminated sites resulting in a similar continuum of detector response (Wei et al., 2010). Therefore, characterisation methods applied for ^{226}Ra contamination must be robust enough to cope with fluctuations in background but at the same time be sensitive enough to provide reliable estimates of activity and depth.

The important spectral unfolding process, providing insight into relative spectral contributions, is not an instructive one and firstly requires extensive knowledge of the individual detectors response to known source geometries which must be provided by a robust calibration procedure (ICRU, 1994). Complications often arise when trying to account for, by empirical calibration methods, the extensive environmental scenarios that can lead to spectral changes particularly for extended sources. Monte Carlo simulations (MCS) present a more suitable way to account for environmental variables such as density, soil composition and source geometry (Forster et al., 1990, Hendriks et al., 2002).

Once a dynamic calibration dataset has been collected, relating it to field observations can be problematic. A commonly applied method of interpreting the signal from a detector is gross counting. This approach provides only a relative measure of the total flux of photons (or dose rate) and little information of source distribution since energy discrimination is not performed (Adsley et al., 2004). A more adequate method that relies on the differential attenuation of two or more of the numerous intense full energy peaks, ^{214}Bi (609, 1020, 1764 and 2240 keV) and to a lesser extent ^{214}Pb (295, 351 keV), can be used to establish the amount of shielding between the source and detector (Miller et al., 1994, Haddad et al., 2014). However, the method can be severely hindered by the need to strip out background counts and poor counting statistics, often peaks in low-resolution detectors cannot be formed. Alternatively, a more sophisticated approach, coined “Full Spectral Analysis”, can be applied. This method attempts to add linear combinations of calibration data to the vast majority of the channels of a field spectrum by a Poisson weighted least squares fitting procedure (Hendriks et al., 2001, Maučec et al., 2004) or non-negative least squares algorithm (Caciolli et al., 2012, Guastaldi et al., 2013) followed by a χ^2 goodness of fit test. Unfortunately, this method requires sufficiently low counting uncertainty across the spectrum to reliably fit individual spectral contributions: a scenario that is not always obtainable in the field. Moreover, fitting calibration spectra for this application may become complicated by the fact there is a continuum of contamination and multiple source distribution under investigation.

It is well understood that gamma-spectrometry data taken from the environment will contain similarities in spectral shape, or, more precisely, channels will regularly exhibit correlation from one measurement to next. This will be predominantly due to background contributions to each individual spectrum. Difficulties can arise when trying to apply conventional statistical approaches to a dataset when this redundant cross-channel correlation has not been taken into consideration (Fagan et al., 2012). Principal Component Analysis (PCA) is a method commonly used to explore the underlying structure of a multivariate dataset and was employed in this study to contend with variation in background.

The mathematical derivation (Hotelling, 1933, Chatfield & Collins, 1980) and in depth discussions regarding the different implementations of PCA (Hovgaard, 1997, Runkle, 2006) can be found in the literature. Essentially, PCA multiplies the spectral matrix by its, mean-centred, Singular Value Decomposed matrix producing a set of uncorrelated variables. Generally the first few sets of loadings associated with their corresponding Principal components (PCs) of the decomposed matrix can then be considered as representative of the source signal and can be set aside for further statistical analysis (Im et al., 2007). Another convenient outcome of the PCA process is that the number of dimensions is significantly reduced as lower order elements are generally discounted as noise contributions.

The second step utilised the pattern recognition capabilities of an Artificial Neural Network (NN) to classify source geometry and approximate activity, mass depth (D)

and vertical depth (E_d) from higher order PCs. The basic design framework of neural networks (NNs) is analogous to the human brain and they have been used to solve many complex non-linear problems across a variety of fields including gamma-ray spectroscopy (Dragovic et al., 2005, Dragović et al., 2006). They have even been used to map counts directly to activity and source burial depth (Wei et al., 2010) .

A NN is composed of a number of processing units known as nodes that are, by convention, separated into three distinct layers: the input, hidden and output. The input layer is a collection of the nodes defining the explanatory variables of the problem. The hidden layer can in fact be made up of one or more layers and the output layer, contains the desired response variables. The hidden layer provides the NN the ability to learn non-linear transformations. Each node has its own weight set, with the weights defining the strength of the connections between neurons in adjacent layers (Pilato et al., 1999). The weights are established during a training phase where the error between predicted outputs and desired output of the specified training set is minimised in an iterative fashion (Medhat, 2012). For a detailed review of the workings of NNs refer to Gurney (2003).

The aims of this study were

- Investigate whether PS and EHS can be distinguished from each other in the borehole geometry.
- Apply optimised method to a RCLS providing estimates of activity and source distribution.

4.4 Materials and methods

4.4.1 Field Site: Headland dataset

Dalgety bay, Fife, Scotland, is a former military site where wartime and post-wartime activities have led to specific areas of the site becoming associated with ^{226}Ra contamination (Tyler et al., 2013). Following the sites decommissioning a new town was built on the area (also called Dalgety Bay) with a sailing club located on the on the west coast where much of the radium contamination was believed to be deposited (Figure 4-2). Public access along the coast provides the opportunity for the general public to come into contact with potentially harmful sources via either direct contact, ingestion or inhalation (Dale et al., 2008, Tyler et al., 2013)

An intrusive survey was undertaken and borehole measurements were obtained from an area on the headland around the sailing club previously suspected of having contamination at depths beyond the capabilities of conventional surface measurements (Tyler et al., 2011). Cores were not necessarily concentrated around the highest surface signal as indicated by the *in situ* survey (Figure 4-2), as surface sources and contaminated material were recovered from many of these locations. Another feature is a large proportion of the cores were situated either on the edge of the headland and around the main sailing clubhouse (middle top) as re-deposition of contamination by sea erosion and contact with the general public were the primary concerns of the original survey.

Due to the heterogeneous composition of the soil matrix, a relatively small diameter auger (60 mm diameter) was used since penetration into the contaminated site with an auger with a larger diameter was likely to have been unviable. A total 30 of augered holes with varying depths (0.2-1.6 m) were taken over identified hotspots and a 51 x 51 mm Sodium iodide (NaI:Tl) detector, encased in plastic tubing, was lowered into each hole. Spectra with 1024 channels representing an energy range of 20-3000 keV were recorded using Ortec’s Maestro software, at 0.1 m depth intervals for at least 600 seconds to attain reasonable counting statistics. This dataset is referred to as the “Headland dataset” (HD) for the remaining discussions.

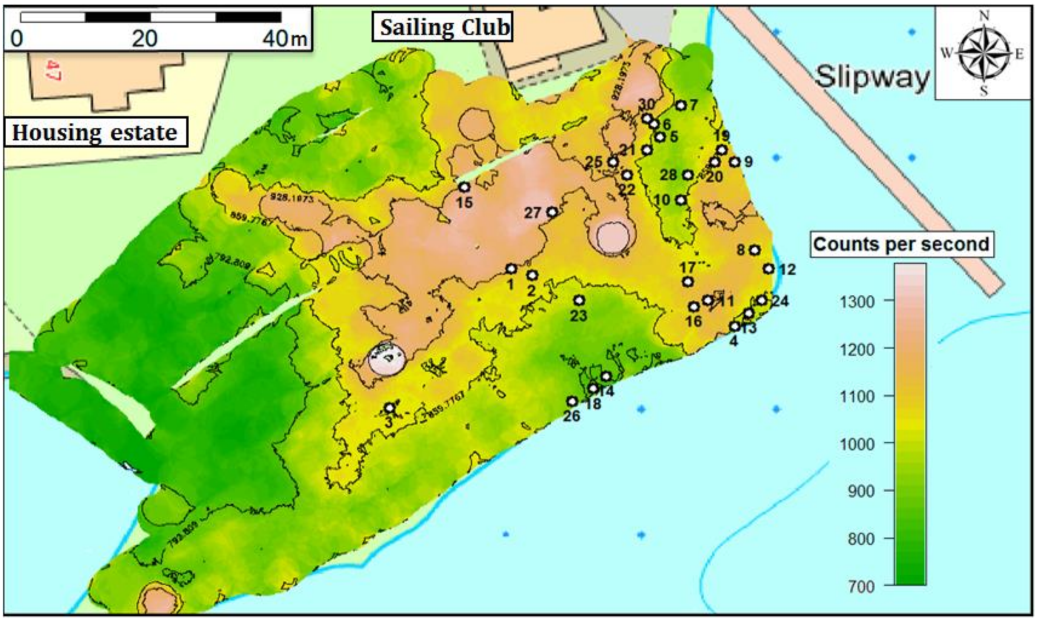

Figure 4-2. Map of the headland with gross counts using a 76 x 76 mm handheld Lanthanum bromide detector overlaid. The surface was interpolated using ordinary Kriging. Locations and numbers of boreholes have been included.

4.4.2 Monte Carlo

Monte Carlo codes offer a robust alternative to either labour intensive and expensive experimental calibration or mathematically cumbersome deterministic approaches (Stromswold, 1995). For example, acquiring representative laboratory spectra can be hindered by the need to strip out the laboratory background, which can vary slightly over long acquisition times due to problems of radon exhalation. This can, for example, introduce significant error when using relatively weak calibration sources at large distances. Field calibration although more characteristic of the background at the HD site presents practical problems of burying the source and being confident of its distance from the detector and the exact amount of shielding (i.e. density of soil) between the source and the detector. Numerous studies, facing similar challenging calibration situations, have opted for and successfully applied Monte Carlo Simulations (MCS) to a variety of environmental measurements (Maučec et al., 2004, Allyson & Sanderson, 1998). The code used in this study was Monte Carlo N-Particle eXtented (MCNPX) (Briesmeister, 1993).

4.4.2.1 *MCNPX optimisation*

The simulations used in this study only retained key features of the NaI:Tl detector, such as the active volume, aluminium outer canning and protective plastic piping, since this was found to accurately account for scattering within the real detector. Beck's "standard" soil composition was used for all simulations since the actual soil composition was not known (Beck et al., 1972). Decay data were obtained from the National Nuclear Data Centre (2013) and only emissions with relative abundance of 1% were used in the simulations for all radionuclides.

Although MCS possess clear advantages over conventional calibration procedures, there is a major drawback in that the time it can take to obtain acceptable uncertainty on average particle fluxes can be unfeasible (Likar et al., 2004). This is because each particle must be tracked from birth until death where during its lifetime a large number of irrelevant interactions take place consuming computer time. Although there are a number of accessible variance reduction techniques available to use in MCNPX, for example population control methods, if the modeller does not exercise considerable precaution, bias can be introduced to the final tally results (Allyson, 1994, Serov et al., 1998).

This study used a more straightforward procedure. Firstly multigroup/adjoint calculations were utilised, to estimate the vertical and lateral extent needed to accurately reconstruct an entire environmental spectrum from extended sources; commonly described as the detector's Field Of View (De Groot et al., 2009). In short, this special treatment of photons sees the problem effectively reversed, with photons starting in the detector and gaining energy until a cut off of 2614 keV (the highest environmental photon energy) was reached (Maučec et al., 2004). Covering the density range that was likely to be present at the site (1.1-1.8 g cm^{-3}), it was found that the soil thickness needed to accurately recreate a borehole spectrum was 0.5 m above and below the detector and 0.55 m parallel to the borehole. After this, a method outlined by Hendriks et al. (2002) was used involving only electrons in close proximity to the detector being tracked and sampling bremsstrahlung energies for those that were terminated outside this proximity. This was accomplished by the use of surface source write/surface source read cards within MCNPX.

4.4.2.2 *Benchmark experiments*

To validate the code defining the geometry, materials and response of the detector a benchmark investigation to a known source geometry and activity was undertaken. At the time of measurement, no borehole calibration facility was available. A set of flat concrete pads doped with ^{40}K, ^{238}U and ^{232}Th geared more towards *in situ* and airborne calibration were used instead. The MCNPX Gaussian Energy Broadening (GEB) feature was used to reconstruct the broadened peaks generated by the detector.

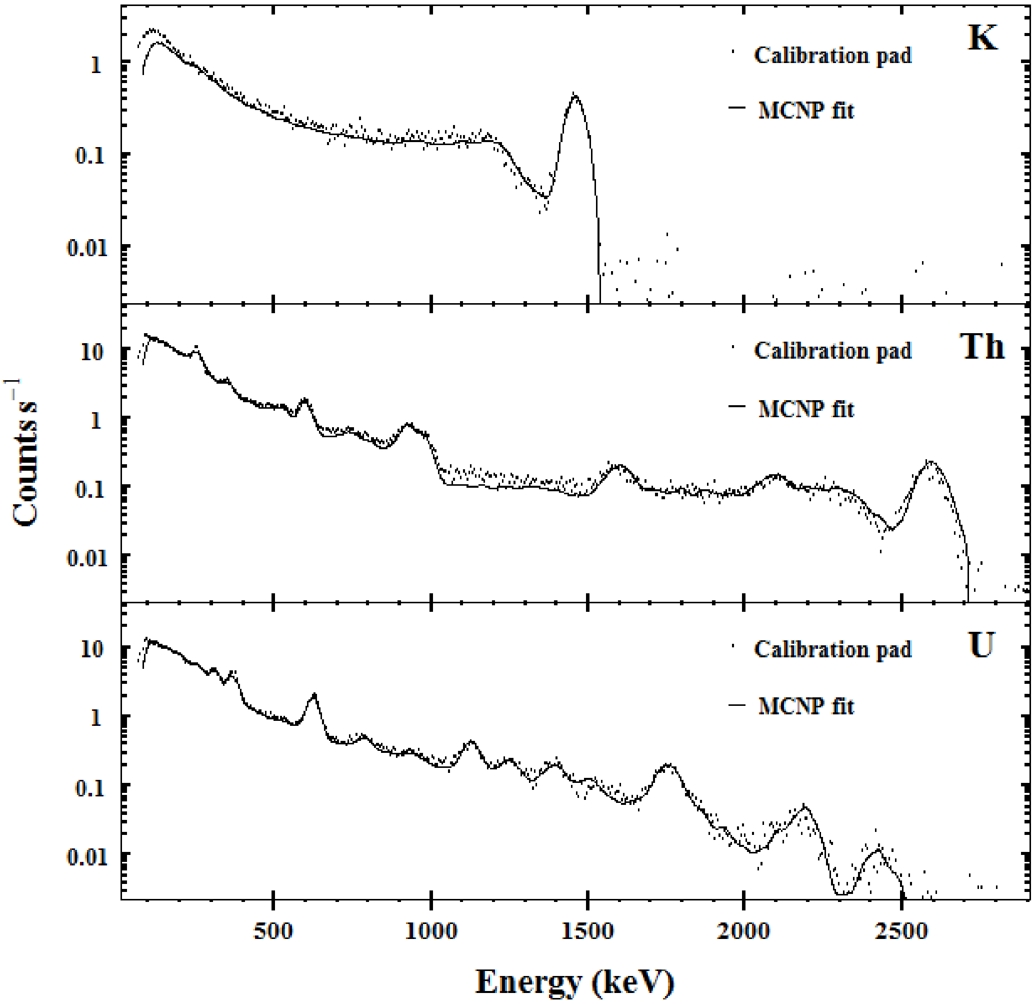

Figure 4-3. Benchmark experiment results showing MCNPX fitting data (lines) to calibration pad (potassium, thorium and uranium) data (dots).

Spectra from the concrete calibration pads and MCS are in good agreement (Figure 4-3). The ^{232}Th and ^{238}U pads were reproduced well using MCS. Minor discrepancies were found in the simulated Compton continuum of the ^{40}K pad where it was overestimated compared to the pad, this was noted by another study (Hendriks et al., 2002). This is likely to be caused by the different positions of pads at the calibration facility resulting in incomplete removal of background contribution by the background pad.

4.4.3 Spectral compilation

Before any spectral interpretation of the HD could be performed, enough data spanning the range of environmental variables thought to be present at the site had to be generated so as to embody the relevant spectral shapes. Additionally, establishing the overall spread of the spectral population obtained by sensibly varying model parameters provides uncertainty estimates for any conclusions made about the parent source distribution. This step is also essential prior to training a neural network as extrapolations outside of datasets are known to be very unreliable (Moreira et al., 2010).

This procedure could not be performed purely in MCNPX because of time constraints, because on average it took approximately 4 hours for each simulation to attain acceptable statistical uncertainty even with optimisation. Instead a resampling procedure of a discrete range of MCNPX generated spectra, encompassing only changes in source geometry and density variation, was undertaken. This permitted more straightforward parameters, such as spectral drift and relative spectral contribution (or activity) to be sampled and adjusted afterwards allowing a larger and more robust spectral dataset to be produced. The rest of this section details this methodology.

All source and background spectra were simulated within MCNPX covering representative densities from 1.1 to 1.8 g cm^{-3} with intervals of 0.1 g cm^{-3}, typical of the densities range found within the cores taken at the site. Energies below 300 keV were disregarded to avoid systematic uncertainties associated with variations in geological matrix (Hendriks et al., 2002, Caciolli et al., 2012). Figure 4-4A demonstrates good agreement in count rate below 300keV between MCS and field spectra “28 90cm” although this was not the case for spectra obtained. Good agreement in spectral shape was nonetheless maintained across the remaining energy range for the remaining measurements.

A base count rate of ~24 counts per second (for the energy range above 300 keV) was used as the mode count rate of a lognormal distribution established from a background core with minimum and maximum count rates of 13 and 65 counts s^{-1} respectively. Whilst, the probability of reaching background count rates of 65 counts s^{-1} was considered extremely unlikely at Dalgety bay headland, it was thought best to take a conservative approach with the little spatial coverage of background data that were available. Although, this would raise the limit of detection and uncertainty on final activity and depth predictions the spectral shape recognition capabilities of the proposed method was anticipated to negate such fluctuations. Relative contributions from each of the natural decay series were found to be reasonable well correlated within background cores demonstrated by Pearson’s linear correlation coefficient above 0.8. This deviation was accounted for within the model.

The background dataset was then spiked using selected simulated source spectra of corresponding density and a randomly sampled activity. Spectral drift was introduced into each spectrum by sampling a Gaussian distribution with a standard deviation of

3 keV (at 1461 keV) typically found within the temperature and magnetic field variations within the environment for the detector in question. The MCS were recorded to a much higher statistical accuracy, typically >95%, to form the “Training dataset (Figure 4-4). Field results were known to have a greater noise element due to the limited counting time and detector volume (Minty & Hovgaard, 2002). Accordingly, Poisson noise was introduced into individual bins depending on a sampled count rate (>600 seconds). The addition of noise established the “Validation dataset” and was considered to be more representative of the error structure of the HD (Figure 4-4A).

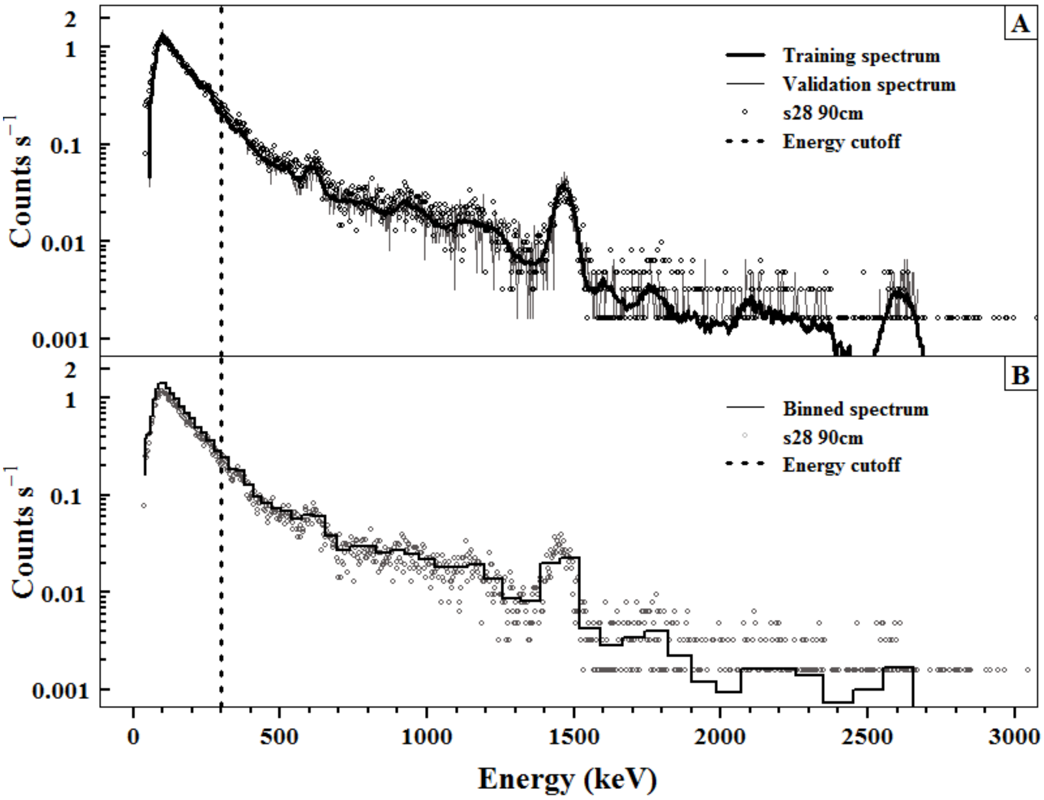

Figure 4-4. A) Example of a simulated background alongside a field measurement taken from core 28 at 90 cm. Note that the "Training spectrum" is far more statistically defined than either the Poisson noise induced "Validation spectrum" and "s28 90cm". The energy cut off used is also displayed. B) Demonstrates the binning intervals used on all spectra prior to further analysis. Notice the width bin size increases with energy and Full Width at Half Maximum.

Clearly using over 1000 energy bins presents a large relative variation within individual bins from one spectrum to the next, particularly as counts become sparse at higher energies. To reduce this surplus noise without too much loss of energy distinction, the energy range 300-2918 keV was irregularly binned according to the estimated Full Width at Half Maximum established using the same Gaussian Energy

Broadening model fit implemented in MCNPX (Briesmeister, 1993). Higher energy spectral features can be observed more easily as the sparse nature of counts is diminished, for instance the ^{208}Th (2614 keV) and ^{214}Bi (1764 keV) peaks (Figure 4-4B). Conversely, at low energy where the FWHM is lower spectral structure is not lost, observe the low energy ^{214}Bi (609 keV) can still be observed.

All relevant sample data: source Activity (A), PS depth (D) and vertical depth (E_d) was recorded for individual spectra. PCA was then carried out on the combined simulated dataset and HD to allow comparison. All steps mentioned were carried out using the base features in the software package R (R Development Core Team, 2012).

4.4.4 Neural network: Training procedure

To optimise the performance of the NN and ensure that the trained network was learning general patterns within the problem rather than adapting to the training data itself, three separate data sets were produced: the training set, a test set and cross validation set (Dragovic et al., 2005). All datasets were mean centred and scaled relative to the variance. Initially, each NN was trained and tested with statistically defined MCNP spectra (spectral drift was added to ensure SCs remained similar). The essential stage of cross validation was performed using data with Poisson noise introduced "Validation dataset" which was known to be more characteristic of the noisy HD (Figure 4-4). The transformation used in the hidden layer was a sigmoidal function and the algorithm used to train the network was resilient backpropogation (Riedmiller & Braun, 1993). The R package RSNNS was used to construct and train all NNs (Bergmeir & Benítez, 2012a).

The architecture of a NN may be different from one problem to the next depending on the problem's level of complexity. It was discovered early on to reach the optimised level of performance for this problem it was better to divide the procedure into three separate networks since this eliminated crosstalk effects between the output neurons specifying the activity and depth parameters of an EHS and a PS. The first NN purpose was to classify spectra into one of the three classes: background, EHS or PS. The final networks were then used to make estimates regarding activity (kBq or Bq kg^{-1}), burial depth (g cm^{-1}) and lateral extent (cm). Crucially, they were only trained and tested with spectra that were identified by the classification network. To ensure that the correct architecture for each network was selected an exhaustive search was conducted to: establish the number of PCs to use in the input layer, the number of hidden nodes and hidden layers, and the number of learning epochs. Decisions made regarding the design of the network were based around minimising the error within the validation dataset. This was checked again using confusion matrices for classification results (Zell et al., 1993) and R^2 values for any regression results produced by the EHS and PS networks (Moreira et al., 2010). Between 1000 and 2000 training data were found to adequately train all the networks. Test and validation sets were 30% of the training set.

Uncertainty on regression results was estimated by resampling the predicted output values 50 times using the original background parameters. These values were then fed back into the original network alongside the training data and the standard deviation of the injected values was used as the uncertainty. Caution was taken not to bias the latent variables used by PCA with introduction of new values, since this would have influenced final NN outputs. To avoid this eventuality the procedure was looped where error spectra values were introduced into the original dataset one at a time.

4.5 Results and discussion

4.5.1 Analysis of principal component

90% of the total variance within the dataset was explained by the first 5 principal components, which suggests the latter PCs possess largely noise elements. Visual analysis of the PC 1 and PC 2 loadings demonstrates the merit of the PCA transform: at this early stage of analysis point source effective depth is being separated within PC space with shielding thickness variation (Figure 4-5). This is confirmed by the shallow point source depth (larger lighter points towards the bottom of the plot), in contrast to deeper sources (smaller darker points) towards the top left of the plot. Interestingly, distance from the background pack (Crosses) would appear to infer activity.

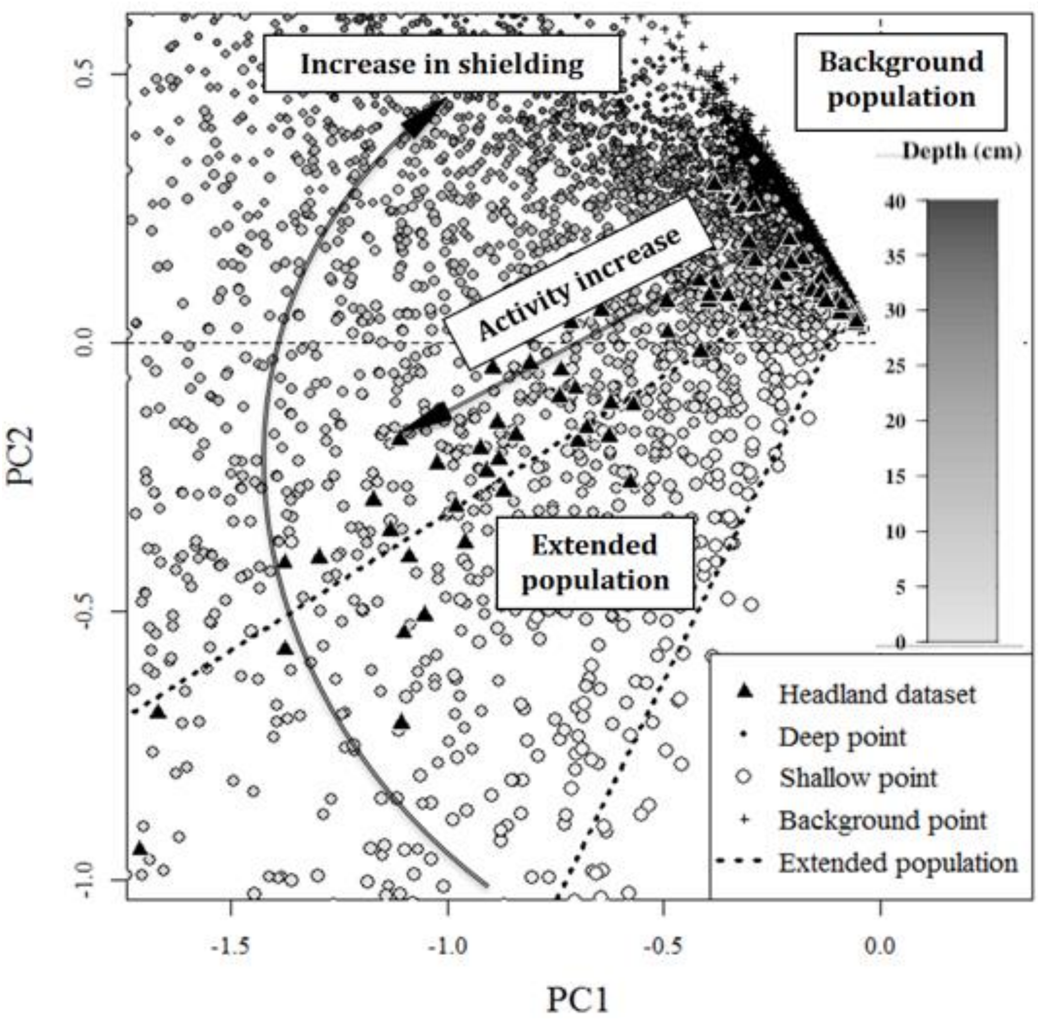

Figure 4-5. Plot of Principal components 1 and 2 loadings. Background spectra (Black crosses) are tightly clustered in the top right of the plot. Progressively smaller and darker points indicate increase shielding between point source and detector and greater distance from the background pack inferring greater activity. The extended population are bound by the black dotted lines. The headland dataset are represented by black triangles.

Arguably conventional separation techniques, such as a Mahalanobis distance metric could be used to delineate a boundary between source and background (Runkle, 2006).

Moreover, a linear regression between PC1 and PC2 could be performed to establish a relationship with depth and activity (Adams et al., 2012). However, a number of problems may be encountered using these approaches. Firstly, separation via parametric methods (i.e. Mahalanobis distance) invariably contains a distribution-based assumption, normally a multivariate Gaussian distribution, to define separation limits from the background dataset. This assumption is often not correct leading to misclassification. Secondly and most crucially, separation of the extended source population, encompassed by the black lines in Figure 4-5, from point sources in the intermediate range (2-20 g cm^{-2}) is not possible through a linear regression technique, and this is of particular importance since a large proportion of the HD lie within this region. Furthermore analyses of lower order PCs, using a similar approach, becomes increasingly challenging. This suggests that to reliably separate extended sources from point sources more information from lower order PCs is needed but the relationship is likely to be non-linear. To confront these issues three separate NN were used to establish structure within the PC loadings.

4.5.2 Classification network

The first NN was used to classify spectra into one of the three classes. It was established by using the first 5 PCs, a hidden layer with 16 neurons and 1500 learning epochs gave the smallest relative mean squared error (RMSE) on the cross validation dataset (~15%) in the case of the classification network. It must be noted at this early stage, throughout this work comparatively large errors were encountered on output neurons for the cross validation sets due to the noise introduced during spectral compilation (Section 2.3). Another outcome was that networks were trained using relatively few iterations compared to other studies (Moreira et al., 2010, Dragović et al., 2006)

The final output of the classification NN (CNN) was decided by the "Winner takes all" approach and the overall performance assessed by calculating the misclassification rate (Zell et al., 1993). The highest misclassification was witnessed on the background results (10.2%) due to the low activities used at large depths for both PS and EHS within the cross validation set. It was decided to include these levels in order to attain detection limits. Generally PS's were classified well above a certain threshold, dependent on the activity and depth, representing the minimum detectable activity (MDA) where source becomes misclassified as background as source count contributions became negligible (Figure 4-6A). EHS were also characterised well, however misclassified shallow depth PS (5-20 g cm^{-2}) can be seen distributed along on the MDA boundary (< 10 Bq kg^{-1}) (Figure 4-6B). As expected as the extent depth (E_d) becomes less and the overall volume of the contaminated layer is reduced, leading to less source contributions, the MDA increases to about 30 Bq kg^{-1}. The most significant case of misclassification can be seen subtended within PS results between 5 and 20 g cm^{-2} and below 10 kBq in which a 37% classification rate was found (Figure 4-6A). This implies the two populations must still significantly overlap within PC space and the NN struggles to separate as too few source counts were contributed to the already noisy background spectra. The second reason is that the spectral shape, regardless of noise, in these specific geometries is too similar, using only energies above 300 keV, for the NN to separate. It is likely a combination of the two has led to this misclassification uncertainty. If energies below 300 keV could be sufficiently characterised these populations could be more effectively resolved. This however presents a real challenge.

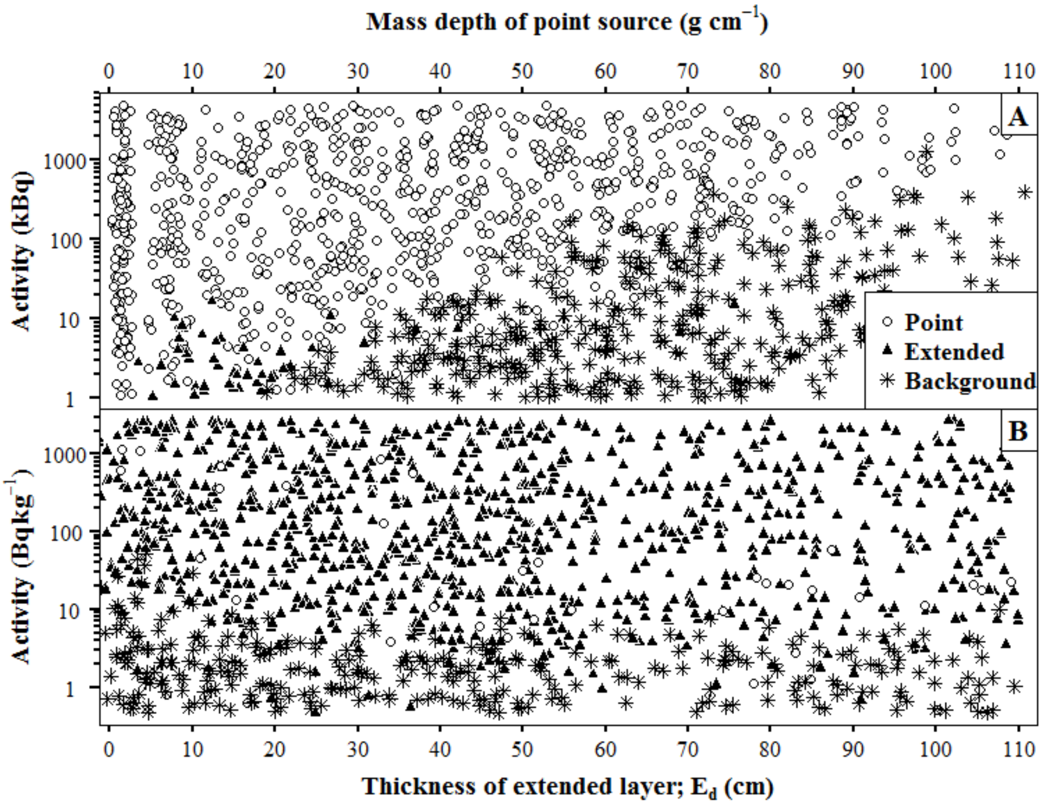

Figure 4-6. Classification Neural Network output for A) Point source and B) Extended source. Discrete points, caused by the discrete sampling of depth, have been jittered slightly to give a better sense of population density. The legend in plot A conceals largely background-misclassified points.

This method presents a real improvement in comparison to a traditional parametric approach where this degree of separation would not be possible (Figure 4-5). Consideration must also be drawn to the areas of significant misclassification, for example, PS's under 10 kBq at depths below 20 g cm^{-1}. This circumstance does not pose a great risk compared to more active PS which are more than likely be classified correctly (Figure 4-6A).

4.5.3 Point and Extended Neural Networks

Quantification of activity and depth (both *D* and E_d) was performed using two final NNs: Point (PNN) and Extended (ENN). Interestingly both required only 3 PCs as inputs to accurately estimate depth, but it was soon recognised that to stabilise activity estimates a fourth input neuron specifying total counts should be included. The number of hidden neurons and the size of training set needed to accurately map the problem in both NN cases were roughly similar to the CNN (Table 4-1). Again, a relatively small number of iterations were required to attain RMSE minima on the cross validation datasets (<25000) and it was documented during training that both networks were found to diverge rapidly after convergence: indicative of sudden overtraining (Medhat, 2012)

Table 4-1 Input parameters and R2 values (and accompanying p-values in brackets) produced for the cross validation dataset for Point Neural

Neural Network	Iteration number	Hidden layer neurons	Size of training set	R^2 value	
				Depth	Activity
Point	25000	16	1000	0.942 (<0.001)	0.910 (<0.001)
Extended	8000	10	2000	0.670 (<0.001)	0.965 (<0.001)

4.5.4 Network and Extended Neural Network

During the training of preliminary networks it was established by limiting the maximum activity of training and test sets to realistic environmental constraints, for example PS and EHS less than 5 MBq and 5MBq kg^{-1} respectively, uncertainties on more probable lower activity sources could be reduced. Such activity constraints are well within activities found during intrusive surveys of Dalgety bay headland (Patton et al., 2013).

Drawing attention to accuracy of the models, the overall ability of both NN's to generalise a relationship was good for activity estimates. This is supported by high R^2 values (PNN = 0.955 (<0.001) and ENN = 0.937 (<0.001)) for both NN's. PS depth prediction was additionally very good (R^2 value of 0.942 (<0.001)). Predictions made by the ENN for vertical depth (E$_d$) were not as reliable (R^2 value of 0.670(<0.001)). This suggests that very subtle changes in spectral shape occur as the thickness of the layer contamination is varied, and these cannot be identified as easily as the change in spectral shape of PS with variable depth. This is understandable since the majority of photons that reach the detector will have originated from areas close to the detector. Thus with increasing thickness of contamination relatively less signal is received due to the inverse square law. Consequentially, accurate measurements of E$_d$ are unlikely and predictions made by the ENN for this parameter should be treated with caution

4.5.5 Analysis of the Headland Dataset

To demonstrate the capacity of the method, analysis of two cores from the HD is included (Figure 4-7). Firstly, confidence within the ENN predictions is provided by comparing the similarity in shape of the total count rate (Figure 4-7A plot 1 and Figure 4-7B plot 1) and activity estimates (Bq kg^{-1}) (Figure 4-7A plot 2 and Figure 4-7B plot 2) with core depth for both the cores. Interestingly, the majority of the HD measurements (~70%) that were identified as having contamination were predicted to be EHS. This outcome supports general intrusive findings at the headland where the majority of contaminated material is well distributed ash and clinker from the burning of radioactive artefacts (Patton et al., 2013).

An important finding was the identification of a relatively thick (~90 cm) elevated activity extended layer (357 ± 69 Bq kg^{-1}) at 130 cm within “s21” (Figure 4-7B plot 2). This coincides with a large spike in total count rate (Figure 4-7B plot 1). In the original survey this was disputed to be a point source due to the Gaussian nature of the total count rate increase within the depth series. Even with further analysis using the differential peak method the source signal could not be classified. This scenario clearly demonstrates the value of the current approach.

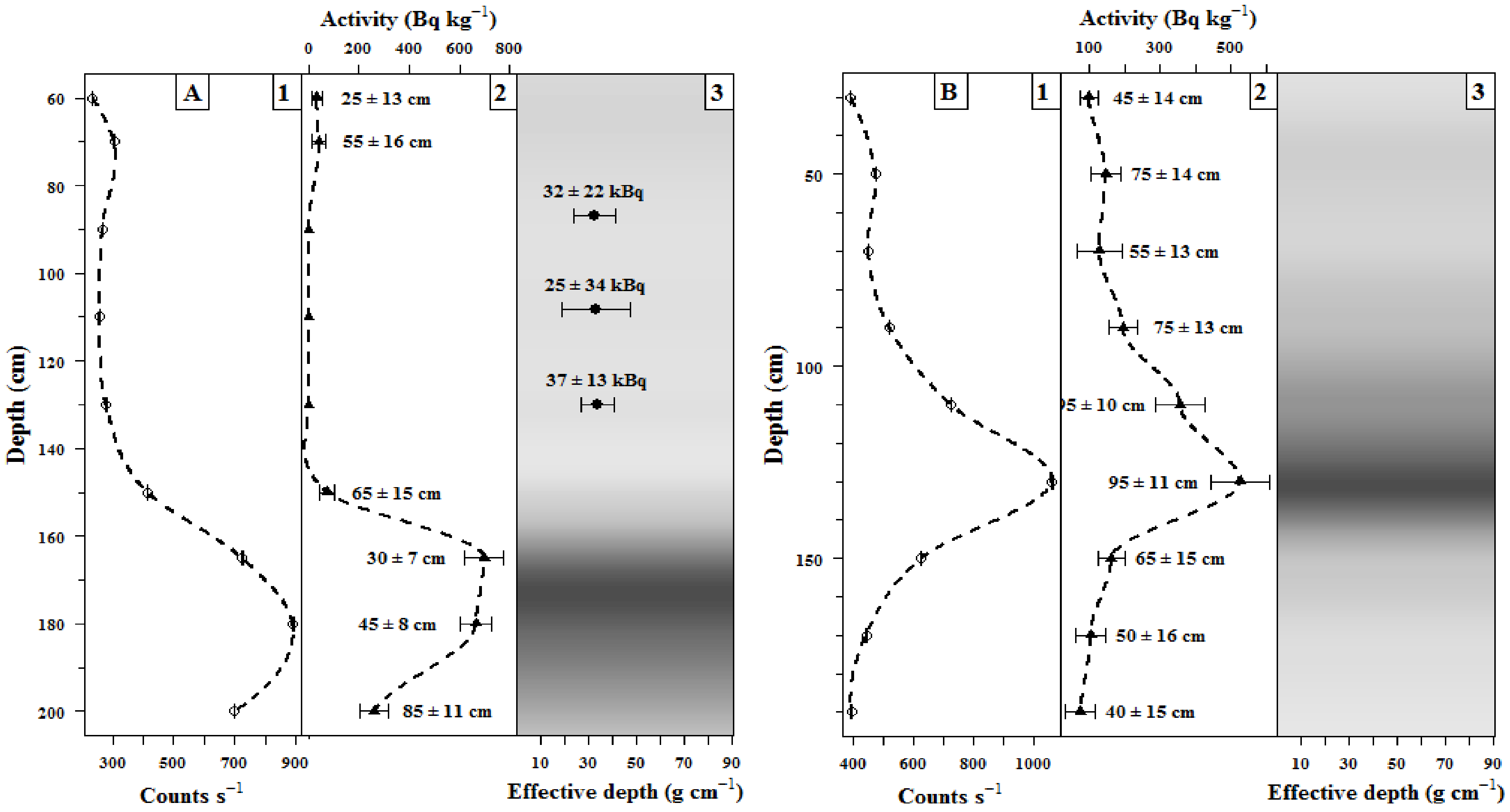

Figure 4-7. Neural network results for cores "s7" (A) and "s21" (B) taken from the Headland dataset. Individual core results have been separated into three individual plots 1, 2 and 3. Plot 1 provides total count rate (20 – 3000 keV) as a function of depth (error bars are very small and hidden behind points). Plot 2 gives the Extended Neural Network predictions for activity (Bq kg^{-1}) on the x axis and vertical depth (cm) estimates are accompanying text values. Plot 3 offers a visual representation of the core with darker shading indicating higher activity heterogeneous contamination (similar to plot B) and whether a point source is present and at what depth (x axis) and activity (accompanying text values) it occurs.

The highest predicted extended activities (600-700 Bq kg^{-1}) were found in a relatively thin contaminated section of core "s7" at 160-180 cm (Figure 4-7A plot 2). This area did not contribute the highest total count rate (>1000 counts per second) though as seen in core "s21" (Figure 4-7B plot 1). This highest count rate was caused by a thicker (95 ± 11 cm) less active (520 ± 85 Bq kg^{-1}) layer. This shows that using this technique can provide insight into the thickness of a layer meaning that more accurate estimations of activity can be made instead of assuming a completely distributed source. Another key feature that the CNN identified at core depths between 90-130 cm was the presence of PS's in between two extended layers (Figure 4-7A plot 3). The PNN provided clarification that these sources were a relatively short distances away from the detector (~35 g cm^{-1}) and at low activities (~30 kBq). Although PS were identified by the network, the consistency of the activities and depth would suggest the detector is in a pocket of low contaminated soil with larger activities at greater distances from the detector. Algorithmic identification of this situation would be very challenging. This emphasises the importance of human interpretation. To verify this notion, further cores would have to be taken. This scenario highlights a real limitation of the borehole measurement without substantial spatial coverage. Similar geometries that are beyond the scope of the technique to differentiate, and that would require further spatial coverage would be for example, localised areas of homogeneous contamination that are not distributed symmetrically around the borehole and measurements above or below an extended layer.

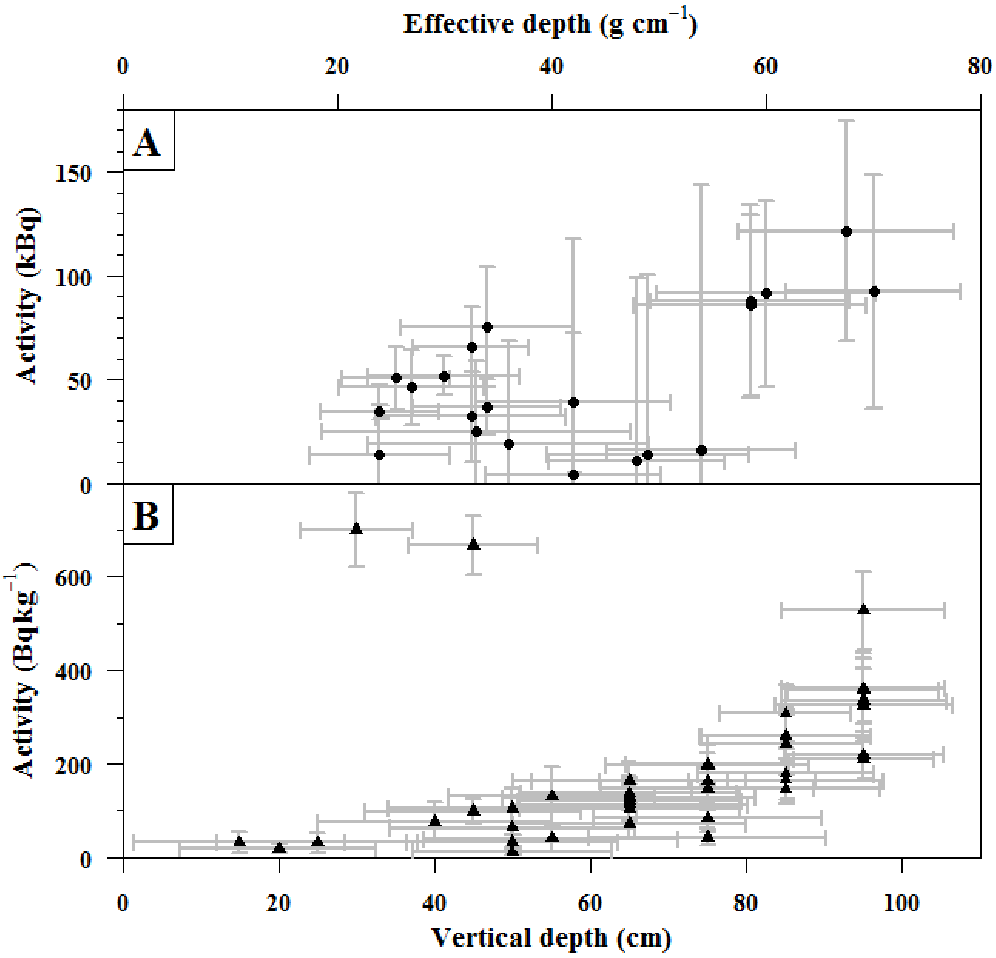

Figure 4-8. Estimated uncertainties associated with Headland dataset source measurements A) point source and B) extended homogeneous source.

Attention must be drawn to the errors associated with predictions of activity and depth from the NN's (Figure 4-8). Standard deviations from both networks showed similar patterns, generally with increasing burial depth and decreasing activity the relative standard deviation increased. This is particularly prevalent with the point source estimations at effective depths of 30-40 g cm^{-1} and less than 20 kBq (Figure 4-8A), and low activity (<100 Bq kg^{-1}) sections (<40 cm) of contamination (Figure 4-8B), and this practically renders these readings unusable. This is understandable as source shape would have become increasingly difficult to differentiate from background as source counts became too few.

Interestingly, the deepest and highest activity predictions for PS occurred at the base of two cores that were positioned close together, suggestive of high activity at depth. Without further boreholes to confirm this, the actual activities are challenging to deduce as they are so far away from the detector.

There are practical ways to alleviate some of the uncertainty associated with field results, indicated by the large error bars (Figure 4-8). Firstly reduction in counting uncertainty across the energy range could be attained by using another detector. NaI(Tl) detectors have relatively low energy resolution and the size used in this survey was particularly small (51 x 51 mm). If a larger, higher resolution detector was used, such as a larger volume Lanthanum bromide, uncertainties could be reduced (Yongpeng & Bin, 2012).

Another way to reduce uncertainty would be to collect more background results to provide a better understanding of the background population. This study was limited by this fact resulting in a conservative estimate of background population being made. This would have would have invariably raised the limit of detection and introduced more uncertainty on final activity and depth predictions. Other than collecting further background cores at the site, cores could have also been drilled deeper beyond contamination (providing little stratification of background constituents was present), giving more reliable background estimates for individual cores. However, this was not possible at much of the site as hard rock restricted further augering.

4.6 Conclusions

^{226}Ra contamination at depths typically below 50cm cannot be reliably measured using conventional surface gamma-ray measurements. Borehole gamma-ray spectroscopy is used for the purpose of characterisation, where details of the geometric nature of contamination and activity estimates are vital if formal risk assessments are to be developed in order to protect the general public. Current methods of spectral processing, however, either do not have the ability to perform the task or prove unreliable.

An approach has been described based upon feature extraction using PCA, followed by NN's to relate key features of representative MCS to obtained field results. This method provided a reliable means to characterise the geometric nature of contamination, offer activity and depth estimates of point sources, and give insight into potential layers of homogeneous contamination. The potential of the technique was demonstrated by analysis of core data taken from Dalgety Bay Headland where prediction from the majority of cores suggested that contamination was mostly dissociated, supporting intrusive surveys.

Nevertheless, limitations associated with the nature of the borehole measurement still remain and cannot realistically be solved unless adequate spatial coverage is performed, making some predictions very uncertain, particularly of PS at distance. The use of improved detector technology and better understanding of the background could, however, alleviate some of the estimated uncertainty associated with predictions from the method.

5 Remediating radium contaminated legacy sites: advances made through Machine Learning in routine monitoring of “hot” particles.

Adam Varley[1], Andrew Tyler[1] , Leslie Smith[2], Paul Dale[3], Mike Davies[4]

[1]Department of Biological and Environmental Sciences, University of Stirling, Stirling, FK9 4LA

[2]Department of Computing Science and Mathematics, University of Stirling, Stirling, FK9 4LA

[3] Scottish Environmental Protection Agency, Radioactive Substances, Strathallan House, Castle Business Park, Stirling, FK9 4TZ

[4] Nuvia Limited, The Library, Eight Street, Harwell Oxford, Didcot, Oxfordshire, OX11 0RL, United Kingdom.

Varley A., Tyler A., Smith L., Dale P. and Davies M. (2015) Remediating radium contaminated legacy sites: Advances made through machine learning in routine monitoring of “hot” particles, *Science of the Total Environment*, **521–522**, 270–279

5.1 Abstract

The extensive use of radium during the 20th century for industrial, military and pharmaceutical purposes has led to a large number of contaminated legacy sites across Europe and North America. Sites that pose a high risk to the general public can present expensive and long-term remediation projects. Often the most pragmatic remediation approach is through routine monitoring operating gamma-ray detectors to identify, in real-time, the signal from the most hazardous heterogeneous contamination (*hot particles*); thus facilitating their removal and safe disposal. However, current detection systems do not fully utilise all spectral information resulting in low detection rates and ultimately an increased risk to the human health. The aim of this study was to establish an optimised detector-algorithm combination. To achieve this, field data were collected using two handheld detectors (Sodium Iodide and Lanthanum Bromide) and a number of Monte Carlo simulated *hot particles* were randomly injected into the field data. This allowed for the detection rate of conventional deterministic (gross counts) and Machine Learning (Neural Networks and Support Vector Machines) algorithms to be assessed. The results demonstrated that a Neural Network operated on a Sodium Iodide detector provided the best detection capability. Compared to deterministic approaches, this optimised detection system could detect a *hot particle* on average 10 cm deeper into the soil column or with half of the activity at the same depth. It was also found that noise presented by internal contamination restricted Lanthanum Bromide for this application.

5.2 Introduction

5.2.1 Radium contamination

Radium (^{226}Ra) was used extensively during the 20th century predominantly in the form of luminescent paint. Waste generated from military, industrial and pharmaceutical products was regularly buried with little record of its location and inventory (Harvie, 1999). With a half-life of 1600 years, ^{226}Ra contamination is a multigenerational issue. In the UK, a recent government report conservatively estimated there to be 150 to 250 contaminated legacy sites, whilst acknowledging there could be as many as a 1000 (DECC, 2012). Similar extents of ^{226}Ra contamination have been found across Europe and North America (Harvie, 1999). Ultimately, the risk of human exposure at these sites is dependent on a number of potential pathways and the form of contamination and not exclusively on external dose (Dale et al., 2008).

One such pathway, that has the potential to cause significant radiological harm, is ingestion of small highly radioactive items often referred to as *hot particles* (Baker & Toque, 2005). One study explored the committed dose that could be received by a member of the public through simulated stomach acid digestions of a range of radium *hot particles* found in Scotland (Tyler et al., 2013). It was concluded that ingestion of a *hot particle* with an activity higher than 20 kBq could result in a committed dose to an infant exceeding the 100 mSv threshold deemed to cause significant radiological harm (ICRP, 2007). At particular sites in Scotland, it has been recognised by the Scottish Environment Protection Agency (SEPA) that there is the possibility of a member of the public coming into contact with such a *hot particle*. To safeguard against this at Dalgety Bay, Fife, Scotland, routine monitoring is undertaken to detect and retrieve any significant radioactive items (Dale et al., 2013). To confirm monitoring is undertaken with sufficient accuracy, SEPA have outlined the following criterion:

- A 20 kBq *hot particle* at a burial depth of 0.1 m must be detected 95 % of the time.

This paper aims to develop an optimised detection system that provides better detection capability than systems currently available. This will allow more effective identification of *hot particles* at radium legacy sites, ultimately reducing the risk posed to the general public in both the short and long term.

5.2.2 Challenges of "hot" particle detection

The most effective method of detecting *hot particles* in real-time is through a series of mobile measurements using either handheld or vehicle mounted gamma-ray sensors (Tyler, 2008). At many sites where vehicular access is limited handheld detectors are often the only option. Handheld detectors produce gamma-ray spectra, the shape and magnitude of which will provide information of the localised radiation field that the detector has passed through during acquisition. To ensure an area is adequately covered by a survey in a reasonable time frame, typically a spectrum is acquired every second and a walking speed of 0.5 m s^{-1} is maintained. This maximises the spatial density of measurements and ultimately the probability of detecting any *hot particles*. To initiate the immediate identification of a *hot particle* real-time analysis of the spectral time series is critical (Kock et al., 2012).

The spectral response or signal quality of a detector will largely be governed by the composition of the detector’s active volume. Lightweight scintillators tend to be used for handheld detectors, of these Sodium Iodide (NaI:Tl) is the standard as it is relatively cheap and robust (Knoll, 2010). Nevertheless alternatives are available. One such detector, Lanthanum Bromide (LaBr:Ce), has recently received much attention (Guss et al., 2010). It has better energy resolution (~2.5% at 662 keV) than the NaI:Tl (~7% at 662 keV) (Figure 5-1), greater photon efficiencies and better temperature stability. However, a relatively large intrinsic background signal attributed to internal isotopes (^{138}La and ^{227}Ac) can be found distributed throughout the spectrum (Iltis et al., 2006). Considerable contamination can be observed at 1468 keV (gamma and x-ray summation peak), between 786 and 1100 keV (beta continuum) and over 1700 keV (alpha) (Menge et al., 2007). This raises concerns about its potential in low source signal situations as these are frequently encountered in the environment.

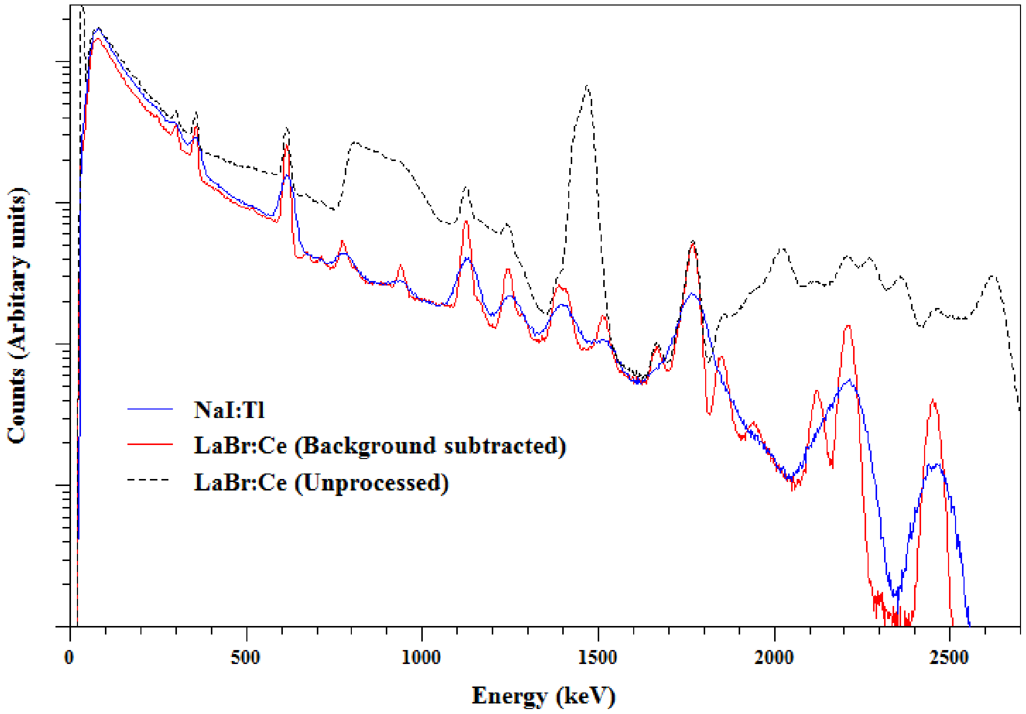

Figure 5-1. Detector responses to a ^{226}Ra *hot particle*: NaI:Tl (Blue), LaBr:Ce background subtracted (Red) and LaBr:Ce unprocessed (broken black).

The second element of a detection system is the algorithm used to process the detector's signal in real-time to determine whether there are signal contributions from a *hot particle* (Figure 5-1). If the algorithm is tripped, an alarm is sounded, allowing the operator to locate and retrieve any potential radioactive items (Jarman et al., 2008). Yet processing environmental gamma-ray spectra is not straightforward.

First of all the vast majority of spectral changes are benign and can occur over the scale of a few metres (Fagan et al., 2012). This spatial variation is brought about by changes in the natural radioelements (^{40}K, and the ^{238}U and ^{232}Th series) contained within the local geology. Changes can also occur temporally due to variations in the density and chemical composition of the geological matrix and radon exhalation (IAEA, 2003). Temporal fluctuations can be very challenging to account for particularly as they can occur on varying time scales, for example deviations in density over a tidal cycle and radon exhalation caused by atmospheric pressure changes (Ball et al., 1991, De Groot et al., 2009). Furthermore, weak source signals can appear very similar to background signals given that ^{226}Ra forms part of the ^{238}U series. Consequently, in an attempt to isolate source signal from benign signal, it is often appropriate to use the most recent observations in the time series as estimates of background (Ely et al., 2004).

Another issue is that source signal will not remain constant. Firstly, the signal will decrease significantly with increasing distance between the detector and source. Secondly, non-linear changes will occur across the spectrum as the amount of shielding (depth in soil) is increased and often the majority of photons that reach the detector are scattered to low energy (Wei et al., 2010). These occurrences can easily lead to weak source signals, for instance a source at depth or a low activity surface source, not being identified.

Finally, the short acquisition times (typically 1 second) demanded by the high density of measurements during a survey, which when combined with the low energy efficiency of handheld detectors, results in spectra containing a large stochastic noise element (Du et al., 2010). This renders conventional spectral analysis methods founded on determination of peak area unworkable (Alamaniotis et al., 2013b).

These complications mean source-background separation is never going to be seamless and a trade-off between detection rate and false alarm rate is encountered (Ely et al., 2006). To safeguard against the operator losing confidence in the detection system, a typical false alarm rate of 1 in 200 ($\alpha = 0.005$) should be attained (Kock et al., 2012). Subsequently to attain this false alarm rate, straightforward deterministic algorithms such as the gross counting algorithm are still heavily relied upon and can produce poor detection rates (Runkle, 2006).

5.2.3 Machine Learning

Here we hypothesise whether *it is more appropriate to track general changes in spectral shape* by dividing raw spectra into more appropriate energy bins (Fagan et al., 2012). However, this procedure is complicated by the fact source and background populations may overlap considerably within the new high dimensional feature space (depending on the number of energy bins used) and possibly exhibit non-linear class boundaries. This scenario can be unfeasible to separate using conventional Newtonian mathematics (Smola et al., 1998). Instead, supervised Machine Leaning (ML) algorithms can be employed to map the underlying relationship between explanatory and response variables (Galushkin, 2007). For this reason, ML has been employed previously to develop alarm thresholds for gamma-ray data (Sharma et al., 2012, Wei et al., 2010, Kangas et al., 2008, Varley et al., 2015b).

Customarily ML attempts to address a statistical problem by learning the underlying structure of a sample of data provided to it during a training phase. Once training is complete, the performance of the model fit can be assessed using independent cross-validation dataset (Dragović et al., 2006). There are a number of possible ML methods available (Ao et al., 2010). However, preliminary investigations demonstrated Neural Networks (NN) and Support Vector Machines (SVM) to be the most encouraging for this application.

5.2.4 Neural Networks

The structure of an NN is analogous of the brain in that it is made up of processing units called neurons connected by synaptic weights (Olmos et al., 1992). Neurons are separated into three individual layers: input, hidden and output. Spectral data can be fed into the input layer, where it is passed through weighted synapses to the hidden layer where a non-linear function is used to map the problem to the output layer. Global convergence of the problem is attempted by minimising the error between training outputs and actual outputs through an iterative procedure of updating the weights between neurons (Gurney, 2003). To avoid getting trapped in local minima during this process training algorithms such as “resilient backpropogation” are used (Riedmiller & Braun, 1993).

5.2.5 Support Vector Machines

SVM approach the problem differently to NN, instead making use of kernel functions to enlarge the feature space ensuring dot products of the support vectors can be easily computed (Smola et al., 1998). This allows the introduction of maximal-separating hyperplanes providing a means of separating complex populations without using vast quantities of computer memory (James et al., 2013). This technique is referred to as the “kernel trick”. There are a number of commonly applied kernels to perform this task including: polynomial, sigmoid, radial basis function and spline (Sangeetha & Kalpana, 2010).

The aim of this study was to assess the performance of a number of different detector-algorithm combinations (henceforth referred to as detector configurations) by spiking background spectra with representative Monte Carlo source spectra providing a means of establishing detection rate and false alarm rate.

5.3 Materials and Methods

5.3.1 Field site

In the early 1990s ^{226}Ra was discovered at Dalgety Bay, Fife, Scotland (-3.3505 ºE, 56.0349 ºN) (Figure 5-2) attributed to actions once carried out at its historical airfield, notably during wartime periods (Patton et al., 2013). A housing estate, sailing club and public footpath now exist in close proximity to known contaminated areas and erosion events have redistributed large quantities of contaminated material onto the public beach. As a result of the dynamic nature of the beach, *hot particles* are regularly brought to the surface or relocated laterally (Dale et al., 2013). This has prompted initially intense and subsequently large-scale routine monitoring efforts to reduce the risk to the public. The beach however presents a challenging environment in which to monitor, since there are considerable variations in background and density gradients, alongside large sections that contain relatively benign homogeneously distributed contamination (Figure 5-2). Tyler et al. (2013) present an interesting study into the physical and chemical formation and the resultant risks associated with a number of *hot particles* found at Dalgety Bay.

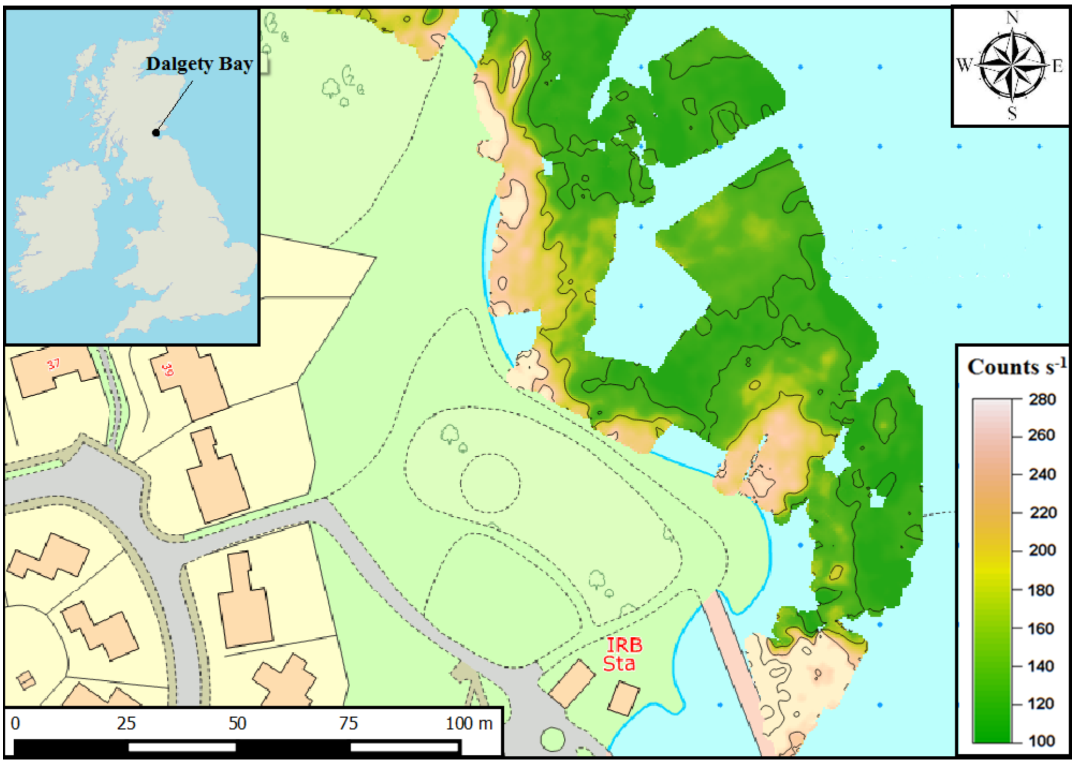

Figure 5-2. Location of Dalgety Bay and a heat map demonstrating the variation in total count rate (counts s^{-1}) taken using a 71 x 71 mm NaI:Tl detector.

5.3.2 Background data acquisition

Background spectra can change considerably from one site to next and over time. Therefore, background data were acquired from Dalgety beach using a NaI:Tl and LaBr:Ce (both 71 x 71 mm) attached to a wheeled mounted frame, one behind the other, to ensure the same ground was being covered by each detector. The detectors were mounted at a height of 0.1 m. 1024 channel spectra were acquired every second using Ortec's Maestro software alongside GPS coordinates and integrated for real time mapping and assessment using software developed at the University of Stirling. A walking speed of 0.5 m s^{-1} and transect spacing of 0.5 m was maintained during the survey. A 1 second lag was introduced to ensure comparable background spectra were used to test algorithms. A total of 35,000 “background” spectra were recorded for each detector over the course of 3 days.

5.3.3 Simulating the radiation field of a “hot” particle

Monte Carlo calibration spectra were preferred over empirically-derived calibration spectra given that laboratory calibration can introduce large systematic uncertainties (Hendriks et al., 2002). The software package Monte Carlo N-Particle 5 (MCNP5) was used to produce full-spectral responses (Briesmeister, 1993). To validate the modelling method, Monte Carlo spectral responses were compared to experimental spectra taken from concrete calibration pads (Minty et al., 1997). Above 150 keV, good agreement was found between calibration pad and Monte Carlo spectra, therefore only energies above 150 keV were used. The background dataset was known to exhibit a large range of shielding conditions brought about by changes in geological matrix composition and density. Attempting to model and then correlate this variation would have been unfeasible, therefore a standard geological matrix (Wet sand; 17% water) and density (1.5 g cm^{-3}) was used (Table 5-1).

Table 5-1. MCNP5 model parameters inputs

Parameter	**Inputs**
Geological matrix	Wet sand 17% water
Soil density	1.5 g cm^{-3}
Detector height	0.1 m
[a]x offset (direction of travel)	0 – 0.25 m
[a]y offset (perpendicular to travel)	0 – 0.5 m
[a]Depth	0 – 0.9 m
[b]Activity	1 – 100,000 kBq

[a] 50 mm discrete increments were applied between geometric constraints

[b] Systematic sampling used between activity constraints

To recreate realistic monitoring conditions a transect spacing of 0.5 m and walking speed of 0.5 m s^{-1} was assumed. In MCNP5 geometry, this involved integrating the detector's response 0.5 m through the radiation field of a point source. Table 1 describes the geometric range for the integration. A random sample was taken from the four dimensional array, possessing the dimensions x, y, depth and activity. To ensure an unbiased routine the random number seed in MCNP5 was changed between individual runs (Moreira et al., 2010). To reproduce the characteristic resolution of each detector statistical broadening was introduced after individual runs. Secular equilibrium was assumed and physical data were obtained from the National Nuclear Data Centre (2013). Source spectra were then injected into the different detector "background" datasets at the same point to ensure consistency. A total of 20,000 spikes (with varying depth, activity and offset) were introduced and the spike rate was kept below 1% of the background dataset to prevent substantial overlap. To accurately assess SEPA mandate detection rate, a separate dataset was generated spiked with 6000 20 kBq sources at 0.1 m burial depth.

5.3.4 Pre-processing and algorithm execution

5.3.4.1 *Gross counting algorithm*

Gross counting (GC) algorithms are used extensively on handheld detectors, as they are relatively easy to setup (Ely et al., 2004, Jarman et al., 2008). GC is currently the only algorithm to be employed at Dalgety Bay (Dale et al., 2013). The method treats the entire spectrum as a single bin, using a rolling mean filter of the previous few measurements to estimate the background (N) (eq 20).

$$T = N + K\sqrt{N} \tag{20}$$

K (sigma multiplier) defines the number of standard deviations ($\sqrt{N}$) above N the alarm threshold should be set (Figure 5-3). If a substantial increase in signal is received the alarm should sound as T is breached. The parameters K and the number of lags used on the moving mean were optimised on part dataset.

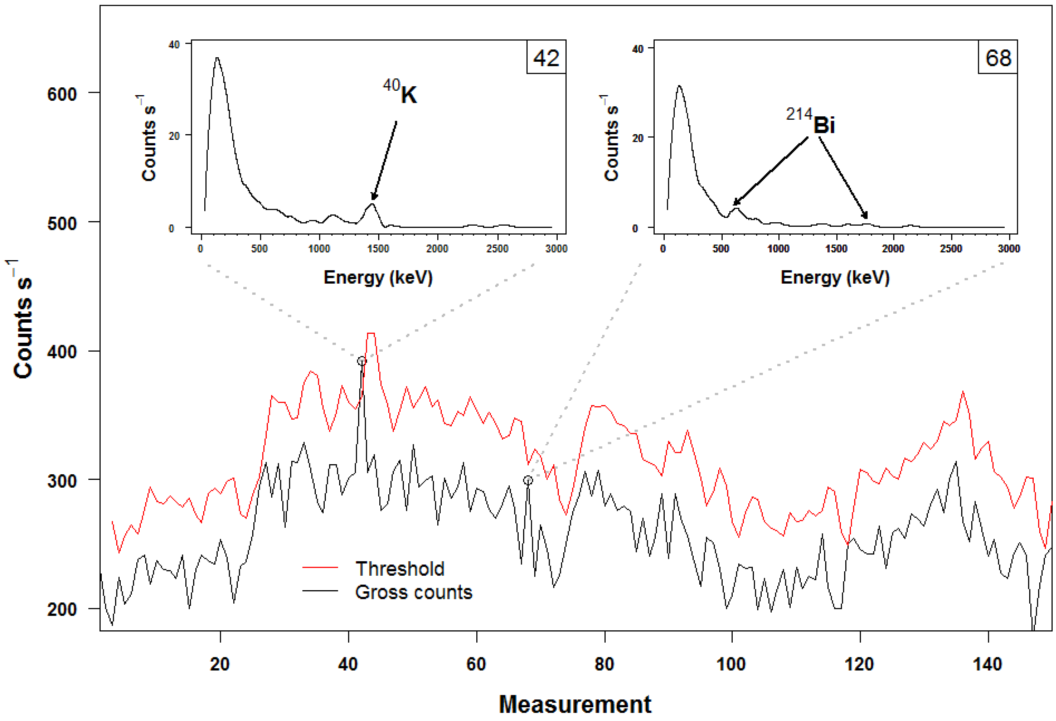

Figure 5-3 Gross counting obstacles: a ^{40}K dominated spectrum (42) triggers the alarm as the threshold is broken, but the ^{226}Ra spike possessing characteristic ^{214}Bi peaks (68) is missed as it does not reach the threshold.

5.3.4.2 *Spectral comparison ratios*

Dividing the raw spectrum into broad energy bins, instead of using raw data, alleviates some counting noise and reduces input dimensionality, although some loss of energy distinction is inevitable (Pfund et al., 2010) (Figure 5-4). Selecting optimal energy bins is a contentious subject and novel algorithms have been implemented to optimise their number, placement and size (Wei et al., 2011). In this study though, two systematic binning systems were applied as input for ML. The first, Resolution Bins (RB), focused on the deterioration of resolution with increasing energy (Runkle, 2006) (Figure 5-4). This produced 30 energy bins for LaBr:Ce and 18 for NaI:Tl. Whilst systematic, this approach cannot account for the fact that many of the bins, particularly at higher energy, may contain zero counts for a single measurement. A second method, Regions Of Interest Bins (ROIB), focussed around full energy peaks and scattering regions was implemented producing 13 energy bins for each detector. Note, energy bins are narrower for LaBr:Ce given its superior energy resolution, although significantly more background counts were encountered in each bin caused by intrinsic contamination.

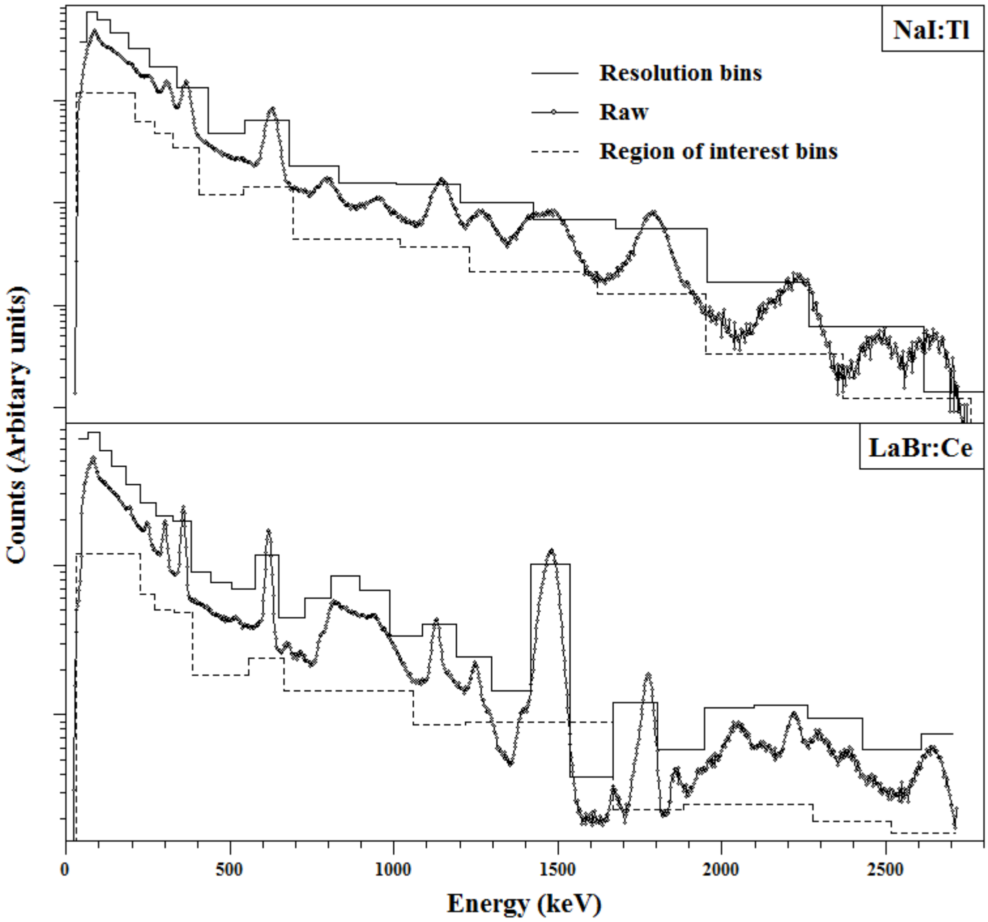

Figure 5-4 Binning systems for NaI:Tl and LaBr:Ce detectors. Note the magnitude of bins has been altered for visual clarity.

Spectral Comparison Ratios (SCR) outlined by Trost and Iwaschenko (2002), were used to transform energy bins into the time series to measure how closely the observed spectrum matched that of the previous background measurement (eq 21).

$$SCR_i = N_1^c - \frac{N_1^B}{N_i^B} N_i^c \tag{21}$$

Where N_i^c is bin *i*, and N_1^c is the first bin, of the current measured spectrum. N_i^B and N_1^B are a respective moving means of bin *i* and the first bin of the previous spectra. This produces a transformed spectrum where the first channel is 0 and all channels contained within a background spectrum should be close to zero as small temporal variations are expected to occur (Du et al., 2010). Source contributions are anticipated to introduce larger deviations in spectral comparison ratios, though these are expected to occur across the spectral energy range, be non-linear in nature and contain a large counting noise element. Therefore, the effectiveness of conventional source-background separation approaches often relying on Gaussian distribution statistics tends to be too simplistic (Runkle, 2006).

5.3.4.3 *Machine Learning implementation*

To train and assess the performance of detector configurations two datasets were formed: a training dataset and a cross-validation dataset. Typically 3000-5000 samples were used to train ML. For NN, 30% of the training set was set aside as a test set to track the progress of training. The remaining data (~30,000) were used as the cross-validation dataset. Data were mean centred and scaled to the variance prior to training. Importantly, to produce the desired False Alarm Rate (FAR), approximately 5-7 times more background samples were included during training. It was discovered that by adding two more inputs (alongside spectral comparison ratios), one containing a moving mean of gross counts and the other the total counts, an overall improvement in detection for both detectors could be realised. In my previous work this has also been found to be a benefit (Varley et al., 2015b). This is not surprising given areas of high background and homogeneous contamination will exhibit larger systematic variation, which ML could take into account by considering the total count rate and its localised variation. One other study employed a similar approach only alongside a deterministic gross alarm instead of providing it as an input for ML (Kangas et al., 2008).

5.3.4.4 *Neural Network optimisation*

To optimise the number of hidden neurons for NNs an extensive grid search was conducted (Medhat, 2012). As anticipated, NNs implemented on RB needed more hidden neurons compared to ROIB due to the greater number of inputs (Dragovic et al., 2005). That said, 15-20 hidden neurons provided the lowest Root Mean Squared Error (RMSE) for all NNs. RMSE on training and test sets for all NNs tended to converge after a few hundred learning epochs. The R package “RSNNS” was used for the development of NNs (Bergmeir & Benítez, 2012b).

5.3.4.5 *Support Vector Machine optimisation*

A radial basis function was found to provide the best degree of separation for this application. Each radial basis function had two parameters that were optimised by an extensive grid search for each individual problem. The so-called cost parameter (C) providing the tolerance of the number of support vectors to include either side of the hyperplane presented no clear pattern between detector systems (600-2000) (Hornik et al., 2006). However, the gamma parameter specifying the width of the radial basis function varied between the binning systems, RB (< 3) and ROIB (~300). The R package “e1071” was used (Dimitriadou et al., 2008).

5.3.4.6 *Quality assessment*

Quality assessment of individual detector configurations was based on the Overall Detection Rate (ODR) (eq 22), SEPA’s 20 kBq Mandate Detection Rate (MDR) (eq 23) and the False Alarm Rate (FAR) (eq 24) of an independent cross-validation dataset. Once ML architectures were obtained, 10 resamples (section 5.3.4.3) were taken to obtain a mean and standard deviation to ensure final values were not a chance representation.

$$ODR = \frac{Number\ of\ sources\ detected}{Total\ number\ of\ injected\ sources} \tag{22}$$

$$MDR = \frac{Number\ of\ mandate\ sources\ detected}{Total\ number\ of\ injected\ mandate\ sources} \tag{23}$$

$$FAR = \frac{Number\ of\ background\ alarms}{Total\ number\ of\ background} \tag{24}$$

ODR is a general measure of detectability and does not provide information into the Minimum Detectable Activity (MDA) as a function of depth. For example, certain detection systems might be better at identifying sources at the surface but less effectively at depth or vice versa. Subsequently, MDA ($\alpha = 0.95$) was fitted through maximum likelihood using a binary logistic regression (Crawley, 2012).

5.4 Results and discussion

5.4.1 Optimisation of Gross Count algorithm

Initially, K values and the number of lags used in the moving mean were required to generate a GC baseline to compare ML to. Exponential moving mean formulations, 2/(n+1) and (1/n) for LaBr:Ce and NaI:Tl respectively, were found to yield the highest ODR and MDR for the require FAR ($\alpha > 0.005$). ODR and MDR behaved very similarly with varying lag and K values for both detectors, subsequently only MDR is discussed at this stage (Figure 5-5). Final ODR for the optimised alarms can be found in (Table 5-2).

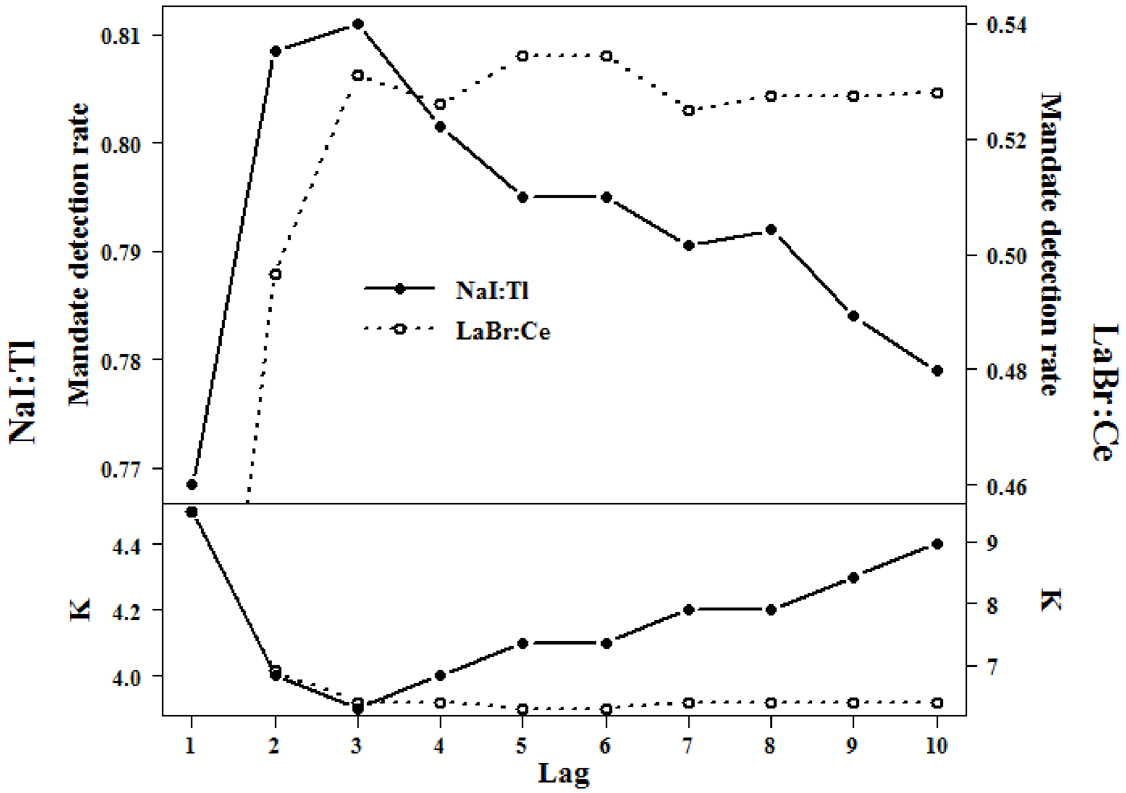

Figure 5-5 Mandate detection rates (top plot) and K values (bottom plot) as a function lag for NaI:Tl (empty circles and broken line) and LaBr:Ce (full circles and unbroken line) detectors. NaI:Tl is on the primary axis and LaBr:Ce on the secondary.

NaI:Tl produced the highest MDR (0.8112), at a lag of 3, either side of this lag a decrease in detectability was witnessed. K values appeared to mirror MDR for both detectors suggestive that, as more noise was added through a change in lag, K attempted to negate its influence. The best detectability was witnessed with the smallest K values (NaI:Tl = 3.9 and LaBr:Ce = 6.3). The higher K value for LaBr:Ce and the greater lag (lag = 5), infers that the algorithm struggled to cope with the additional noise introduced by internal contamination (Figure 5-1). This significantly lowered its MDR (0.5352). Overall, the GC method could not reach the MDR set by SEPA for either detector.

5.4.2 Performance of Machine Learning algorithms

The performance of all algorithms is summarised for different binning and detector configurations (Table 5-2). The combination of a NaI:Tl, an NN and ROIB provided the best ODR of 0.6927 ± 0.008. What is more, it was the only detector configuration able to confidently attain SEPA's contractual mandate (MDR = 0.9531 ± 0.0072). However, ML produced a varying degree of performance depending on the detection configuration it was employed on. This can only be explained through the influence of individual detector constituents.

Table 5-2. Statistics for all detector configurations

	NaI:Tl			LaBr:Ce		
Algorithm	ODR	MDR	FAR	ODR	MDR	FAR
GC	0.6357	0.8112	0.004	0.5055	0.5352	0.0046
NN-*RB*	0.5982 ± 0.0069	0.7044 ± 0.0867	0.0024 ± 0.0008	0.5427 ± 0.0082	0.5277 ± 0.079	0.0034 ± 0.0017
NN-ROIB	0.6927 ± 0.0080	0.9531 ± 0.0072	0.00439 ± 0.001	0.5479 ± 0.0040	0.3642 ± 0.0504	0.0048 ± 0.0015
SVM-*RB*	0.5759 ± 0.015	0.6092 ± 0.0224	0.0049 ± 0.0020	0.4873 ± 0.0153	0.2028 ± 0.0505	0.0041 ± 0.0023
SVM-*ROIB*	0.6693 ± 0.0011	0.8855 ± 0.012	0.0039 ± 0.0017	0.5058 ± 0.0194	0.3858 ± 0.0653	0.0086 ± 0.0056

5.4.3 Detector influence

Between the two detectors, NaI:Tl consistently proved to be the most reliable for all ML (Table 5-2). For instance, the range of MDR for NaI:Tl (0.6092 ± 0.0224 - 0.9531 ± 0.0072) was consistently higher than LaBr:Ce (0.2028 ± 0.0505 - 0.5352). Notice, ML did not show any improvement over GC in MDR for LaBr:Ce (although some improvement is demonstrated in ODR). This indicates LaBr:Ce, although it has higher energy resolution and efficiency, is not suitable for this application. Poor results were almost certainly attributed to the noise introduced, across the entire spectrum, by intrinsic counts over the short acquisition time. This noise would have disguised weaker source signals and made it more difficult for any algorithm to identify the occurrence of source signal. Even after certain bins corresponding to the most contaminated regions were removed no improvement in detection was found.

Conversely, NaI:Tl does not suffer from significant internal contamination permitting algorithms to isolate source signal with more confidence. From an economic perspective this finding is beneficial since NaI:Tl is approximately a fifth of the price of LaBr:Ce. That said, LaBr:Ce's superior energy resolution could play a more significant role in accurate depth and activity estimates useful for mapping purposes. What is more, post processing noise reduction techniques could be applied in this scenario (Green et al., 1988, Aage et al., 1999). However, given the difference in performance between the detectors, further discussion will focus on NaI:Tl due to its superior *hot particle* detection performance.

5.4.4 Binning system influence

ROIB provided a consistent increase in detectability (MDR and ODR) over RB (Table 5-2). In fact RB provided no or little improvement over GC. This implies by operating fewer bins and tracking changes in sensitive areas known to be associated with source contributions, rather than employing more of a formulated approach, source identification can be improved. The reason for this disparity could be down to the fact that many of the relatively narrow bins generated by the RB, for a single measurement, contained very few counts or even zeros, which introduces excessive noise. To add to this complication, some spectral regions of importance were divided between two bins for instance the bin break at 2220 keV for NaI:Tl (Figure 5-4). Some regions may also have been unnecessarily separated into multiple bins (i.e. below 200 keV) exhibiting unnecessary correlation. A combination of these elements resulted in the ML over-fitting to both the noise structure and benign changes, making it less sensitive to more subtle source contribution. The reduction in bins (through ROIB) has alleviated some counting noise and simplified the fitting process. This allowed ML to be more robust to changes in overall spectral shape and ultimately leading to better source discrimination. As highlighted earlier, optimisation algorithms could aid in the decision of bins (Wei et al., 2011).

5.4.5 Machine Learning algorithm comparison

In the majority of cases NN provided better results than SVM (Table 5-2), implying that the NN were more efficient at dividing background-source populations. A possible reason for this difference may be that NN were slightly better at defining non-linear boundaries within the feature space. However, finding support from the literature is difficult since this is the only study (to the best of the authors' knowledge) to compare the methods in a gamma spectroscopy setting. Studies in other scientific areas have found their performance to be similar (Byvatov et al., 2003, Zhang et al., 2008).

5.4.6 Advantages of Machine Learning

The advantage of using ML to interrogate spectral shape as opposed to total signal (GC) can be better understood by reviewing the MDR with total mean count rate

(Figure 5-6). At low total mean count rate, MDR was relatively high for all algorithms (>0.85). However, as total mean count rate increased, GC's MDR decreased to below 0.7 at the highest total mean count rates. Concurrently, ML tended to be significantly more stable across the total mean count range. At the limits of each population a large amount of uncertainty is observed due to the low sampling size.

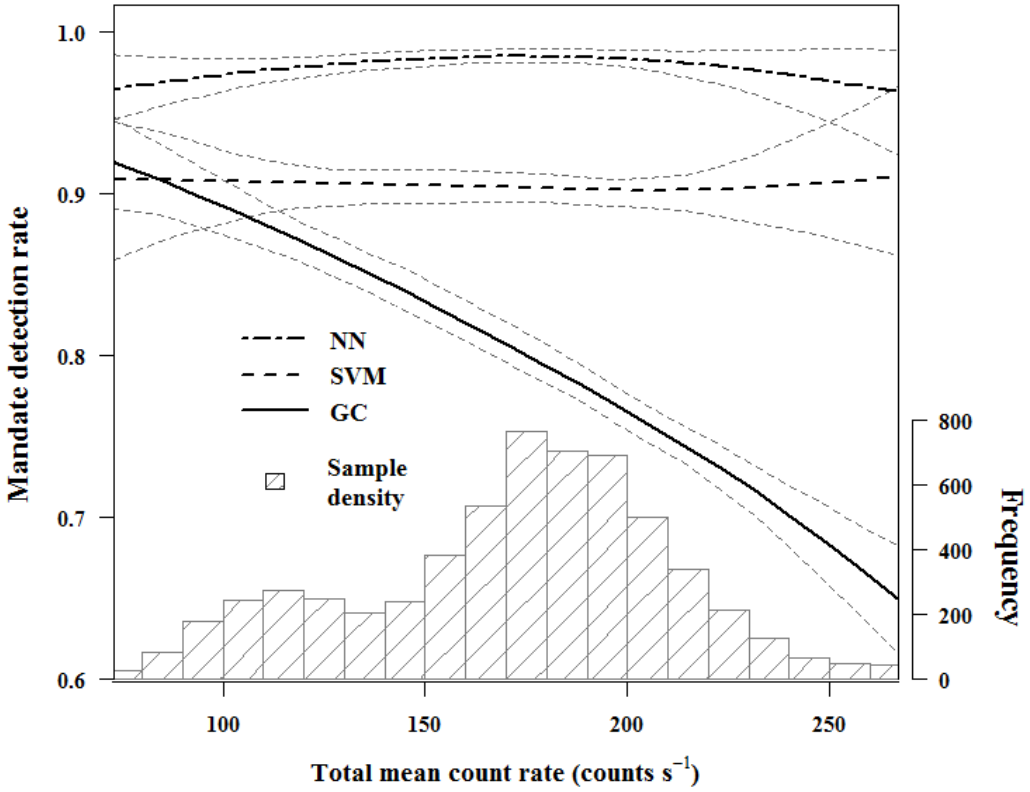

Figure 5-6 General trends in mandate detection rate as a function of total mean count rate for optimised neural network, support vector machine and gross counts algorithms for NaI:Tl. Machine learning algorithms used the region of interest bins. Sample density and confidence intervals (α = 0.95) are included.

One fundamental reason behind this is GC attempts to separate source and background by assuming them to be two independent univariate Gaussian distributions where the standard deviation ($\alpha = 0.68$) is the square root of the mean (Knoll, 2010). To explain this, consider two background count rates of 100 ± 20 and 250 ± 32 and the introduction of a fixed source contribution of 35 ± 12 ($\alpha = 0.95$). For the first scenario, source and background distributions will not significantly overlap allowing the alarm to be triggered seeing as T is confidently breached (eq 20). Yet in the second case, populations will significantly overlap ending up in the source being missed. Subsequently by using one bin, the signal to noise ratio is reduced relatively consistently with increasing count rate.

By dividing the spectrum into ROIB, more subtle spectral changes occurring across the entire spectrum are captured within spectral comparison ratios. Although the amount of counts has not increased an overall increase in signal to noise ratio is witnessed (Ely et al., 2006). This leads to source information being preserved more efficiently with increasing background count rate.

Another factor is that larger benign systematic fluctuations tend to occur with higher total count rate as some areas will be cluttered with discrete background sources (i.e. masonry or rocks). GC tends to false alarms more regularly in such areas (Figure 5-3). To circumvent this occurrence a larger value of K has to be set, thus lowering the MDR in higher count rate areas (eq 1). A dynamic function fitted to K allowing it to take into account general systematic changes with varying mean count rate could arguably be employed. This could decrease FAR slightly. ML methods (NN and SVM), because they take into account changes in shape as well as overall magnitude, they are better able to cope with benign fluctuations and ultimately be more sensitive to source contributions.

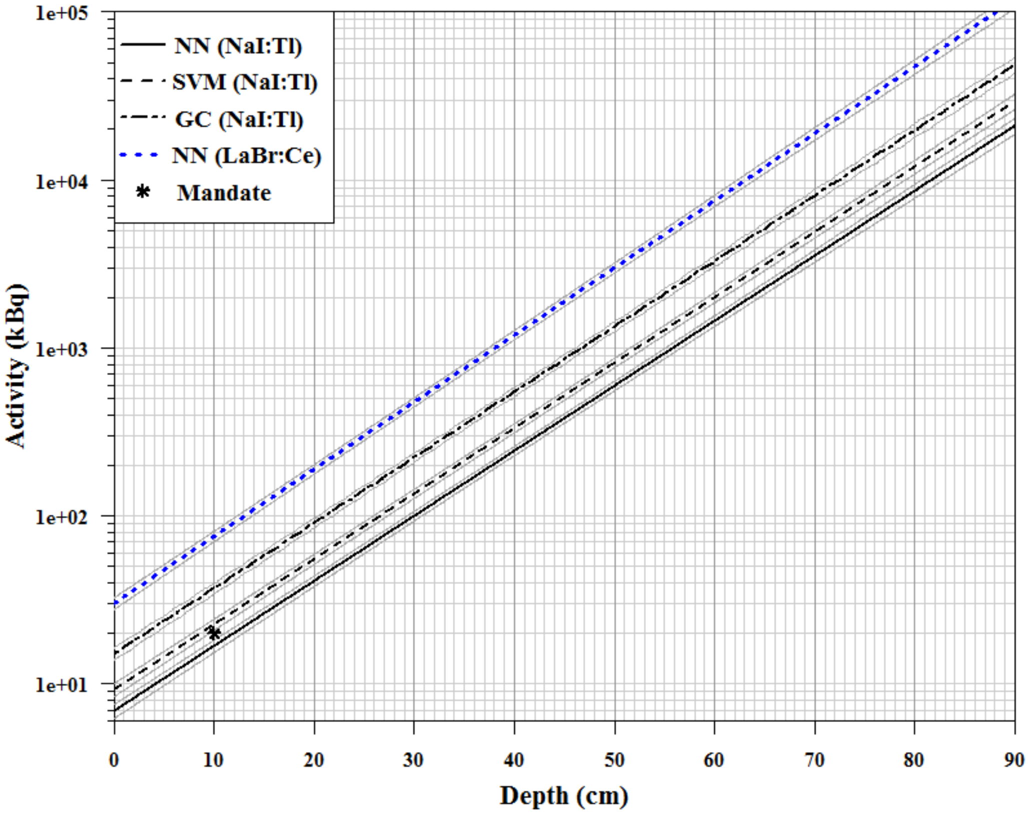

Figure 5-7 Minimum detectable activity (α = 0.95) functions fitted for selected detector configurations. 95% confidence intervals and SEPA's mandate are included. Region of interest bins were applied to all.

The improvement ML offers in comparison to GC is demonstrated by observing the MDA with depth (Figure 5-7). NN permitted the NaI:Tl to detect all activities on average 0.1 m deeper into the soil column compared to GC, for example 1 MBq could be detected down to a depth of 0.46 m using GC whilst NN could distinguish down to a depth of 0.55 m. SVM demonstrated less of an improvement over GC although still noticeable. SVM could detect on average 60 mm further into the soil column.

The influence of detector is apparent. The optimised LaBr:Ce, operating an NN, could only just detect SEPA's mandate at the surface, whereas the optimised NaI:Tl could detect it down to a depth of 0.16 m. Notice at greater depths this disparity diverges slightly, for instance LaBr:Ce could identify a 20 MBq *hot particle* to a depth of 0.7 m, however NaI:Tl (0.9 m) could detect the same activity 0.2 m deeper. This may have been caused by the majority of source photon being scattered to low energy into a region of substantial contamination for LaBr:Ce (< 400 keV) (Figure 5-1).

5.5 Future prospects for Machine Learning in routine monitoring

It has been shown that through the use of ML a marked improvement in detection rate could be obtained by a simple change in software as opposed to expensive hardware changes. However, there are considerations that must be taken into account before employing the technique.

NN, and to some extent SVM, are powerful when making predictions within the confines of the training dataset as demonstrated through this work. Yet when presented with data outside of this convex hull they are very poor extrapolators (Haley & Soloway, 1992, Dragović et al., 2006). One of the main concerns in this application is the ability of NN to manage changes in background populations brought about by variations on spatial and temporal scales. The spectral comparison ratios transformation to some extent negates this influence (eq 21).

However, it was found by using two subsets of my data from different parts of the time series and geographical positions, one to train and test and one to cross validate, the detection systems performance was significantly reduced. This infers that background variations at Dalgety Bay are complex and cannot be taken fully into account by using spectral comparison ratios. Hence for optimum performance, the background population must be well characterised for all individual areas. This eventually is very much attainable in routine monitoring given that large amounts of data, typically hundreds of thousands of spectra, can be generated over a relatively short period of time. This should allow ML to work within the limits of the known population and ultimately be more sensitive to radiation fields from *hot particles*. Nonetheless, the inter-site capability of the approach may be limited for real-time detection.

Another important issue to be addressed is the representativeness of source calibration data. This study adopted a simplified model on the grounds that correlating materials between the Monte Carlo model and background data is unfeasible. However, acquiring data from routine monitoring may provide a means of supplying additional source data to update the model.

5.6 Conclusions

The identification of ^{226}Ra *hot particles* through real-time analysis of gamma-ray spectroscopy data can be problematical particularly in the case of a weak source signal and variable background. It has been demonstrated that ML can significantly improve detection limits in this situation by focussing on changes in spectral shape compared to conventional total count rate algorithms. In this context, the intrinsic contamination of LaBr:Ce resulted in poor detection rates compared to NaI:Tl for the detection of ^{226}Ra hot particles. These findings represent a relatively inexpensive development in routine monitoring. The approach outlined in this study could arguably be applied to other sites and other radioisotopes; notably ^{137}Cs.

6 Mapping the spatial distribution and activity of ^{226}Ra at legacy sites through Machine Learning interrogation of gamma-ray spectroscopy data

Adam Varley[1], Andrew Tyler[1], Leslie Smith[2], Paul Dale[3], Mike Davies[4]

[1]Department of Biological and Environmental Sciences, University of Stirling, Stirling, FK9 4LA

[2]Department of Computing Science and Mathematics, University of Stirling, Stirling, FK9 4LA

[3] Scottish Environmental Protection Agency, Radioactive Substances, Strathallan House, Castle Business Park, Stirling, FK9 4TZ

[4] Nuvia Limited, The Library, Eight Street, Harwell Oxford, Didcot, Oxfordshire, OX11 0RL, United Kingdom.

Varley A., Tyler A., Smith L., Dale P. and Davies M. Mapping the spatial distribution and activity of ^{226}Ra at legacy sites through Machine Learning interrogation of gamma-ray spectroscopy data, *Manuscript submitted to Science of the Total Environment*

6.1 Abstract

Radium (^{226}Ra) contamination derived from military, industrial and pharmaceutical products can be found at a number of historical sites across the world posing a risk to human health. As a consequence of the irregular and sometimes unrecorded disposal patterns, some sites present challenging environments in which to accurately characterise the activity, depth and lateral distribution of contamination. Handheld gamma-ray spectrometry offers a tool to gain an understanding into localised radiation field through the analysis of each spectrum and using a large number of spectral measurements can provide a robust means of characterising an extensive area. However, local heterogeneity of the natural background, statistical counting uncertainty and non-linear source response are confounding problems associated with spectral analysis when attempting to deal with enhanced concentrations of a naturally occurring radionuclide such as ^{226}Ra. As a result, conventional surveys tend to attribute the highest activities to the largest total signal received by a detector (gross counts): an assumption that tends to neglect higher activities at depth. To overcome these limitations, a new approach employing Machine Learning methods is used in the analysis of gamma-ray spectra and a comparison is made to assess the advantage of the superior spectral resolution of Lanthananum Bromide is explored compared with a standard Sodium Iodide. Here representative Monte Carlo simulations were directly compared to field spectra through feature extraction using Principal Component Analysis and the pattern recognition capabilities of Machine Learning methods (Neural Networks and Support Vector Machines). Two handheld scintillators (Sodium Iodide and Lanthanum Bromide) were implemented. It was demonstrated that through a combination of Neural Networks and Lanthanum

Bromide the most accurate depth and activity estimates could be estimated. The optimised approach was demonstrated on a case study site, which revealed areas of significantly higher activity than initially explored surface contamination corresponding to gross counting hotspots.

6.2 Introduction

6.2.1 Radium contaminated legacy sites

Radium (^{226}Ra) was used extensively during the 20th century in military, industrial and pharmaceutical products (Tyler et al., 2013). ^{226}Ra has a half-life of over 1600 years and is the parent of an additional eight radioactive elements that together produce a complex array of alpha, beta and gamma emissions (Pratt, 1993). Follow-up studies into the health implications of radium dial workers in the US typify the risks associated with long-term radium exposure (Stebbings, 2001). Within the UK, radium was used extensively as a composite in luminescent paint principally by the military during wartime periods. Prior to the Radioactive Substances Act 1960 (HMSO, 1996) vast inventories of waste were routinely burned and buried with little record presenting complex remediation challenges (Wilson et al., 2013).

A report published in 2012 by the UK government, conservatively estimated there to be 150-250 Radium Contaminated Legacy Sites (RCLS) linked to Ministry of Defence activities within the UK (DECC, 2012). Moreover, it was recognised that there could be as many as 1000 contaminated sites in the UK alone. Similar RCLS can be found across other parts of Europe and North America (IAEA, 1998).

UK legislation has now provided the Scottish Environmental Protection Agency (SEPA) with a framework to classify radioactively contaminated land and set guidelines to describe the amount of contamination that may give rise to significant harm to humans (The Radioactive Substances Act 1993 Amendment (Scotland) Regulations, 2011). Subsequently, *homogeneous contamination* at RCLS in Scotland is controlled by the following criterion:

a) An effective dose must not exceed 3 mSv per annum (Statutory Guidance to support the Radioactive Contaminated Land (Scotland) Regulations, 2008).

Surface flux measurements using dosimetry can be used to rapidly assess the effective dose (IAEA, 1998). Yet, this measurement is somewhat limited in thoroughly assessing the activity and burial depth of homogeneous contamination, which tend to change significantly across a RCLS (Varley et al., 2015b). These factors are critical pieces of information for long-term remediation purposes, particularly at sites that are exposed to the public, where changes in site use or erosion events may occur increasing the risk of contact (Dale et al., 2013).

Currently, no single Scottish legislation can be used to specifically outline an activity limit that must not be exceeded for suspected homogeneous contamination at a RCLS. Therefore, in this study I accept that ^{226}Ra should be treated under the exemption for Naturally Occurring Radioactive Materials declaring:

b) An activity must not exceed 10 Bq g^{-1}(Statutory Guidance to support the Radioactive Contaminated Land (Scotland) Regulations, 2008).

The discrete nature of the items that were initially disposed of can also lead to the formation of *hot particles*. At one RCLS at Dalgety Bay, Fife, Scotland, a diverse range of *hot particles* and historic artefacts (< 70 MBq) has been found (Dale et al., 2013). If such items were to be picked up by a member of the public this may result in a significant committed dose (Tyler et al., 2013). A method for the real-time identification of ^{226}Ra containing *hot particles* at RCLS has been outlined in my previous work (Varley et al., 2015a).

In light of the uncertainties behind site formation and the lack of disposal records, once a RCLS has been identified the contamination should be systematically characterised to ascertain the risk it poses to long-term human health; thus going beyond limited surface dosimetry estimates (IAEA, 1998). In this paper I propose a method that can be rapidly and inexpensively deployed at a RCLS to provide accurate estimates of near surface *homogenous* ^{226}Ra contamination depth, activity and spatial distribution.

6.2.2 Environmental gamma-ray spectroscopy

Handheld gamma-ray spectroscopy (HGS) or mobile gamma-ray spectroscopy, generally performed using inorganic scintillators, is often the cheapest and most robust technique of characterising RCLS (IAEA, 1998, IAEA, 2003, Knoll, 2010, Dale et al., 2013, Read et al., 2013, Haddad et al., 2014). Using this method the spatial extent and activity of gamma-emitting radionuclides can be estimated using remote surface measurements without the need for time-consuming invasive methods (Tyler, 2008). Individual energy spectra produced during a survey are representative of the localised radiation field a detector has passed through (Beck et al., 1972).

For mapping purposes each spectrum can be post-processed using an algorithm to unfold spectral information (Kock et al., 2012). The first objective of this unfolding process is to identify whether there are characteristic signals from radium contamination (source), which typically differ in shape from background spectra (Figure 6-1A). However, source-background separation is often complicated by spatial fluctuations in background (^{40}K, and the ^{238}U and ^{232}Th series) and benign (^{137}C in the case of RCLS) radioelements, alongside variations in soil density and composition, which together introduce nuisance spectral changes (Runkle, 2006). Fagan (2012) presents an informative review of the challenges associated with, and the techniques employed in, spectral classification.

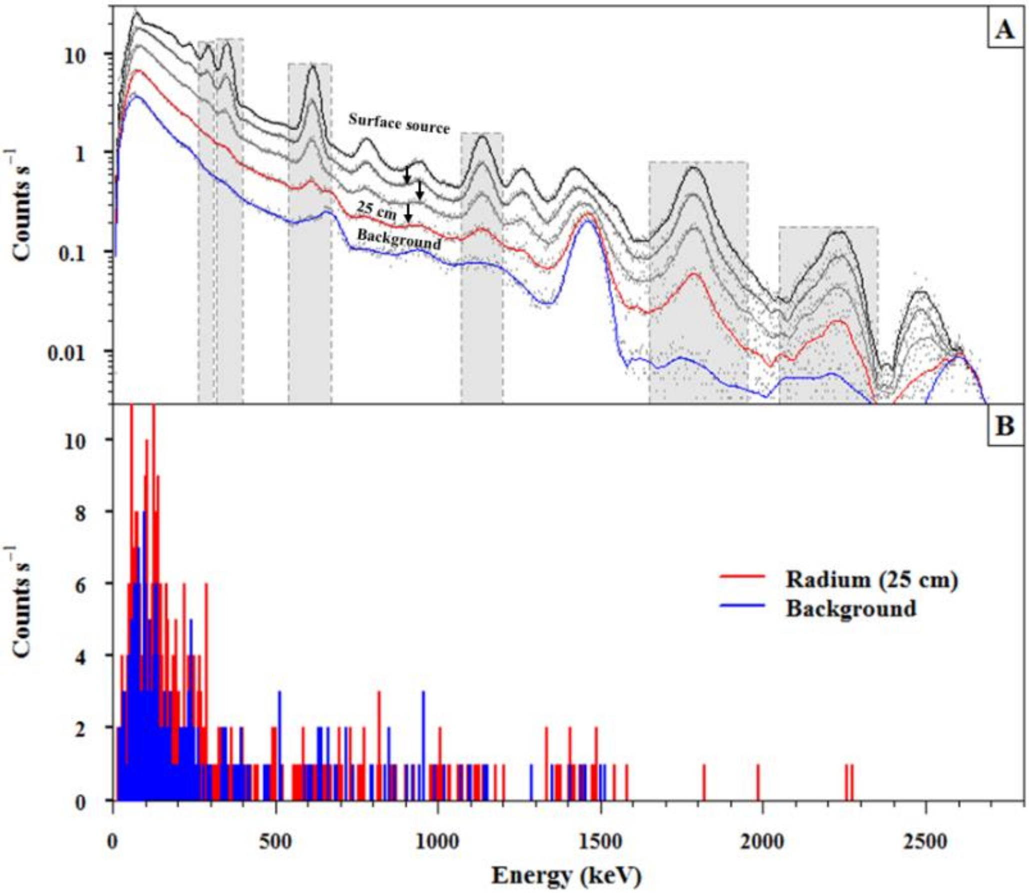

Figure 6-1. A) Nonlinear spectral response as a function of homogeneous source burial depth and a typical background taken using 71 x71 mm NaI:Tl detector. B) Spectra taken over 1 second demonstrating stochastic noise of background and 25 cm extended source.

Once a contaminated spectrum has been identified, the second aim is to identify elements that are symptomatic of source burial depth and activity (Figure 6-1A).

Notice non-linear changes take place across the spectrum as the burial depth of a source varies: for example lower energy peaks are attenuated more relative to higher energy peaks with increasing burial depth.

The multiple photopeak method aims to capture this occurrence by calculating the area under two background-subtracted full energy peaks with the purpose of comparing the observed ratio to that of a calibrated one to estimate source burial depth and activity (Miller et al., 1994, Haddad et al., 2014). Another method that utilises more spectral information is termed Full Spectral Analysis (FSA). FSA compares the spectral similarity of an obtained spectrum to a calibration library by a weighted least-squares fitting procedure using the majority of spectral channels (Maučec et al., 2004, Caciolli et al., 2012, Guastaldi et al., 2013).

The practical application of to these methods is however somewhat limited by stochastic noise presented within individual spectra introduced as a consequence of the short count times required to map a RCLS in high resolution within a limited time period (IAEA, 1998, Alamaniotis et al., 2013a) (Figure 6-1B). Subsequently, many HGS surveys fall back on unsophisticated spatial interpretation methods such as the total signal (gross counting) where the highest activities are attributed to the highest count rates (Adsley et al., 2004). At the majority of RCLS, this assumption is known to break down and higher activities at greater depths fail to be acknowledged (Figure 6-2). For example, a 0.1 Bq g^{-1} homogenous source at the surface will produce an identical signal to a 1 Bq g^{-1} homogenous source (radius 1 m) buried at approximately 40 cm. Furthermore, weaker source signal can easily be mistaken for background.

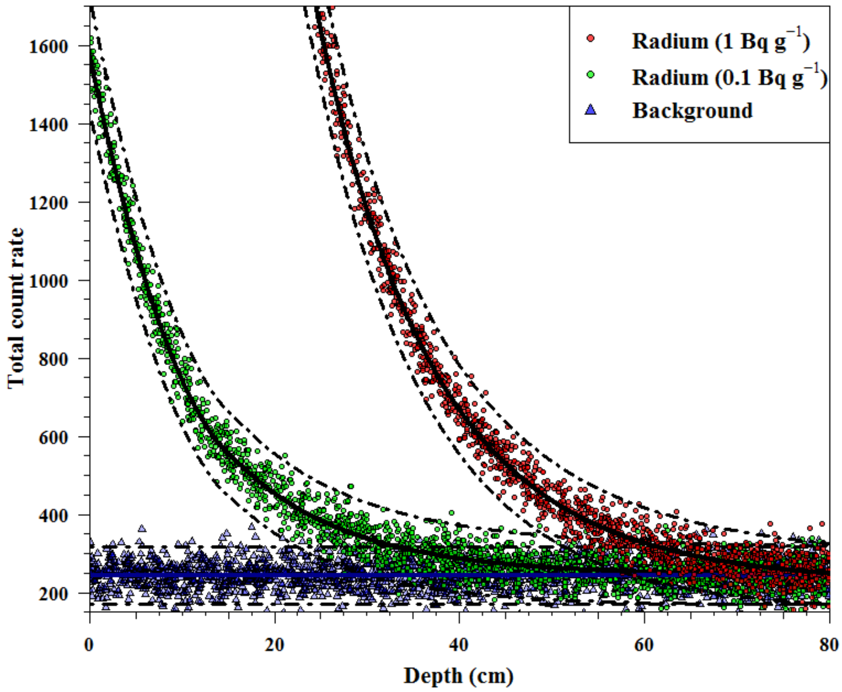

Figure 6-2. Total signal from background, 0.1 and 1 Bq g^{-1} homogeneous sources as a function of burial depth.

This paper investigates i) whether improvements can be made into the identification and estimation of depth and activity of homogeneous ^{226}Ra contamination through *consideration of the distribution of counts across the spectrum* and ii) whether the superior energy resolution of LaBr:Ce can demonstrate improvement compared to conventional NaI:Tl. This was achieved through a novel multivariate approach that develops the noise suppression and dimensionality reduction properties of the Principal Component Analysis (PCA) transform alongside the pattern recognition capabilities of Machine Learning (ML).

6.3 Material and methods

6.3.1 Field site and data collection

The case study site is found in Scotland, although its exact location cannot be disclosed and thus coordinates have been made anonymous and background maps are not included. The site has known to be associated with ^{226}Ra contamination for some time due to the historic disposal of military products. Large sections of the site suspected of being contaminated could not be accessed due to undergrowth. All measurements were taken under the supervision of SEPA.

Site access also provided a good opportunity to perform a supplementary HGS detector comparison alongside novel spectral processing techniques. The first detector, Sodium Iodide (NaI:Tl), was chosen as it is the workhorse of environmental gamma-ray spectroscopy and in my previous work has proved effective at determining the depth and activity of ^{226}Ra (Varley et al., 2015b) (Figure 4A). The second detector, Lanthanum Bromide (LaBr:Ce), has over the past decade received much interest since it provides better energy resolution (~2.5% at 662 keV) than the NaI:Tl (~7% at 662 keV) at the same time as offering similar robustness (Guss et al., 2010) (Figure 4B). However, each LaBr:Ce spectrum presents a large number of background counts distributed throughout the spectrum owing to internal isotopes (^{138}La and ^{227}Ac) (Iltis et al., 2006). Although laboratory comparisons have been performed between these two detectors, limited field comparisons have been performed (Menge et al., 2007, Milbrath et al., 2007).

Over the course of four days, in excess of 25,000 spectra were collected using the two detectors (both 71 x 71 mm). To ensure that spectra acquired by each detector were comparable the detectors were attached to a wheel barrow system, offset longitudinally by 0.5 m and attached at a height of 0.1 m from the floor, to ensure the same ground was covered. 1024 channel spectra were acquired using Ortec's Maestro software every second together with GPS coordinates provided by an SX Blue II differential GPS with a 0.6 m positional accuracy. A walking speed of 0.5 m s^{-1} was maintained during the survey. Data were logged and displayed in real-time with Stirling Mobile Gamma Spectrometry System (SMoGSS), software developed in-house, which also provided alarms when anomalous spectra are acquired.

It was acknowledged to adequately characterise the contaminated areas of the site the background spectral population would have to also be accurately characterised to use as a baseline in later modelling. Therefore, 10,000 spectra (approximately 30 % of the entire dataset) were taken within an area of background radiation next to the site.

6.3.2 Monte Carlo Simulations

To obtain a representative detector spectral response for a given detector to homogeneous source geometry can be problematic if attempted through laboratory based calibrations (Maučec et al., 2009). This is due to complications associated with distributing a radioactive source and also obtaining one active enough to provide acceptable counting uncertainties at greater depths after subtraction of the background (Hendriks et al., 2002). Consequently Monte Carlo Simulations (MCS) were used in this study (Allyson & Sanderson, 2001).

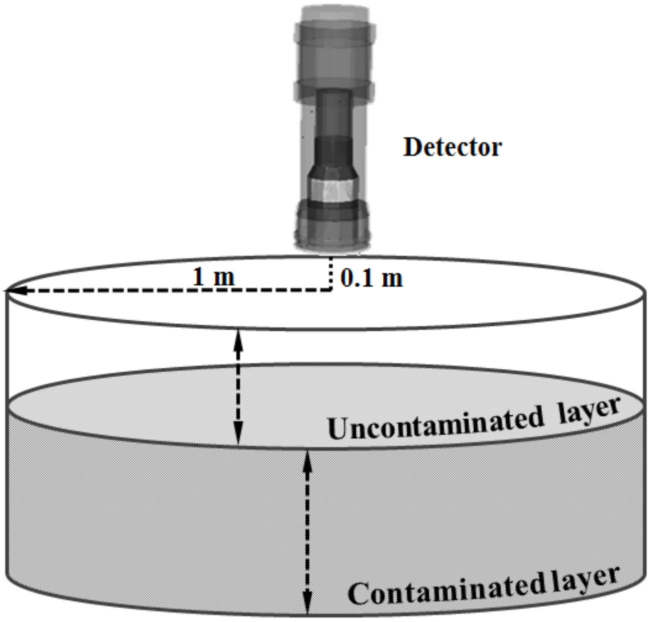

Figure 6-3. Schematic diagram of the two-layer Monte Carlo model used to acquire source spectral responses.

Source spectra were generated using the software package Monte Carlo N-Particle 5 (MCNP5) (Briesmeister, 1993). It was acknowledged that a wide-range of source geometries may be present at the site; thus posing an intricate source population to model. Therefore, for simplicity the majority of contamination was assumed to be heterogeneously distributed and underneath an unknown depth of overburden. This permitted a simple two-layer cylinder model to be developed within MCNP5 (Figure 6-3). The bottom layer was assumed to homogenously contaminated down to a depth of 0.8 m, and the thickness of the upper layer was altered to simulate increasing non-contaminated overburden (Thummerer & Jacob, 1998).

Only the key features of each detector were retained within MCNP5, such as the active volume, aluminium canning, photomultiplier tube, protective outer casing and Ortec's digiBASE unit. Importantly, spectra obtained from coded detector geometries closely matched that of spectra derived from calibration pads (Varley et al., 2015b). The geological matrix was composed of Beck's "standard" soil composition at a density of 1.3 g cm^{-3} (Beck et al., 1972). Radium decay data was sourced from the National Nuclear Data Centre (2013) and only emissions above 1% were used. The detector's field of view was considered to be small as the detector was positioned at 0.1 m height and the majority of contamination was thought to be buried and localised: resultantly a 1 m radius was used in the model (De Groot et al., 2009). What is more, contamination at RCLS has been found to be intermittently spaced often not extended beyond a 1 m radius. To reduce statistical uncertainty in individual energy bins the maximum number of starting particles within MCNP5 (2×10^9) was sourced for each run (Moreira et al., 2010).

6.3.3 Dataset generation

A synthetic spectral calibration dataset was produced by spiking spectra taken from the background area with MCS derived ^{226}Ra spectra (Kangas et al., 2008). The calibration dataset was then compared to spectra obtained from the contaminated area. To confirm model optimisation was being achieved, three different datasets were developed: training, test and cross-validation (Dragović et al., 2006). The training dataset was comprised of background spectra that had been accumulated over a 60 second period and spiked with statistically defined MCS (2×10^9 starting particles). This provided a clear spectrum with well-defined shape to produce an optimised model fit. To confirm the modelling approach fitted to general patterns within the data verification was sought against the test and cross-validated datasets that possessed realistic stochastic noise elements (Moreira et al., 2010). These datasets were formed from 1 second background spectra combined with a noisy MCS ^{226}Ra spectrum, whereby a limited number of starting particles were sourced. This scenario is characteristic of a real activity over a 1 second acquisition i.e. 2,184,000 would be equivalent to 1,000,000 Bq after MCNP5 normalisation where Radium has a decay probability of releasing 2.184 photons Bq^{-1}. Normalised MCNP output was converted to counts second^{-1} Bq^{-1} g^{-1} according to Hendriks et al. (2002) and to reproduce the characteristic resolution of each detector statistical broadening was introduced after individual runs. To improve activity estimates of later fitting processes to within a relevant environmental range, a maximum activity of 20 Bq g^{-1} was used (Varley et al., 2015b).

6.3.4 Spectral binning

HGS spectra obtained over 1 second tend to exhibit large counting uncertainty (Alamaniotis et al., 2013b) (Figure 6-1B). In my previous work (Varley et al., 2015a) using NaI:Tl and LaBr:Ce I have found it more suitable to observe general changes in spectral shape by transforming each spectrum into a smaller number of non-overlapping energy bins (typically 10-25 bins depending on the detector). This negates some counting noise without significant loss of energy differentiation (Jarman et al., 2008). Two binning methods were implemented. The first placed bins around Regions of Interest (ROIB) based on characteristic ^{226}Ra emissions and scattering regions (Figure 6-4). The second more systematic approach, coined Resolution Binning (RB), developed bins based upon the deterioration of energy resolution with increasing energy (Runkle, 2006).

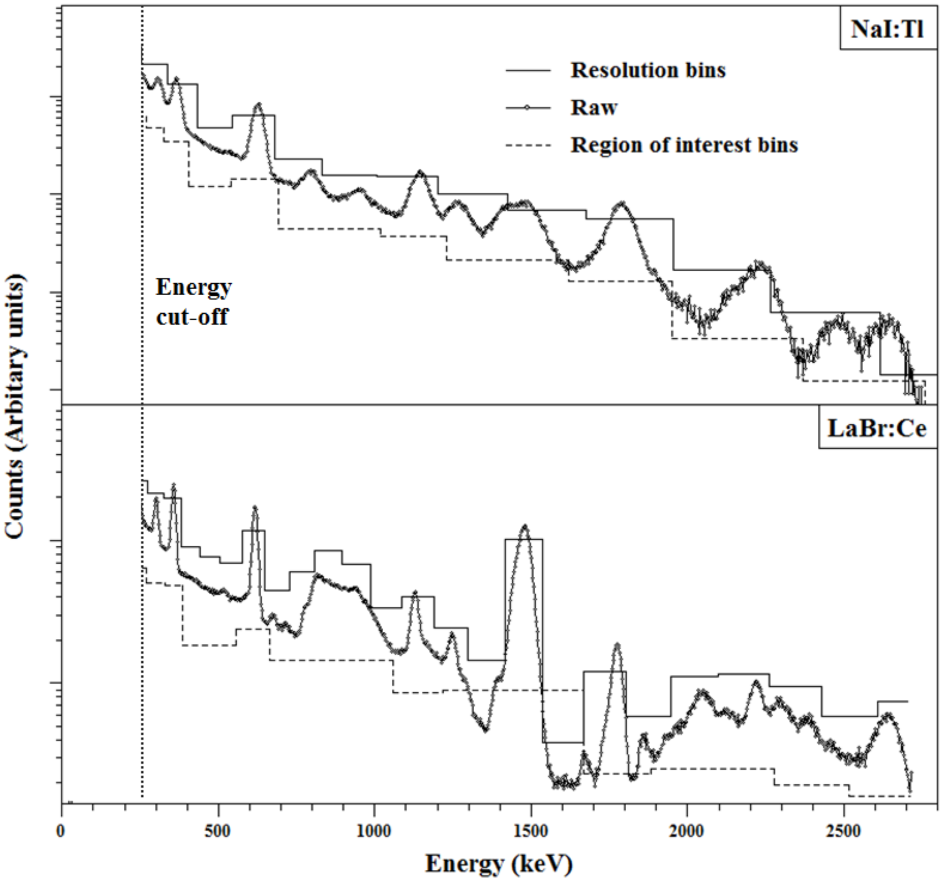

Figure 6-4. Binning methods for NaI:Tl and LaBr:Ce detectors.

ROIB used on a NaI:Tl was shown to be the most effective detector setup in the routine monitoring of ^{226}Ra “hot” particles. However, this work is inherently different given that it is not practical to transform bins into the time series in order to negate local background changes as large areas were known to be homogeneously contaminated. Therefore, the employment of Principal Component Analysis to directly compare background and source could favour more bins (RB) and the superior energy resolution and energy efficiency of LaBr:Ce, since counts from internal contamination may be supressed more efficiently.

Importantly, energies below 250 keV were discarded from analysis given that large systematic variations take place on a spatial scale that can be very challenging to predict (Caciolli et al., 2012). This can be attributed to the photoelectric effect becoming the dominant form of photon interaction, which is controlled by the composition of the soil matrix (Tyler, 2008).

6.3.5 Principal Component Analysis

Principal Component Analysis (PCA) was employed to produce a set of noise reduced uncorrelated spectral shapes known as Principal Components (PCs) (Du et al., 2010). Importantly, before the dataset was spectrally decomposed it was noise adjusted to in attempt to yield equal variance in all channels (Hovgaard, 1997). Subsequently, PCs were ordered according to the total variance contributed to the dataset under the assumption the majority of variance corresponds to signal in the lower order PCs and uncorrelated noise in the higher order PCs (Hotelling, 1933). All but the first few PCs were then discarded substantially reducing the dimensionality of the dataset and alleviating uncorrelated elements associated with counting noise (Runkle, 2006). Furthermore, spectral drift components were also separated out into higher order PCs. Patterns within the first few PC loadings, corresponding to signal, were then used to infer whether there were contributions from ^{226}Ra and at what depth and activity it was occurring (Adams et al., 2012) (Figure 6-5).

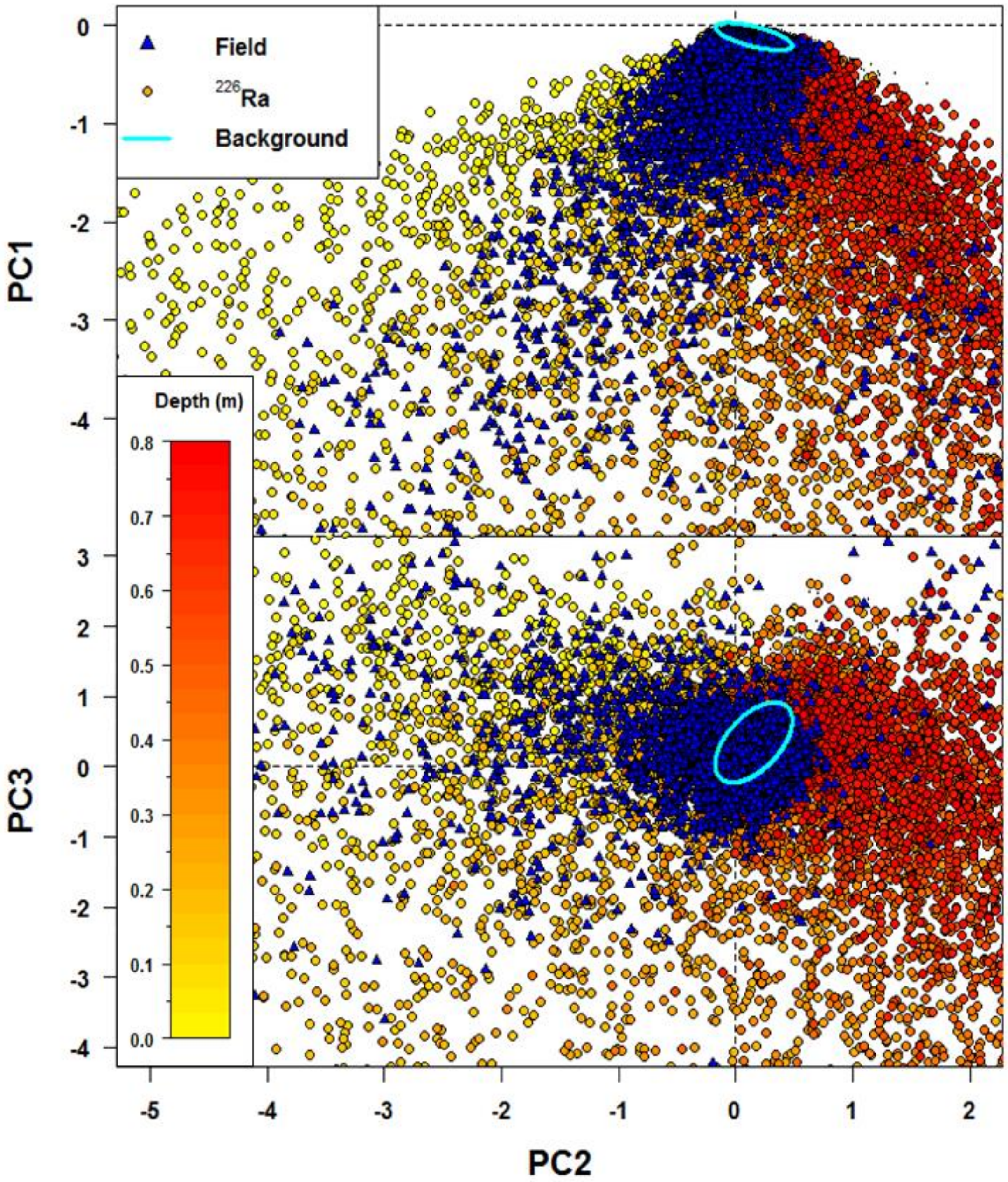

Figure 6-5. Patterns within loadings from the PCs 1,2 and 3 for NaI:Tl between Monte Carlo derived cross-validation set (circles) and field results (triangles). Notably, burial depth is separated within Principal Component space (yellow indicates surface and red buried) and increasing distance from the background pack (Cyan ellipse) infer increases in activity.

PCA was performed on the entire dataset (training, test, cross-validation and field spectra) to enable field spectra to be encompassed into the same PCs structure as known synthetic data providing a direct means of spectral comparison (Varley et al., 2015b) (Figure 6-5). Notice that depth (angle from background population) and activity (distance from the background population) could be inferred from the first few PCs. However, non-linearities were presented within the PCA transformed data that were problematic to encapsulate using convention regression and classification algorithms, such as non-linear regression (Adams et al., 2012) and Mahalanobis distance (Runkle, 2006).

6.3.6 Machine Learning

A solution to extracting significant patterns within PC loadings is offered by data-driven Machine Learning (ML) algorithms (Sharma et al., 2012). Providing there is sufficient data available to robustly train and test models, ML is able to fit to high dimensional, complex feature spaces where noise structure may differ from Gaussian (Figure 6-5). Recent developments in software have provided user-friendly development environments tailored towards practical application (Ao et al., 2010). For these reasons, ML has been used to interpret gamma spectroscopy data previously (Yoshida et al., 2002, Dragovic et al., 2005, Kangas et al., 2008, Wei et al., 2010, Sharma et al., 2012). Early exploration and previous experiences offered two promising ML methods: Neural Networks (NN) and Support Vector Machines (SVM) (Varley et al., 2015a).

It was found early on to generate optimum performance for ML it was more suitable to divide the modelling task into two:

i) To classify PC loadings into source or background.

ii) Apply a regression to provide depth and activity estimates.

Binary classification presents a trade-off between false positive and true positive rates, and as there was no predefined false positive rate, Receiver Operator Characteristics (ROC) was chosen as a robust measure of detection rate (T.J. Stocki et al., 2008). To quantify classification, the Area Under the Curve (AUC) of an ROC plot was calculated where values closer to one were considered better classifiers. To robustly test the classifiers, a uniform random sample of activities (0.1 - 2 Bq g^{-1}) and depth (0 - 0.8 m) was drawn to derive AUC from the cross validation set.

Regression performance was assessed by calculated the R^2 value between model prediction and actual values on the cross validation set which was formed by a uniform random sample of activities (0.1 - 20 Bq g^{-1}) and depths (0 - 0.8 m) (Moreira et al., 2010). To ensure uncertainties on final estimates could be assess for the final optimised model, it was fitted and cross-validated to 10 randomly drawn spiked dataset (section 6.3.3) providing a standard error and mean for each field measurement. PCs were normalised to their mean and variance. Approximately 4000 data points were used to train (70%) and test (30%) ML (Dragovic et al., 2005).

6.3.6.1 *Neural Networks*

The topology of an NN can be compared to the structure of a brain in that it is made of separate processes units or nodes that are connected by synaptic weights (Yoshida et al., 2002). In this study, a Multi-Layered Perceptron was used from the R package “RSNNS”, in which nodes were separated into three individual layers(Bergmeir &

Benítez, 2012a). PC loadings were feed into the first input layer, which was then passed onto the hidden layer where a non-linear sigmoidal transformation was performed to map transformed explanatory variables onto the output nodes or response variable(s) (Olmos et al., 1992). Backpropogation was used to train NN and global convergence was attempted through minimising the Relative Mean Square Error (RMSE) between the training and test sets (Riedmiller & Braun, 1993). The architecture of a NN often reflect the complexity of the problem it is attempting to solve; consequently the number of hidden neurons and learning epochs had to be optimised via an extensive grid search (Dragović et al., 2006). Only a single layer of hidden neurons was explored as it was found a second layer did not significantly enhance performance.

6.3.6.2 *Support Vector Machines*

SVM address a problem in a different manner to NN, through the introduction of maximal-margin separating hyperplanes into the non-linear feature space utilising the so called “kernel” trick (Cortes & Vapnik, 1995). As a result, SVM are particularly powerful binary classifiers however multiple response regression is difficult, thus SVM were only considered for classification. A radial basis function was found to be the most appropriate kernel for this case (Sangeetha & Kalpana, 2010). Therefore, the cost (C) and gamma parameters on the kernel had to be optimised, which was also accomplished using a grid search (Hornik et al., 2006). The R package “e1079” was employed.

6.3.7 Spatial interpolation

Estimations of activity and depth of contamination were found to vary considerably on a sub-metre scale predominantly due to localised spatial variability of contamination, but also as noise introduced through the modelling process. This makes geostatistical methods such as Kriging, which attempt to model spatial autocorrelation, difficult for this application. In addition, spatial extrapolation and significant interpolation would be unfeasible. Therefore, deterministic *Inverse Distance Interpolation* was preferred as it fits through all sample points and is based upon the assumption the weight of a sample is inversely proportional to its distance; a phenomenon that closely follows the inverse square law of a radiation field (Shepard, 1968).

6.4 Results and discussion

6.4.1 Spectral classification

The best classification results, independent of algorithm, detector or binning method, were found by using the first 3 PCs, consistent with source signal being captured within these first few PCs and lower order PCs containing principally noise (Dickson, 2004). This result significantly reduced dimensionality and simplified detection. This could explain the reason why the number of hidden neurons was consistently below 10 and learning tended to converge around 4000 epochs for all optimal classification NNs. SVM gamma (300-1000) and cost (100-800) were relatively large implying the classification boundary required a close-fitting boundary that was highly dependent on individual training points (Meyer & Wien, 2014)

Table 6-1. Area Under the Curve values for different detector, binning system and algorithm combinations.

	NaI:Tl		LaBr:Ce	
Algorithm	Binning system		Binning system	
	RB	ROIB	RB	ROIB
Mahalanobis	0.788 ± 0.004	0.786 ± 0.006	0.785 ± 0.007	0.792 ± 0.005
NN	0.831 ± 0.005	0.830 ± 0.003	0.836 ± 0.004	0.840 ± 0.006
SVM-*ROI*	0.815 ± 0.003	0.793 ± 0.005	0.796 ± 0.006	0.824 ± 0.005

ML methods showed a significant improvement in AUC (0.793 – 0.840) over traditional Mahalanobis distance (0.786 – 0.792) (Table 6-1). This suggests the classification boundary was non-linear and so, a Gaussian assumption was too simplistic to accurately model the boundary, whereas the ML algorithms were capable to define these accurately. Of the two ML methods, NN (0.831 – 0.84) consistently outperformed SVM (0.793 – 0.824) for all detector configurations. However, patterns within the two binning systems are harder to explain since RB produced better results for NaI:Tl whereas ROIB suited LaBr:Ce better. For LaBr:Ce this may be due to the alleviation in counting noise through fewer, logically placed, bins aiding in the de-noising process particularly in contaminated areas (Figure 6-4b). NaI:Tl with almost no internal contamination, more bins may have providing more information in which to draw more representative PCs from.

In previous work where a real-time application was needed the internal contamination posed by LaBr:Ce was found to hinder its detection capabilities (Varley et al., 2015a). However, the ability to post-processing and thus negate the influence of intrinsic counts using a technique such as PCA demonstrates that the superior energy resolution and efficiency of LaBr:Ce can still be utilised to provide improved detection rates over a s short count time. Another reason could be that in a real-time application a relatively large number of input dimensions are required (13 bins) to capture spectral shape changes. The smaller number of noise-reduced PCs (3 loadings) provided a clearer signal for ML to distinguish between.

6.4.2 Depth and activity estimates

As with the classification results it was found that using the first 3 PCs as inputs produced the lowest R^2 values for all NNs. 10,000-15,000 learning epochs was found to be adequate to train all NN before convergence between training and test sets was met. More neurons were needed for RB (18 – 20), in comparison to ROIB (10-15), suggesting the structure of data in the feature space was slightly more complex for RB.

Table 6-2. R^2 values for depth and activity estimates for different detector and binning system combinations.

	NaI:Tl		LaBr:Ce	
Response variable	Binning system		Binning system	
	RB	ROIB	RB	ROIB
Activity	0.693± 0.004	0.691± 0.003	0.738 ± 0.002	0.752± 0.003
Depth	0.527± 0.006	0.544± 0.003	0.590 ± 0.004	0.608 ± 0.005

Consistently higher R^2 values, for activity and depth, using either binning system, were found for LaBr:Ce (0.729-0.752 and 0.584-0.608, respectively) when compared to NaI:Tl (0.691-0.696 and 0.508-0.544, respectively) (Table 6-2). This further supports the argument that the superior energy resolution and efficiency of LaBr:Ce could be utilised for environment monitoring on condition that there is enough training data to implement a post processing algorithm (such as PCA) to lessen the effect of nuisance signals from internal contamination . For HGS monitoring where real-time output is required, NaI:Tl is probably still the most reliable detector. Again using fewer, more systematically placed energy bins (ROIB), provided higher performance.

6.4.3 Analysis of case study site

Spectral classification and regression of field data was performed using two NN on ROIB-LaBr:Ce spectra. Activity and depth estimates of source spectra demonstrate the advantages the approach (Figure 6-6. Activity and depth estimates alongside standard error for source spectra from field site. Colour ramp indicates gross count rate.). The majority of highest activity contamination (> 1 Bq g^{-1}) was estimated to be buried beyond 0.2 m with the highest activities occurring at greater depths (0.3-0.5 m). Hotspots identified during the survey using straightforward gross counting (yellow and red colours), although they represent the highest surface dose rates they were relatively low activity (<1 Bq g^{-1}) positioned at the surface (< 0.05 m).

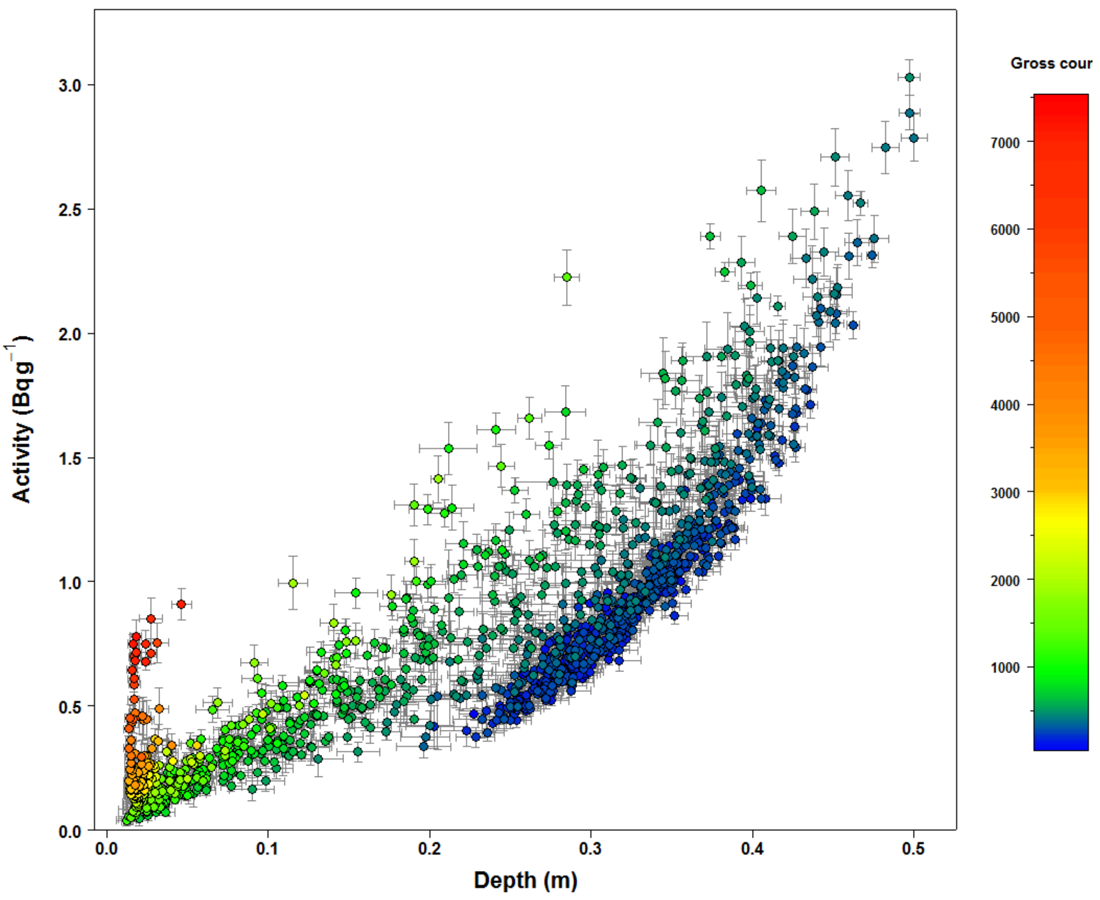

Figure 6-6. Activity and depth estimates alongside standard error for source spectra from field site. Colour ramp indicates gross count rate.

Another feature is the exponentially increasing manner of the activity of detected source spectra with greater depth. This represents the limit of detection, beyond these depths ^{226}Ra could not be confidently separated from background by the classification NN. Notice that the standard error for measurements generally increases with greater depth. This can be attributed to fewer source counts across the spectrum producing a lower signal to noise ratio making the fitting procedure more difficult for the regression NN.

Contamination at this site could not be identified beyond 0.6 m, because at these depths much higher activities would have been beyond the limit of detection (Figure 6-6). This reflects the ultimate limitation of *in situ* and mobile gamma-ray spectroscopy. To gain a better assessment of deeper contamination borehole measurements should be taken and a similar spectral processing approach could be applied (Varley et al., 2015b). Alternatively, longer counting times using a higher resolution detector, for instance a High Purity Germanium detector, could be implemented. However critically, the current investigation provides evidence that the critical value for the exemption of Naturally Occurring Radioactive Material (above 10 Bq g^{-1}) is not exceed at the site at less than 0.6 m.

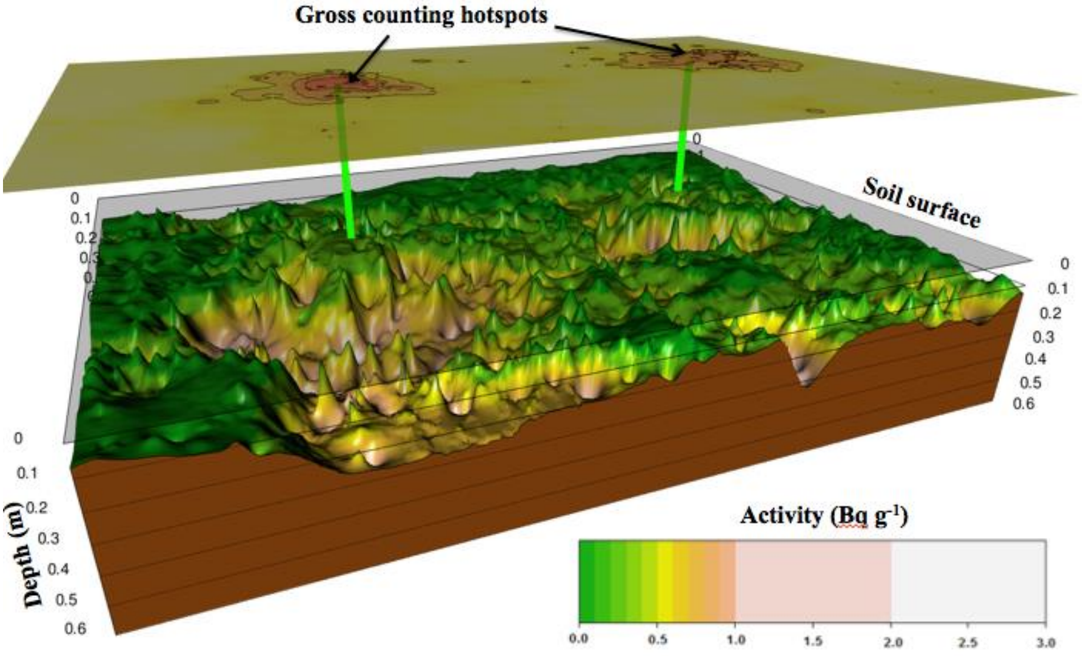

Figure 6-7. 3 dimensional plot demonstrating activity (colours) and vertical depth (z plane) of a section of contamination at the site taken using a LaBr:Ce detector and processed using a Neural Network. The spatial distribution of gross count is provided for comparison.

An interesting section of the site, consisting of an area of ground approximately 600 m^2 in size, has been characterised (Figure 6-7). This area displays a large variation in activity, depth and lateral distribution of contamination. Notice how the highest intensity gross counting hotspots (red sections on upper plot) correspond to relatively low activity (>0.01 Bq g^{-1} or green areas) that are close to the surface (>0.05 cm). However, there tends to be much higher contamination at greater depths in the close vicinity of these areas (pink areas in the foreground). An explanation for this is that hotspots may represent the latest (less contaminated) spoil, laid down at the end of the formation of the tip (ash and clinker can been seen at surface on some of the hotspots). Much higher concentrations of ^{226}Ra would appear to have been laid down earlier in the sites history, perhaps during and immediately after the Second World War when large ^{226}Ra inventories were being disposed of. This contamination occurs at greater depths under a relatively non-contaminated overburden, which is likely to have been used to cover contamination at a later date.

6.5 Conclusions

A novel method, employing Principal Component Analysis and Neural Networks, has been proposed permitting the rapid estimation of the depth and activity of homogeneous ^{226}Ra contamination from surface measurements taken using handheld gamma-ray detectors. This enables the accurate characterisation of an area contaminated with ^{226}Ra and interpolated maps of the processed data ultimately allow for the risk to human health, in both long and short term, to be robustly assessed. The superior energy resolution of LaBr:Ce resulted in better depth and activity resolving capability suggesting that it was more suitable than the standard NaI:Tl for this type of contaminated land application and could easily be applied to other gamma emitting radionuclides such as ^{137}Cs.

7 Rapid high resolution mapping of activity and burial depth of ^{137}Cs deposits using Machine Learning to unfold gamma-ray spectra

Adam Varley[1], Andrew Tyler[1] , Christopher Sneddon[1], Leslie Smith[2], Mike Davies[4]

[1]Department of Biological and Environmental Sciences, University of Stirling, Stirling, FK9 4LA

[2]Department of Computing Science and Mathematics, University of Stirling, Stirling, FK9 4LA

[4] Nuvia Limited, The Library, Eight Street, Harwell Oxford, Didcot, Oxfordshire, OX11 0RL, United Kingdom.

Varley A., Tyler A., Smith L. and Davies M. Rapid high resolution mapping of activity and burial depth of ^{137}Cs deposits using Machine Learning to unfold gamma-ray spectra, *Manuscript*

7.1 Abstract

^{137}Cs, a fission product, is commonly found in the environment owing to significant contributions from fallout, introduced by accidental nuclear reactor meltdowns and weapon detonations, and legitimate marine and riparian discharges made under license from nuclear establishments. A number of applications, such as dose reconstruction, sediment dating and climate change models have become reliant on estimating the activity and burial depth of ^{137}Cs. Conventional means of estimating these parameters, through soil coring or tripod mounted *in situ* gamma-ray spectroscopy, are labour-intensive and often not spatially representative. Here, a different approach is proposed by utilising a large number of short counts mapped across a site using handheld scintillator based detectors. Through a spectral transformation process that makes use of Monte Carlo simulations, Principal Component Analysis and Neural Networks, issues associated with counting noise, nonlinearity source response and variable background are taken into account. The technique is employed on comparable (71 × 71 mm), sodium iodide and lanthanum bromide, detectors at Ravenglass saltmarsh, Cumbria in the UK. The results demonstrated that the method could be used to map extensive ^{137}Cs distribution. However, it was speculated that mean mass per unit area of the vertical activity distribution, at the chosen test site, either exhibited too little variation to validate the approach or was beyond the detection limits of the system. Similar performance was realised for both detectors; although sodium iodide produced marginally better results compared to measured core data.

7.2 Introduction

7.2.1 ^{137}Cs in the environment

^{137}Cs is a fission by-product that has entered the environment through a number of different pathways. Large quantities have been dispersed as fallout from accidental nuclear reactor meltdowns, such as the Chernobyl and Fukishima Daiichi power plants (Steinhauser et al., 2014) and from numerous nuclear weapon detonations (Wright et al., 1999). Substantial inventories are also formed and legitimately discharged from nuclear installations (Povinec et al., 2003).

Sellafield, Cumbria, UK is one of the world's largest nuclear reprocessing plants and has been releasing radioactive liquid effluent discharges since 1952 through pipelines into the Irish Sea (Gray et al., 1995). This has led to approximately 10% of the total ^{137}Cs discharged from the installation becoming associated with an extensive area of silt and mud on the seabed of the Irish Sea (Cook et al., 1997). This contamination together with somewhat dwarfed modern discharges is recognised to be a significant source of ^{137}Cs (Morris et al., 2000). Widespread remobilisation from the Irish Sea, through physical and chemical processes, has led to coastal environments in England (Brown et al., 1999, Jones et al., 2007), Scotland (McKay & Baxter, 1985, Tyler et al., 1996b), Ireland (Watson et al., 1999, Charlesworth et al., 2006) and further afield (Povinec et al., 2003) becoming sinks for ^{137}Cs and other radionuclides derived from Sellafield. However, the complex interactions between a number of biogeochemical processes, varying discharge rates (Figure 7-1) and tidal currents have left a convoluted spatial distribution of ^{137}Cs activity (Jones et al., 1999) that can vary with depth, and on a temporal scale, with localised surface remobilisation (Wakefield et al., 2011).

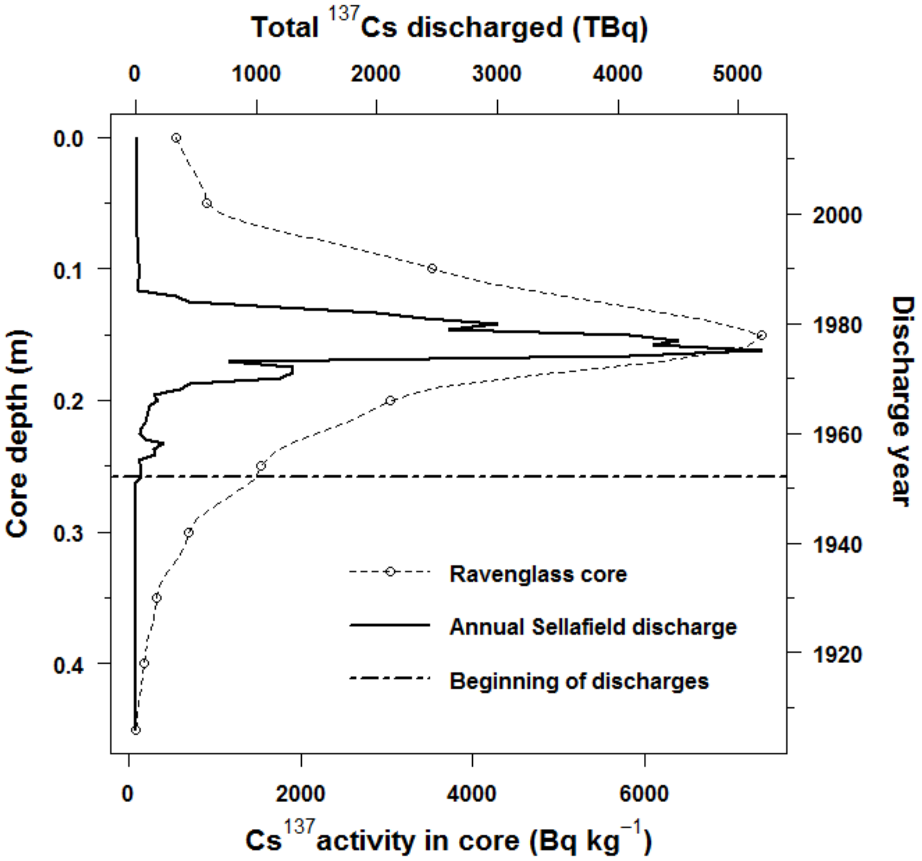

Figure 7-1. The ^{137}Cs activity in a core taken from Ravenglass estuary (primary axis) compared to recorded historical discharges of ^{137}Cs from Sellafield (secondary axis).

7.2.2 Scientific applications

The ability to accurately characterise the depth and activity of ^{137}Cs deposits is important for a number of scientific applications. A key function is to estimate the dose attributed to ^{137}Cs within a particular environment. This is paramount in the protection of human health and non-human biota (OSPAR, 2010). Dating sediments using ^{137}Cs is another useful application extensively employed within saltmarsh environments, whereby known discharges are matched to subsurface maxima observed within the depth profile (Oh et al., 2009) (Figure 7-1). It has also been demonstrated that proxy relationships can be established between other radionuclides, notably ^{214}Am (Miller, 2007), and relevant environmental variables such as grain size (Clifton et al., 1999), clay content (Wakefield et al., 2011) and sedimentation rate (Tyler, 1999).

The possibility of increased storm events and sea level rise, brought about by climate change, has forced large-scale coastal erosion events to be considered. This presents another motive for characterising ^{137}Cs since large inventories could be remobilised and come into contact with humans and non-human biota. Therefore, to better predict the behaviour and ultimately the fate of ^{137}Cs, accurately determined spatial inventories should be integrated into topographical and climate models.

7.2.3 Depth and activity determination of ^{137}Cs

The presence of ^{137}Cs activity can be measured relatively straightforwardly using its abundant (0.8499) gamma emission at 662 keV produced by its daughter product ^{137}Ba (Kluson, 2001). Using this gamma emission, depth and activity from cores taken from a site can be precisely measured on laboratory gamma-ray spectrometers (Figure 7-1). However, the collection, preparation and counting process tend to be time-consuming and labour intensive, which often results in a limited number of cores being taken leading to poor spatial characterisation (Tyler, 1999).

A more practical option is to employ *in situ* gamma-ray spectroscopy thus permitting large areas to be surveyed relatively quickly and smoothing over small-scale heterogeneities (Tyler, 2008). This involves taking a number of static measurements, typically 1 metre above the ground, and using changes in the spectrum to infer the mass depth and activity of ^{137}Cs (Figure 7-1). Hyper Pure Germanium (HPGe) (Kastlander & Bargholtz, 2005), Sodium Iodide (NaI:Tl) (Tyler, 2004), Bismuth Germanate (BGO) (Maučec et al., 2004) and Caesium Iodide (Potapov et al., 2001) are just some of the detectors that have been employed in *in situ* measurements of ^{137}Cs. However, this method is not without its limitations.

Firstly, the height at which the detector tends to be positioned (1 m) leads to a relatively large Field Of View (FOV); typically over 10 m. This reduces its sensitivity to localised variations (on a metre scale) particularly for changes occurring at depth since lateral contributions dominate (Dewey et al., 2011). Whetstone et al. (2011) used lateral and frontal lead collimators to focus the detectors FOV and improve distribution estimates, although counting times were longer and the system weighed considerably more (Dewey et al., 2011, Whetstone et al., 2011).

A second issue is that a substantial calibration effort, generally through a soil coring plan, is often required to encompass a representative number of spectral shapes to statistically define the relationship between spectral response and the mean mass depth and area (Tyler et al., 1996b). Alternatively Monte Carlo calibration can be applied, providing a detector's response by probabilistically sampling the physical interactions of a large number of computer simulated photons with a modelled geometry (Gering et al., 1998, Likar et al., 2004). However, the influence of factors such as the human operator (Plamboeck et al., 2006), ground curvature and roughness (Boson et al., 2008), detector shape (Boson et al., 2009b) and shielding effects and additional contributions from superterranean features for example trees and grass (Sowa et al., 1989, Gering et al., 2002) can be difficult to account for.

Finally, a technique must be employed to relate the pulse height spectrum of field observations to those derived through calibration. One method, coined the Peak to Valley ratio (Zombori et al., 1992), has been successfully demonstrated to map large areas using both NaI:Tl (Tyler, 1999) and HPGe (Kastlander & Bargholtz, 2005). Nevertheless, the resultant regression routine, employed to link calibration and field observations, requires relatively long counting times to attain acceptable uncertainty in the fairly sparse peak and valley regions. Additionally, the necessity to strip counts out of the two regions in lower energy resolution detectors (typically scintillators) introduces uncertainty (Tyler, 2008).

Perhaps a more statistically robust method in this case is Full Spectral Analysis (Hendriks et al., 2002, Caciolli et al., 2012). This method utilises a weighted least-squares fitting scheme to compare the vast majority of spectral counts obtained in the field to a library collected during calibration procedure (Guastaldi et al., 2013). Nevertheless, in the case of very low count rates (for example obtained by low volume detectors over short count times) fitting may become problematic and produce results that are not physically plausible (Caciolli et al., 2012).

7.2.4 Handheld approach

Ideally, to map a large area providing high spatial resolution depth and activity estimates of ^{137}Cs, it is necessary to maximise the spatial density of measurement points (Bivand et al., 2013). Moreover, it is desirable to increase the detector's sensitivity to deeper sources by reducing its FOV (Schaub et al., 2010). To address these issues without making significant changes to the measurement routine a large number of short measurements can be taken close to the ground rather than fewer longer counts at an increased height (i.e. *in situ* method). For this to be pragmatically accomplished, a detection system needs to be lightweight, mobile and robust in order to be operated in rugged environments such as saltmarshes.

Handheld Gamma-ray Spectrometers (HGS) notably scintillators, for example 71 x 71 mm NaI:Tl and Lanthanum Bromide (LaBr:Ce) detectors, adequately satisfy these requirements (Figure 7-2). NaI:Tl detectors have been the mainstay of environmental gamma-ray spectroscopy from its advent given that they are particularly robust (Beck et al., 1972, Davies et al., 2007). However, NaI:Tl possesses reasonably low resolution (~7% at 662 keV). A promising alternative is LaBr:Ce with a better energy resolution (~2.5% at 662 keV) and higher energy efficiency (Guss et al., 2010). This comes at a cost with LaBr:Ce suffering from a large number of intrinsic background counts distributed throughout the spectrum owed to internal isotopes (^{138}La and ^{227}Ac) (Iltis et al., 2006). It was discovered that for real-time detection of ^{226}Ra hot particles intrinsic activity limits its application compared to NaI:Tl (Varley et al., 2015a). Conversely for mapping ^{226}Ra, thus allowing for the deployment of post processing noise suppression techniques on large LaBr:Ce spectral datasets it was found the statistical influence of intrinsic counts could be negated ultimately making it a more appealing detector choice (Varley et al., 2016b). A comparison has not yet been performed for mapping extended distributions of ^{137}Cs.

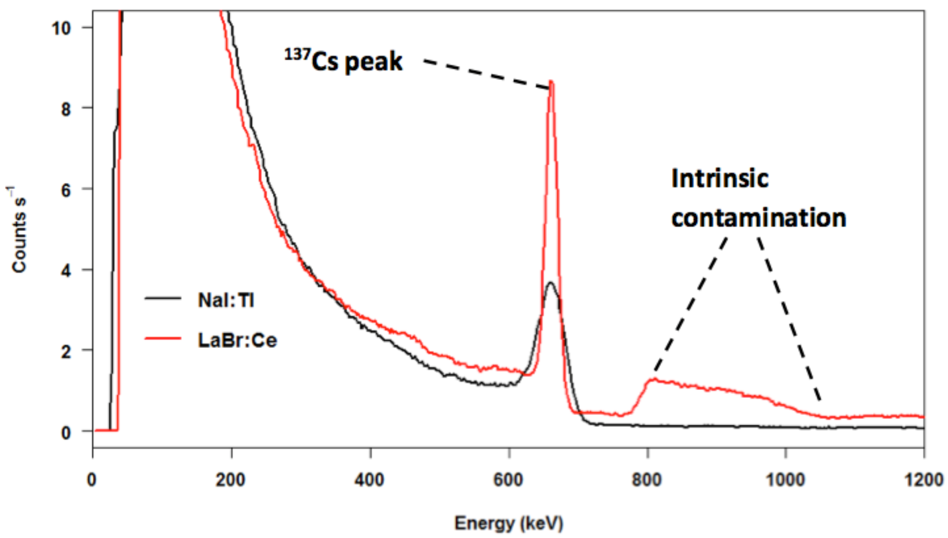

Figure 7-2. Spectra taken using Sodium Iodide and Lanthanum Bromide detectors exposed to a ^{137}Cs source. A section of intrinsic contamination is highlighted.

Regardless of the detector used in HGS, the combination of low detector efficiency (since they ought to be lightweight) and the short counting times enforced by the requirement to cover large areas in high spatial resolution tend to leave individual spectra with large counting uncertainties (Du et al., 2010). In this scenario conventional spectral processing techniques can be difficult to implement (Fagan et al., 2012).

7.2.5 Principal Component Analysis

Instead this study explores using Principle Component Analysis (PCA) to transform and extract key source information from a spectral dataset whilst alleviating nuisance background changes and counting noise (Runkle, 2006). PCA has been implemented on gamma-ray spectroscopy data before, but generally acquired by large volume detectors such as those employed on aircraft (Hovgaard & Grasty, 1997) and radiation portal monitors (Runkle, 2006). PCA performs an orthogonal transformation in an attempt to reduce cross-talk between spectral channels and produce a more useful set of uncorrelated signals. Mathematically, this is undertaken by singular value decomposition of the, mean-centred, correlation matrix (Hotelling, 1933). This produces a matrix of Principal Components (PCs) or uncorrelated signals that are placed in ascending order of variance contributed to the total dataset. Accompanying PCs, is a separate matrix of loadings, which indicate the relative intensities for each PC taken by an individual spectrum. Thus it is within the loadings changes in source characteristics can be inferred (Runkle, 2006).

Generally the first few PCs and their respective loadings (typically 1-5) can be considered as representative of the source signal and can be set aside for further statistical analysis (Im et al., 2007). A convenient outcome of PCA is that the number of dimensions is significantly reduced as lower order elements are generally discounted as correlated noise contributions.

7.2.6 Neural Networks

Patterns within calibration loadings can then be learned using innovative Machine Learning regression methods and related to field observations to predict activity and depth of ^{137}Cs (Wei et al., 2010, Varley et al., 2015b). Neural Networks (NN) were preferred by this study due to my previous experience and the fact they can proficiently capture multiple response variables within the same model.

NN are data-driven algorithms that have been applied to gamma-ray spectroscopy data previously (Pilato et al., 1999, Yoshida et al., 2002, Kangas et al., 2008, Wei et al., 2011). The topology of an NN can be compared to the structure of a brain in that it is made of separate processes units or nodes that are connected by synaptic weights (Yoshida et al., 2002). The first layer, referred to as input layer receives input signal, this signal is then passed onto the hidden layer where a non-linear transformation is performed to map transformed explanatory variables onto the output nodes or response variable(s) (Olmos et al., 1992). This provides the NN the ability to define highly complex problems since it learns patterns from the data itself rather than the user having to define complex mathematically relationships between explanatory and response variables.

Robust training algorithms such as resilient backpropagation are used to update weights between neurons after each learning epoch, in an attempt to achieve global convergence through the minimisation of the Relative Mean Square Error (RMSE) between a training and test set (Riedmiller & Braun, 1993). Importantly the architecture of a NN and the number of learning epochs often reflect the complexity of the problem it is attempting to solve (Dragović et al., 2006). Therefore, a concentrated effort is needed to acquire a suitable architecture.

7.3 Methods

7.3.1 Field site

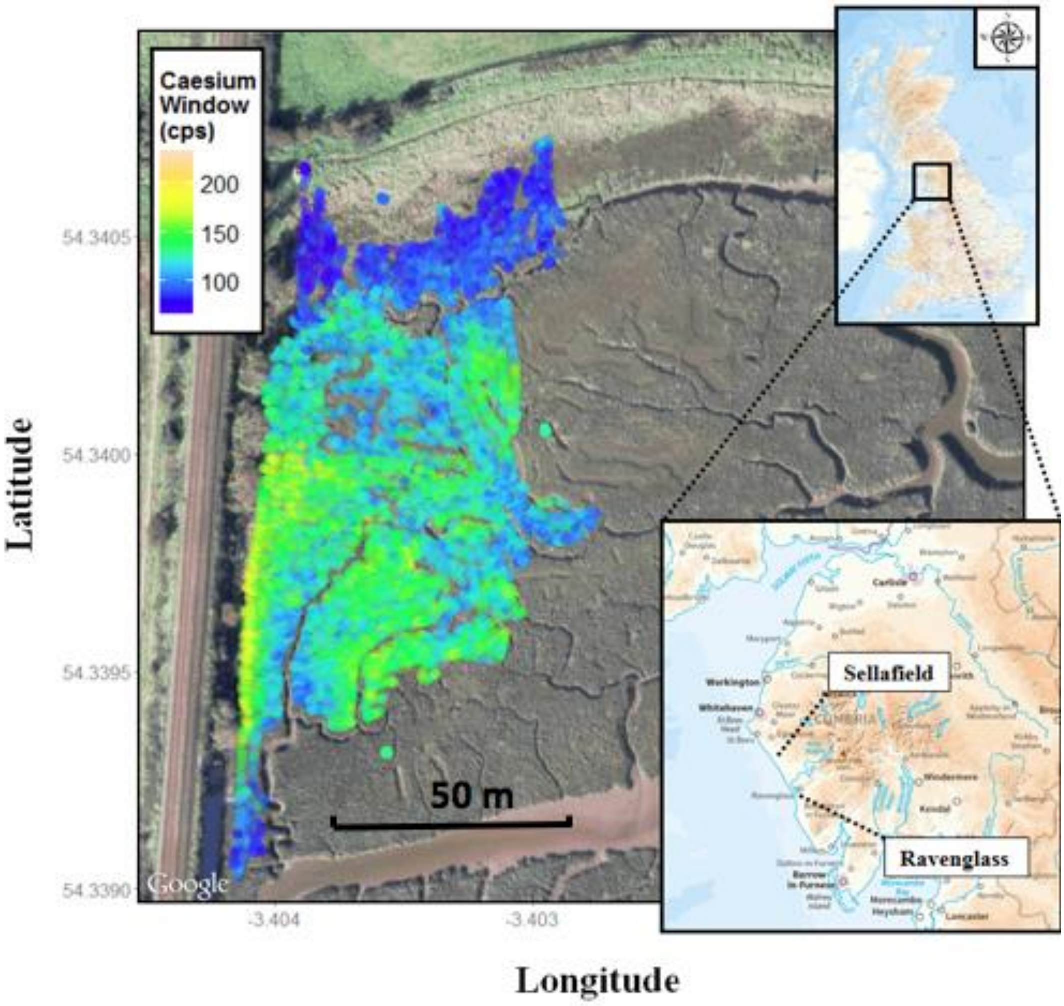

Figure 7-3. ^{137}Cs window counts obtained over 1 second count time using a 71 x 71 mm LaBr:Ce detector at Ravenglass saltmarsh.

Ravenglass estuary is located approximately 16 km to the south of Sellafield in the mouth of the Esk estuary in Cumbria, UK (Figure 7-3). On its north bank (-3.403 ºE, 54.34 ºN) exists perhaps one the most contaminated (Sellafield-derived) and resultantly well-characterised sections of saltmarsh in the UK (Horrill, 1983, Morris et al., 2000, Oh et al., 2009). The distribution of ^{137}Cs activity has been documented to exhibit significant spatial variation and this can be crudely acknowledged by observing Cs window taken using a LaBr:Ce detector, although this provides no real clarification of depth and activity.

7.3.2 Field data acquisition

Two 71 x 71 mm detectors (NaI:Tl and LaBr:Ce) were mounted to a wheeled system at 0.1 m height and one behind the other to ensure that similar radiation fields were being considered by each detection system. A walking speed of 0.5 m s^{-1} was maintained and a measurement was taken by each detector every 1 s using Ortec's Maestro software. A GPS coordinate was recorded for each spectrum by a differential GPS unit the Stirling University Mobile Gamma Spectrometry System (SMoGSS. For the most part, a 0.5 m transect spacing was maintained, but inevitable deviations around eroded creeks were unavoidable (Figure 7-3). Approximately 10,000 spectra were collected by each detector.

In addition, a number of soil cores, down to a depth of 0.5 m, were collected using a golf-hole corer (diameter of 100 mm) and sectioned into 50 mm increments at the site and then counted on laboratory HPGe detectors. At the time of coring, moisture content tended to be greater on the surface (60%) compared to increasing depths (35%) and the mean wet density was 2 g cm^{-3}.

7.3.3 Monte Carlo simulations

To successfully include enough spectral shapes, brought about by the burial of ^{137}Cs within the saltmarsh sediments, Monte Carlo Simulations (MCS) were carried out. MCS were undertaken using Monte Carlo N-Particle 5 (MCNP5) software (Briesmeister, 1993). Coded detector geometries for both detectors were first validated against those derived from calibration pads (Varley et al., 2015a). All relevant (> 1% abundance) gamma-ray energies were sourced from the National Nuclear Data centre (2013) and secular equilibrium was assumed. For simplicity in all simulations a density of 2 g cm^{-3} and water content of 60% on the surface and linearly decreasing to 35% at 0.55 m was assumed.

Contrasting to my previous work (Varley et al. 2016b) by which representative background were collected from an uncontaminated analogue site, no site was deemed to be suitable nearby for this study given the widespread nature of contamination within the estuary. Subsequently, background spectra containing the naturals (^{40}K and the ^{238}U and ^{232}Th series) were also generated using MCS.

For MCS to be both accurate and feasible, the detectors FOV to a homogeneous source should be ascertained for individual radionuclides to avoid the geometry being under or over sampled. This can be achieved using adjoint calculations (Maučec et al., 2004, De Groot et al., 2009). This involves photons being essentially reversed within the coded geometry, starting from the detector at an energy of zero and eventually being terminated in the soil column once a maximum energy is reached (for example for ^{137}Cs the termination energy would be 662 keV). This produces fundamentally a 3-dimensional photon density map. The geometric limits required to produce a full spectral response are typically considered to extend to 99.3% of the overall intensity (Maučec et al., 2004). It can be shown for homogenous distributions, with a detector placed at 0.1 m above the soil column, a maximum offset of 10 m is required to fully incorporate a spectral response (Figure 7-4). Observe higher energy emitting radionuclides, for example the ^{232}Th (2614 keV) and ^{238}U (2447 keV) series, the FOV was deeper and less extended laterally compared to lower energies (i.e. ^{40}K and ^{137}Cs).

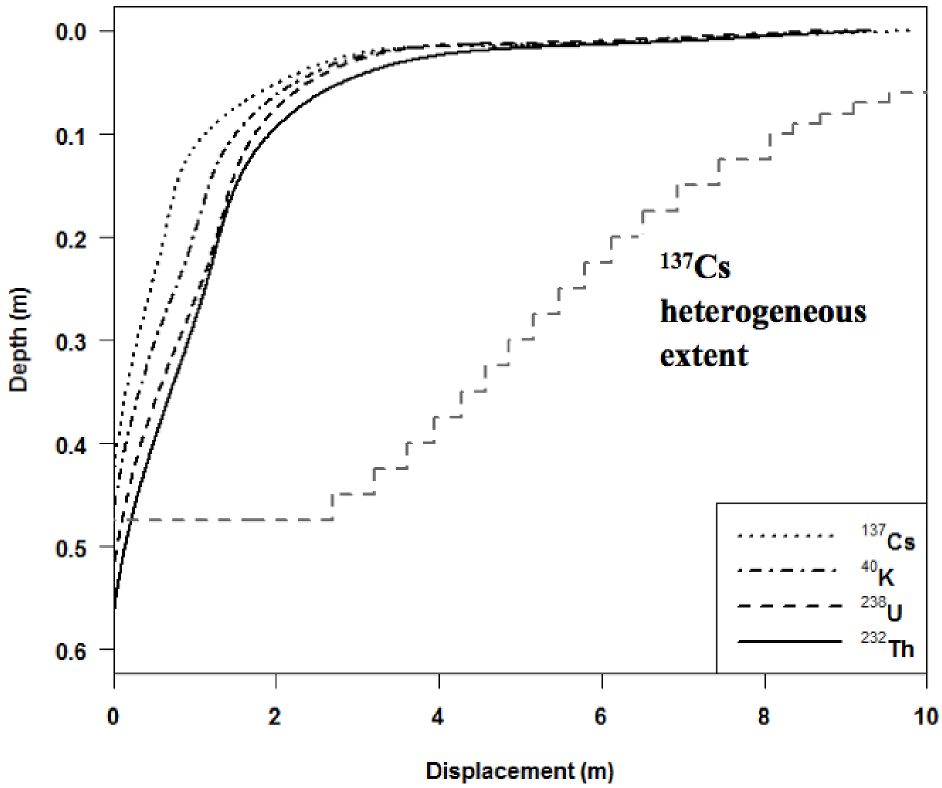

Figure 7-4. Field of view for homogenous ^{137}Cs, ^{40}K, ^{238}U and ^{232}Th distributions and ^{137}Cs heterogeneous depth profile.

Given that ^{137}Cs was known not to be homogenously distributed in z plane since it was likely to be formed in layers (Figure 7-1), the FOV was determined for each individual depth layer simulated in MCNP5. This made the extent limits much wider for layered ^{137}Cs (Figure 4). Non-conformities were found between *in situ* spectra obtained over core sites (300 s count time) and ones predicted by MCS. This was attributed to the slight curve of the saltmarsh and vegetation cover (Sowa et al., 1989, Boson et al., 2008). It was concluded by reducing the extent of top few sections (>3 cm) to approximately 6 meters, rather than the theoretical 15 m, non-conformities could be resolved (Figure 7-4). For all MCS, geometries were cut on the z plane into

0.05 m sections and the maximum number of starting particles in MCNP (2×10^9) was run for individual sections. This was done in attempt to minimise tally uncertainty. As layers above 0.1 m (vertical depth) grew increasingly larger in volume, to ensure sampling efficiency of tallies was not too low, layers were cut into 0.01 m vertical sections (Figure 7-4).

Good agreement between field spectra derived from long *in situ* counts (300 s) and core profiles coded into the model derived from MCS were observed for the majority of cores. Energies below 250 keV were considered too complex to model, owing to the dominance of the photoelectric effect, which is heavily influenced by chemical composition (Tyler, 2008), and the complex nature of backscattered photons (Caciolli et al., 2012). Resultantly analysis was only performed on energies above 250 keV. Figure 5 illustrates the agreement between a modelled spectrum (black line) and one derived above core K5 (red circles). Interestingly, 300 s spectra were fitted using a non-negative least squared fitting procedure (Guastaldi et al., 2013), but the same method applied to the 1 s count spectrum (blue points and lines) produced erroneous results. This demonstrates the methods limitation to very noisy spectra.

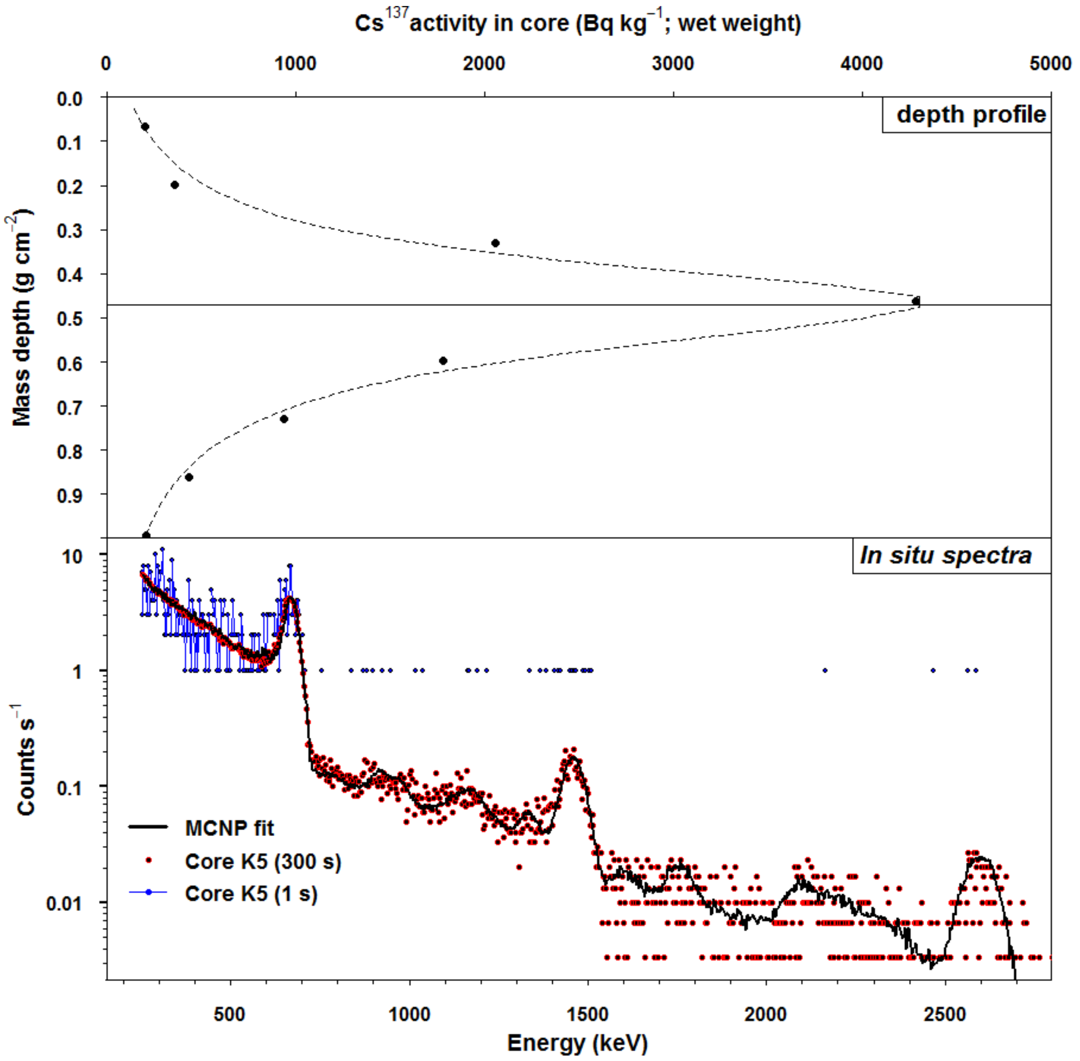

Figure 7-5. K5 core profile alongside Monte Carlo simulated spectrum and *in situ* spectra taken using a 71 × 71 mm Sodium Iodide detector above the ground where K5 was taken.

7.3.4 Spectral model development

Originally straightforward Cauchy and Gaussian distributions were experimented with, yet contributions from the deeper tail, formed from a non-symmetrical discharge history (Gray et al., 1995), produced a significant scattering component (Figure 7-1). Therefore, a modified Cauchy distribution, in which the deeper tail was broader and forced to lower activities (~10 Bq kg^{-1}) was used to model the depth profile (Figure

7-5). It was also appreciated that cores with low sedimentation rates particularly towards the back of the saltmarsh would have a more compact profile. This was accounted for by narrowing the Cauchy distribution for profiles with subsurface-maxima closer to the surface. From this point, the model was somewhat simplified by only changing the surface activity (Bq kg^{-1}), and the mean mass depth (g cm^{-2}) and activity of the subsurface peak (Bq kg^{-1}) as thought to be the driving factors behind spectral change. Random sampling of these parameters was used to embody the spectral population with the knowledge the distribution could be ultimately transformed into inventory or Bq m^{-2} (Tyler, 1999). Sampling took place between realistic environmental ranges: surface activity (30-5000 Bq kg^{-1}), mean mass depth (3.5 - 60 g cm^{-2}) and activity of the subsurface peak (500 – 20000 Bq kg^{-1}).

Relative spectral contributions from each of the natural decay series (^{40}K and the ^{238}U and ^{232}Th series) were found to be reasonable well correlated from the core data collected at the marsh demonstrated by Pearson's linear correlation coefficients above 0.55. However, estimating the background spectral population from the small sample of cores (n=12) would be naive. Therefore, the deviation in the background spectral population was accounted for within the model using wet weight ranges for ^{40}K (100-1000 Bq/kg), ^{238}U (0.5-40 Bq/kg) and ^{232}Th (0.5-40 Bq/kg). Lognormal distributions were used to shape the variation in background population. A mean bias was stated so that lower concentrations would be dominant: a scenario often found in the environment (Caciolli et al., 2012). Additionally small activities of ^{60}Co (0.2 – 5 Bq/kg) were introduced into to final models (Figure 7-5). Using such a conservative could possibly introduce a large amount uncertainty in final results as ^{137}Cs could potentially be masked, particularly for lower concentrations.

Three datasets (a training set, test set and cross validation set) were produced in order to robustly fit a Neural Network (Dragović et al., 2006). The training dataset, composed of model spectra with low statistical uncertainty were is used to fit the NN. The test set, which was 30% of the training set, was devoted to tracking whether the model was over or under fitted. The training and test sets were MCNP results, in which tallies had been recorded to high level of statistical accuracy (i.e. 2×10^9 particles run in each section). The cross-validation dataset was used to test the regression capabilities of the final model to spectra, as similar as possible, to those collected out in the field. To recreate this noisy dataset, spectral drift and Poisson noise was added to individual spectra (Varley et al., 2015b).

7.3.5 Pre-processing

To alleviate some counting noise prior to PCA, particularly for higher energy background areas, a spectral binning regime implemented in my previous work was used (Varley et al., 2015a). Early investigations demonstrated 5 bins below the full energy peak to accurately captured relevant changes in spectral shape (above 250keV). One bin was dedicated to the forward scattering region (Zombori et al., 1992). This left 1 bin covering the full energy peak and 6 bins above the full energy peak tracking changes in the natural radioelements.

PCA was performed on all the data combined (i.e. field spectra, training, test and cross validation) to ensure comparability. All bins were normalised according to Mauring and Smethhurst (2005) prior to singular value decomposition. The response variables were normalised between 0 and 1.

7.3.6 Neural Networks optimisation

A single Multi-Layered Perceptron from the R package "RSNNS" was used in this study (Bergmeir & Benítez, 2012a). Each NN was trained, tested and cross-validated using normalised PC loadings and response variables. The transformation used in the hidden layer was a sigmoidal function and the algorithm used to train the network was resilient backpropogation (Riedmiller & Braun, 1993).

In an attempt to optimise the number of hidden neurons, number of input PCs and learning epochs for each NN a grid search was performed whereby the final performance was based upon the Root Mean Square Error (RMSE) for the predictor variables on the cross-validation dataset (Hornik et al., 2006). 4000 training data were found to adequately train each network, leaving 30% to test the network. 2000 independent cross-validation samples were used to establish RMSE. Each NN architecture was fitted 10 times (reinitialising random numbers between runs) to provide a mean and standard error on final field predicts.

7.4 Results and discussion

7.4.1 Neural Network performance

Using more than one layer of hidden neurons was found not to enhance performance of NN; hence all NNs contained one hidden layer. The NNs used on LaBr:Ce and NaI:Tl data required 6 and 9 PC loadings, respectively, to provide the lowest RMSE on the cross validation datasets. Perhaps LaBr:Ce spectral data presented a clearer signal for the NN to interpret, therefore the number of PCs required to successfully map the relationship was relatively less.

Table 7-1. Root mean square error for Surface activity, Peak activity and Peak depth for lanthanum bromide and sodium iodide detectors.

	Root Mean Square Error		
Detector	Surface activity (Bq kg^{-1})	Peak activity (Bq kg^{-1})	Peak Depth (g cm^{-2})
NaI:Tl	0.1397	0.9422	0.1720
LaBr:Ce	0.1231	0.9543	0.1849

It was found using 15 and 18 neurons, for NaI:Tl and LaBr:Ce respectively, in the hidden layer gave optimal performance. A comparatively small number of learning epochs were required to fit NNs, 200 and 150 respectively. This general outcome suggests that spectral patterns in the dataset were reasonably straightforward owing to the limited number of hidden neurons, compared to input neurons, required to accurately map inputs to outputs. However, the presence of noise in the dataset quickly resulted in the over-fitting of NNs as demonstrated by the relatively small number of learning epochs. A similar finding was concluded in my previous work (Varley et al. 2015, submitted)

RMSE values indicate that for purposes of characterising subsurface ^{137}Cs contamination detectors produced a similar performance (Table 7-1). For instance, LaBr:Ce (0.1231) marginally outperforms NaI:Tl (0.1397) with respect to identifying surface activities. Conversely, the depth of the peak can more reliably estimated using NaI:Tl (0.1720) compared to LaBr:Ce (0.1849). Similar performance was encountered for characterising the activity of the maximum of the peak (LaBr:Ce = 0.9543; NaI:Tl = 0.9543).

Results can be explained by focussing on individual detector properties. LaBr:Ce, for example, has a better energy resolution and efficiency, consequently counts in the full energy peak may present a stronger signal for the NN to identify (Figure 7-2). This is a scenario presented by surface contamination where there will be large number of non-scattered photons reaching the detector. In contrast, as contamination is buried, a much greater proportion of photons are scattered to lower energies. Perhaps in these much broader energy regions, the increased energy resolution of LaBr:Ce becomes less important compared to the noise posed by intrinsic counts within this area. This influencing factor is especially relevant with increasing burial depth of source as the ratio of scattered to non-scattered photons becomes much more sensitive to changes in depth. Therefore, intrinsic counts at lower energies could limit the NN's ability to identify changes.

7.4.2 Core and time-series analysis

NN results for NaI:Tl and LaBr:Ce taken at the same coordinates suggest that real change in activity distribution could be observed through the method at the saltmarsh (Figure 7-6). However, using single measurements to demonstrate this is difficult; hence a loess smoothing function has been applied (R Development Core Team, 2012). For the most part, smoothed data for individual detectors adhered to each other through the time series. Interestingly, for surface activity results it would appear that slightly more detail is captured by LaBr:Ce, implied by more episodic variation in the time series. This outcome is supported by the slightly lower RMSE value for surface activity for LaBr:Ce (Table 7-1). Another notable feature, given that it partially refutes RMSE results produced on the cross validation dataset, is the increased uncertainty (suggested by the wider prediction intervals) for peak activity estimates made by LaBr:Ce compared to NaI:Tl (Figure 7-6). Interestingly, this can also be seen in the core predictions discussed later (Figure 7-7).

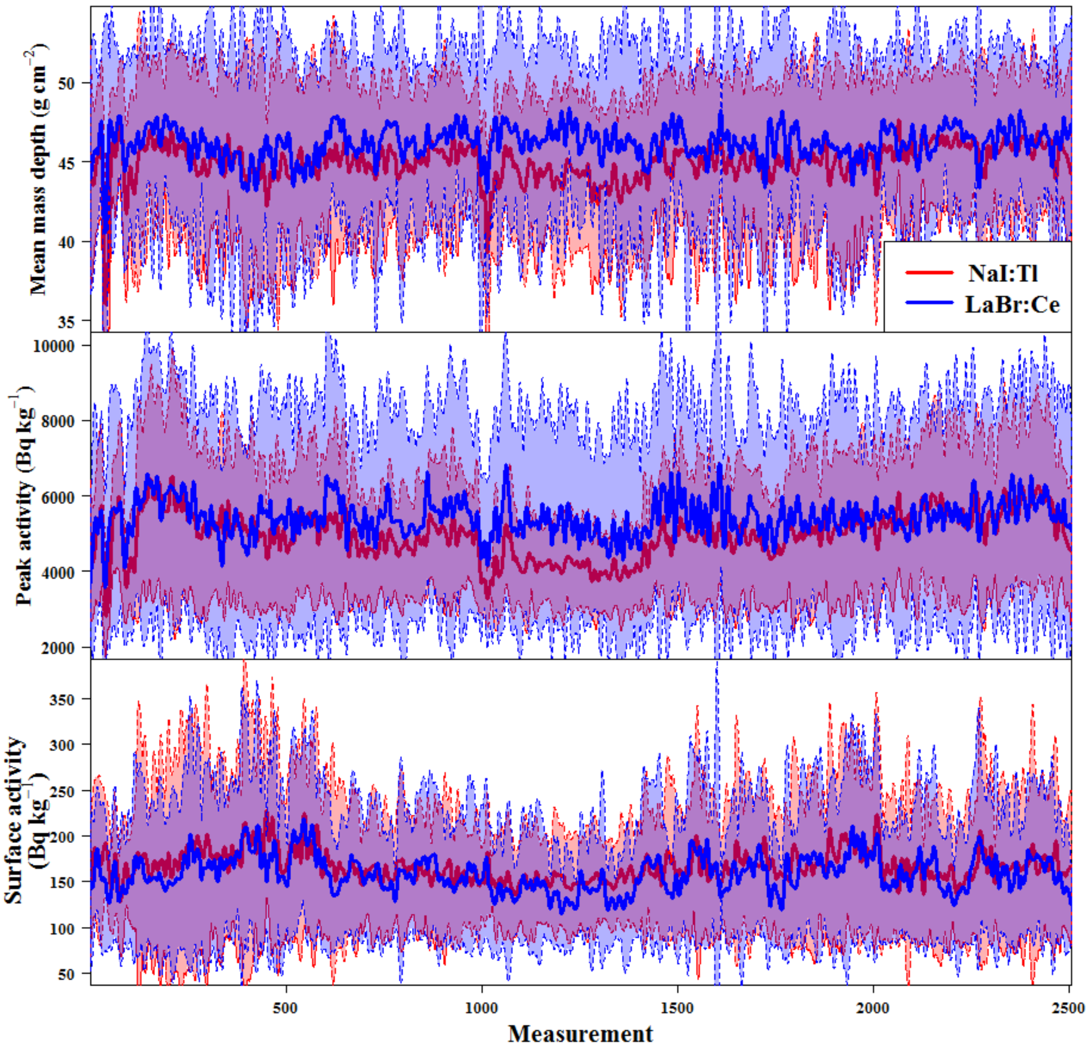

Figure 7-6. Depth, peak activity and surface activity neural network predictions for identical coordinates taken by 71 × 71 mm sodium iodide (red) and lanthanum bromide (blue). Smoothed data are represented by thick lines and 95 prediction intervals by dashed thin lines and shaded regions.

The manner in which data has been prepared in Figure 7-6, for instance a loess smoothing function with 95 prediction interval, was a reflection of the noise presented at a single measurement level. For instance, correlation coefficients (surface activity

= 0.07; peak activity = 0.07; depth = 0.04) between comparable readings taken by the two detectors were very low. There are two possible explanations for this outcome. Firstly, no significant change, particularly in depth, was taking place across the site and thus noise was the dominant source of variation.

However, through analysis of core results it can be seen that this is probably not the case as some of the cores were recorded to have mean mass depth over 50 g cm^{-2}, which was considerably deeper than any estimated depth by either NN. An example is found in core C5 (71 g cm^{-2}), which was close to the front of the marsh, this would in turn theoretically invalidate peak activity estimates (Figure 7-7). Hence, a more plausible justification could be due to a significant proportion of the contamination being below the detection limits of the method, especially with the relatively high surface contamination activities that may have drowned out signal originating from greater depths. Preliminary investigations into the predictions made on the cross validation dataset suggest that data, within the environmental range found at Ravenglass can only reliably predict down to a depth 30 g cm^{-2} before significant uncertainty is encountered. In this scenario the NN would attempt to fit individual spectra with the little signal it had, potentially leading to the data being skewed. This is understandable given the infinitesimal small spectral changes that occur in the feature space at this burial depth.

This presents a challenging physical boundary that would be exceptionally difficult to overcome. A practical means to negate this occurrence, and avoid erroneous data beyond detection limits, would be to define a classification network prior to a regression step. This could act as a filter to screen potentially homogeneous signals, or similarly, contamination too deep to reliably detect. A similar approach was taken in my previous work (Varley et al., 2015b).

Ultimately, to lower detection limits, longer count times would have to be used, or a more sensitive detector, such as conventional HPGe (Tyler et al., 1996a). Alternatively, spectra could be summed over square metres to minimise counting uncertainty, although this would lower spatial resolution. It is worth mentioning that this study is part of a larger field campaign, utilising longer measurements and cores, to characterise the inventory at the site.

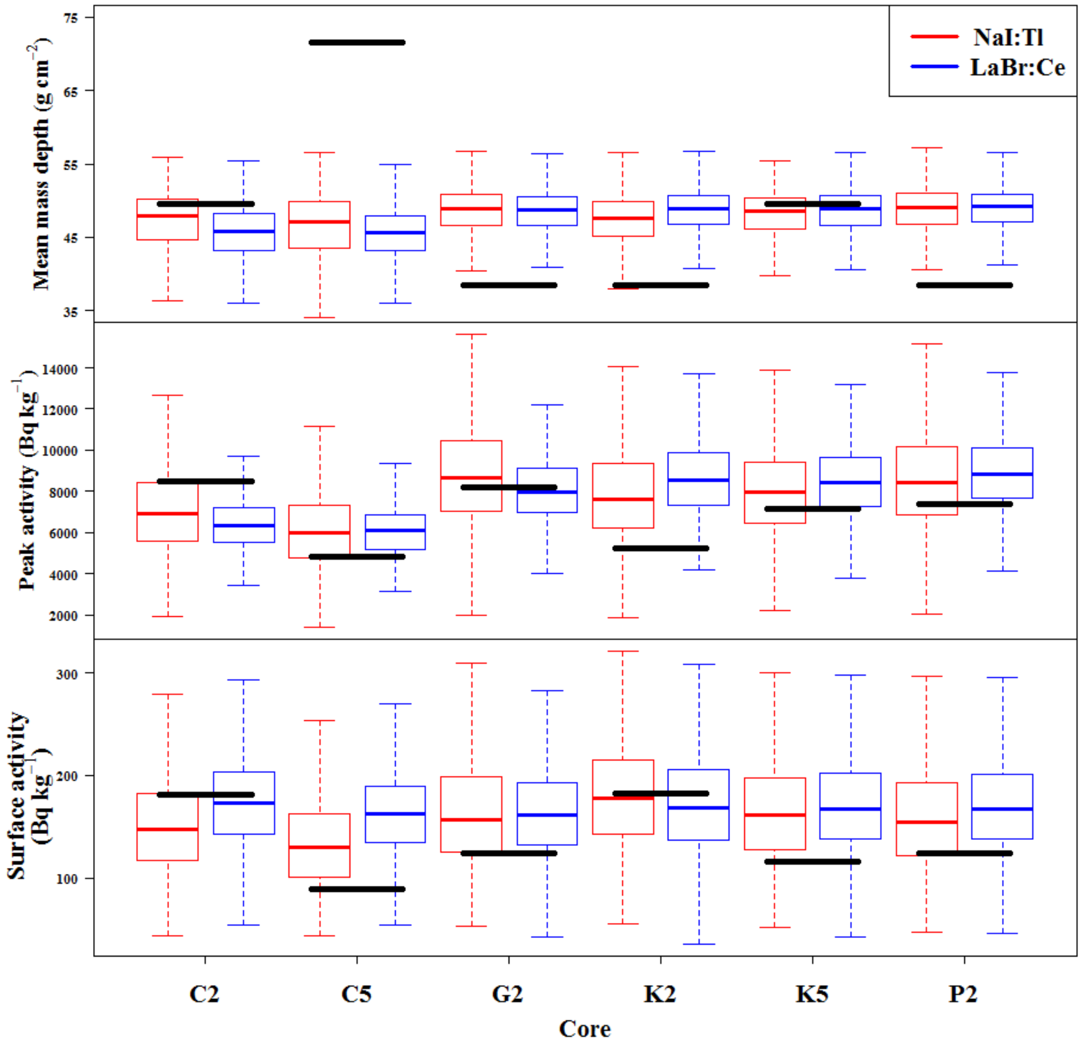

Figure 7-7. NN depth, peak and surface activity estimates of 1 second spectra taken over cores alongside core values measured in the laboratory (black bars).

Overlooking the uncertainties associated with estimating the depth of contamination at this site, predictions made by the network regarding activity were still within an acceptable range of the core results (Figure 7-7). Furthermore, acceptable estimates were acquired despite the large initial activity ranges used to build the training and cross validation datasets: surface activity (30-5000 Bq kg^{-1}) and subsurface peak (500

– 20000 Bq kg^{-1}). This reveals that although single measurements are noisy, large scale estimates could be spatially smoothed to reveal interesting radiological features such as hotspots or surface depth changes.

Although both detectors technically demonstrated similar performance through RMSE, NaI:Tl was able to predict the core results with slightly more precision (Figure 7-7). Subsequently, NaI:Tl results have been used to map the inventory and mean mass depth of the site (Figure 7-8). It must be noted that the R package “automap” was employed to fit a spherical semivariogram model to the spatial correlation of the NN estimates permitting interpolation via kriging (Pebesma et al., 2013). To smooth data a relatively large number of neighbouring points (n=50) were utilised.

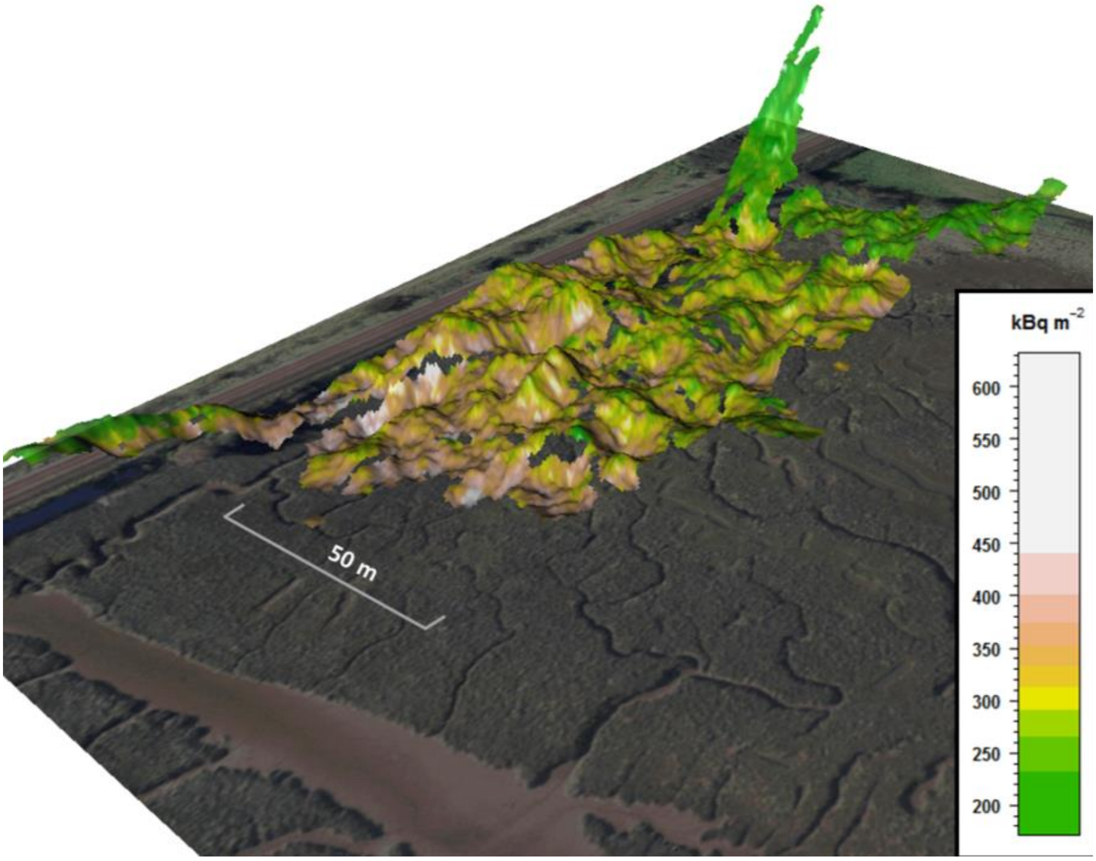

Figure 7-8. Spatially interpolated ^{137}Cs inventory and relative mean mass depth (vertical axis) for Sodium Iodide Neural Network results.

7.4.3 Site analysis

Ravenglass saltmarsh has for some time been considered a source of contamination rather than a sink for contaminants being remobilised from the Irish Sea (Morris et al., 2000). Interpretation of mapped NN estimates would appear to provide evidence in support of this theory (Figure 7-8). Discernible features, such as the ridge following the course of the creek, in the middle of the marsh, capture this erosion process. Notice the mean mass depth is shallower at the edge of the creek edge compared to surrounding areas since the top layers may have been removed by erosion processes. Suggestions of this development could also be evident in the episodic nature of LaBr:Ce surface contamination estimates (Figure 7-6). Additionally, higher activities are estimated to be in more stable areas away from creeks in the middle of the saltmarsh. Plausibly in these areas less erosion has taken place.

Regrettably, the front of the marsh was not surveyed due to the incoming tide and time restraints. However, measurements over the top of core C5 were taken within this area. Notice C5 had the lowest total activities out of all the cores (peak activity = 5010 Bq kg^{-1}, surface activity = 85 Bq kg^{-1}). Although the mean mass depth would likely have been too high to be confidently identified, it would have been interesting to see whether the technique could identify lower activities on the surface. Nonetheless, lower activity shallow areas at the back of the saltmarsh and in a small area surveyed at the front of saltmarsh indicate regions that have rarely been inundated (Figure 7-8). These areas can also be identified as the sharp inverted peaks in mean mass depth and peak activity within the time series data (Figure 7-6).

7.5 Conclusions

From this relatively small survey, Ravenglass saltmarsh would appear to deviate from the simple hydrological model assuming the highest activities, at the least burial depth, are found at the back of the marsh. Instead, the site exhibits a complex activity distribution of ^{137}Cs, probably as a result of a number of years of erosion events, which conventional techniques such as soil coring or long *in situ* measurements, may struggle to identify in high resolution. This exemplifies the merit of the described approach. Nonetheless, uncertainty regarding the reliability of depth estimates still remains as the mean mass depth of much of the saltmarsh did not appear to change significantly, which did not allow rigorous environmental assessment. Moreover, much deeper sections that did deviate were concluded to be below the limit of detection of this approach. To robustly test the approach, another site with lower sedimentation rates would have to be assessed or fresh fallout would have to be utilised. Identifying a relevant site will be the aim of future work.

With that said, the approach could be used to support existing approaches and in environments with fresh fallout or close to surface activity, such as emergency response scenarios. Another application that will be the subject of further work, and utilising larger detection volumes, is the identification of soil disturbance that has taken place at archaeological sites.

8 General summary and further suggestions

8.1 Outline

This final chapter of the thesis attempts to place the research into the context of the wider field of environmental gamma-ray spectroscopy. To achieve this, implications of the general research findings are summarised, alongside suggestions for further work.

8.2 The context of environmental gamma-ray spectroscopy research

It has become widely accepted that environmental gamma-ray spectroscopy offers a rapid means to estimate source characteristics compared to traditional sampling methodologies combined with laboratory-based analysis (Tyler, 2008). This realisation has only been made possible through pioneering research developments in: instrument calibrations (Grasty et al., 1991, Allyson & Sanderson, 1998, Maučec et al., 2004); computational processing (Guillot, 2001); noise reduction techniques (Hovgaard, 1997, Dickson, 2004); spectral fitting regimes (Hendriks et al., 2001, Caciolli et al., 2012) and understanding into the relationship between source geometry and spectral response (Beck et al., 1964, Beck et al., 1972, Helfer & Miller, 1988, Zombori et al., 1992, Tyler et al., 1996b).

Subsequently, through years of development of the method, considerable improvements have been made in the spatial representativeness and reliability of source estimates, which has enabled it to become increasingly useful to a growing number of radiological applications. In the case of this thesis, it has become the mainstay of the applications featured, such as routine monitoring for *hot particles* and contaminant characterisation using borehole measurements and terrestrial handheld instruments.

However, as with many established detection methodologies, reliance on conventional detection setups, particularly over the past decade or so in the case of environmental gamma-ray spectroscopy, has left the field lacking in significant developments. This lack of progress is perhaps in part due to an over-reliance on existing detector technology and reluctance to move away from the usage of well understood physically founded models to interpret spectral data. This potentially means large amounts of data collected during a survey are either not being collected using the most suitable instrument for that application or large amounts of useful information is not being utilised.

Therefore, this thesis has attempted to address these fundamental issues by adopting a two-pronged approach. Firstly, time was invested into researching novel detector technology, in which a lanthanum bromide detector was purchased then deployed in the field as handheld detector. This was performed alongside an equivalent sodium iodide detector to allow for direct comparisons in the field to be made. Secondly, it identified and utilised Machine Learning algorithms to intelligently process spectral output to estimate source characteristics. Such algorithms have rarely been implemented in environmental gamma-ray spectroscopy. To draw attention to potential advances this work has contributed to the field, a brief summary of the thesis, discussing the merits of individual work and overall implications of the work, will now be given.

8.3 Thesis summary

The first research manuscript (chapter 4) aimed to develop a method to characterise ^{226}Ra contamination at depth using borehole measurements with particular interest in identifying significantly radioactive *hot particles* (Figure 8-1B). This work took place at the headland at Dalgety Bay, Fife, Scotland.

As a consequence of the irregular disposal patterns used at the site, characterising contamination presented a significant challenge, as intrusive investigations had demonstrated much of the contamination was dissipated heterogeneous material to such a level much of it could be considered homogenous. Note the black deposits of ash and clinker containing ^{226}Ra (Figure 8-1A). Consequently, interpretation of borehole spectra was fundamentally difficult and ultimately required a technique to be developed to separate out detector signals that could be considered homogeneous (ash and clinker) from ones that could contain contributions from *hot particles*: thus allowing for a more accurate activity estimation to be made at the site. To the author's knowledge this type of analysis had rarely been performed for any radio-contaminant within a borehole geometry, let alone for a site as potentially complex as a radium contaminated legacy site such as Dalgety Bay.

Figure 8-1. A) Ash and clinker deposits containing ^{226}Ra next to relatively uncontaminated soil B) Example of the detector setup.

Therefore, a method had to be developed that was sensitive enough to cope with both the statistical noise presented within individual spectra together with the noise associated with natural background variation. Deterministic approaches, such as gross counting or the multiple peaks method, were considered not sensitive enough for this type of analysis. Therefore, the study took inspiration from data driven methods, specifically Neural Networks, which were used to analyse general changes in spectral shape to derive source characterisation information.

The overall technique utilised a large number of robustly Monte Carlo simulated target geometries to train numerous Neural Networks with, to first determine whether the field spectra were derived from homogeneous, heterogeneous or simply from background geometries. Then, appropriately estimate the depth, in case of a *hot particle*, or extent for a heterogeneous source and finally an activity for respective geometries.

Although, large uncertainties were associated with final results, notably at lower activities and greater depths, and considerable human interpretation was still needed to qualify final estimates (Figure 4-7), the method demonstrated a significant breakthrough in characterisation of deep ^{226}Ra that previous methods have failed to capture. Foreseeably, this type of technique could be routinely deployed at further radium contaminated legacy sites and potentially for different radionuclides.

Perhaps the most distinguished piece of work in this thesis is present in chapter 5, which describes the optimisation of a detection system for the identification of ^{226}Ra containing *hot particles* for routine monitoring purposes. The manifestation of these radioactive items is of genuine public concern, especially in certain parts of Scotland, such as on the beach at Dalgety Bay, Fife, Scotland, where many particles have been located and removed (Dale et al., 2013).

Nonetheless, difficulties have been documented at the site when trying to reliably locate particles that are concealed by overburden using conventional detector systems. It is thought that the failure to detect smaller *hot particles* close to the surface (~20 kBq), could significantly endanger the public (Wilson et al., 2013).

The study concluded that using conventional systems it was difficult to detect the subtle changes in signal presented by such particles, at an acceptable depth (10 cm), due to the algorithms incapacity to manage large variations in background and statistical noise, which tended to lead to a high false alarm rate. It was concluded that the use of a neural network, coupled to a 71 × 71 mm sodium iodide detector, working on the bases of spectral shape change, could potentially detect particles at twice the depth when compared to the same detector operating a deterministic gross counting alarm.

Therefore, it was confirmed through results that instead of investing large amounts of money in potentially novel detector technology (i.e. lanthanum bromide), reasonably straightforward changes to spectral processing procedures, through the implementation of Machine Learning algorithms, could generate much higher detection rates of ^{226}Ra *hot particles*.

There were a number of novelties to this research. Firstly, this was the first documented field comparison between sodium iodide and lanthanum bromide. Secondly, this is one of the first implementations of Machine Learning to enhance detection rates for handheld gamma spectrometry instruments in an environmental setting (Alamaniotis et al., 2013b, Alamaniotis et al., 2013a).

The most encouraging realisation is that this type of work could realistically provide better safety for those that live in and around radium contaminated legacy sites. At Dalgety Bay for instance, the beach is deemed to be such a hazard it has had to be cordoned off and regularly monitored. This has a knock-on effect to the surrounding community that used the beach routinely in the past, in terms of potential dose, but more importantly psychologically. Flatteringly, the Scottish Sunday Times newspaper reviewed this research in an article entitled “Scots formula could clean up toxic beaches”. This media attention highlights the general public’s concern towards radiological hazards of this nature.

Figure 8-2. A homogeneous hotspot being measured with a 51 × 51 mm sodium iodide detector

Chapter 6 follows on from chapter 5 as it used the same detector setup, but with a new objective: to characterise homogeneous ^{226}Ra contamination at a different site.

This site perhaps posed the most difficult contamination to characterise, since it was a relatively small ex-military tip, where large contamination gradients existed. Notably, this work was carried out alongside the Scottish Environmental Protection Agency (SEPA), who used gross counts from a 51 × 51 mm sodium iodide detector to identify hotspots and possibly *hot particles* (Figure 8-2).

The original aim was to use evenly spaced spectral data (i.e. taken in 0.5 m transects), post survey, to identify the presence of highly active *hot particles*, more than likely at depth, amongst well-dissipated heterogeneous contamination that potentially might have been missed by SEPA gross counting method. However, it became apparent early on in investigations that using a post processing approach to identify anomalous signal, possibly caused by the presence of *hot particles*, introduced a significant challenge. Such a technique would have to involve real-time feedback to the operator to allow for further investigation. This subject will be discussed later in this chapter.

Instead, a different tact was taken, simplifying the objective somewhat, by rather providing a high-resolution map of assumed homogeneous ^{226}Ra contamination estimated as activity per gram (Bq g^{-1}), which could then be compared to legislative limits. Although, this did not satisfy original aims, this type of work, for example including depth as a variable, had not been performed before in the literature for ^{226}Ra using small handheld detectors.

Neural Network results from chapter 6 concluded that much of the contamination associated with the investigated hotspots (identified by gross counting) was more than likely associated with surface contamination, which was backed up by intrusive investigations undertaken by SEPA at the time. Although the gross counting method perhaps failed at identifying the most radioactive parts of the sites, it did identify areas with the highest dose rates that are of immediate threat to the general public. However, as highlighted in this work, to characterise much more radioactive contamination at depth, which could potentially be more harmful in the long term, a more intelligent algorithm is needed such as the Neural Network. This type of research could potentially aid in the remediation and redevelopment of sites, identifying areas of the worst contamination alleviating the potential for dose during construction and inhabitation.

The method used in chapter 6 took on a similar structure to chapter 4, whereby a Neural Network was first used to filter background spectra and then another Neural Network was employed to derive activity and depth estimations. By this stage in the thesis, it becomes clear that the use of multiple models, first classification and finally for regression, potentially provided the most appropriate way of characterising ^{226}Ra contamination. Additionally, this was a very effective way of reducing significant error reported by the Neural Network, particularly for results on the edge or out of its prediction range. Resultantly, this reduced the potential for erroneous results.

Another interesting finding was that Neural Networks trained on raw spectral data produced much more uncertainty on the cross validation dataset when compared to Principal Component Analysis transformed data: hence the reason for results not being reported in chapters 4 and 6. This overall finding suggests that real-time activity and depth estimates, for example estimates that could be displayed on computer screen in real-time, would be significantly nosier than post-processed results. Although not stated, results produced using raw data on average produced approximately twice the uncertainty of post-processed noise reduced results.

Nevertheless, a combination of the two could easily be realised given that conventional surveying methods often take a similar real-time/post-processing route to identify anomalies. The development of a system, which could provide depth and activity estimates in real-time, would have been a desirable outcome from this research, and remains the next research priority. Operated by a human, perhaps the real-time feedback could be invaluable in the search for *hot particles*.

Chapter 7, once again aimed to test the two handheld detectors against one another alongside the implementation of a Machine Learning method. Only this time the objective was to characterise the depth distribution of ^{137}Cs on a saltmarsh; hence estimating an inventory for the assessed area. There are countless works that have focussed their efforts on characterising ^{137}Cs in this type of environment (Brown et al., 1999, Charlesworth et al., 2006). Yet, the vast majority have used soil cores or surface scrapes, which may not efficiently sample the environment, noticeably if there are large spatial deviations occurring in depth and activity. This work attempted to develop a similar method to chapter 6, whereby a large number of 1 second spectra were collected to potentially capture any heterogeneity in high resolution.

From results, it was clear that there was considerable heterogeneity on the saltmarsh that almost certainly would not have been captured using conventional sampling means. Nonetheless, a significant conclusion was drawn that the reliability of mean mass depth estimates was difficult to assess on the saltmarsh for two reasons. Firstly, there did not appear to be significant change in mean mass depth on the area of saltmarsh investigated, which was supported by core evidence. Secondly, in the event of any real mean mass depth change it would likely have been far below the limits of detection of the method (> 30 g cm^{-2}). Similar limits of detection were concluded by Tyler et al. (1999) using a 35 % HPGe detector and 600s count time. In any case, activity estimates were deemed acceptable, but it was further concluded another site would have to be identified to robustly assess the approach.

At present, I am intending on applying the method to data collected from various sites. Firstly, data collected from the Chernobyl exclusion zone, as part of a wider study called the TREE project, which will be backed up using soil cores. Data are also being collected from Poleskie national park in Belarus as part of an international inter-comparison exercise. At these two specific sites count rates will be significantly higher than Ravenglass estuary, possibly providing much clearer shape and therefore more method sensitivity.

Another interesting site, where unusual erosion and deposition patterns could have potentially occurred is that of an area of re-established saltmarsh at Hesketh in the Ribble estuary, Lancashire, England. This site also has core data in support of handheld data, yet, this area might prove even harder to characterise than Ravenglass as lower activities will be encountered although probably at less effective depth.

9 General conclusions and future prospects

9.1 General detector conclusions

This thesis has produced mixed results on whether or not lanthanum bromide could be used as an alternative or even replace sodium iodide environmental detector. From chapter 6, lanthanum bromide clearly outperformed sodium iodide as it was shown that Principal Component Analysis could negate the influence of intrinsic counts, harnessing its better energy resolution and efficiency. This allowed for better mapping of the distribution ^{226}Ra contamination at the site. However, in chapter 5, where real-time detection of ^{226}Ra was involved, and intrinsic counts could not be resolved using post-processing noise suppression techniques, sodium iodide by far outperformed its counterpart using both the deterministic and Machine Learning algorithms. This general result suggests that for short dwell time applications the superior energy resolution and efficiency of lanthanum bromide can only be utilised if the intrinsic can be suppressed. This is particularly the case for the higher energy peaks (i.e. 1120, 1764 and 2204 keV) where significantly more signal can be detected (Appendix I.B), as it is more energy efficient, thus allowing for deeper detection of ^{226}Ra sources as demonstrated in chapter 6.

Another fact that draws this conclusion is that in chapter 7, wherein source signal was produced at energies below 662 keV, despite the implementation of Principal Component Analysis, no real advantage was found. Probably this was again as a result of the intrinsic counts, acting in combination with short dwell time, superseding its general capability to produce stronger signal. In support of this argument relatively less advantage in efficiency is gained at these energies using much longer counts (Appendix I.B).

In summary, taking into account the evidence gained during this thesis, advice would be suggested that if short count times are being employed, the operator should really consider carefully what type of spectral analysis they will be implementing and what are the energies of interest to their study. Importantly these suggestions only consider 71 × 71 mm detectors. For example, if a straightforward deterministic algorithm is to be used, such as the gross counting algorithms or energy windows, then consider sodium iodide or another equivalent detector (i.e. bismuth germanate). If low energies are of importance, regardless of the algorithm implemented, sodium iodide will provide better detection. In the case of post-processing and if higher energies can be utilised, there is an argument for the use of lanthanum bromide. Another consideration is that a 71 × 71 mm lanthanum bromide detector is over an order of magnitude more expensive than an equivalent sodium iodide detector. For all of the above reasons lanthanum bromide will probably not be displacing sodium iodide as the workhorse of surveys operating a large number of short count time measurements.

9.2 General algorithm conclusions

It was concluded early on Neural Networks, pitted against Support Vector Machines and Gaussian Processes (not mentioned, but investigated behind the scenes), produced the most appropriate regression and classification tool to capture variations taking place for the investigated contaminants. The nonlinear fitting capabilities and noise suppression abilities of Neural Networks were in general attributed to producing this final outcome.

Nevertheless, considerations must also be given to the relative development of individual methods, notably with regards to the accessibility of computer packages and their overall user friendliness. For instance, throughout this work I coded everything in the software package R (R Development Core Team, 2012). At the present time, there are a number of different packages available in R that implement Machine Learning methods, to name a few: RSNNS (Bergmeir & Benítez, 2012b), e1071 (Dimitriadou et al., 2008), Kernlab (Karatzoglou et al., 2004), tgp (Gramacy, 2007), RWeka (Hornik et al., 2009) and Neuralnet (Günther & Fritsch, 2010). Therefore, inevitably some bias will be introduced as some packages are more user friendly than others, of note in this research RSNNS (Bergmeir & Benítez, 2012b) and e1071 (Dimitriadou et al., 2008).

Inevitably as algorithms become more accessible to scientists, who do not necessarily have a background into their development, and as general advancements are made into the optimisation of specific algorithms perhaps the less accessible methods might become more common in a wide variety of applied topics, such as environmental gamma-ray spectroscopy.

Furthermore, uncertainty still remains regarding the infamous lack of ability of Neural Networks to predict in an area outside the data used to train it (Haley & Soloway, 1992, Dragović et al., 2006). In this study, it must be appreciated that relatively well controlled data was used to train and cross-validate data i.e. Monte Carlo simulations alongside collected background. However, exactly how representative of the potential range of real environmental spectral data these datasets were is not exactly known. One example is some contamination would have invariably been evident in some of the acquired background spectral dataset, particularly for ^{226}Ra, as it is part of the natural decay series and is very challenging to separate.

Therefore, to robustly assess the reliability of algorithms, thorough testing would have to be undertaken. This could involve a robust field trial with a number of known buried sources to demonstrate its practical limit of detection. After which, the algorithm could be implemented at a site, either instead of, or alongside a conventional algorithm, to statistically identify whether any real change in detection rate was occurring (Tyler et al., 2010).

9.1 Future prospects of environmental gamma-ray

We are currently in an encouraging time of development. Firstly, advancements are constantly being made in detection technology, for example the refinement of Ce^{3+}, Pr^{3+} and Eu^{2+} as doping agents into a range of host inorganic crystals (Nikl & Yoshikawa, 2015). Potentially this could deliver the next generation of faster, lightweight, higher energy resolution and efficiency detectors. The promise of further crystal growth developments regarding cerium bromide (a detector that was initially considered by this study, but was deemed too small) could also provide better detection technology that could displace sodium iodide.

There are also large possibilities in the area of spectral processing. This could potentially be driven by "big data" algorithms that could be used to trawl large data libraries; whereby many establishments begin to share spectral data instead of producing independent models. Even at a site level, routine monitoring produces enormous amounts of potentially useful data that could be harnessed to improve models, for example temperature data and GPS coordinates could be built into models providing them with far greater prediction powers. Also, there is the distinct possibility of data integration with other data derived from remote sensing, geological maps or ground penetrating radar. Integration on such a level would almost certainly require something similar to the Machine Learning algorithms to interpret complex multivariate patterns from a number of disciplines. An amalgamation of these principles could potentially allow the lower end of the energy spectrum to be tamed permitting for far greater predictions to be made regarding source characteristics.

Cited literature

Aage, H.K., & Korsbech, U. (2003). Search for lost or orphan radioactive sources based on NaI gamma spectrometry. *Applied Radiation and Isotopes, 58*, 103-113

Aage, H.K., Korsbech, U., Bargholz, K., & Hovgaard, J. (1999). A new technique for processing airborne gamma ray spectrometry data for mapping low level contaminations. *Applied Radiation and Isotopes, 51*, 651-662

Ackermann, M., Ajello, M., Allafort, A., Baldini, L., Ballet, J., Barbiellini, G., et al. (2013). Detection of the characteristic pion-decay signature in supernova remnants. *Science (New York, N.Y.), 339*, 807-811

Adams, A. (1993). The origin and early development of the Belgian radium industry. *Environment international, 19*, 491-501

Adams, J.C., Joyce, M.J., & Mellor, M. (2012). The advancement of a technique using principal component analysis for the non-intrusive depth profiling of radioactive contamination. *Nuclear Science, IEEE Transactions on, 59*, 1448-1452

Adsley, I., Davies, M., Murley, R., Pearman, I., & Scirea, M. (2004). 3D GPS mapping of land contaminated with gamma-ray emitting radionuclides. *Applied radiation and isotopes, 60*, 579-582

Alamaniotis, M., Hernandez, H., & Jevremovic, T. (2013a). Application of support vector regression in removing Poisson fluctuation from pulse height gamma-ray spectra, *Nuclear Science, IEEE Transactions on, 60,*1-4

Alamaniotis, M., Heifetz, A., Raptis, A.C., & Tsoukalas, L.H. (2013b). Fuzzy-Logic Radioisotope Identifier for Gamma Spectroscopy in Source Search. *Nuclear Science, IEEE Transactions on, 60*, 3014-3024

Allyson, J.D. (1994). Environmental gamma-ray spectrometry: simulation of absolute calibration of in-situ and airborne spectrometers for natural and anthropogenic sources (PhD thesis), University of Glasgow,

Allyson, J.D., & Sanderson, D.C.W. (2001). Spectral deconvolution and operational use of stripping ratios in airborne radiometrics. *Journal of environmental radioactivity, 53*, 351-363

Allyson, J.D., & Sanderson, D.C.W. (1998). Monte Carlo simulation of environmental airborne gamma-spectrometry. *Journal of environmental radioactivity, 38*, 259-282

Ao, S., Rieger, B.B., & Amouzegar, M.A. (2010). *Machine Learning and Systems Engineering.* : Springer

Baker, A., & Toque, C. (2005). A review of the potential for radium from luminising activities to migrate in the environment. *Journal of Radiological Protection, 25*, 127

Ball, T., Cameron, D., Colman, T., & Roberts, P. (1991). Behaviour of radon in the geological environment: a review. *Quarterly Journal of Engineering Geology and Hydrogeology, 24*, 169-182

Ballhausen, C.J. (1962). Ligand field theory. *McGrow Hill, Newyork*

Beck, H.L., Condon, W.J., & Lowder, W.M. (1964). Spectrometric techniques for measuring environmental gamma radiation. *US Department of Energy, Environmental Measurements Laboratory, HASL-150, New York*

Beck, H., De Campo, J., & Gogolak, C. (1972). In situ Ge (Li) and Na (Tl) gamma-ray spectrometry. *US Department of Energy, Environmental Measurements Laboratory, HASL-258, New York*

Bergmeir, C., & Benítez, J.M. (2012a). Neural networks in R using the Stuttgart neural network simulator: RSNNS. *Journal of Statistical Software, 46*, 1-26

Bergmeir, C., & Benítez, J.M. (2012b). Package 'RSNNS'.

Birowosuto, M., Dorenbos, P., Van Eijk, C., Krämer, K., & Güdel, H. (2006). Scintillation properties and anomalous Ce_3 emission of $Cs_2NaREBr_6$: Ce_3 (RE= La, Y, Lu). *Journal of Physics: Condensed Matter, 18*, 6133

Bivand, R.S., Pebesma, E., & Gómez-Rubio, V. (2013). *Applied spatial data analysis with R.* : Springer Science & Business Media

Boser, B.E., Guyon, I.M., & Vapnik, V.N. (1992). A training algorithm for optimal margin classifiers. , 144-152

Boson, J., Plamboeck, A.H., Ramebäck, H., Ågren, G., & Johansson, L. (2009a). Evaluation of Monte Carlo-based calibrations of HPGe detectors for *in situ* gamma-ray spectrometry. *Journal of environmental radioactivity, 100*, 935-940

Boson, J., Nylén, T., Hånell Plamboeck, A., Ågren, G., & Johansson, L. (2008). Improving accuracy of *in situ* gamma-ray spectroscopy.

Boson, J., Johansson, L., Rameback, H., & Agren, G. (2009b). Uncertainty in HPGe detector calibrations for *in situ* gamma-ray spectrometry. *Radiation Protection Dosimetry, 134*, 122-129

Boubaker Askri, Adel Trabelsi, & Brahim Baccari. (2008). Method for converting in-situ gamma ray spectra of a portable Ge detector to an incident photon flux energy distribution based on Monte Carlo simulation. *Nuclear Science and Techniques, 19*, 358-364

Briesmeister, J.F. (1993). MCNP-A general Monte Carlo N-particle transport code. *LA-12625*

Brown, J.E., McDonald, P., Parker, A., & Rae, J.E. (1999). The vertical distribution of radionuclides in a Ribble Estuary saltmarsh: transport and deposition of radionuclides. *Journal of environmental radioactivity, 43*, 259-275

Bugai, D., Kashparov, V., Dewiere, L., Khomutinin, Y., Levchuk, S., & Yoschenko, V. (2005). Characterization of subsurface geometry and radioactivity distribution in the trench containing Chernobyl clean-up wastes. *Environmental Geology, 47*, 869-881

Byvatov, E., Fechner, U., Sadowski, J., & Schneider, G. (2003). Comparison of support vector machine and artificial neural network systems for drug/nondrug classification. *Journal of chemical information and computer sciences, 43*, 1882-1889

Caciolli, A., Baldoncini, M., Bezzon, G.P., Broggini, C., Buso, G.P., Callegari, I., et al. (2012). A new FSA approach for *in situ* γ ray spectroscopy. *Science of The Total Environment, 414*, 639-645

Carrazana González, J., Cornejo Díaz, N., & Jurado Vargas, M. (2012). Application of the Monte Carlo code DETEFF to efficiency calibrations for *in situ* gamma-ray spectrometry. *Applied Radiation and Isotopes, 70*, 868-871

Charlesworth, M.E., Service, M., & Gibson, C.E. (2006). The distribution and transport of Sellafield derived ^{137}Cs and ^{241}Am to western Irish Sea sediments. *Science of The Total Environment, 354*, 83-92

Chatfield, C., & Collins, A.J. (1980). Principal component analysis. *Introduction to multivariate analysis* (pp. 57-81) : Springer

Clifton, J., McDonald, P., Plater, A., & Oldfield, F. (1999). Derivation of a Grain-size Proxy to Aid the Modelling and Prediction of Radionuclide Activity in Salt Marshes and Mud Flats of the Eastern Irish Sea. *Estuarine, Coastal and Shelf Science, 48*, 511-518

Cook, G.T., MacKenzie, A.B., McDonald, P., & Jones, S.R. (1997). Remobilization of Sellafield-derived radionuclides and transport from the north-east Irish Sea. *Journal of environmental radioactivity, 35*, 227-241

Cortes, C., & Vapnik, V. (1995). Support-vector networks. *Machine Learning, 20*, 273-297

Crawley, M.J. (2012). *The R book* : John Wiley & Sons

Cresswell, A.J., & Sanderson, D.C.W. (2009). The use of difference spectra with a filtered rolling average background in mobile gamma spectrometry measurements. *Nuclear Instruments and Methods in Physics Research Section A: Accelerators, Spectrometers, Detectors and Associated Equipment, 607*, 685-694

Dale, P., Robertson, I., & Toner, M. (2008). Radioactive particles in dose assessments. *Journal of environmental radioactivity, 99*, 1589-1595

Dale, P., Gemmill, J., & Milne, J. (2013). Dalgety Bay Radioactive Contaminated Land Risk Assessment.

Dauer, L.T. (2002). Radiation at Home, Outdoors and in the Workplace, *Health physics, 82*, 109-120

Davies, M., McCulloch, G., & Adsley, I. (2007). Experience of monitoring beaches for radioactive particles. *Journal of Radiological Protection, 27*, A51

De Groot, A., Van der Graaf, E., De Meijer, R., & Maučec, M. (2009). Sensitivity of< i> in-situ γ-ray spectra to soil density and water content. *Nuclear Instruments and Methods in Physics Research Section A: Accelerators, Spectrometers, Detectors and Associated Equipment, 600*, 519-523

de Haas, J.T.M., Dorenbos, P., & van Eijk, C.W.E. (2005). Measuring the absolute light yield of scintillators. Nuclear Instruments and Methods in Physics Research Section A: Accelerators, Spectrometers, Detectors and Associated Equipment, 537, 97-100

DECC. (2012). Radioactive Contaminated Land Statutory Guidance Environmental Protection Act 1990: Part 11A. Contaminated land. Department of Energy and Climate.

Dennis, F., Morgan, G., & Henderson, F. (2007). Dounreay hot particles: the story so far. *Journal of Radiological Protection, 27*, A3-A11

Dewey, S.C., Whetstone, Z.D., & Kearfott, K.J. (2011). A method for determining the analytical form of a radionuclide depth distribution using multiple gamma spectrometry measurements. *Journal of environmental radioactivity, 102*, 581-588

Dickson, B.L. (2004). Recent advances in aerial gamma-ray surveying. *Journal of environmental radioactivity, 76*, 225-236

Dimitriadou, E., Hornik, K., Leisch, F., Meyer, D., & Weingessel, A. (2008). Misc functions of the Department of Statistics (e1071), TU Wien. *R package*, 1.5-24

Dowdall, M., Smethurst, M., Watson, R., Mauring, A., Aage, H.K., Andersson, K., et al. (2012). Car-borne gamma spectrometry: a virtual exercise in emergency response. *Journal of environmental radioactivity, 107*, 68-77

Dragovic, S., Onjia, A., Stankovic, S., Anicin, I., & Bacic, G. (2005). Artificial neural network modelling of uncertainty in gamma-ray spectrometry. *Nuclear Instruments & Methods in Physics Research Section A-Accelerators Spectrometers Detectors and Associated Equipment, 540*, 455-463

Dragović, S., Onjia, A., & Bačić, G. (2006). Simplex optimization of artificial neural networks for the prediction of minimum detectable activity in gamma-ray spectrometry. *Nuclear Instruments and Methods in Physics Research Section A: Accelerators, Spectrometers, Detectors and Associated Equipment, 564*, 308-314

Drozdowski, W., Dorenbos, P., Bos, A.J.J., Bizarri, G., Owens, A., & Quarati, F.G.A. (2008). CeBr^3 scintillator development for possible use in space missions. *IEEE Transactions on Nuclear Science, 55*, 1391-1396

Du, Q., Wei, W., May, D., & Younan, N.H. (2010). Noise-adjusted principal component analysis for buried radioactive target detection and classification. *Nuclear Science, IEEE Transactions on, 57*, 3760-3767

Eisenbud, M., & Gesell, T.F. (1997). Environmental Radioactivity from Natural, Industrial & Military Sources: From Natural, Industrial and Military Sources: Academic Press

Ely, J.H., Kouzes, R.T., Geelhood, B.D., Schweppe, J.E., & Warner, R.A. (2004). Discrimination of naturally occurring radioactive material in plastic scintillator material. *Nuclear Science, IEEE Transactions on, 51*, 1672-1676

Ely, J., Kouzes, R., Schweppe, J., Siciliano, E., Strachan, D., & Weier, D. (2006). The use of energy windowing to discriminate SNM from NORM in radiation portal monitors. *Nuclear Instruments and Methods in Physics Research Section A: Accelerators, Spectrometers, Detectors and Associated Equipment, 560*, 373-387

Evans, R.D., & Noyau, A. (1955). *The atomic nucleus*: McGraw-Hill New York

Fagan, D.K., Robinson, S.M., & Runkle, R.C. (2012). Statistical methods applied to gamma-ray spectroscopy algorithms in nuclear security missions. *Applied Radiation and Isotopes, 70*, 2428-2439

Fehrenbacher, G., Meckbach, R., & Jacob, P. (1996). Unfolding the response of a Ge detector used for in-situ gamma-ray spectrometry. *Nuclear Instruments & Methods in Physics Research Section A-Accelerators Spectrometers Detectors and Associated Equipment, 383*, 454-462

Feng, T.C., Jia, M.Y., & Feng, Y.J. (2012). Method-sensitivity of in-situ gamma spectrometry to determine the depth-distribution of anthropogenic radionuclides in soil. *Nuclear Instruments & Methods in Physics Research Section A-Accelerators Spectrometers Detectors and Associated Equipment, 661*, 26-30

Feng, T.C., Pa, M.Y., Long, B., Su, C.Y., Wu, R., & Cheng, J.P. (2008). Delaminated method to determine the depth distribution of Eu-152 in soil by in-situ HPGe gamma spectrometry. *Nuclear Instruments & Methods in Physics Research Section A-Accelerators Spectrometers Detectors and Associated Equipment, 597*, 192-197

Ford, J. (2004). Radiation, people and the environment. Internation Atomic Energy Agency (Vienna)

Forster, R., Little, R., Briesmeister, J., & Hendricks, J. (1990). MCNP capabilities for nuclear well logging calculations. *Nuclear Science, IEEE Transactions on, 37*, 1378-1385

Galushkin, A.I. (2007). *Neural networks theory*: Springer

Gering, F., Kiefer, P., Fesenko, S., & Voigt, G. (2002). *In situ* gamma-ray spectrometry in forests: determination of kerma rate in air from ^{137}Cs. *Journal of environmental radioactivity, 61*, 75-89

Gering, F., Hillmann, U., Jacob, P., & Fehrenbacher, G. (1998). *In situ* gamma-spectrometry several years after deposition of radiocesium II. Peak-to-valley method. *Radiation and environmental biophysics, 37*, 283-291

Giaz, A., Pellegri, L., Riboldi, S., Camera, F., Blasi, N., Boiano, C., et al. (2012). Properties of a very large volume LaBr:Ce detector. , 331-334

Giles, J., & Dooley, K. (1998). High resolution gamma-spectroscopy well logging system. *Journal of Radioanalytical and Nuclear Chemistry, 233*, 125b-130

Gillmore, G.K., Crockett, R., Denman, T., Flowers, A., & Harris, R. (2012). Radium dial watches, a potentially hazardous legacy? *Environment international, 45*, 91-98

Gramacy, R.B. (2007). tgp: an R package for Bayesian nonstationary, semiparametric nonlinear regression and design by treed Gaussian process models. *Journal of Statistical Software, 19*, 6

Grasty, R., Holman, P., & Blanchard, Y. (1991). Transportable calibration pads for ground and airborne gamma-ray spectrometers: Geological Survey of Canada

Gray, J., Jones, S., & Smith, A. (1995). Discharges to the environment from the Sellafield site, 1951-1992. *Journal of Radiological Protection, 15*, 99

Green, A.A., Berman, M., Switzer, P., & Craig, M.D. (1988). A transformation for ordering multispectral data in terms of image quality with implications for noise removal. *Geoscience and Remote Sensing, IEEE Transactions on, 26*, 65-74

Guastaldi, E., Baldoncini, M., Bezzon, G., Broggini, C., Buso, G., Caciolli, A., et al. (2013). A multivariate spatial interpolation of airborne γ-ray data using the geological constraints. *Remote Sensing of Environment, 137*, 1-11

Guillot, L. (2001). Extraction of full absorption peaks in airborne gamma-spectrometry by filtering techniques coupled with a study of the derivatives. Comparison with the window method. *Journal of environmental radioactivity, 53*, 381-398

Günther, F., & Fritsch, S. (2010). neuralnet: Training of neural networks. *The R Journal, 2*, 30-38

Gurney, K. (2003). An introduction to neural networks: CRC press

Guss, P., Reed, M., Yuan, D., Reed, A., & Mukhopadhyay, S. (2009). $CeBr_3$ as a room-temperature, high-resolution gamma-ray detector. *Nuclear Instruments & Methods in Physics Research Section A-Accelerators Spectrometers Detectors and Associated Equipment, 608*, 297-304

Guss, P., Reed, M., Yuan, D., Cutler, M., Contreras, C., & Beller, D. (2010). Comparison of $CeBr_3$ with $LaBr_3$:Ce, $LaCl_3$:Ce, and NaI:Tl Detectors. *Hard X-Ray, Gamma-Ray, and Neutron Detector Physics Xii, 7805*, 78050L

Gutierrez, S., Guillot, L., & Bourgeois, C. (2002). Contribution of a germanium detector in mobile gamma-ray spectrometry. Spectral analysis and performance. *Nuclear Instruments & Methods in Physics Research Section A-Accelerators Spectrometers Detectors and Associated Equipment, 482*, 425-433

Haddad, K., Al-Masri, M.S., & Doubal, A.W. (2014). Determination of ^{226}Ra contamination depth in soil using the multiple photopeaks method. *Journal of environmental radioactivity, 128*, 33-37

Haley, P.J., & Soloway, D. (1992). Extrapolation limitations of multilayer feedforward neural networks.

Harvie, D.I. (1999). The radium century. *Endeavour, 23*, 100-105

Helfer, I.K., & Miller, K.M. (1988). Calibration Factors for Ge Detectors used for Field Spectrometry. *Health physics, 55*, 15-29

Hendriks, P., Limburg, J., & De Meijer, R. (2001). Full-spectrum analysis of natural γ-ray spectra. *Journal of environmental radioactivity, 53*, 365-380

Hendriks, P.H.G.M., Maučec, M., & de Meijer, R.J. (2002). MCNP modelling of scintillation-detector γ-ray spectra from natural radionuclides. *Applied Radiation and Isotopes, 57*, 449-457

Hillmann, U., Schimmack, W., Jacob, P., & Bunzl, K. (1996). In situ gamma-spectrometry several years after deposition of radiocesium .1. Approximation of depth distributions by the Lorentz function. *Radiation and environmental biophysics, 35*, 297-303

HMSO. (1996). CM 2919 (1995) Review of Radioactive Waste Management Policy-Final Conclusions.

Hornik, K., Buchta, C., & Zeileis, A. (2009). Open-source machine learning: R meets Weka. *Computational Statistics, 24*, 225-232

Hornik, K., Meyer, D., & Karatzoglou, A. (2006). Support vector machines in R. *Journal of statistical software, 15*, 1-28

Horrill, A. (1983). Concentrations and spatial distribution of radioactivity in an ungrazed saltmarsh. *Ecological aspects of radionuclide release*

Hotelling, H. (1933). Analysis of a complex of statistical variables into principal components. *Journal of educational psychology, 24*, 417

Hovgaard, J. (1997). Airborne gamma-ray spectroscopy. *Airborne gamma-ray spectrometry*

Hovgaard, J., & Grasty, R. (1997). Reducing statistical noise in airborne gamma-ray data through spectral component analysis. *Radiometric metric and remote sensing, 97*, 753-764

IAEA. (2003). Guidelines for radioelement mapping using gamma ray spectrometry data *, Nuclear Fuel Cycle and Materials Section,* International Atomic Energy Agency (Vienna)

IAEA. (1998). Characterization of radioactively contaminated sites for remediation purposes.

ICRP,. (2007). ICRP Publication 103. *Ann.ICRP, 37*, 2

ICRU. (2006). Report 75: Sampling for Radionuclides in the Environment.

Iltis, A., Mayhugh, M.R., Menge, P., Rozsa, C.M., Selles, O., & Solovyev, V. (2006). Lanthanum halide scintillators: Properties and applications. *Nuclear Instruments and Methods in Physics Research Section A: Accelerators, Spectrometers, Detectors and Associated Equipment, 563*, 359-363

Im, H., Lee, Y., Park, Y.J., Song, B.C., Cho, J., & Kim, W. (2007). Noise reduction in prompt gamma spectra acquired in short times. *Nuclear Instruments & Methods in Physics Research Section A-Accelerators Spectrometers Detectors and Associated Equipment, 574*, 272-279

James, G., Witten, D., Hastie, T., & Tibshirani, R. (2013). *An introduction to statistical learning*: Springer

Jarman, K.D., Runkle, R.C., Anderson, K.K., & Pfund, D.M. (2008). A comparison of simple algorithms for gamma-ray spectrometers in radioactive source search applications. *Applied Radiation and Isotopes, 66*, 362-371

Jones, D.G., Roberts, P.D., Strutt, M.H., Higgo, J.J., & Davis, J.R. (1999). Distribution of ^{137}Cs and inventories of ^{238}Pu, $^{239/240}$Pu, ^{241}Am and ^{137}Cs in Irish Sea intertidal sediments. *Journal of environmental radioactivity, 44*, 159-189

Jones, D.G., Kershaw, P.J., McMahon, C.A., Milodowski, A.E., Murray, M., & Hunt, G.J. (2007). Changing patterns of radionuclide distribution in Irish Sea subtidal sediments. *Journal of environmental radioactivity, 96*, 63-74

Kangas, L.J., Keller, P.E., Siciliano, E.R., Kouzes, R.T., & Ely, J.H. (2008). The use of artificial neural networks in PVT-based radiation portal monitors. *Nuclear Instruments and Methods in Physics Research Section A: Accelerators, Spectrometers, Detectors and Associated Equipment, 587*, 398-412

Karatzoglou, A., Smola, A., Hornik, K., & Zeileis, A. (2004). kernlab-an S4 package for kernel methods in R.

Kastlander, J., & Bargholtz, C. (2005). Efficient *in situ* method to determine radionuclide concentration in soil. Nuclear Instruments & Methods in Physics Research Section A-Accelerators Spectrometers Detectors and Associated Equipment, 547, 400-410

Kathren, R.L. (1998). NORM sources and their origins. *Applied radiation and isotopes, 49*, 149-168

Kluson, J. (2001). Environmental monitoring and *in situ* gamma spectrometry. *Radiation Physics and Chemistry, 61*, 209-216

Knoll, G.F. (2010). *Radiation detection and measurement*: John Wiley & Sons

Kobr, M., Mareš, S., & Paillet, F. (2005). Geophysical well logging. *Hydrogeophysics* (pp. 291-331): Springer

Kock, P., Lanke, J., & Samuelsson, C. (2012). A real-time statistical alarm method for mobile gamma spectrometry—Combining counts of pulses with spectral distribution of pulses. *Nuclear Instruments and Methods in Physics Research Section A: Accelerators, Spectrometers, Detectors and Associated Equipment, 681*, 55-60

Kock, P., Finck, R.R., Nilsson, J.M.C., Östlund, K., & Samuelsson, C. (2010). A deviation display method for visualising data in mobile gamma-ray spectrometry. *Applied Radiation and Isotopes, 68*, 1832-1838

Korun, M., Likar, A., Lipoglavsek, M., Martincic, R., & Pucelj, B. (1994). In-Situ Measurement of Cs Distribution in the Soil. *Nuclear Instruments & Methods in Physics Research Section B-Beam Interactions with Materials and Atoms, 93*, 485-491

Laedermann, J.-., Byrde, F., & Murith, C. (1998). *In-Situ* gamma-ray spectrometry: the influence of topography on the accuracy of activity determination. *Journal of environmental radioactivity, 38*, 1-16

Landa, E.R. (1993). A brief history of the American Radium Industry and its ties to the Scientific Community of its early twentieth century. *Environment international, 19*, 503-508

L'Annunziata, M.F. (2012). *Handbook of radioactivity analysis* : Academic Press

Likar, A., Vidmar, T., Lipoglavšek, M., & Omahen, G. (2004). Monte Carlo calculation of entire *in situ* gamma-ray spectra. *Journal of environmental radioactivity, 72*, 163-168

Likar, A., Omahen, G., Vidmar, T., & Martincic, R. (2000). Method to determine the depth of Cs-137 in soil from in-situ gamma-ray spectrometry. *Journal of Physics D: Applied Physics, 33*, 2825

Long, S., & Martin, L. (2007). Optimisation of systems to locate discrete gamma-ray sources within a large search area. *Journal of environmental radioactivity, 94*, 41-53

Mahalanobis, P.C. (1936). On the generalized distance in statistics. *Proceedings of the National Institute of Sciences (Calcutta), 2*, 49-55

Martin, P., Payton, O., Fardoulis, J., Richards, D., & Scott, T. (2015). The use of unmanned aerial systems for the mapping of legacy uranium mines. *Journal of environmental radioactivity, 143*, 135-140

Maučec, M., Hendriks, P.H.G.M., Limburg, J., & de Meijer, R.J. (2009). Determination of correction factors for borehole natural gamma-ray measurements by Monte Carlo simulations. *Nuclear Instruments and Methods in Physics Research Section A: Accelerators, Spectrometers, Detectors and Associated Equipment, 609*, 194-204

Maučec, M., de Meijer, R.J., Rigollet, C., Hendriks, P.H.G.M., & Jones, D.G. (2004). Detection of radioactive particles offshore by γ-ray spectrometry Part I: Monte Carlo assessment of detection depth limits. *Nuclear Instruments and Methods in Physics Research Section A: Accelerators, Spectrometers, Detectors and Associated Equipment, 525*, 593-609

Mauring, E., & Smethurst, M.A. (2005). Reducing noise in radiometric multi-channel data using noise-adjusted singular value decomposition (NASVD) and maximum noise fraction (MNF). *Geological Survey of Norway, Report*

McKay, W.A., & Baxter, M.S. (1985). Water transport from the North-east Irish Sea to western Scottish coastal waters: Further observations from time-trend matching of Sellafield radiocaesium. *Estuarine, Coastal and Shelf Science, 21*, 471-480

Medhat, M.E. (2012). Artificial intelligence methods applied for quantitative analysis of natural radioactive sources. *Annals of Nuclear Energy, 45*, 73-79

Meisner, J., Nicaise, W., & Stromswold, D. (1995). CsI (Tl) with photodiodes for identifying subsurface radionuclide contamination. *Nuclear Science, IEEE Transactions on, 42*, 288-291

Menge, P.R., Gautier, G., Iltis, A., Rozsa, C., & Solovyev, V. (2007). Performance of large lanthanum bromide scintillators. Nuclear Instruments and Methods in Physics Research Section A: Accelerators, Spectrometers, Detectors and Associated Equipment, 579, 6-10

Meyer, D., & Wien, F.T. (2014). Support vector machines. *The Interface to libsvm in package e1071*

Milbrath, B.D., Choate, B.J., Fast, J.E., Hensley, W.K., Kouzes, R.T., & Schweppe, J.E. (2007). Comparison of LaBr3:Ce and NAI(Tl) scintillators for radio-isotope identification devices. *Nuclear Instruments and Methods in Physics Research Section A: Accelerators, Spectrometers, Detectors and Associated Equipment, 572*, 774-784

Miller, M.L. (2007). Cesium-137 in the Environment: Radioecology and Approaches to Assessment and Management. NCRP Report No.154, Cesium-137 in the Environment: Radioecology and Approaches to Assessment and Management, 151

Miller, K.M., Shebell, P., & Klemic, G.A. (1994). In-Situ Gamma-Ray Spectrometry for the Measurement of Uranium in Surface Soils. *Health physics, 67*, 140-150

Minty, B., & Hovgaard, J. (2002). Reducing noise in gamma-ray spectrometry using spectral component analysis. *Exploration Geophysics, 33*, 172-176

Minty, B., Luyendyk, A., & Brodie, R. (1997). Calibration and data processing for airborne gamma-ray spectrometry. *AGSO Journal of Australian Geology and Geophysics, 17*, 51-62

Moreira, M.C.F., Conti, C.C., & Schirru, R. (2010). A new NaI(Tl) four-detector layout for field contamination assessment using artificial neural networks and the Monte Carlo method for system calibration. *Nuclear Instruments and Methods in Physics Research Section A: Accelerators, Spectrometers, Detectors and Associated Equipment, 621*, 302-309

Morris, K., Butterworth, J.C., & Livens, F.R. (2000). Evidence for the Remobilization of Sellafield Waste Radionuclides in an Intertidal Salt Marsh, West Cumbria, U.K. *Estuarine, Coastal and Shelf Science, 51*, 613-625

Moszyński, M., Nassalski, A., Syntfeld-Każuch, A., Szczęśniak, T., Czarnacki, W., Wolski, D., et al. (2006). Temperature dependences of LaBr3(Ce), LaCl3(Ce) and NaI(Tl) scintillators. *Nuclear Instruments and Methods in Physics Research Section A: Accelerators, Spectrometers, Detectors and Associated Equipment, 568*, 739-751

Narayan, R.D., Miranda, R., & Rez, P. (2012). Monte Carlo simulation for the electron cascade due to gamma rays in semiconductor radiation detectors. *Journal of Applied Physics, 111*, 649-660

National Nuclear Data Center. (2013). Nuclear datasheets*, accessed 2013*

Nikl, M., & Yoshikawa, A. (2015). Recent R&D Trends in Inorganic Single-Crystal Scintillator Materials for Radiation Detection. *Advanced Optical Materials, 3*, 463-481

Nilsson, J.M.C. (2010). Using a $LaBr_3$:Ce scintillation detector for mobile γ-spectrometry.

Oh, J.-., Warwick, P.E., & Croudace, I.W. (2009). Spatial distribution of ^{241}Am, ^{137}Cs, ^{238}Pu, ^{239,240}Pu and ^{241}Pu over 17 year periods in the Ravenglass saltmarsh, Cumbria, UK. *Applied Radiation and Isotopes, 67*, 1484-1492

Olmos, P., Diaz, J., Perez, J., Garcia-Belmonte, G., Gomez, P., & Rodellar, V. (1992). Application of neural network techniques in gamma spectroscopy. *Nuclear Instruments and Methods in Physics Research Section A: Accelerators, Spectrometers, Detectors and Associated Equipment, 312*, 167-173

Onsager, L. (1938). Initial recombination of ions. *Physical Review, 54*, 554

ORTEC. (2005). MAESTRO*, version 6.08*

OSPAR. (2010). Quality Status Report 2010. OSPAR Commission, 176

Paschoa, A.S. (1998). Potential environmental and regulatory implications of naturally occurring radioactive materials (NORM). *Applied radiation and isotopes, 49*, 189-196

Patton, N., Gemmill, J., & Milne, J. (2013). Appropriate Person Report. Report prepared by the Scottish Environmental Protection Agency

Pausch, G., Herbach, C., Hillebrands, R., Kreuels, A., Lentering, R., Lueck, F., et al. (2007). Application of $LaBr_3(Ce_3)$ scintillators in radio-isotope identification devices*, 2*, 963-968

Pebesma, E., Bivand, R., Rowlingson, B., & Gomez-Rubio, V. (2013). Sp: classes and methods for spatial data. URL http://CRAN.R-project.org/package= sp, R package version, 1.0-14

Pfund, D.M., Jarman, K.D., Milbrath, B.D., Kiff, S.D., & Sidor, D.E. (2010). Low count anomaly detection at large standoff distances. *Nuclear Science, IEEE Transactions on, 57*, 309-316

Pilato, V., Tola, F., Martinez, J.M., & Huver, M. (1999). Application of neural networks to quantitative spectrometry analysis. *Nuclear Instruments & Methods in Physics Research Section A-Accelerators Spectrometers Detectors and Associated Equipment, 422*, 423-427

Plamboeck, A.H., Nylén, T., & Ågren, G. (2006). Comparative estimations of ^{137}Cs distribution in a boreal forest in northern Sweden using a traditional sampling approach and a portable NaI detector. *Journal of environmental radioactivity, 90*, 100-109

Potapov, V., Ivanov, O., Chirkin, V., & Ignatov, S. (2001). A dip detector for *in situ* measuring of Cs-137 specific soil activity profiles. *Nuclear Science, IEEE Transactions on, 48*, 1194-1197

Povinec, P.P., Bailly du Bois, P., Kershaw, P.J., Nies, H., & Scotto, P. (2003). Temporal and spatial trends in the distribution of ^{137}Cs in surface waters of Northern European Seas—a record of 40 years of investigations. *Deep Sea Research Part II: Topical Studies in Oceanography, 50*, 2785-2801

Pratt, R. (1993). Review of radium hazards and regulation of radium in industry. *Environment international, 19*, 475-489

R Development Core Team. (2012). R: A language and environment for statistical computing. *R: A language and environment for statistical computing*

Read, D., Read, G., & Thorne, M. (2013). Background in the context of land contaminated with naturally occurring radioactive material. *Journal of Radiological Protection, 33*, 367

Riedmiller, M., & Braun, H. (1993). A direct adaptive method for faster backpropagation learning: The RPROP algorithm, *Neural Networks*, 586-591

Rundo, J. (1993). History of the determination of radium in man since 1915. *Environment international, 19*, 425-438

Runkle, R. (2006). Analysis of spectroscopic radiation portal monitor data using principal components analysis. *IEEE Transactions on Nuclear Science, 53*, 1418-1423

Sangeetha, R., & Kalpana, B. (2010). A comparative study and choice of an appropriate kernel for support vector machines. , 549-553

Santo, A.S.E., Wasserman, F.G., & Conti, C.C. (2012). HPGe well detector calibration procedure by MCNP5 Monte Carlo computer code. *Annals of Nuclear Energy, 46*, 213-217

Schaub, M., Konz, N., Meusburger, K., & Alewell, C. (2010). Application of in-situ measurement to determine ^{137}Cs in the Swiss Alps. *Journal of environmental radioactivity, 101*, 369-376

Serov, I.V., John, T.M., & Hoogenboom, J.E. (1998). A new effective Monte Carlo Midway coupling method in MCNP applied to a well logging problem. *Applied Radiation and Isotopes, 49*, 1737-1744

Sharma, S., Bellinger, C., Japkowicz, N., Berg, R., & Ungar, K. (2012). Anomaly detection in gamma ray spectra: A machine learning perspective. , 1-8

Shepard, D. (1968). A two-dimensional interpolation function for irregularly-spaced data, *Proceedings of the 23rd ACM conference* , 517-524

Shumway, R.H., & Stoffer, D.S. (2013). *Time series analysis and its applications*: Springer Science & Business Media

Slovak, P. (2012). The perception of risk: Radiation and risk. *Bulletin of Atomic Scientists, 68*, 67-75

Smola, A.J., Schölkopf, B., & Müller, K. (1998). The connection between regularization operators and support vector kernels. *Neural Networks, 11*, 637-649

Sowa, W., Martini, E., Gehrcke, K., Marschner, P., & Naziry, M. (1989). Uncertainties of *in situ* gamma spectrometry for environmental monitoring. *Radiation Protection Dosimetry, 27*, 93-101

Stannard, J.N., & Baalman Jr, R. (1988). *Radioactivity and health: a history:* Springer

Statutory Guidance to support the Radioactive Contaminated Land (Scotland) Regulations. (2008). http://www.scotland.gov.uk/Publications/2008/03/31102033/0; *, 2015*

Stebbings, J.H. (2001). Health risks from radium in workplaces: an unfinished story. *Occupational medicine (Philadelphia, Pa.), 16*, 259-270

Steinhauser, G., Brandl, A., & Johnson, T.E. (2014). Comparison of the Chernobyl and Fukushima nuclear accidents: A review of the environmental impacts. *Science of The Total Environment, 470–471*, 800-817

Stromswold, D. (1995). Calibration facilites for borehole and surface environmental radiation measurements. *Journal of Radioanalytical and Nuclear Chemistry, 194*, 393-401

Sullivan, J.P., Rawool-Sullivan, M.W., & Wenz, T.R. (2008). LaCl3(Ce) and LaBr3(Ce) gamma-ray spectra with various plutonium isotopic and uranium enrichment standards. *Journal of Radioanalytical and Nuclear Chemistry, 276*, 699-705

T.J. Stocki, N. Japkowicz, G.Li, R.K. Ungar, I. Hoffman, & J. Yi. (2008). Summary of the Data Mining Contest for the IEEE International Conference on Data Mining, Pisa, Italy 2008. , 1

The Radioactive Substances Act 1993 Amendment (Scotland) Regulations. (2011). http://www.legislation.gov.uk/sdsi/2011/9780111012758/introduction. *, January, 2015*

Thummerer, S., & Jacob, P. (1998). Determination of depth distributions of natural radionuclides with *in situ* gamma-ray spectrometry. *Nuclear Instruments & Methods in Physics Research Section A-Accelerators Spectrometers Detectors and Associated Equipment, 416*, 161-178

Trost, N., & Iwatschenko, M. (2002). Method and Device for Detecting Man-Made Radiation (patent)

Tyler, A., Dale, P., Copplestone, D., Bradley, S., Ewen, H., McGuire, C., et al. (2013). The radium legacy: contaminated land and the committed effective dose from the ingestion of radium contaminated materials. *Environment international, 59*, 449-455

Tyler, A.N. (2004). High accuracy *in situ* radiometric mapping. *Journal of environmental radioactivity, 72*, 195-202

Tyler, A.N., Ruffell, A., & Dale, P. (2011). Dalgety Bay headland investigation (Prepared for Scottish Environmental Protection Agency).

Tyler, A.N., Scott, E.M., Dale, P., Elliott, A.T., Wilkins, B.T., Boddy, K., et al. (2010). Reconstructing the abundance of Dounreay hot particles on an adjacent public beach in Northern Scotland. *Science of the Total Environment, 408*, 4495-4503

Tyler, A.N. (1999). Monitoring anthropogenic radioactivity in salt marsh environments through *in situ* gamma-ray spectrometry. *Journal of environmental radioactivity, 45*, 235-252

Tyler, A.N., Sanderson, D.C.W., & Scott, E.M. (1996a). Estimating and accounting for Cs-137 source burial through in-situ gamma spectrometry in salt marsh environments. *Journal of environmental radioactivity, 33*, 195-212

Tyler, A.N., Sanderson, D.C.W., Scott, E.M., & Allyson, J.D. (1996b). Accounting for spatial variability and fields of view in environmental gamma ray spectrometry. *Journal of environmental radioactivity, 33*, 213-235

Tyler, A.N. (2008). *In situ* and airborne gamma-ray spectrometry. *Radioactivity in the Environment* (pp. 407-448): Elsevier

Varley, A., Tyler, A., Smith, L., Dale, P., & Davies, M. (2015a). Remediating radium contaminated legacy sites: Advances made through machine learning in routine monitoring of "hot" particles. *Science of The Total Environment, 521*, 270-279

Varley, A., Tyler, A., Smith, L., & Dale, P. (2015b). Development of a neural network approach to characterise 226Ra contamination at legacy sites using gamma-ray spectra taken from boreholes. *Journal of environmental radioactivity, 140*, 130-140

Varley, A., Tyler, A., Smith, L., Dale, P., & Davies, M. (2016). Mapping the spatial distribution and activity of ^{226}Ra at legacy sites through Machine Learning interrogation of gamma-ray spectroscopy data. *Science of the Total Environment,* **545-546**, 654-661

Wainio, K., & Knoll, G.F. (1966). Calculated gamma ray response characteristics of semiconductor detectors: Springer

Wakefield, R., Tyler, A.N., McDonald, P., Atkin, P.A., Gleizon, P., & Gilvear, D. (2011). Estimating sediment and caesium-137 fluxes in the Ribble Estuary through time-series airborne remote sensing. *Journal of environmental radioactivity, 102*, 252-261

Wallace, P.R. (1947). The band theory of graphite. *Physical Review, 71*, 622

Watson, W.S., Sumner, D.J., Baker, J.R., Kennedy, S., Reid, R., & Robinson, I. (1999). Radionuclides in seals and porpoises in the coastal waters around the UK. *Science of The Total Environment, 234*, 1-13

Wei, W., Du, Q., & Younan, N.H. (2011). Parallel optimization-based spectral transformation for detection and classification of buried radioactive materials. *Neural Networks*, 373-376

Wei, W., Du, Q., & Younan, N.H. (2010). Particle swarm optimization based spectral transformation for radioactive material detection and classification. *Neural Networks*, 1-6

Whetstone, Z.D., Dewey, S.C., & Kearfott, K.J. (2011). Simulation of a method for determining one-dimensional ^{137}Cs distribution using multiple gamma spectroscopic measurements with an adjustable cylindrical collimator and center shield. *Applied Radiation and Isotopes, 69*, 790-802

Wilson, C.A., Adderley, W.P., Tyler, A.N., & Dale, P. (2013). Characterising the morphological properties and surface composition of radium contaminated particles: a means of interpreting origin and deposition. *Environmental Science: Processes & Impacts, 15*, 1921-1929

Wilson, R., & Conaway, J. (1991). Simulations of a spectral gamma-ray logging tool response to a surface source distribution on the borehole wall. , 1118-1122

Wilson, R.D., Koizumi, C.J., Meisner, J.E., & Stromswold, D.C. (1997). Spectral shape analysis for contaminant logging at the Hanford site. Internal report, 457-461

Wright, S.M., Howard, B.J., Strand, P., Nylén, T., & Sickel, M.A.K. (1999). Prediction of ^{137}Cs deposition from atmospheric nuclear weapons tests within the Arctic. *Environmental Pollution, 104*, 131-143

Yongpeng, W., & Bin, T. (2012). Monte-Carlo Simulation of Response Functions for Natural Gamma-Rays in LaBr3 Detector System with Complex Borehole Configurations. *Plasma Science and Technology, 14*, 481

Yoshida, E., Shizuma, K., Endo, S., & Oka, T. (2002). Application of neural networks for the analysis of gamma-ray spectra measured with a Ge spectrometer. *Nuclear Instruments & Methods in Physics Research Section A-Accelerators Spectrometers Detectors and Associated Equipment, 484*, 557-563

Zell, A., Mache, N., Huebner, R., Mamier, G., Vogt, M., Herrmann, K., et al. (1993). SNNS-Stuttgart Neural Network Simulator.

Zhang, Y., Cong, Q., Xie, Y., & Zhao, B. (2008). Quantitative analysis of routine chemical constituents in tobacco by near-infrared spectroscopy and support vector machine. *Spectrochimica Acta Part A: Molecular and Biomolecular Spectroscopy, 71*, 1408-1413

Zombori, P., Németh, I., Andrási, A., & Lettner, H. (1992). In-situ gamma-spectrometric measurement of the contamination in some selected settlements of Byelorussia (BSSR), Ukraine (UkrSSR) and the Russian Federation (RSFSR). *Journal of environmental radioactivity, 17*, 97-106

Appendix I : PRELIMINARY LABORATORY TESTING

Appendix I.A Energy resolution

To ensure the LaBr:Ce detector purchased from Saint Gobain matched up to the manufacturer's specification laboratory investigations were undertaken. This also provided an opportunity to compare to the two 71 x 71 mm handheld detectors (NaI:Tl and LaBr:Ce) in a controlled environment before testing out in the field.

Saint Gobain specified energy resolution of below 3.1% at 662 keV (actually 2.9%) was obtained by my tests. LaBr:Ce can clearly be seen as the intermediate resolution detector sitting between the lower energy resolution NaI:Tl and higher energy resolution HPGe detectors (Figure 9-1). Interestingly, LaBr:Ce losses its energy resolution advantage at lower energies (< 100 keV) due to self-absorption (Giaz et al., 2012). Therefore, for the detection of low energy gamma emitting sources, such as ^{241}Am, its application holds little, if any, advantage in comparison to NaI:Tl. In the case of project energies at this energy are of little significance.

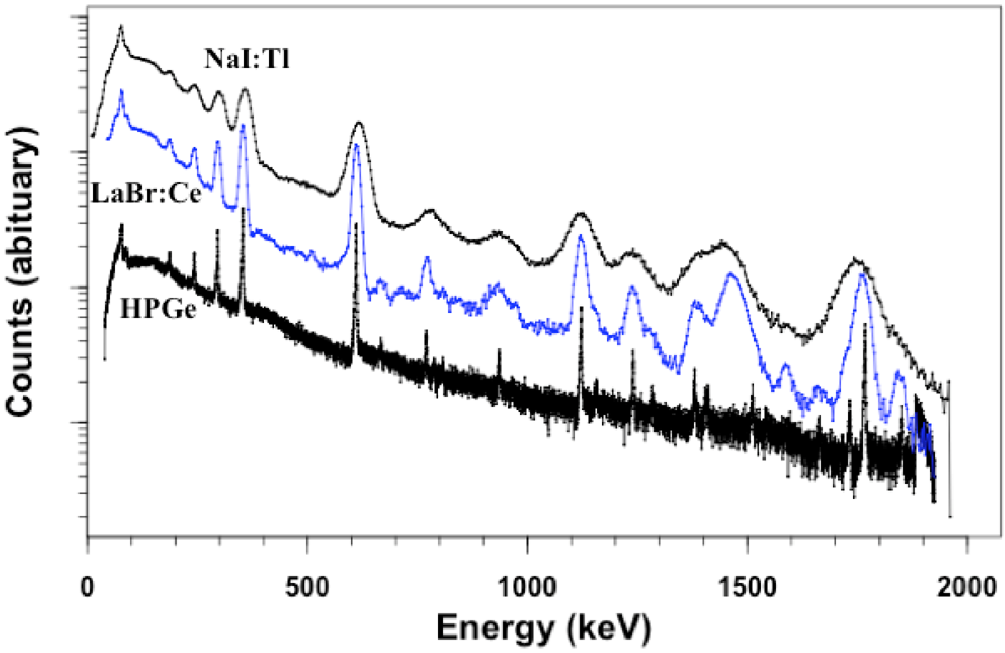

Figure 9-1 Spectral responses of NaI:Tl, LaBr:Ce and HPGe to ^{226}Ra. Spectra have been rescaled for visual purposes.

Appendix I.B Minimum detectable activity

Within the laboratory environment, longer count times were used to assess the Minimum Detectable Activity (MDA) as a function of burial depth using the areas under the full energy peaks 609 and 1764 keV produced by a ^{226}Ra source. This was conducted for 71 x 71 mm NaI:Tl and LaBr:Ce, under background conditions and with the source present at different burial depths of perspex. This allowed, under the assumption of Poisson statistics, the depth and activity with which the number of source counts under a peak (N_D) can be confidently identified above the critical level (L_C) calculated from the lab background ($\alpha = 0.05$) (eq 25).

$$N_D = L_C + 1.64\sigma_{N_D} \tag{25}$$

It can be seen that the higher energy resolution and greater efficiency of LaBr:Ce permit a source to be detected with greater confidence (α = 0.05) deeper into the Perspex column compared to NaI:Tl using both the 609 and 1764 keV peaks (Figure 9-2). With respects to environmental handheld detection, these results are of little significant as the short count times employed in the field mean that peaks can rarely be confidently identified in this manner. However, in terms of laboratory use or for radioisotope identification, LaBr:Ce could be a promising alternative to NaI:Tl (Milbrath et al., 2007, Knoll, 2010).

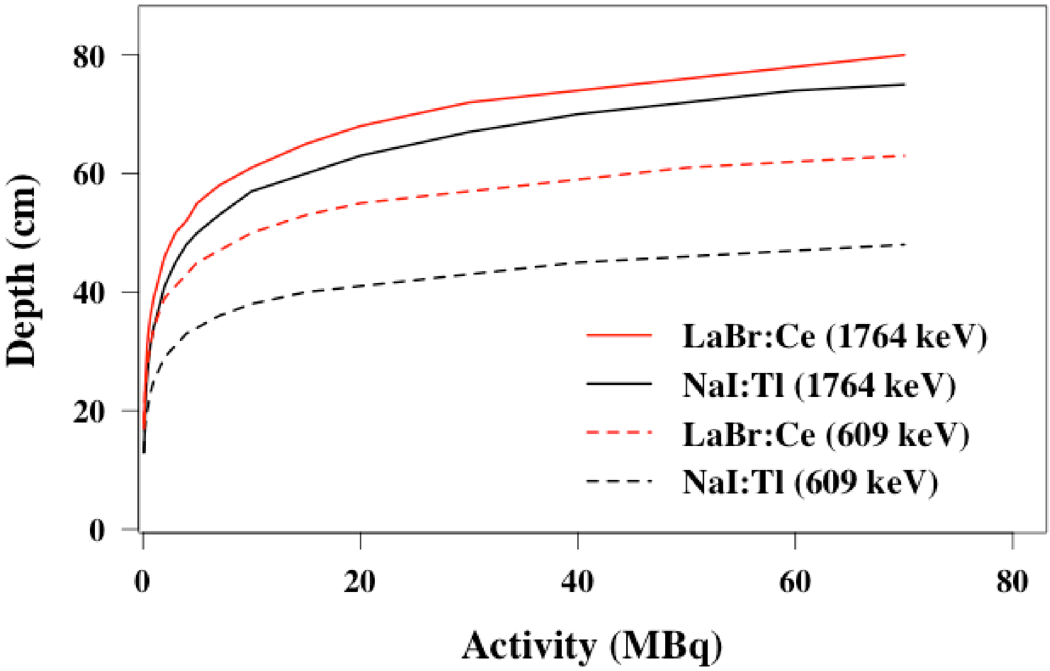

Figure 9-2 Minimum detectable activity (α= 0.05) as a function of burial depth for the 609 and 1764 keV ^{226}Ra peaks, for 71 x 71 mm NaI:Tl and LaBr:Ce detectors.

Appendix I.C Temperature stability

To assess drifts in gain that can take place in the environment to temperature variations a climate control study was undertaken. The two detectors connected to a digiBase (with their respective cases) were placed in a climate control cabinet, alongside a ^{226}Ra source and the ambient temperature was varied over the course of 12 hours. To recreate realistic field conditions, Maestro’s (Ortec) gain stabilisation software was centred around the ^{40}K peak (1462 keV) for the NaI:Tl detector (ORTEC, 2005). In the case of LaBr:Ce this was centred around the intrinsic peak (1468 keV). 1-minute spectra were taken hourly. Monitoring the central position of the 609 keV peak allowed for the assessment of drifts in gain.

LaBr:Ce performed better under these conditions as less spectral drift was encountered, in fact less than 1 keV over the environmentally relevant temperature range of -10 to 40 °C Figure 9-3. The NaI:Tl detector tended to drift more over this range (3 keV). The reason for this may be due to clarity of peak presented by LaBr:Ce (Figure 2-7), enabling the gain stabilisation software to accurately track its central position. On the other hand, the comparatively smaller in intensity peak, presented by ^{40}K in the case of NaI:Tl, resulted in more spectral drift as the gain stabilisation software could not track it as efficiently. Nilsson (2010) demonstrates that without gain stabilisation the photomultiplier tube contained within a DigiBase can drift up to 50 keV over a similar ambient temperature range.

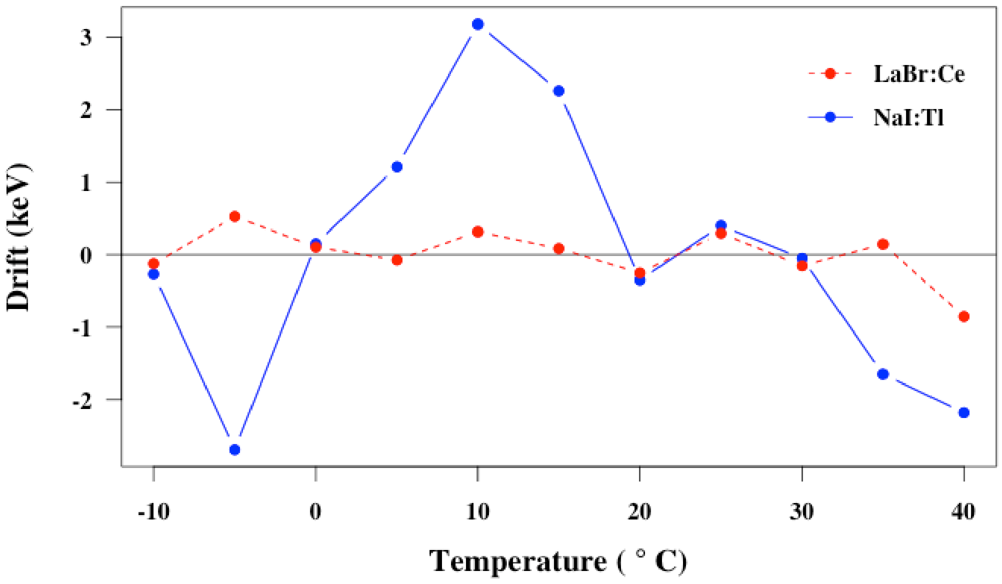

Figure 9-3 Gain drifts for the 609 keV peak, for NaI:Tl and LaBr:Ce detectors, taken over the temperature range -10 to 40 °C.

Appendix II : CONCRETE CALIBRATION PADS

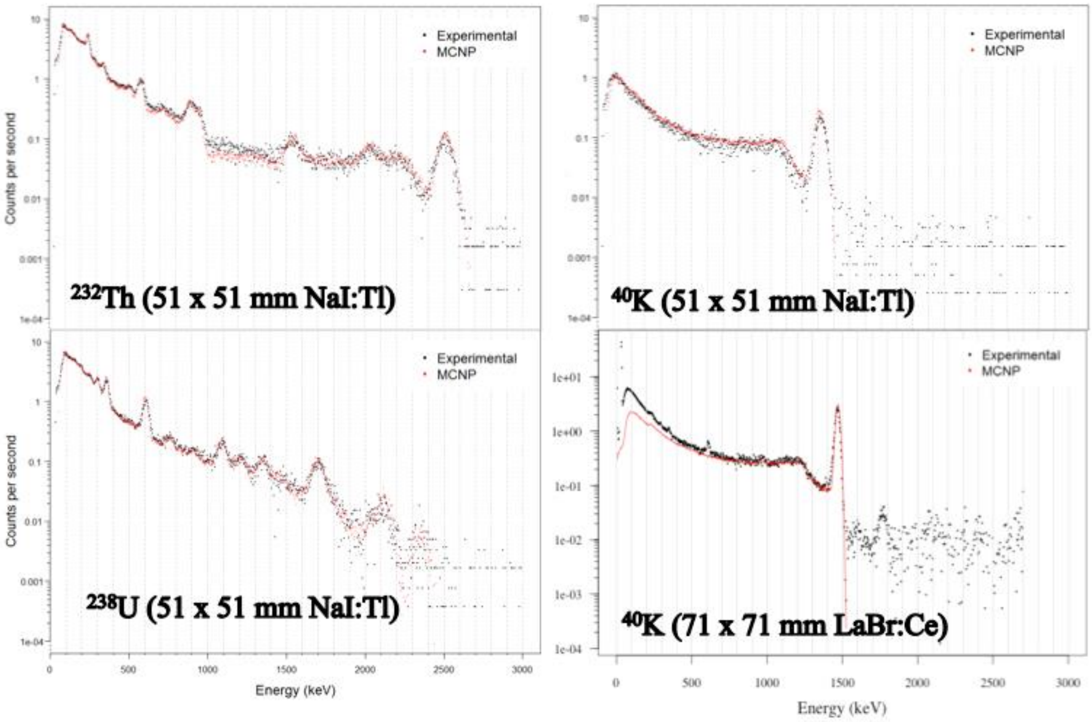

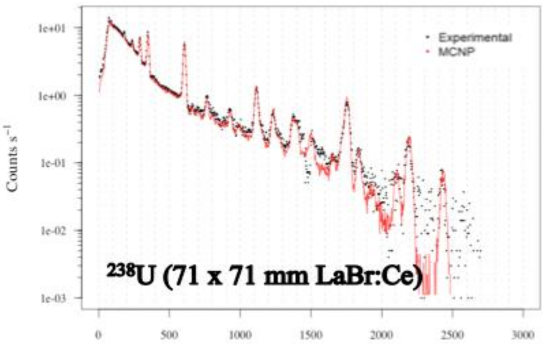

Experimental
MCNP
Counts s^{-1}
1e+01
1e+00
1e-01
1e-02
1e-03
0
500
1000
1500
2000
2500
3000
^{238}U (71 x 71 mm LaBr:Ce)

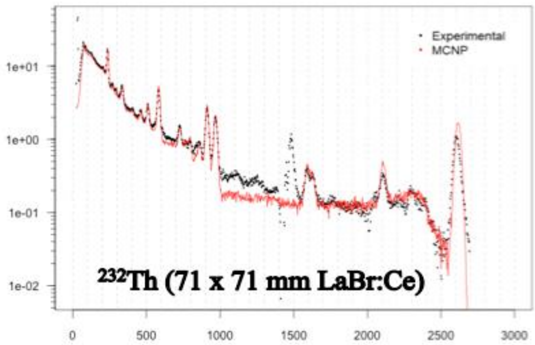

Experimental
MCNP
1e+01
1e+00
1e-01
1e-02
0
500
1000
1500
2000
2500
3000
^{232}Th (71 x 71 mm LaBr:Ce)

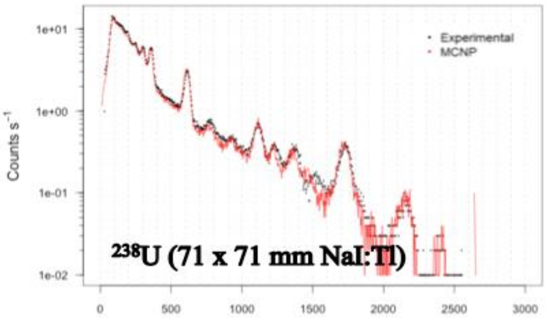

Experimental
MCNP
Counts s^{-1}
1e+01
1e+00
1e-01
1e-02
0
500
1000
1500
2000
2500
3000
^{238}U (71 x 71 mm NaI:Tl)

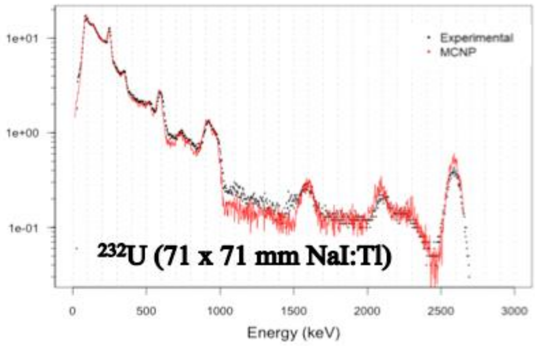

Experimental
MCNP
1e+01
1e+00
1e-01
0
500
1000
1500
2000
2500
3000
Energy (keV)
^{232}U (71 x 71 mm NaI:Tl)

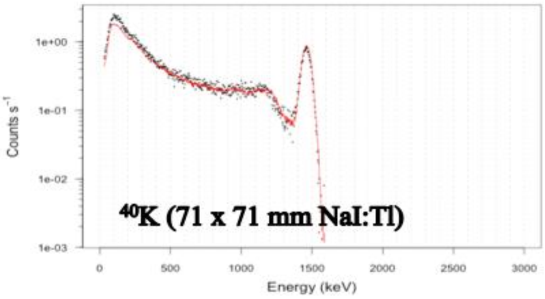

Counts s^{-1}
1e+00
1e-01
1e-02
1e-03
0
500
1000
1500
2000
2500
3000
Energy (keV)
^{40}K (71 x 71 mm NaI:Tl)